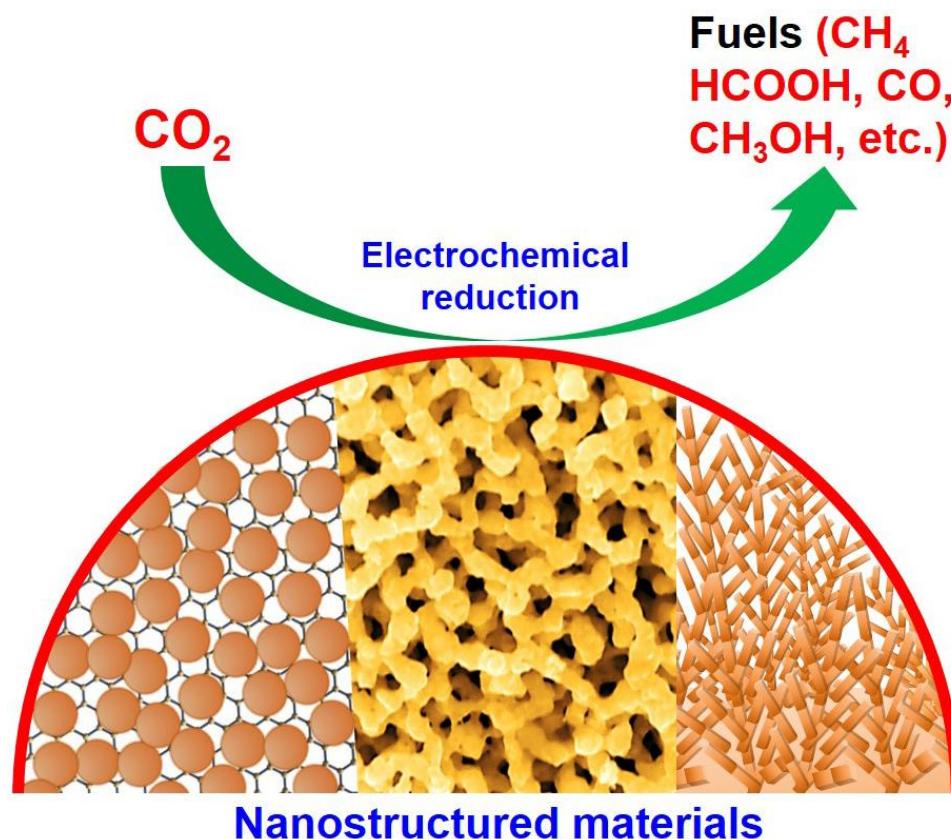


# Electrochemical reduction of carbon dioxide on nanostructured catalysts



By

**Md Nur Hossain**

A thesis submitted in conformity with the requirements for the Degree of  
Doctor of Philosophy in Chemistry and Materials Science Faculty of Science and  
Environmental Studies Department of Chemistry

Lakehead University

Copyright©2018 by Md Nur Hossain

## Abstract

There is great interest in the conversion of carbon dioxide (CO<sub>2</sub>) to useful chemicals and fuels toward addressing the increasingly serious impacts of global climate change. The electrochemical reduction of CO<sub>2</sub> has garnered keen and broad interest due to the development of efficient electrocatalysts. In this thesis I initially demonstrated a facile approach for the synthesis of a novel nanostructured thin film comprised of Cu nanoparticles (NPs) and reduced graphene oxide (rGO) on a glassy carbon electrode (GCE), via the direct electrochemical reduction of a mixture of copper and graphene oxide (GO) precursors. The effects of an applied potential on the electrochemical reduction of CO<sub>2</sub> was investigated using linear sweep voltammetric (LSV) and chronoamperometric (CA) techniques. Carbon monoxide (CO) and formate were found as the primary products based on gas chromatograph (GC) and high performance liquid chromatography (HPLC) analysis. The electrochemical reduction of CO<sub>2</sub> at the Cu/rGO thin film was further studied using in situ electrochemical ATR-FTIR spectroscopy to identify the liquid products that were generated at different applied cathodic potentials. Our experimental measurements revealed that the nanostructured Cu/rGO thin film exhibited excellent stability and superb catalytic activity for the electrochemical reduction of CO<sub>2</sub> in an aqueous solution, with a high current efficiency of 69.4% at -0.6 V vs. RHE.

To enhance the catalytic activity for the reduction of CO<sub>2</sub> on the rGO and Cu thin film, I further synthesized a unique nanocomposite that consisted of Cu NPs and rGO, which were supported on a Cu substrate. This nanocomposite was optimized in terms of the composition of the Cu NPs and rGO, as well as the overall quantity. A GC was employed to analyze the gaseous products, whereas a chemical oxygen demand (COD) method was proposed and utilized to quantify the overall liquid products. The optimized nanocomposite had the capacity to

effectively reduce CO<sub>2</sub> to CO, HCOOH, and CH<sub>4</sub> with a Faradaic efficiency (FE) of 76.6% at -0.4 V (vs. RHE) in a CO<sub>2</sub> saturated NaHCO<sub>3</sub> solution.

Subsequently, I electrodeposited Cu NPs on a Ti substrate as an electrocatalyst for the reduction of CO<sub>2</sub>, where the catalytic performance of the deposited Cu was further enhanced via a thermal treatment wherein different chemicals were used. Novel Cu nanodendrites were formed when treated with a mixture of CuSO<sub>4</sub> and H<sub>2</sub>SO<sub>4</sub>. These Cu nanodendrites exhibited superior catalytic activity for the electrochemical reduction of CO<sub>2</sub>. The instant current efficiency (ICE) and steady-state current efficiency (SSCE) for CO<sub>2</sub> reduction were determined at different applied electrode potentials by employing LSV and CA, respectively. The highest ICE (84.3%) and SSCE (82%) were obtained on the formed Cu nanodendrites at -0.4 V (vs. RHE) in a CO<sub>2</sub>-saturated 0.1 M NaHCO<sub>3</sub> over 6 h of electrolysis. The mechanisms of the CO<sub>2</sub> reduction were further investigated using in situ electrochemical ATR-FTIR spectroscopy, which confirmed the formation of formate and hydrocarbons at electrode potentials of lower than -0.2 and -0.5 V (vs. RHE), respectively. The facile approach for the synthesis of the unique Cu nanodendrites, their superior catalytic activity and high FE, made these Cu nanodendrites a promising electrocatalyst for the efficient reduction of CO<sub>2</sub> to fuels.

Finally, I designed and prepared three-dimensional (3D) nanoporous gold (Au), resulting from a facile electrochemical alloying/dealloying technique, for the efficient electrochemical reduction of CO<sub>2</sub> to CO. The formed nanoporous Au was further thermally treated with H<sub>2</sub>SO<sub>4</sub>, whereupon a significant enhancement of its electrocatalytic activity was achieved. The treated nanoporous Au exhibited a current density that was over 65 times higher than a polycrystalline Au surface, with a threefold higher current density than untreated nanoporous Au at -0.6 V vs. RHE in a CO<sub>2</sub>-saturated 0.1 M NaHCO<sub>3</sub> solution. Further, the FE of the treated nanoporous Au

at applied potentials of -0.6 V for 10 h was extremely high (95.9%), which revealed that the surface structure played a critical role in the electrochemical reduction of CO<sub>2</sub>. The superior catalytic activity, high production rate, excellent FE, and high stability made this acid treated nanoporous Au a promising electrocatalyst for the selective conversion of CO<sub>2</sub> to CO to address pressing environmental and energy challenges.

## Acknowledgements

First and foremost, I would like to offer my heartfelt gratitude, reverence, and sincere respect to my most honorable supervisor of this thesis, Dr. Aicheng Chen for selecting such an important topic. I thank him for his scholarly guidance and research insight; for his expert suggestions; and finally for his active engagement and tireless efforts through the whole period of my research work. To him, I owe so much of my success.

Sincere thanks are also to my committee members, Dr. Gautam Das and Dr. Zi-Hua (Justin) Jiang for their encouragement, constructive suggestions, and feedback on my thesis. I would like to express my gratitude to Dr. Robert Mawhinney, the coordinator of the PhD Chemistry and Materials Science program, and Dr. Craig MacKinnon, the Chair of the Department of Chemistry for their generous help and cooperation.

I am profoundly grateful to Jiali Wen for her valuable time, willingness to share knowledge, significant suggestions and extensive effort in helping me prepare my experiments during my Ph. D. study. I am also grateful to Dr. Gousheng Wu, Dr. Maduraiveeran Govindhan, Dr. Zhonggang Liu, Dr. Suresh Kumar Konda, and Shuai Chen for their suggestions, support, and help during the research work.

I am thankful to all my fellow lab members of Dr. Chen's research group, past and present, including Dr. Kai Yan, Antony Raj Thiruppathi, Dr. BalRam Adhikari, Dr. Boopathi Sidhureddy, Dr. Mona Amiri, Dr. Sapan Thind, Dr. Xin Chang, Dulanjana Wijewardena, Jesse Smiles Dondapati, Md. Motasser Hossain, Sharmila Durairaj, Venkateshsubramanian Manikandan, Cody Jarvis, Emily Puumala, Zhaoyang Zhang, Cassandra Ostrom, Walaa Alammari, and Frank Boehm for their suggestions, support, help, collaboration, time and

friendship. They have also made my study, research work, and time in the labs more enjoyable and productive through the entirety of my Ph. D. study.

I would like to extend my thanks to both faculty and staff members of the Department of Chemistry for their support, help, and cooperation over the last few years. Thank you also to the Department of Chemical Engineering & Applied Chemistry at the University of Toronto for accomplishing the XPS analysis.

I acknowledge the Ontario Trillium Scholarship for their financial support during my Ph. D. study over last four years. This thesis project was also supported by a Discovery Grant from the Natural Sciences and Engineering Research Council of Canada. Thank you for providing this research opportunity.

In addition, I am grateful to all my friends, well-wishers, and all those who have directly or indirectly helped me in the whole period of my thesis work. In particular, Azom, Jakir, Noor, Imrul, Rohit, Kamrul, and Shafiq have made my times enjoyable, and I am lucky to have friends like you all. Moreover, I must thank all the Bangladeshi family and friends in Thunder Bay for their invitations, spicy foods, time and friendship.

Lastly, I must mention my respect and heartfelt gratitude towards my beloved Mom and all the family members for their all-time love and care, blessings and sacrifice, inspiration and mental support.

# Table of Contents

<b>Abstract</b> .....	I
<b>Acknowledgements</b> .....	IV
<b>List of Figures</b> .....	IX
<b>List of Tables</b> .....	XVI
<b>List of Abbreviations and Symbols</b> .....	XVIII
<b>Chapter 1: Introduction</b> .....	1
<b>1.1 Chemical nature of CO<sub>2</sub></b> .....	2
<b>1.2 Energy consumption and CO<sub>2</sub> emissions</b> .....	4
<b>1.3 Technologies for CO<sub>2</sub> conversion</b> .....	6
<b>1.4 Challenges in the electrochemical reduction of CO<sub>2</sub></b> .....	11
<b>1.4.1 Thermodynamic issues</b> .....	13
<b>1.4.2 Kinetic concerns</b> .....	14
<b>1.4.3 Technological challenges</b> .....	15
<b>1.5 The objectives and outline of this thesis</b> .....	17
<b>Chapter 2: Literature Review</b> .....	24
<b>2.1 Introduction</b> .....	24
<b>2.2.1 Copper (Cu) catalysts</b> .....	25
<b>2.2.2 Gold (Au) catalysts</b> .....	37
<b>2.2.3 Ag catalysts</b> .....	40
<b>2.2.4 Other metal catalysts</b> .....	42
<b>2.2.5 Alloy catalysts</b> .....	43
<b>2.2.6 Carbon and carbon-based electrocatalysts</b> .....	44
<b>2.3 Reaction pathways of CO<sub>2</sub> electroreduction</b> .....	49
<b>2.3.1 Theoretical insights</b> .....	50
<b>2.3.2 Proposed pathways based on experimental results</b> .....	54
<b>2.4 Stability and activity degradation of catalysts</b> .....	57
<b>2.5 Summary and perspectives</b> .....	59
<b>Chapter 3: Electrochemical and FTIR spectroscopic study of CO<sub>2</sub> reduction at a nanostructured Cu/reduced graphene oxide thin film</b> .....	72
<b>3.1 Introduction</b> .....	72
<b>3.2 Methods</b> .....	73
<b>3.3 Results and Discussion</b> .....	75

3.4 Conclusions.....	84
<b>Chapter 4: Unique copper and reduced graphene oxide nanocomposite toward the efficient electrochemical reduction of carbon dioxide.....</b>	<b>87</b>
4.1 Introduction.....	87
4.2 Methods.....	88
4.2.1 Materials .....	88
4.2.2 Synthesis of Cu-rGO nanocomposites.....	89
4.2.3 Structural characterization .....	90
4.2.4 Electrochemical characterization .....	90
4.2.5 Product analysis .....	91
4.3 Results .....	91
4.3.1 Syntheses and characterization of Cu-rGO nanocomposites.....	91
4.3.2 Bulk electrolysis of CO <sub>2</sub> .....	104
4.4 Discussion.....	108
<b>Chapter 5: Synthesis, electrochemical and in situ FTIR study of Cu nanodendrites toward efficient CO<sub>2</sub> reduction .....</b>	<b>113</b>
5.1 Introduction.....	113
5.2 Experimental section .....	116
5.2.1 Chemicals and materials .....	116
5.2.2 Fabrication of electrodes .....	116
5.2.3 Characterization of electrodes .....	118
5.2.4 Electrochemical characterization .....	118
5.2.5 Electrochemically active surface area (EASA) determination.....	119
5.2.6 In situ electrochemical ATR-FTIR study .....	119
5.2.7 Bulk electrolysis of CO <sub>2</sub> .....	120
5.3 Results and discussion .....	122
5.3.1 Characterization of electrodes .....	122
5.3.2 Electrochemical characterization .....	130
5.3.3 In situ electrochemical ATR-FTIR study .....	134
5.4 Conclusions.....	141
<b>Chapter 6: Enhanced catalytic activity of nanoporous Au for the efficient electrochemical reduction of carbon dioxide .....</b>	<b>145</b>
6.1 Introduction.....	145



<b>6.2 Experimental section</b> .....	146
<b>6.2.1 Chemicals and materials</b> .....	146
<b>6.2.2 Fabrication of nanoporous Au electrodes</b> .....	147
<b>6.2.3 Structural characterization</b> .....	148
<b>6.2.4 Electrochemical characterization</b> .....	148
<b>6.2.5 Electrochemically active surface area (EASA) measurement and roughness factor (RF) calculation</b> .....	149
<b>6.2.6 Product analysis</b> .....	151
<b>6.3 Results and discussion</b> .....	151
<b>6.4 Conclusions</b> .....	166
<b>Chapter 7: Summary and future directions</b> .....	170
<b>7.1 Summary</b> .....	170
<b>7.2 Future work</b> .....	176

## List of Figures

<b>Figure 1.1</b> World energy consumption by fuel, based on BP Statistical Review of World Energy 2015.....	3
<b>Figure 1.2</b> Global greenhouse gas emissions by energy sectors.....	3
<b>Figure 1.3</b> (A) Global anthropogenic CO <sub>2</sub> emissions from forestry and other land uses, as well as from fossil fuel combustion, cement production, and flaring, (A) Atmospheric concentrations of CO <sub>2</sub> determined from ice core data (dots) and from direct atmospheric measurements (lines) ....	4
<b>Figure 1.4</b> The minimum potential requirement with a sufficient number of electrons for the formation of different products resulting from the electrochemical reduction of CO <sub>2</sub> calculated according to thermodynamic reactions. ....	12
<b>Figure 2.1</b> Faradaic yields of the products in the electrochemical reduction of CO <sub>2</sub> , at 19 °C in KHCO <sub>3</sub> aqueous solutions of various concentrations. Current density = 5 mA cm <sup>-2</sup> . Bottom: Δ, C <sub>2</sub> H <sub>4</sub> ; O, CH <sub>4</sub> ; Top: □, H <sub>2</sub> ; ◇, EtOH; Δ, Pr <sup>n</sup> OH.....	26
<b>Figure 2.2</b> Variation of the Faradaic efficiencies of the products in the electrochemical reduction of CO <sub>2</sub> obtained in controlled potential electrolysis, 0.1 mol dm <sup>-3</sup> KHCO <sub>3</sub> at 19 °C.....	27
<b>Figure 2.3</b> Scanning electron microscopy of three surfaces: (a) Sample A (electropolished surface), (b) Sample B (copper nanoparticle covered surface) and (c) Sample C (sputtered surface).....	28
<b>Figure 2.4</b> (A) CO <sub>2</sub> reduction current as a function of time for catalysts A (Cu mesocrystals), B (Cu nanoparticles), and C (electropolished Cu). Potential applied: -0.99 V. The inset is a zoomed-in picture of the reduction currents at the start of the CO <sub>2</sub> reduction process. (B) Faradaic efficiencies of the CO <sub>2</sub> electroreduction products of catalyst A as a function of potential. A comparison of the (C) Faradaic efficiencies and (D) production rates of CO <sub>2</sub> electroreduction products on catalysts A, B, and C at -0.99 V.....	29
<b>Figure 2.5</b> Determination of double-layer capacitance for an electrode annealed at 500 °C for 12 h and subsequently reduced in 0.5 M NaHCO <sub>3</sub> at -0.5 vs. RHE. a) CVs taken over a range of	

scan rates in a potential window where only double-layer charging and discharging is relevant. b) Current due to double-layer charge/discharge plotted against CV scan rate. .... 31

**Figure 2.6** Oxygenate/hydrocarbon ratios for  $>2e^-$  reduction products as a function of potential for Cu (111), (751), and (100).. .... 34

**Figure 2.7** (a) Linear sweep voltammetry of  $CO_2$  electroreduction over Au NP catalyst samples. Data were acquired at room temperature in 0.1 M  $KHCO_3$  with a  $-5$  mV/s scan rate, and were normalized by the respective Au surface areas after the subtraction of a background signal measured on clean glassy carbon. (b) Faradaic current densities at  $E = -1.2$  V vs RHE as a function of Au NP size, with error bars indicating NP size distributions..... 38

**Figure 2.8** Proposed reaction paths for electrochemical  $CO_2$  reduction on Cu(111), producing methane ( $CH_4$ ), methanol ( $CH_3OH$ ), and ethylene ( $C_2H_4$ ). The ( $H^+ + e^-$ ) reactants and  $H_2O$  product are left off the scheme..... 51

**Figure 2.9** (A) The lowest energy pathways of  $CO_2$  reduction on the  $Cu_{55}$ -defective graphene. (B and C) Relative free energy diagrams without (B) and with (C) applied potential for  $CO_2$  reduction on Cu(111) (empty rectangle with dashed lines),  $Cu_{55}$ -defective graphene (filled rectangle with solid lines), and  $Cu_{55}$  cluster (empty rectangle in the inset).. .... 52

**Figure 2.10** Proposed reaction pathway for  $C_2$  and  $C_3$  products with enol-like surface intermediates. Arrows between overlapping circles indicate changes between the enol, keto, and diol forms of each product. Arrows between non-overlapping circles indicate electrochemical reduction steps involving the addition of  $2H^+$  and  $2e^-$ . For simplification, product names are intended to refer to all forms of the product. .... 55

**Figure 2.11** Proposed mechanisms for  $CO_2$  reduction to CO on polycrystalline Au and oxide-derived Au..... 56

**Figure 3.1** SEM images of rGO (a), Cu NPs (b), and Cu/rGO thin film (c); (d) EDX spectra of Cu NPs (i), rGO (ii), and Cu-rGO thin film (iii)..... 75

**Figure 3.2** XPS spectra of the C1s region (a) and the Cu2p region (b) of the precursor mixture film before (i) and after (ii) the cyclic voltammetric treatment, where red and blue lines represent the raw data and the total fitting curve, respectively. .... 76

**Figure 3.3** (a) LSVs of the bare GCE and the GCEs modified with rGO, Cu NPs, and Cu/rGO thin films recorded in a CO<sub>2</sub>-saturated 0.1M NaHCO<sub>3</sub> solution; (b) LSVs of the Cu/rGO thin film measured in the CO<sub>2</sub>-saturated 0.1M NaHCO<sub>3</sub> solution (blue) and in the Ar-saturated 0.05M Na<sub>2</sub>SO<sub>4</sub> solution whose pH was adjusted to 6.65 (black) at 20 mV s<sup>-1</sup>; the insert displays the calculated instant current efficiency. .... 78

**Figure 3.4** In situ electrochemical ATR-FTIR spectra recorded during the electrochemical reduction of CO<sub>2</sub> at the Cu/rGO thin film at the different applied potentials varied from -0.1 to -0.6 V vs. RHE in a CO<sub>2</sub>-saturated 0.1M NaHCO<sub>3</sub> solution..... 80

**Figure 3.5** CA curves of the Cu/rGO thin film recorded in the Ar-saturated 0.05M Na<sub>2</sub>SO<sub>4</sub> solution (a) and the CO<sub>2</sub>-saturated 0.1M NaHCO<sub>3</sub> solution (b) at the different applied potentials of -0.4, -0.5, -0.6 and -0.7 V. .... 82

**Figure 3.6** Corresponding steady-state current efficiency (%) for CO<sub>2</sub> reduction calculated from the CA curves displayed in Figure 3.5a and 3.5b. .... 83

**Figure 4.1** SEM images of the formed Cu NPs (a) and the Cu-rGO nanocomposite (b) on a Cu substrate. (c) EDX spectra of the Cu NPs (i) and the Cu-rGO nanocomposite electrode (ii). ..... 92

**Figure 4.2** High-resolution XPS spectra of the C1s region (a and c) and the Cu2p region (b and d) of the CuSO<sub>4</sub>-GO thin film before the electrochemical treatment and the formed Cu-rGO nanocomposite. .... 93

**Figure 4.3** (a) LSV curves of the bare Cu substrate, rGO, Cu NPs and Cu-rGO nanocomposite electrodes; and (b) corresponding CA curves of the bare Cu substrate (black), Cu NPs (red), rGO (green), Cu-rGO nanocomposite (blue) electrodes recorded at -0.4 V in a CO<sub>2</sub>-saturated 0.1 M NaHCO<sub>3</sub> solution..... 96

**Figure 4.4** Nyquist plots measured at the potential of -0.4 V in a CO<sub>2</sub>- saturated 0.1 M NaHCO<sub>3</sub> solution on different electrodes. Inset: the equivalent electric circuit used for fitting the EIS data, where R<sub>s</sub> = solution resistance; CPE = constant phase element; R<sub>ct</sub> = charge-transfer resistance; W<sub>s</sub> = Warburg impedance (short). .... 97

**Figure 4.5** LSV curves (a) and CA plots (b) of the Cu-rGO nanocomposite electrodes prepared with a constant GO concentration (0.5 mg mL<sup>-1</sup>) while the concentration of the Cu precursor was changed from 5 to 25 mM as listed in Figure 4.5a. LSV curves (c) and CA plots (d) for the

optimization of the GO concentration while the concentration of the Cu precursor was maintained at 10 mM. .... 99

**Figure 4.6** LSV curves (a) and CA plots (b) of the Cu-rGO nanocomposite electrodes prepared with the optimized GO ( $0.5 \text{ mg mL}^{-1}$ ) and Cu (10 mM) concentration while the volume of the mixed solution was altered from 25 to 150  $\mu\text{L}$  as listed in Figure 4.6a..... 100

**Figure 4.7** Nyquist plots of the optimized Cu-rGO nanocomposite electrode recorded at -0.3, -0.4, -0.5, and -0.6 V in a  $\text{CO}_2$  saturated 0.1 M  $\text{NaHCO}_3$  solution. The symbols denote the experimental data and the solid lines correspond to the fitted results using the equivalent electrical circuit (inset). The amplitude of the modulation potential was 10 mV and the frequency was altered from 100 kHz to 10 mHz. .... 101

**Figure 4.8** (a) CA curves of the optimized Cu-rGO nanocomposite recorded at the selected potentials of -0.4, -0.5, and -0.6 V for product analysis. (b) The corresponding Faradaic efficiency of the formed products at the different applied potentials over the six hours. (c) The rates of product formation during the electrochemical reduction of  $\text{CO}_2$  at the applied potentials on the Cu-rGO nanocomposite electrode..... 103

**Figure 4.9** The stability test of the optimized nanocomposite electrode carried at -0.5 V in a  $\text{CO}_2$ -saturated 0.1 M  $\text{NaHCO}_3$  solution under continuous  $\text{CO}_2$  purging..... 107

**Figure 5.1** SEM images depict the uncalcined Cu thin film (A); OD-Cu thin film (B); Cu particles (C); Cu NPs (D); Cu nanodendrites (E)..... 121

**Figure 5.2** Surface morphology of the formed copper oxides; (A) Low magnification SEM image, (B) High magnification SEM images..... 122

**Figure 5.3** EDX spectra (A) and XRD pattern of the formed CuO. .... 124

**Figure 5.4** (A) XRD spectrum of the differently formed Cu electrodes, (i) Cu thin film, (ii), OD-Cu thin film, (iii) Cu particles, (iv) Cu NPs, (v) Cu nanodendrites; XPS spectrum at Cu2p region of copper oxides, prior to electrochemical reduction, (B); and Cu nanodendrites, following electrochemical reduction (C)..... 125

**Figure 5.5** Reduction of copper oxides to form the Cu nanodendrites applying  $-10 \text{ mA cm}^{-2}$  current density for 1800 s in a  $\text{CO}_2$ -saturated 0.1 M  $\text{NaHCO}_3$  solution. .... 126

**Figure 5.6** Electrochemical surface area measurement; determination of double-layer capacitance by cyclic voltammograms over a range of scan rates for (A) Cu plate, (B) Cu thin film, (C) OD-Cu thin film, and (D) Cu nanodendrites in 0.1 M HClO<sub>4</sub> solution. .... 127

**Figure 5.7** Corresponding current due to double-layer charging/discharging plotted against cyclic voltammetry's scan rate of Figure 5.6; (A) Cu plate, (B) Cu thin film, (C) OD-Cu thin film, and (D) Cu nanodendrites. .... 128

**Figure 5.8** LSV recorded on different nanostructured Cu, (A) Cu thin film (i), OD-Cu thin film (ii), Cu particles (iii), Cu NPs (iv), Cu nanodendrites (v); (B) Different Cu nanodendrites electrodes changing the volume of the mixture of the treating agent during calcination at 500 °C for 1 h; (C) Changing the calcination temperature where the volume of the treating agents was 50 μL on etch electrode during 1 hour calcination; (D) Changing the calcination time where the volume of the mixture of the treating agents was 50 μL on etch electrode during calcination at 500 °C; in a CO<sub>2</sub>-saturated 0.1 M NaHCO<sub>3</sub> solution. .... 129

**Figure 5.9** CA recorded at -0.4 V on different nanostructured Cu, (A) Cu thin film (i), OD-Cu thin film (ii), Cu particles (iii), Cu NPs (iv), Cu nanodendrites (v); (B) Different Cu nanodendrites electrodes changing the volume of the mixture of the treating agent during calcination at 500 °C for 1 h; (C) Changing the calcination temperature where the volume of the treating agents was 50 μL on etch electrode during 1 hour calcination; (D) Changing the calcination time where the volume of the mixture of the treating agents was 50 μL on etch electrode during calcination at 500 °C; in a CO<sub>2</sub>-saturated 0.1 M NaHCO<sub>3</sub> solution. .... 131

**Figure 5.10** (A) LSV recorded on Cu nanodendrites in an Ar-saturated 0.05 M Na<sub>2</sub>SO<sub>4</sub> solution (blue curve), and in a CO<sub>2</sub>-saturated 0.1 M NaHCO<sub>3</sub> solution (red curve); the inset presents the corresponding instant current efficiency; and (B) Steady-state current efficiency (%) for CO<sub>2</sub> reduction at different applied potentials. .... 133

**Figure 5.11** (A) In situ ATR-FTIR for the electrochemical reduction of CO<sub>2</sub> on Cu nanodendrites in a CO<sub>2</sub>-saturated 0.1 M NaHCO<sub>3</sub> solution under different applied potentials (vs. RHE), (B) At -0.4 and -0.6 V (vs. RHE); (C) Integration area of CO<sub>2</sub> absorption at these potentials. The reference spectra were obtained at +0.2 V (vs. RHE) where all of the spectra were collected with 32 co-added scans. .... 136

<b>Figure 5.12</b> $^1\text{H}$ NMR spectra of the formed products from the electrochemical reduction of $\text{CO}_2$ at -0.6 V (vs. RHE) for 2 h on Cu nanodendrites catalysts. TMS is used as the reference. ....	137
<b>Figure 5.13</b> Time-resolved ATR-FTIR spectra of $\text{CO}_2$ electroreduction on Cu nanodendrites at -0.4 V (vs. RHE). (A) 6 to 60 s; (B) 66 to 120 s. The reference spectra were obtained at +0.2 V (vs. RHE), and all of the spectra were collected with 8 co-added scans. ....	139
<b>Figure 5.14</b> Integration area of $\text{CO}_2$ adsorption from the figure (5.13A and 5.13B) during the electrolysis $\text{CO}_2$ on the formed Cu nanodendrites electrode surface at -0.4 V (vs. RHE). ....	140
<b>Figure 6.1</b> Schematics of the preparation of the NP Au and the acid treated NP Au. ....	149
<b>Figure 6.2</b> (A) SEM image, (B) EDX spectra and (C) XRD patterns of the formed Au/Zn alloy. ....	150
<b>Figure 6.3</b> Low-magnification SEM images of (A) the NP Au electrode, and (B) the acid-treated NP Au electrode; High-magnification SEM images of (C) the NP Au electrode and (D) the acid-treated NP Au electrode. ....	152
<b>Figure 6.4</b> (A) EDX spectra and (B) XRD patterns of the three different Au electrodes. ....	153
<b>Figure 6.5</b> The XPS survey spectra of the NP Au (A) and the acid treated NP Au (B) electrodes. ....	155
<b>Figure 6.6</b> High-resolution XPS spectra of the Zn $2p_{3/2}$ region of the formed NP Au (A), the Au 4f region of the NP Au, (B) the treated NP Au (C) electrodes. ....	156
<b>Figure 6.7</b> Cyclic voltammograms of: (A) the smooth polycrystalline Au electrode; and (B) the NP Au electrode (red) and the acid treated NP Au electrode (blue). Scan rate: $20 \text{ mV s}^{-1}$ ; Electrolyte: $0.1 \text{ M H}_2\text{SO}_4$ . ....	157
<b>Figure 6.8</b> (A) LSVs of the three different Au electrodes recorded in a $\text{CO}_2$ -saturated $0.1 \text{ M}$ solution. (B) The corresponding Nyquist plots measured at -0.4 V. Inset: the equivalent electric circuit used for fitting the EIS data, where $R_s$ = solution resistance; $R_1$ and $R_2$ = charge-transfer resistances; $\text{CPE1}$ and $\text{CPE2}$ = constant phase elements; $W_s$ = Warburg impedance (short) ....	159
<b>Figure 6.9</b> The CA curves of the polycrystalline Au electrode (A), the NP Au electrode (B) and the acid treated NP Au electrode (C), recorded under different applied electrode potentials in $\text{CO}_2$ saturated $0.1 \text{ M NaHCO}_3$ over the 10 h electrolysis. ....	161

**Figure 6.10** (A) FE of the CO formation on the polycrystalline Au (black bar), the NP Au (red bar) and the acid-treated NP Au electrodes (blue bar); (B) the CO production rates during the electrolysis of CO<sub>2</sub> under different applied potentials on the Au, the NP Au and the acid-treated NP Au electrodes. .... 163

**Figure 6.11** Schematic diagram of the proposed mechanism for the accessibility of the solvated CO<sub>2</sub> into the pores of NP Au (left) and treated NP Au (right) during the electrochemical reduction of CO<sub>2</sub> to CO..... 165

**Figure 6.12** A video clip of CO evolution resulting from CO<sub>2</sub> electrolysis at -0.6 V in CO<sub>2</sub>-saturated 0.1 M NaHCO<sub>3</sub> on the NP Au electrode (A) and the acid treated NP Au electrode (B). .... 166

**Figure 7.1** Schematic representation of the electrocatalytic conversion of CO<sub>2</sub> into fuels on different nanostructured materials. .... 172



## List of Tables

<b>Table 1.1</b> Selected standard potentials of CO <sub>2</sub> in aqueous solutions (V vs. SHE) at 1.0 atm and 25 °C, calculated according to the standard Gibbs energies of the reactants in reactions. ....	13
<b>Table 2.1</b> Calculated free energies of adsorption, in eV, of key adsorbates on the (111), (100), and (211) crystal facets, shown with their optimized binding geometries, where a lower number indicates stronger binding. Reported energies are referenced to the electronic energy of a clean slab and reference atoms for H, C, and O of 1/2 H <sub>2</sub> , graphene, and (H <sub>2</sub> O–H <sub>2</sub> ), respectively. ....	33
<b>Table 4.1</b> XPS analysis of C1s peak of the CuSO <sub>4</sub> -GO thin film before the electrochemical treatment and the formed Cu-rGO nanocomposite. ....	94
<b>Table 4.2</b> XPS analysis of the Cu2p <sup>3/2</sup> peak of the CuSO <sub>4</sub> -GO thin film before the electrochemical treatment and the formed Cu-rGO nanocomposite. ....	94
<b>Table 4.3</b> Values of the elements in equivalent electric circuit fitted in the Nyquist plots of Figure 4.4 (error percentage for each element is given in parentheses). ....	98
<b>Table 4.4</b> Values of the elements in equivalent electric circuit fitted in the Nyquist plots of Figure 4.7. (Error percentage of each element is given in the parentheses). ....	102
<b>Table 4.5</b> Comparison of some promising Cu-based catalysts for the electrochemical reduction of CO <sub>2</sub> recently reported in the literature. ....	105
<b>Table 5.1</b> Different crystallite size of Cu and Cu <sub>2</sub> O of the formed Cu samples. ....	126
<b>Table 5.2</b> Determination of capacitance values and surface roughness factors of the different nanostructured Cu electrodes using CV. The surface roughness factor for Cu plate is defined to be 1. ....	128
<b>Table 6.1</b> Determination of the EASA of the three different Au electrodes. ....	157
<b>Table 6.2</b> Values of the elements in an equivalent electric circuit fitted in the Nyquist plots shown in Figure 6.8B (error percentage for each element is given in parentheses) ....	160
<b>Table 6.3</b> The FE and production rate of the CO at different Au electrodes at different applied electrode potentials. ....	164

**Table 7.1** Products obtained on different catalysts from the electrochemical reduction of CO<sub>2</sub>.  
..... 174

## List of Abbreviations and Symbols

atm	Atmospheric pressure
ATR-FTIR	Attenuated total reflection Fourier transform infrared spectroscopy
BP	British petroleum
CA	Chronoamperometry
CE	Current efficiency
CPE	Constant phase element
CH <sub>4</sub>	Methane
CO <sub>2</sub>	Carbon dioxide
CO	Carbon monoxide
COD	Chemical oxygen demand
CV	Cyclic Voltammetry
DFT	Density functional theory
<i>E</i>	Potential
EASA	Electrochemically active surface area
EC	Electrochemical
EDX	Energy dispersive X-ray spectroscopy
EIS	Electrochemical Impedance Spectroscopic
F	Faraday constant
FE	Faradaic efficiency
GC	Gas chromatography
GCE	Glassy carbon electrode
GC-MS	Gas chromatography mass spectrometry
GO	Graphene oxide
Gt	Gigaton
h	Hour
HCOOH	Formic acid
HPLC	High-performance liquid chromatography
ICE	Instant current efficiency
ICP-AES	Inductively coupled plasma atomic emission spectroscopic

IEA	International Energy Agency
IPCC	Intergovernmental Panel on Climate Change
$j$	Current
LSV	Linear Sweep Voltammetry
M	Molarity
N	Nitrogen
NaHCO <sub>3</sub>	Sodium bi-carbonate
NHE	Normal hydrogen electrode
NP	Nanoporous
NP, NPs	Nanoparticles
OD	Oxide derived
ppm	Parts per million
Q	Charge
R <sub>s</sub>	Solution resistance
R <sub>ct</sub>	Charge-transfer resistance
RF	Roughness factor
RHE	Reversible hydrogen electrode
rGO	Reduced graphene oxide
SCE	Saturated calomel electrode
FE-SEM	Field-emission scanning electron microscopy
SHE	Standard hydrogen electrode
SSCE	Steady-state current efficiency
T	Temperature
TEM	Transmission electron microscopy
$V$	Volume
W <sub>s</sub>	Warburg impedance (short)
XPS	X-ray photoelectron spectroscopy
XRD	X-ray diffraction spectroscopy
3D	Three dimensional

## Chapter 1: Introduction

Over the last century, the expansion of the global population coupled with technology advances has increased energy consumption to an unprecedented level. The combustion of fossil fuels by industry, automobiles, and other human activities has increased continuously to meet ever higher demands. Unless the significant expansion of alternative and sustainable energy sources is implemented, there could well be an energy crisis that will be a common feature of life in the future. Considerable efforts are currently being invested to research and develop suitable pathways that will minimize the overall crisis. Carbon dioxide (CO<sub>2</sub>) is the primary product that is generated by the burning of fossil fuels. It is also produced from the Earth's oceans, as well as through soil respiration, biological decomposition, and volcanoes. The level of CO<sub>2</sub> in the atmosphere is ~400 ppm today, which is approximately 25% higher than it was 100 years ago [1, 2].

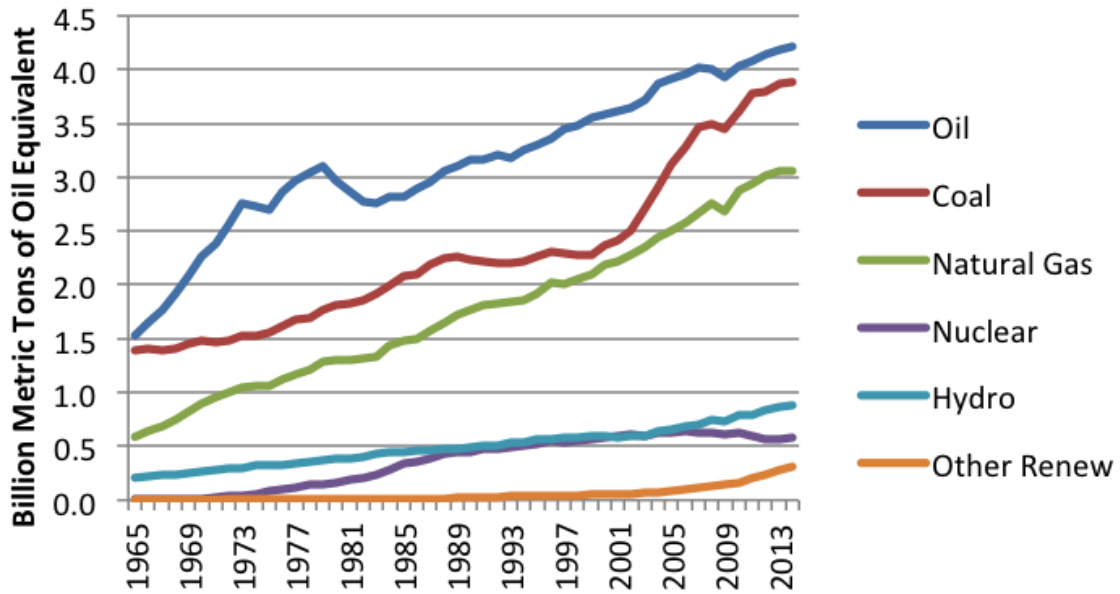
CO<sub>2</sub> is odorless, tasteless, colorless, and appears to be harmless and non-toxic to humans; however, it is also known to be one of the primary greenhouse gases, which absorbs infrared radiation. If the concentration of CO<sub>2</sub> in the ambient atmosphere is unbalanced by anthropogenic activities, it will initiate increases in average global temperatures. The rise of the average temperature in the environment is referred to as global warming that could cause widespread climate change. Therefore, significant efforts are being invested in research worldwide to investigate how we might prevent and reduce CO<sub>2</sub> emissions into the environment, including the conversion of CO<sub>2</sub> into fuels and usable chemicals to avert potential global catastrophe [1-3]. Presently, it is very challenging to prevent the release of CO<sub>2</sub> emissions, due to the increasing consumption of energy in daily human life, which entails fossil fuel combustion for the most part. The transformation of CO<sub>2</sub> to alternative energy sources might serve as a viable pathway for

its reduction in the ambient atmosphere. Catalytic conversion is a potential efficient strategy for converting CO<sub>2</sub> to fuels and value-added products such as carbon monoxide (CO), hydrocarbons, acids, alcohols, and more [4,5,6].

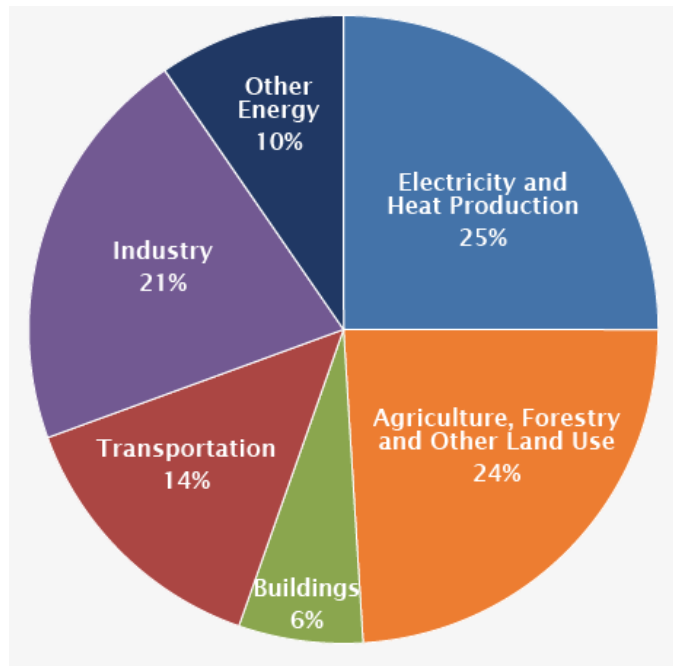
### 1.1 Chemical nature of CO<sub>2</sub>

CO<sub>2</sub> is known as a fully oxidized inert molecule, which is non-combustible, and thermodynamically stable. This small nonpolar linear molecule consists of a carbon atom that is covalently double-bonded to two oxygen atoms, with a C-O bond length of 1.16 Å. Although CO<sub>2</sub> is nonpolar overall, it contains polar bonds due to the electronegative difference between O and C atoms. The electronic structure of CO<sub>2</sub> could be O<sup>-δ</sup>-C<sup>+2δ</sup>-O<sup>-δ</sup>, which indicates the possibility of an electrophilic attack at the oxygen, and a nucleophilic attack at the carbon. As the ionization potential of CO<sub>2</sub> is 13.78 eV, it might weakly interact with only Bronsted and Lewis acids [7,8]. The solubility of CO<sub>2</sub> in water is higher than H<sub>2</sub>, N<sub>2</sub>, and O<sub>2</sub>, and the concentration of CO<sub>2</sub> in solution is 0.033 M at 25 °C under 1 atm CO<sub>2</sub>. It can be hydrated and reversibly forms carbonic acid (H<sub>2</sub>CO<sub>3</sub>) when in water and is stabilized at equilibrium (CO<sub>2</sub> + H<sub>2</sub>O ↔ H<sub>2</sub>CO<sub>3</sub>). The equilibrium constant for hydration (K<sub>h</sub>) of H<sub>2</sub>CO<sub>3</sub> at 25 °C, [H<sub>2</sub>CO<sub>3</sub>] / [CO<sub>2</sub>], is 1.70 x 10<sup>-3</sup>. Hence, the majority of the CO<sub>2</sub> is not converted into H<sub>2</sub>CO<sub>3</sub>, but remains as a CO<sub>2</sub> molecule known as dissolved CO<sub>2</sub>; however, it does not affect the pH of the solution. Equilibrium is obtained slowly in the absence of a catalyst, and the rate constants for the forward reaction (CO<sub>2</sub> + H<sub>2</sub>O → H<sub>2</sub>CO<sub>3</sub>) and reverse reaction (H<sub>2</sub>CO<sub>3</sub> → CO<sub>2</sub> + H<sub>2</sub>O) are 0.039 and 23 s<sup>-1</sup>, respectively. Being diprotic, H<sub>2</sub>CO<sub>3</sub> is initially dissociated into the bicarbonate ion (HCO<sub>3</sub><sup>-</sup>), which can be further dissociated to a carbonate ion (CO<sub>3</sub><sup>2-</sup>) [7,9,10]:

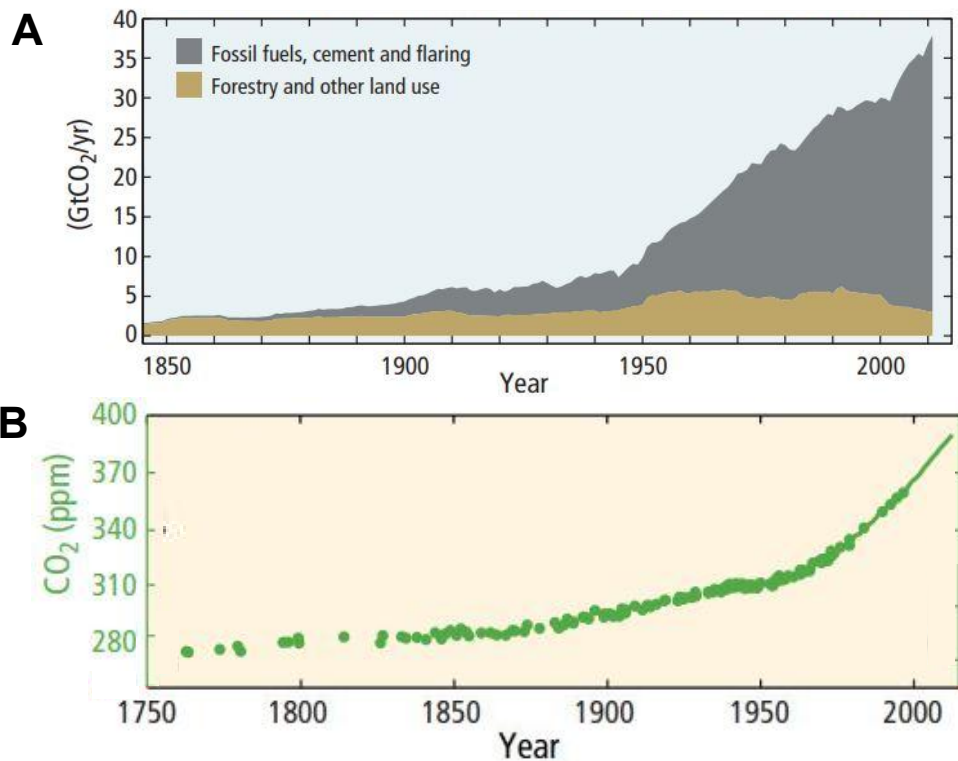




**Figure 1.1** World energy consumption by fuel, based on BP Statistical Review of World Energy 2015 [11].



**Figure 1.2** Global greenhouse gas emissions by energy sectors [1].



**Figure 1.3** (A) Global anthropogenic CO<sub>2</sub> emissions from forestry and other land uses, as well as from fossil fuel combustion, cement production, and flaring, (A) Atmospheric concentrations of CO<sub>2</sub> determined from ice core data (dots) and from direct atmospheric measurements (lines) [1].

The dissociation constants are  $pK_1 = 6.37$  and  $pK_2 = 10.25$  for reactions (1) and (2), respectively, where the first is calculated to include dissolved CO<sub>2</sub> in solution.

## 1.2 Energy consumption and CO<sub>2</sub> emissions

As the world population is growing faster, energy consumption is also gradually increasing. Since the industrial revolution, to mitigate the daily human energy demands, the burning of fossil fuels such as coal, gas, oil, petroleum, etc. have been the primary sources. According to the British Petroleum (BP) Statistical Review of World Energy 2015 [11], Figure 1.1 displays the world energy consumption, from 1965 to 2013, on the basis of oil use



equivalents, which shows that the overall global energy consumption rate is increasing. The consumption of fossil fuels (oil, coal, and gas) is increasing in parallel, whereas other energy production sources are growing at a relatively slow rate; however, not as rapidly as required (Figure 1.1). Based on available data in 2014, only 2.5% of the total world energy supply was in the form of renewable energy. Moreover, if the rate of fossil fuel consumption continues to rise, global fossil fuels reserves will soon be depleted. Hence, the world will undoubtedly face a severe energy crisis in the future, which would significantly disrupt everyday life, unless new alternative energy sources can be implemented.

Anthropogenic activities, particularly the burning of fossil fuels, result in the greenhouse gas emissions. Fossil fuels are widely used in industry, vehicles, electricity production, agriculture, and for other purposes. Figure 1.2 shows the global greenhouse emissions by different energy sectors according to the Intergovernmental Panel on Climate Change (IPCC) based on global emissions from 2010 [1]. The highest levels of global greenhouse gases are released from the burning of coal, natural gas, and oil, where approximately 35% of greenhouse gases are contributed by the transportation and industry sectors. Deforestation and cultivation comprise the second largest source of greenhouse gas emissions (Figure 1.2).

According to the International Energy Agency (IEA) 2013, close to 22 million tons of coal, 10 billion m<sup>3</sup> of natural gas, and 12 million tons of oil are used every day to fulfill ~82% of the world's energy needs [3,13]. As the result of the burning of these fossil fuels, CO<sub>2</sub> is the primary waste gas. Figure 1.3 displays global annual anthropogenic CO<sub>2</sub> emissions and atmospheric CO<sub>2</sub> concentrations, showing that both gradually increased after 1950 [1]. Over the last 100 years, cumulative CO<sub>2</sub> emissions have increased by about 25%, whereas annual global CO<sub>2</sub> emissions have recently reached about 36 billion tons in 2013 which comprises 78% of the

total current greenhouse gas emissions [1,2]. The rate of CO<sub>2</sub> emissions is continuously rising as shown in Figure 1.3A, which is projected to be equivalent to 43 billion tons annually by 2030 [2,13]. The corresponding CO<sub>2</sub> concentrations in the atmosphere is also increasing, as seen in Figure 1.3B, which has recently surpassed 400 ppm currently, which was measured at the Mauna Loa Observatory, Hawaii [1,14]. Therefore, the level of CO<sub>2</sub> in the earth's atmosphere has now surpassed its maximum level over the last 800,000 years. The natural carbon cycle has thus been severely affected due to the vast amount of anthropogenic CO<sub>2</sub> emissions, which can be observed as occurring via several increasingly destructive climate change phenomena [3,15]. Several adverse effects of climate change include increasing global average temperatures, ocean acidification, rising sea levels, melting of the polar ice caps, and the depletion of the ozone layers. More frequent and stronger storms, the spread of diseases and high rates of species extinctions are the result of high levels of greenhouse gases in the atmosphere caused by the unprecedented levels of fossil fuel combustion. For instance, the average global surface temperature and sea level have risen by about 1.1 °C and 8 inches over the last century, respectively [16]. Therefore, even though it represents an immense challenge, it is essential that we control CO<sub>2</sub> emissions into the atmosphere. A potential pathway toward the utilization and control of CO<sub>2</sub> emissions might be to turn this gas into fuels or value-added chemicals.

### **1.3 Technologies for CO<sub>2</sub> conversion**

Great efforts are being applied to the conversion and utilization of CO<sub>2</sub> for the purpose of the minimization of CO<sub>2</sub> emissions to balance the global carbon cycle. Different technologies have been used to convert CO<sub>2</sub> into fuels and usable chemicals. For example, CH<sub>4</sub>, methanol, etc. can be produced from the CO<sub>2</sub> by employing electrochemical and chemical methods. Further, a process known as CO<sub>2</sub> capture and storage could control the massive emissions that emanate

from thermal power plants, industries, and coal-fired plants, as these are responsible for around 40% of total emissions. This process could then convert CO<sub>2</sub> to a liquid under high pressure, which might be transported to a storage sites or could be buried underground [17]. Some of the CO<sub>2</sub> conversion technologies, and those that can efficiently produce value-added products are listed and discussed briefly below [18,19]:

- (a) Inorganic process: carbonates (Na<sub>2</sub>CO<sub>3</sub>, CaCO<sub>3</sub>, etc.)
- (b) Chemical conversion: carbamates, synthesis gas (CO + H<sub>2</sub>), hydrocarbons, methanol, ethanol, etc.
- (c) Photochemical reduction: carbon monoxide, formic acid, methane, etc.
- (d) Biological conversion: sugar, acetic acid, etc.
- (e) Electrochemical reduction: carbon monoxide, formic acid, methanol, ethanol, etc.

**(a) Inorganic process:** Inorganic base absorbents may be used to capture CO<sub>2</sub> from the atmosphere. Carbonate salts are formed from basic compounds such as CaCO<sub>3</sub>, which can be obtained by absorbing CO<sub>2</sub> in Ca(OH)<sub>2</sub> [20]. More than 7 Mt of synthetic CaCO<sub>3</sub> is produced annually from limestone, where CO<sub>2</sub> is used in the process that forms CaCO<sub>3</sub> [21]. Moreover, CO<sub>2</sub> is employed to synthesize SrCO<sub>3</sub>, Na<sub>2</sub>CO<sub>3</sub>, NaHCO<sub>3</sub>, and other carbonates. However, the reverse process of carbonate formation is endothermic. To recover the base from the formed carbonate salts requires a significant amount of energy. Hence, additional efforts are yet to be employed to discover suitable absorbents to capture CO<sub>2</sub> from the atmosphere that can be easily recycled.

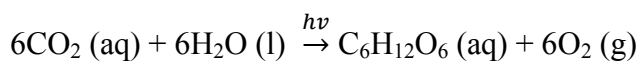
**(b) Chemical conversion:** As O atoms possess higher electronegativity than C atoms, the C-O bond is polar; hence, CO<sub>2</sub> molecules show a high affinity toward nucleophiles. CO<sub>2</sub> is also known as an anhydrous carbonic acid, which has a high attraction to basic compounds.

Therefore, CO<sub>2</sub> is used as a viable chemical feedstock in industry to manufacture various chemicals on a large scale, such as urea, salicylic acid, copolymers, polycarbonates, etc.. Approximately 130 megatons of CO<sub>2</sub> are used annually to prepare chemicals under suitable experimental conditions. For instance, urea is the most commonly produced chemical that consumes huge volumes of industrial CO<sub>2</sub>. Ammonia reacts with CO<sub>2</sub> at about 185-190 °C under high pressures of 180-200 atm to produce urea [5,22]. Moreover, the hydrogenation of CO<sub>2</sub> is widely used to synthesize methanol and hydrocarbons through heterogeneous catalysis [19]. Besides, CO<sub>2</sub> and CH<sub>4</sub> are used to produce synthetic gas (CO + H<sub>2</sub>) at around 800-1000 °C using a nickel-based catalyst (Ni/MgO) [23,24]. Synthetic gas is used for long-chain alkanes production by Fischer-Tropsch process, iron ore reduction, and is a crucial intermediate resource for organic synthesis [19]. However, these chemical technologies require high temperatures and pressures with limited catalysts to transform CO<sub>2</sub> into value-added chemicals.

**(c) Photochemical reduction:** Solar energy, utilized with photocatalysts to convert CO<sub>2</sub> into fuels and chemicals is known as the photochemical reduction of CO<sub>2</sub>. Intense efforts have been invested to develop efficient CO<sub>2</sub> photocatalysts, considering their high catalytic activity, long-term stability, and low cost [25-27]. Therefore, semiconductors (e.g., TiO<sub>2</sub>), transition metal complexes (e.g. Ru(Me)-C<sub>2</sub>-Re{P(FPh)<sub>3</sub>})<sub>2</sub>), and other composite materials (e.g., Mg-doped CuFeO<sub>2</sub>) have been used as catalysts for the photochemical conversion of CO<sub>2</sub> using solar light as the energy source and H<sub>2</sub>O as an electron and proton source [28-30]. The photocatalytic conversion of CO<sub>2</sub> is carried out at normal temperatures under atmospheric pressure, and the typical products are CO, HCOOH, CH<sub>4</sub>, and CH<sub>3</sub>OH. However, the quantity of CO<sub>2</sub> in the solvent is low; hence, photochemical reduction technologies are not energy efficient with the use

of current photocatalysts, and the production rate is very slow, which is quite distant from practical applications [6].

**(d) Biological conversion:** The biological conversion of CO<sub>2</sub> refers to the production of chemicals from CO<sub>2</sub> by living organisms through photosynthesis and respiration processes. Nature has evolved sophisticated mechanisms for the conversion of CO<sub>2</sub> into complex molecules, and has adopted carbon fixation over billions of years [31-33]. For instance, trees absorb CO<sub>2</sub> and convert it to glucose via the process of photosynthesis; moreover, many organisms such as algae, cyanobacteria, clostridia, etc. show an excellent ability to produce value-added chemicals through the utilization of CO<sub>2</sub> [33]. Natural processes involve energy consuming or releasing reactions to produce biomass. Classical photosynthesis reactions use solar radiation, where CO<sub>2</sub> reacts with H<sub>2</sub>O to produce glucose as shown below:



Approximately 200 Gt glucose (C<sub>6</sub>H<sub>12</sub>O<sub>6</sub>) is naturally formed by trees annually through the photosynthesis process [32]. Hence, the development of biomimetic processes to emulate biological CO<sub>2</sub> conversion may be used to synthesize bioplastics, biodiesel, and other valuable chemicals. However, the reaction rate in the biological CO<sub>2</sub> conversion process is very slow, and prototypes of this biological conversion have been developed, which is an ongoing process and more research is yet to be done to reach an ultimate goal for practical applications.

**(e) Electrochemical reduction:** The use of electrical energy by employing electrocatalysts to synthesize fuels and value-added chemicals from CO<sub>2</sub> is known as the electrochemical reduction of CO<sub>2</sub>. To produce thermodynamically more stable molecules from CO<sub>2</sub>, proton-couple electron steps and multi-electron reductions are more favorable than the single electron step process [34]. Electrochemical methods might provide an easy pathway to multielectron

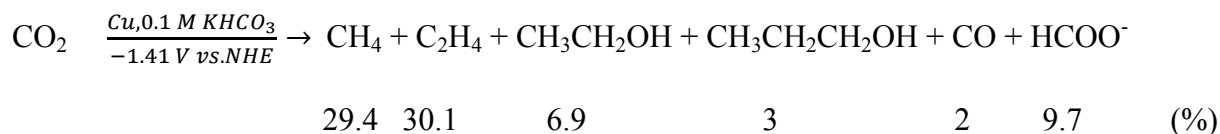
reduction steps, using unreactive metals, or other materials, to transform CO<sub>2</sub> into usable chemicals. Active electrocatalysts serve as an electron provider to CO<sub>2</sub>, which possess active sites on their surfaces where reaction intermediates can stabilize. Therefore fuels and chemicals such as CO, CH<sub>4</sub>, CH<sub>3</sub>COOH, and more, can be produced during the electrochemical reduction of CO<sub>2</sub>.

Among these current technologies, the conversion of CO<sub>2</sub> into fuels using electrochemical reduction technologies could serve as a viable approach for renewable energy generation [35,36]. The electrochemical reduction of CO<sub>2</sub> is rapidly becoming more popular as electrochemical technologies have several advantages [37,38]:

- (i) The technology is greener, and it does not produce any new CO<sub>2</sub>.
- (ii) The electrode potentials can easily control the electrochemical reduction systems.
- (iii) The electrical energy can be used directly for the conversion of CO<sub>2</sub> into fuel without harming the environment.
- (iv) The electrolyte solution can be recycled by isolating the generated liquid CO<sub>2</sub> reduction products.
- (v) The electrochemical technology is compact, simple to operate and can easily be scaled up for industrial applications.

Moreover, the electrocatalytic reduction of CO<sub>2</sub> is highly energy efficient toward acquiring target products, which could be integrated with renewable energy resources. Furthermore, the use of electrolyte solutions with electrocatalysts can lower the overpotential, increase the reaction rates, and can improve the selectivity of the CO<sub>2</sub> electrolysis [34,39]. Over the last few decades, scientists have developed various electrocatalysts to reduce CO<sub>2</sub> that are active in aqueous and non-aqueous solutions [9,37,40,41]. For instance, Cu and Au are well

known catalysts that can produce hydrocarbon fuels and CO from CO<sub>2</sub> in a NaHCO<sub>3</sub> aqueous solution under low applied potentials, respectively [42,43]. Transition metals and other metal-based materials are commonly explored as CO<sub>2</sub> electrocatalysts, which might be because they possess vacant d orbitals and active electrons that facilitate an easy pathway for the formation of reduction products by establishing bonds between CO<sub>2</sub> and the metal, which stabilizes the reaction intermediates [37]. Typical reduction products from the reduction of CO<sub>2</sub> on different electrocatalysts include carbon monoxide, hydrocarbons (CH<sub>4</sub>, C<sub>2</sub>H<sub>4</sub>), alcohols (CH<sub>3</sub>OH, CH<sub>3</sub>CH<sub>2</sub>OH), organic acids (HCOOH, CH<sub>3</sub>COOH), and other oxygenates (HCHO, CH<sub>3</sub>COCH<sub>3</sub>). For instance, the electrochemical reduction of CO<sub>2</sub> on a Cu metal electrode in 0.1 M KHCO<sub>3</sub> solution at -1.41 V (vs. NHE) gives CH<sub>4</sub>, C<sub>2</sub>H<sub>4</sub>, CH<sub>3</sub>CH<sub>2</sub>OH, CH<sub>3</sub>CH<sub>2</sub>CH<sub>2</sub>OH, CO, and HCOO<sup>-</sup> with an overall Faradaic efficiency (FE) of ~81% as shown below [44]:

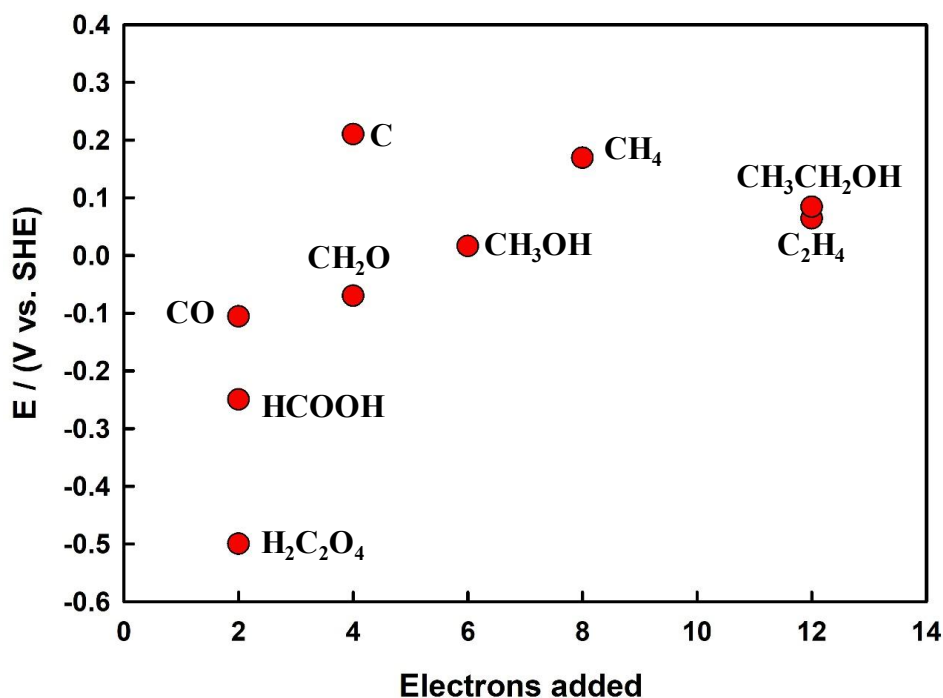


Several carbon and carbon-based materials have also been explored as electrocatalysts for the reduction of CO<sub>2</sub>.

#### 1.4 Challenges in the electrochemical reduction of CO<sub>2</sub>

The electrocatalytic conversion of CO<sub>2</sub> has drawn wide attention over the last few decades. The ultimate goal is to balance the global carbon cycle by recycling CO<sub>2</sub> into fuels and useful chemicals. Electrochemical reduction is considered as one of the most feasible technologies due to several advantages as the process is practical, controllable, compact, modular, and scalable. The process is highly energy efficient using suitable catalysts, and can be operated by renewable energy, or integrated into the renewable energy systems. Moreover, there is no new CO<sub>2</sub> evolved during the electroreduction of CO<sub>2</sub>; hence, the CO<sub>2</sub> electrolysis method is

a green technology [37,38]. However, several challenges remain that should be considered and overcome to achieve the potential rewards. CO<sub>2</sub> is a small inert, fully oxidized, and thermodynamically stable molecule, where the appropriate electrocatalysts for selective high throughput production via energy inputs is still unknown. The CO<sub>2</sub> reduction kinetics are slow even when a large electrode potential is employed, the energy efficiency of the process in aqueous solutions is low due to hydrogen evolution at high cathodic potentials, and the technology consumes high energy. The primary challenges for the reduction of CO<sub>2</sub> as relates to the electrocatalysts are low catalytic activity and stability. To overcome these challenges, researchers have considered thermodynamic and kinetic factors, as well as technological barriers to subjugate their limitations for the CO<sub>2</sub> conversion to carbon products [34,37].



**Figure 1.4** The minimum potential requirement with a sufficient number of electrons for the formation of different products resulting from the electrochemical reduction of CO<sub>2</sub> calculated according to thermodynamic reactions.



**Table 1.1** Selected standard potentials of CO<sub>2</sub> in aqueous solutions (V vs. SHE) at 1.0 atm and 25 °C, calculated according to the standard Gibbs energies of the reactants in reactions.

Reprinted with permission from ref. [45]. Copyright © 1985 CRC Press.

Electrochemical thermodynamic half-reactions	Electrode potentials (V vs. SHE) under standard conditions
$\text{CO}_2 (\text{g}) + 4\text{H}^+ + 4\text{e}^- = \text{C} (\text{s}) + 2\text{H}_2\text{O} (\text{l})$	0.210
$\text{CO}_2 (\text{g}) + 2\text{H}_2\text{O} (\text{l}) + 4\text{e}^- = \text{C} (\text{s}) + 4\text{OH}^-$	-0.627
$\text{CO}_2 (\text{g}) + 2\text{H}^+ + 2\text{e}^- = \text{HCOOH} (\text{l})$	-0.250
$\text{CO}_2 (\text{g}) + 2\text{H}_2\text{O} (\text{l}) + 2\text{e}^- = \text{HCOO}^- (\text{aq}) + \text{OH}^-$	-1.078
$\text{CO}_2 (\text{g}) + 2\text{H}^+ + 2\text{e}^- = \text{CO} (\text{g}) + \text{H}_2\text{O} (\text{l})$	-0.106
$\text{CO}_2 (\text{g}) + 2\text{H}_2\text{O} (\text{l}) + 2\text{e}^- = \text{CO} (\text{g}) + 2\text{OH}^-$	-0.934
$\text{CO}_2 (\text{g}) + 4\text{H}^+ + 4\text{e}^- = \text{CH}_2\text{O} (\text{l}) + \text{H}_2\text{O} (\text{l})$	-0.070
$\text{CO}_2 (\text{g}) + 3\text{H}_2\text{O} (\text{l}) + 4\text{e}^- = \text{CH}_2\text{O} (\text{l}) + 4\text{OH}^-$	-0.898
$\text{CO}_2 (\text{g}) + 6\text{H}^+ + 6\text{e}^- = \text{CH}_3\text{OH} (\text{l}) + \text{H}_2\text{O} (\text{l})$	0.016
$\text{CO}_2 (\text{g}) + 5\text{H}_2\text{O} (\text{l}) + 6\text{e}^- = \text{CH}_3\text{OH} (\text{l}) + 6\text{OH}^-$	-0.812
$\text{CO}_2 (\text{g}) + 8\text{H}^+ + 8\text{e}^- = \text{CH}_4 (\text{g}) + 2\text{H}_2\text{O} (\text{l})$	0.169
$\text{CO}_2 (\text{g}) + 6\text{H}_2\text{O} (\text{l}) + 8\text{e}^- = \text{CH}_4 (\text{g}) + 8\text{OH}^-$	-0.659
$2\text{CO}_2 (\text{g}) + 2\text{H}^+ + 2\text{e}^- = \text{H}_2\text{C}_2\text{O}_4 (\text{aq})$	-0.500
$2\text{CO}_2 (\text{g}) + 2\text{e}^- = \text{C}_2\text{O}_4^{2-}$	-0.590
$2\text{CO}_2 (\text{g}) + 12\text{H}^+ + 12\text{e}^- = \text{C}_2\text{H}_4 (\text{g}) + 4\text{H}_2\text{O} (\text{l})$	0.064
$2\text{CO}_2 (\text{g}) + 8\text{H}_2\text{O} (\text{l}) + 12\text{e}^- = \text{C}_2\text{H}_4 (\text{g}) + 12\text{OH}^-$	-0.764
$2\text{CO}_2 (\text{g}) + 12\text{H}^+ + 12\text{e}^- = \text{CH}_3\text{CH}_2\text{OH} (\text{l}) + 3\text{H}_2\text{O} (\text{l})$	0.084
$2\text{CO}_2 (\text{g}) + 9\text{H}_2\text{O} (\text{l}) + 12\text{e}^- = \text{CH}_3\text{CH}_2\text{OH} (\text{l}) + 12\text{OH}^-$	-0.744

#### 1.4.1 Thermodynamic issues

With respect to the electrochemical reduction of CO<sub>2</sub>, usable chemicals proceeding through multiple electron reduction pathways are more favorable than single electron steps to obtain thermodynamically more stable molecules. Possible reduction products are carbon monoxide (CO), formic acid (HCOOH), acetic acid (CH<sub>3</sub>COOH), oxalic acid (H<sub>2</sub>C<sub>2</sub>O<sub>4</sub>), formaldehyde (CH<sub>2</sub>O), methanol (CH<sub>3</sub>OH), ethanol (CH<sub>3</sub>CH<sub>2</sub>OH), methane (CH<sub>4</sub>), ethylene

(C<sub>2</sub>H<sub>4</sub>), as well as others. Figure 1.4 reveals the minimum potential required with the sufficient number of electrons for the formation of the different reduced products under standard conditions from the electrochemical reduction of CO<sub>2</sub>, calculated according to the standard Gibbs energies of the reactants. Table 1.1 summarizes the thermodynamic electrochemical half-reactions associated with their standard electrode potentials (V vs. SHE) in aqueous solutions. Note that the standard potentials mentioned in Table 1.1 are under the conditions of 25 °C, 1 atm gas pressure, and 1 M solutes in aqueous solutions; the potentials (V vs. SHE) values might be different in non-aqueous solutions. In addition, the reactions given in Table 1.1 are thermodynamic, indicating the reactions tendency and possibility, but giving no certainty of the kinetics [37,45]. As seen in Figure 1.4, it appears that the formations of some products are easy (for example, HCHO and CH<sub>3</sub>OH) under low electrode potentials and standard conditions, but this is not always the case. There are multiple steps involved in the reaction mechanisms, where some of them are required to overcome high energy barriers.

#### **1.4.2 Kinetic concerns**

CO<sub>2</sub> is a small, fully oxidized, thermodynamically stable, and linear molecule. Hence, the kinetics of the electrocatalytic reduction of CO<sub>2</sub> comprises a very complicated reaction mechanism and slow reaction rates. One of the key challenges for the conversion of CO<sub>2</sub> into energetic molecules is the assembly of the nuclei and formation of new chemical bonds to obtain more complex molecules than CO<sub>2</sub>, even in the presence of catalysts. Typically, for electrocatalytic reduction, CO<sub>2</sub> molecules bind to a catalyst through the electrophilic carbon atom, which modifies linear CO<sub>2</sub> to a bent structure; hence, requiring a large amount of energy, which is even more difficult in the absence of protons. Furthermore, occasionally, a mixture of multiple species are formed, rather than a single product, from the electrochemical reduction of

CO<sub>2</sub>, resulting in very tricky kinetics in the reaction mechanism. Further, the number of species and their quantity are strongly dependent on the activity and selectivity of the catalyst and the applied electrode potentials. Therefore, on a comprehensive basis, the kinetic challenges are immense. One of the potential possibilities is to identify specific catalysts that can overcome these kinetic barriers to complete all the sequence of steps involved in the reaction mechanism to obtain the targeted species. Another possibility toward the formation of a complex molecule, might be to identify a group of catalysts, where each catalyst can overcome a specific barrier in the reaction mechanism steps, to ultimately transform CO<sub>2</sub>, [34,37,46].

### **1.4.3 Technological challenges**

Over the last few decades, researchers have developed various electrocatalysts for the electrochemical reduction of CO<sub>2</sub> to produce usable carbon products [9,34-37,47-51]. However, several technological challenges remain as relates to catalysts for practical applications, including (i) low activity, (ii) poor product selectivity, (iii) poor stability, (iv) lack of fundamental understanding, and (v) insufficient knowledge to design systems for industrial-scale implementation.

(i) *Low catalytic activity:* In general, the activities of the electrocatalysts that have currently been developed for the reduction of CO<sub>2</sub> are still not sufficient for practical applications. The developed catalysts presently being employed normally show a large reaction overpotential for the electroreduction of CO<sub>2</sub>. Although some electrocatalysts are able to produce low hydrocarbon fuels under low electrode potentials, the rate of the reactions is very poor [35,36,46]. The production rate might be made higher by increasing the electrode potential; however, the possibility of the generation of hydrogen gas may also increase in aqueous solutions, due to the high affinity for H<sup>+</sup> reduction, rather than solvated CO<sub>2</sub>, at the cathode.

Hence, the activity of current catalysts is inadequate for actual applications in terms of energy efficiency.

(ii) *Poor product selectivity:* In most cases, the developed catalysts produce a mixture of products (e.g., CO, HCHO, HCOOH, CH<sub>3</sub>CH<sub>2</sub>OOH, CH<sub>3</sub>OH, CH<sub>3</sub>CH<sub>2</sub>OH, CH<sub>4</sub>, CH<sub>2</sub>CH<sub>2</sub>, and so on) rather than a single species during the electrolysis of CO<sub>2</sub>. Although some of the catalysts show desirable product selectivity, unfortunately, the stability is very low for practical applications [38,52,53]. Applied electrode potentials also play a critical role in the formation of different products, and the quantity of each species on the catalyst surface. The separation of the generated products from the electrolyte solution, as well as the gaseous component, may be counted as an additional challenge. Studies suggest that the majority of the electrocatalysts explored to date have insufficient product selectivity.

(iii) *Poor catalyst stability:* Catalyst stability comprises the single most significant challenge for the electrochemical reduction of CO<sub>2</sub>. Most of catalysts typically lose their activity within few hours while performing electrolysis. Some of them are able to survive for longer, but never more than 100 hours [54,55], which is quite distant from the requirements for industrial applicability; hence, further long-term testing is required. The deactivation of the active sites of the catalysts by blocking and poisoning, dissolution of particles from catalyst surfaces, and the deposition of reaction intermediates and byproducts on the electrode surface, may lead to the rapid degradation of catalytic activity as CO<sub>2</sub> electrolysis proceeds [52].

(iv) *Lack of fundamental understanding:* Present CO<sub>2</sub> electroreduction technologies are still quite distant from industrial applicability, due to unsatisfactory catalysis, requirement of high overpotentials, low selectivity, slow reduction rates, and poor stability. Therefore, further

efforts are required to elucidate fundamental kinetics, and to tailor high-performance electrocatalysts for CO<sub>2</sub> conversion.

(v) *Insufficient knowledge to design systems for industrial-scale implementation:*

The combustion of fossil fuels at an unprecedented scale has caused CO<sub>2</sub> concentrations in the ambient atmosphere to increase rapidly; recently reaching its highest level at ~400 ppm. Hence, the conversion of CO<sub>2</sub> to fuels using electrocatalysts would be a remarkable renewable energy path to balance the global carbon cycle. Although several current electrocatalysts are promising for the conversion of CO<sub>2</sub> to fuels, systems for scaled-up electrochemical reduction remain infeasible for industrial applications; thus, necessary steps should be urgently taken to ensure the success of these electrochemical technologies [56]. Therefore, additional research should focus on the development of system designs to overcome the above challenges for practical applications.

### **1.5 The objectives and outline of this thesis**

Studies have shown that nanostructured materials have unique surface morphologies, extensive surface areas, higher populations of active sites, and different crystal facets. Moreover, they have gained a wide attention for the development of CO<sub>2</sub> electrocatalysts. Therefore, the main intent of this study will be to develop various novel nanostructured materials with enhanced catalytic performance, such as high activity, high product selectivity, and excellent stability. Moreover, the reaction kinetics on the synthesized nanocatalyst surfaces toward the electrochemical reduction of CO<sub>2</sub> in aqueous solutions will be investigated. The primary research objectives of this thesis are:

- (a) To synthesis a reduced graphene oxide (rGO)/Cu nanoparticle (NP) thin film and their nanocomposites, uniquely structured Cu nanodendrites, and novel three dimensional nanoporous Au.

- (b) To characterize the synthesized materials via scanning electron microscope (SEM), energy dispersive X-ray (EDX), X-ray diffraction (XRD), and X-ray photoelectron spectroscopy (XPS).
- (c) To electrochemically study of the fabricated catalysts for the reduction of CO<sub>2</sub>.
- (d) To identify the liquid products, and to determine the mechanisms of the CO<sub>2</sub> reduction using in situ electrochemical ATR-FTIR spectroscopy.
- (e) To develop a COD analysis technique to determine the Faradaic efficiency (FE) of the formed liquid products derived from the electroreduction of CO<sub>2</sub>.
- (f) To qualitatively and quantitatively determine the CO<sub>2</sub> derived products by gas chromatography (GC), high performance liquid chromatography (HPLC), and nuclear magnetic resonance (NMR).

This thesis is divided into seven chapters. The present chapter briefly discussed current anthropogenic energy consumption and CO<sub>2</sub> emissions on a global scale. The technologies that are presently applied for the transformation of CO<sub>2</sub> to value-added chemicals were also briefly described. Moreover, current challenges facing the electrochemical reduction of CO<sub>2</sub> were sketched out.

In the next chapter, an overview of the electrochemical reduction of CO<sub>2</sub> on various metal electrodes, nanostructured metals, and carbon-based nanomaterials will be conveyed, as well as the reaction mechanisms, catalyst stability, and perspectives in this field.

In chapters 3 and 4, a one-pot approach will be described for the synthesis of a novel nanostructured thin film, and a unique nanocomposite comprised of Cu NPs and rGO, on a glassy carbon electrode (GCE) and Cu plate, respectively. The surface morphologies and compositions of the synthesized samples were characterized using field-emission scanning

electron microscopy (FE-SEM) equipped with an energy dispersive X-ray spectrometer (EDX) (Hitachi SU70) and X-ray photoelectron spectroscopy (XPS). The electrocatalytic activity of the formed catalysts was studied by employing linear sweep voltammetry (LSV), whereas chronoamperometry (CA), and attenuated total reflection Fourier transform infrared spectroscopy (ATR-FTIR) techniques were used to identify the liquid products at the electrode surface. Moreover, the formed products from the reduction of CO<sub>2</sub> were analyzed by gas chromatography (GC), high-performance liquid chromatography (HPLC), and a chemical oxygen demand method.

Chapter 5 will discuss a facile approach for the synthesis of novel Cu nanodendrites under thermal treatment, where a mixture of CuSO<sub>4</sub> and H<sub>2</sub>SO<sub>4</sub> was used that exhibited superior catalytic activity over a Cu thin film, particles, and nanoparticles for the electrochemical reduction of CO<sub>2</sub>. Detailed structural and electrochemical characterization was carried out by SEM, XRD, XPS, LSV, and CA. The electrochemically active surface area (EASA) of the formed Cu nanodendrites was estimated relative to the polycrystalline Cu electrode by determining double-layer capacitances in a 0.1 M HClO<sub>4</sub> electrolyte, which showed the highest roughness factors among the synthesized Cu materials. In order to obtain the highest catalytic activity for the Cu nanodendrites, the annealing temperatures, duration, and quantity of treating agents were optimized. Further, in situ electrochemical ATR-FTIR spectroscopy was employed to investigate CO<sub>2</sub> consumption and the formation of intermediates and products at different applied electrode potentials on the synthesized Cu nanodendrites during the electrochemical reduction of CO<sub>2</sub>. This confirmed the formation of formate and hydrocarbons at electrode potentials of lower than -0.2 V (vs. RHE).

Chapter 6 will report on the superb catalytic performance of three-dimensional nanoporous Au for the highly selective production of CO from the electroreduction of CO<sub>2</sub>, which was synthesized via a simple electrochemical alloying/dealloying, associated with an acid treatment. The EASA, surface structure, elemental composition, electrocatalytic activity, and the charge-transfer resistance for the electrochemical reduction of CO<sub>2</sub> of the formed nanoporous Au were studied in detail. The Faradaic efficiency and production rate under different applied electrode potentials were calculated and determined through gas chromatography analysis. The pore dimensions of the formed 3D network structures might play a vital role in increasing the catalytic activity of the Au, and we proposed a mechanism for the accessibility of the solvated CO<sub>2</sub> into the pore cavities, which enabled the efficient utilization of localized electric fields. Finally, a summary of the results will be provided in Chapter 7, as well as a discussion of corresponding future work.

#### Reference:

- [1] IPCC, **2014**: Climate Change 2014: Synthesis Report. Contribution of Working Groups I, II and III to the Fifth Assessment Report of the Intergovernmental Panel on Climate Change [Core Writing Team, R. K. Pachauri, L. A. Meyer (eds.)]. *IPCC*, Geneva, Switzerland, <https://www.ipcc.ch/report/ar5/wg3/>
- [2] <https://data.giss.nasa.gov/modelforce/ghgases/Fig1A.ext.txt>
- [3] A. Goeppert, M. Czaun, J.-P. Jones, G. K. S. Prakash, G. A. Olah, *Chem. Soc. Rev.* **2014**, 43, 7995.
- [4] A. Rosas-Hernández, H. Junge, M. Beller, M. Roemelt, R. Francke, *Catal. Sci. Technol.* **2017**, 7, 459.
- [5] E. Alper, O. Y. Orhan, *Petroleum* **2017**, 3, 109.



- [6] J. Cheng, M. Zhang, G. Wu, X. Wang, J. Zhou, K. Cen, *Sol. Energy Mater. Sol. Cells* **2015**, 132, 606.
- [7] A. M. Appel, J. E. Bercaw, A. B. Bocarsly, H. Dobbek, D. L. DuBois, M. Dupuis, J. G. Ferry, E. Fujita, R. Hille, P. J. A. Kenis, C. A. Kerfeld, R. H. Morris, C. H. F. Peden, A. R. Portis, S. W. Ragsdale, T. B. Rauchfuss, J. N. H. Reek, L. C. Seefeldt, R. K. Thauer, G. L. Waldrop, *Chem. Rev.* **2013**, 113, 6621.
- [8] D. M. D'Alessandro, B. Smit, J. R. Long, *Angew. Chem. Int. Ed.* **2010**, 49, 6058.
- [9] Y. Hori, In *Modern Aspects of Electrochemistry*; C. G. Vayenas, R. E. White, M. E. Gamboa-Aldeco, Eds.; Springer: New York, **2008**, 42, 89.
- [10] M. R. Singh, E. L. Clark, A. T. Bell, *Phys. Chem. Chem. Phys.* **2015**, 17, 18924.
- [11] BP Statistical Review of World Energy **2015**, <https://ourfinitemworld.com/2015/06/23/bp-data-suggests-we-are-reaching-peak-energy-demand/>
- [12] Key World Energy Statistics 2013, International Energy Agency (IEA), Paris, **2013**.
- [13] P. Styring, K. Armstrong, *Front. Energy Res.* **2015**, 3, 8.
- [14] Atmospheric CO<sub>2</sub> level for October 2017, Mauna Loa Observatory, <https://www.co2.earth/2017>.
- [15] J. P. Smol, *Nature* 2012, 483, S12.
- [16] Global climate change, NASA, <https://climate.nasa.gov/evidence/>
- [17] H. Balat, C. Oz, *Energy Explor. Exploit.* **2007**, 25, 357.
- [18] T. Sakakura, J.-C. Choi, H. Yasuda, *Chem. Rev.* **2007**, 107, 2365.
- [19] M. Mikkelsen, M. Jørgensen, F. C. Krebs, *Energy Environ. Sci.* **2010**, 3, 43.
- [20] M. C. J. Bradford, M. A. Vannice, *Appl. Catal. A* **1996**, 142, 73.
- [21] S. Teir, S. Eloneva, R. Zevenhoven, *Energy Convers. Manage.* **2005**, 46, 2954.
- [22] M. Aresta, *Carbon Dioxide as Chemical Feedstock*, 1st edition, Wiley-VCH, **2010**.
- [23] G. A. Olah, A. Goepfert, G. K. S. Prakash, *J. Org. Chem.* **2009**, 74, 487.
- [24] O. Takayasu, C. Soman, Y. Takegahara, I. Matsuura, *Stud. Surf. Sci. Catal.* **1994**, 88, 281.

- [25] W. B. Hou, W. H. Hung, P. Pavaskar, A. Goeppert, M. Aykol, S. B. Cronin, *ACS Catal.* **2011**, 1, 929.
- [26] G. Qin, Y. Zhang, X. Ke, X. Tong, Z. Sun, M. Liang, S. Xue, *Applied Catal. B: Environ.* **2013**, 129, 599.
- [27] E. Kecsenvity, B. Endrodi, Zs. Papa, K. Hernadi, K. Rajeshwar, C. Janaky, *J. Mater. Chem. A* **2016**, 4, 3139.
- [28] S. N. Habisreutinger, L. Schmidt-Mende, J. K. Stolarczyk, *Angew. Chem. Int. Ed.* **2013**, 52, 7372.
- [29] Y. Yamazaki, H. Takedaa, O. Ishitani, *J. Photochem. Photobio. C: Photochem. Reviews* **2015**, 25, 106.
- [30] J. Gu, A. Wuttig, J. W. Krizan, Y. Hu, Z. M. Detweiler, R. J. Cava, A. B. Bocarsly, *J. Phys. Chem. C* **2013**, 117, 12415.
- [31] H. Yang, Z. Xu, M. Fan, R. Gupta, R. B. Slimane, A. E. Bland. I. Wright, *J. Environ. Sci.* **2008**, 20, 14.
- [32] A. Behr, Carbon Dioxide Activated by Metal Complexes, VCH, Weinheim, Germany, **1988**.
- [33] P. Jajesniak, H. E. M. O. Ali, T. S. Wong, *J. Biopro. Biotechniq* **2014**, 4, 3.
- [34] E. E. Benson, C. P. Kubiak, A. J. Sathrum, J. M. Smieja, *Chem. Soc. Rev.* **2009**, 38, 89.
- [35] M. Liu, Y. Pang, B. Zhang, P. D. Luna, O. Voznyy, J. Xu, X. Zheng, C. T. Dinh, F. Fan, C. Cao, F. P. G. de Arquer, T. S. Safaei, A. Mepham, A. Klinkova, E. Kumacheva, T. Filleter, D. Sinton, S. O. Kelley, E. H. Sargent, *Nature* **2016**, 537, 382.
- [36] J. S. Gao, X. Jiao, Z. Sun, W. Zhang, Y. Sun, C. Wang, Q. Hu, X. Zu, F. Yang, S. Yang, L. Liang, J. Wu, Y. Xie, *Angew. Chem. Int. Ed.* **2016**, 55, 698.
- [37] J. Qiao, Y. Liu, F. Hong, J. Zhang, *Chem. Soc. Rev.* **2014**, 43, 631.
- [38] A. S. Agarwal, Y.M. Zhai, D. Hill, N. Sridhar, *ChemSusChem* **2011**, 4, 1301.
- [39] J.-M. Saveant, *Chem. Rev.* **2008**, 108, 2348.
- [40] Y. Chen, M. W. Kanan, *J. Am. Chem. Soc.* **2012**, 134, 1986.
- [41] C. Costentin, M. Robert, J.-M. Saveant, *Chem. Soc. Rev.* **2013**, 42, 2423.
- [42] K. Manthiram, B. J. Beberwyck, A. P. Alivisatos, *J. Am. Chem. Soc.* **2014**, 136, 13319.

- [43] Y. Chen, C. W. Li, M. W. Kanan, *J. Am. Chem. Soc.* **2012**, 134, 19969.
- [44] Y. Hori, A. Murata, R. Takahashi, *J. Chem. SOC. Faraday Trans. I* **1989**, 85, 2309.
- [45] A. J. Bard, R. Parsons, J. Jordan, Standard potentials in aqueous solutions, CRC press, **1985**.
- [46] J. Schneider, H. Jia, J. T. Muckerman, E. Fujita, *Chem. Soc. Rev.* **2012**, 41, 2036.
- [47] K. Nakata, T. Ozaki, C. Terashima, A. Fujishima, Y. Einaga, *Angew. Chem. Int. Ed.*, **2014**, 53, 871.
- [48] N. V. Rees, R. G. Compton, *Energy Environ. Sci.*, **2011**, 4, 403.
- [49] A. Loiudice, P. Lobaccaro, E. A. Kamali, T. Thao, B. H. Huang, J. W. Ager, R. Buonsanti, *Angew. Chem. Int. Ed.* **2016**, 55, 5789.
- [50] M. N. Hossain, J. Wen, A. Chen, *Sci. Rep.* **2017**, 7, 3184.
- [51] M. N. Hossain, J. Wen, S. K. Konda, M. Govindhan, A. Chen, *Electrochem. Commun.* **2017**, 82, 16.
- [52] H. Li, C. Oloman, *J. Appl. Electrochem.* **2006**, 36, 1105.
- [53] H. Li, C. Oloman, *J. Appl. Electrochem.* **2007**, 37, 1107.
- [54] I. Bhugun, D. Lexa, J. M. Saveant, *J. Phys. Chem.* **1996**, 100, 19981.
- [55] K. Y. Wong, W. H. Chung, C. P. Lau, *J. Electroanal. Chem.* **1998**, 453, 161.
- [56] A. H. Zhou, D. L. He, N. X. Xie, Q. J. Xie, L. H. Nie, S. Z. Yao, *Electrochim. Acta* **2000**, 45, 3943.

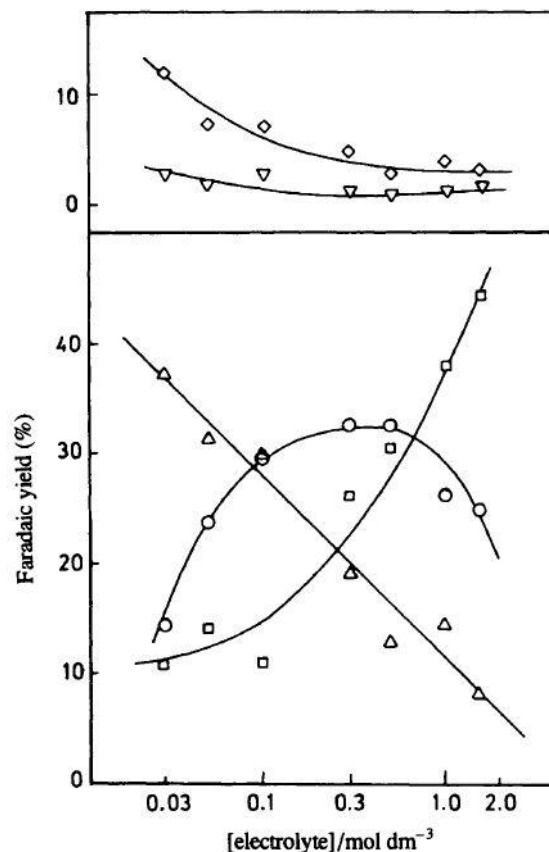
## Chapter 2: Literature Review

### 2.1 Introduction

Several potential metal-based catalysts have been used for the electrochemical reduction of CO<sub>2</sub> in aqueous solutions [1-3]. Generally, CO<sub>2</sub> is converted to CO or formate during the first step of the electrochemical reduction of CO<sub>2</sub> on every catalyst, and is a primary product on some electrocatalysts. However, it can further be reduced to oxygenates and hydrocarbons while continuing the electroreduction reaction on various catalysts [4-6]. For example, metals such as Au, Ag, Zn, Pd, and Ga form CO as the primary product, whereas hydrocarbons, aldehydes, and alcohols can be obtained on Cu. The metals Pb, Hg, In, Sn, Cd, Tl, and Bi give formate ions as the major product. The group 4 element, Ni, Fe, and Pt, do not show catalytic activity for the reduction of CO<sub>2</sub>, but hydrogen evolution does occur [7]. Moreover, studies have shown that catalytic activity and selectivity may be enhanced by forming alloys of different metals [8,9]. Bimetallic alloys such as Cu-Ni, Ni-Cd, Sn-Cd, Zn-Sn, Cu-Sn, Pb-Cu, Cu-Au, Cu-Fe, and so on, are potential electrocatalysts that can yield CH<sub>4</sub>, HCOO<sup>-</sup>, CO, and C<sub>2</sub>H<sub>4</sub> [10-14]. Further, carbon-based metal catalysts have been investigated for the electroreduction of CO<sub>2</sub>. For example, carbon-supported Cu nanoparticles [15] carbon nanotube/copper sheets [16], graphene-supported Cu nanoparticles [17], Pd-Cu/graphene [18], and graphene confined Sn quantum sheets [19] exhibit promising catalytic properties for the reduction of CO<sub>2</sub> due to their large surface areas, good specific conductivity, and high chemical stability. These carbon materials also have synergistic interactions with metal particles [20,21]. In this chapter, progress and prospects for the electrochemical reduction of CO<sub>2</sub> are classified and discussed on the basis of currently investigated electrocatalysts.

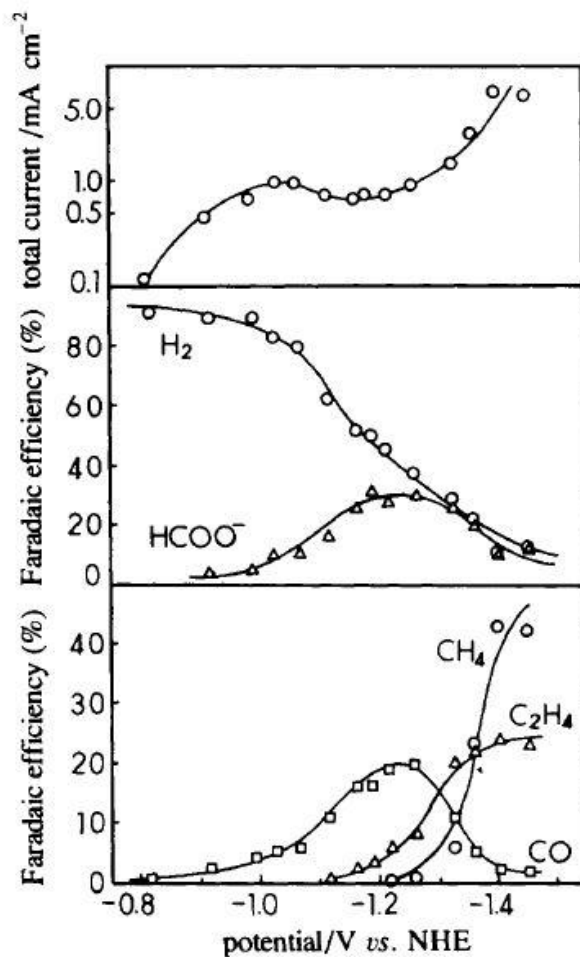
### 2.2.1 Copper (Cu) catalysts

Cu is the most studied material as an electrocatalyst for the reduction of CO<sub>2</sub>. Different types of Cu electrodes have been investigated and developed as CO<sub>2</sub> electrocatalysts, such as bulk Cu electrodes, thin Cu metals, Cu coated gas diffusion electrodes, Cu electrodeposited glassy carbon electrodes, nanostructured Cu such as nanoparticles, nanowires, nanoflowers, nanofoams, and nanoporous and copper-based nanomaterials [11,21-30]. According to the literature, among explored electrocatalysts, Cu is unique material that can break the C-O bonds of CO<sub>2</sub> molecules during electrochemical reduction, resulting the formation of hydrocarbons (CH<sub>4</sub>, C<sub>2</sub>H<sub>4</sub>, HCOOH, CH<sub>3</sub>COOH), alcohols (CH<sub>3</sub>OH, C<sub>2</sub>H<sub>5</sub>OH), esters, and several high hydrocarbons that contain up to six carbon atoms [31]. A number of these products and Faradaic efficiencies were significantly dependent on operating conditions, such as the concentration, type, and pH of the electrolytes, applied electrode potential, particle size, purity, crystal faces, and physical state of the Cu electrode surface. For example, in terms of Faradaic yields for the electrochemical reduction of CO<sub>2</sub>, products measured at the Cu sheet electrode as a function of electrolyte concentration have been reported by Hori et al. [32], as shown in Figure 2.1. Electrolysis was performed at a constant cathodic current density of 5 mA cm<sup>-2</sup>, revealing that the Faradaic efficiency (FA) of C<sub>2</sub>H<sub>5</sub>OH and C<sub>2</sub>H<sub>4</sub> was high in dilute KHCO<sub>3</sub> solutions, whereas CH<sub>4</sub> yields were higher with increased electrolyte concentrations, which then dropped after reaching a maximum. The FA of HCOO<sup>-</sup> and CO did not strongly depend on the KHCO<sub>3</sub> electrolyte concentration; however, the formation of H<sub>2</sub> increased with the electrolyte concentration. In addition, Hori's group found that the changing trend of FA did not follow the altered electrode potentials. Figure 2.2 displays the dependence of the FA of the products of CO<sub>2</sub> electrolysis with an applied controlled electrode potential, showing that the FA of CO and



**Figure 2.1** Faradaic yields of the products in the electrochemical reduction of CO<sub>2</sub>, at 19 °C in KHCO<sub>3</sub> aqueous solutions of various concentrations. Current density = 5 mA cm<sup>-2</sup>. Bottom: Δ, C<sub>2</sub>H<sub>4</sub>; ○, CH<sub>4</sub>; Top: □, H<sub>2</sub>; ◇, EtOH; Δ, Pr<sup>n</sup>OH. Reprinted with permission from ref. [32]. Copyright © 1989 The Royal Society of Chemistry.

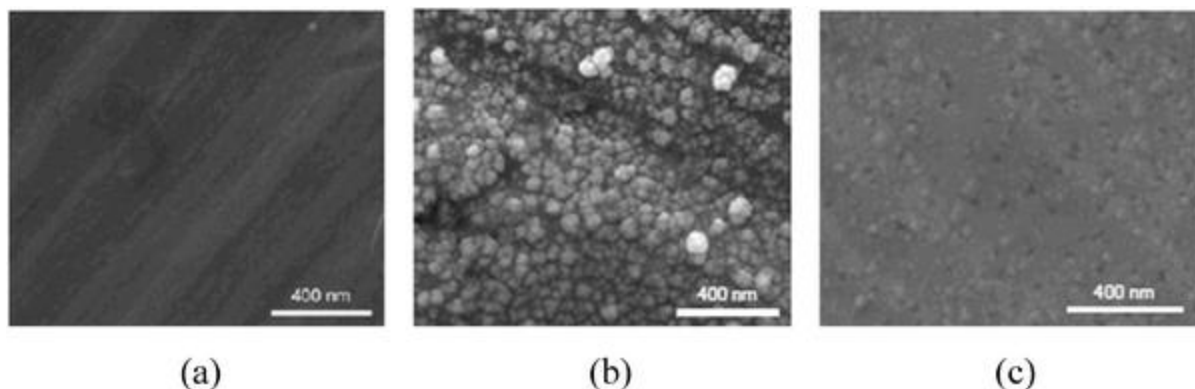
HCOO<sup>-</sup> increased at -0.9 V (vs. NHE), reaching the maximum at ~-1.25 V and then dropped at more negative potentials. The FAs for C<sub>2</sub>H<sub>4</sub> and CH<sub>4</sub> increased steeply with the rise of the cathode potential, beginning at -1.1 and -1.2 V, respectively. The formation of hydrocarbons and alcohols was prevalent in KCl, KClO<sub>4</sub>, and KHCO<sub>3</sub>, whereas H<sub>2</sub> was found to be the main product in the K<sub>2</sub>HPO<sub>4</sub> solution [32].



**Figure 2.2** Variation of the Faradaic efficiencies of the products in the electrochemical reduction of CO<sub>2</sub> obtained in controlled potential electrolysis, 0.1 mol dm<sup>-3</sup> KHCO<sub>3</sub> at 19 °C. Reprinted with permission from ref. [32]. Copyright @ 1989 The Royal Society of Chemistry.

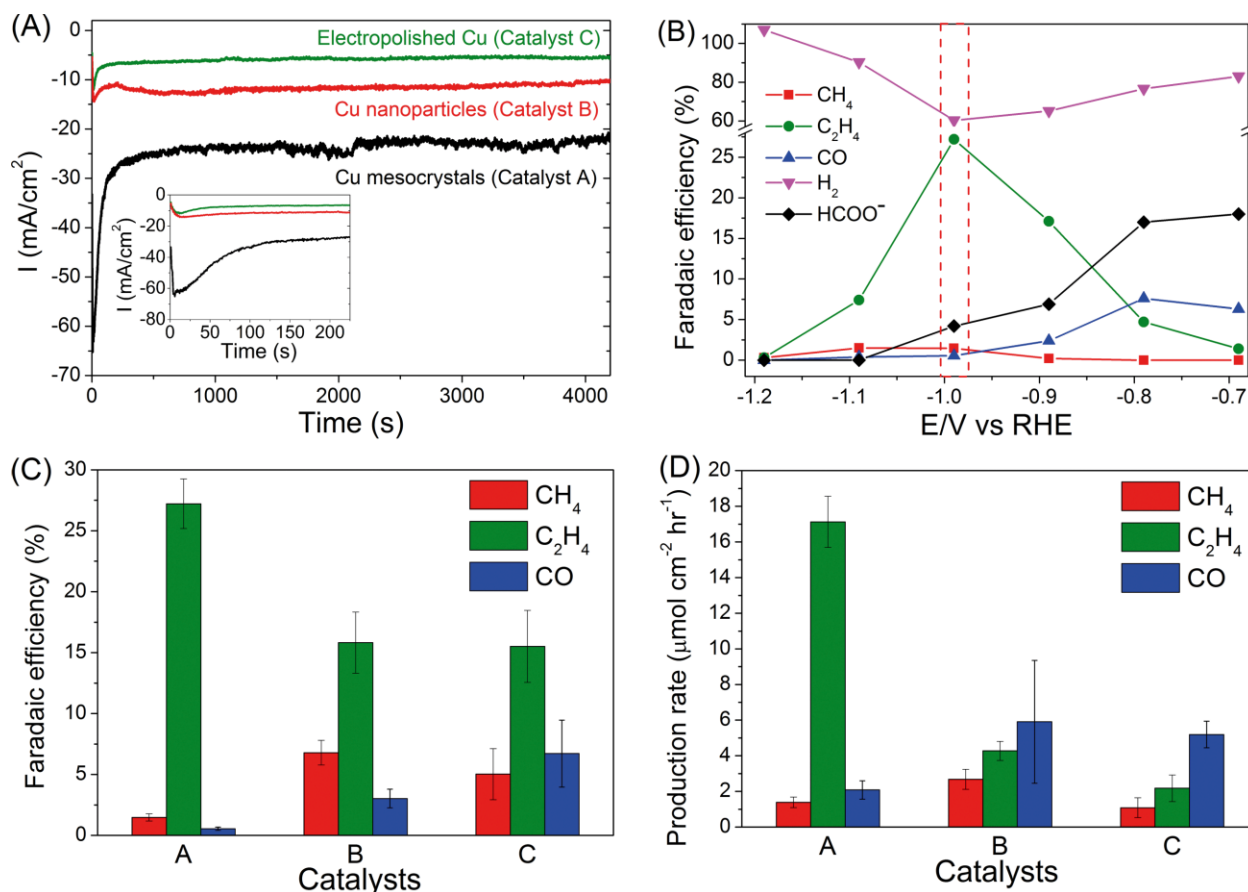
To enhance the catalytic performance of Cu for the electroreduction of CO<sub>2</sub>, efforts have been invested in tailoring the formation of supernanostructures, modifying the surface morphology of the Cu electrodes, increasing the electrochemical surface area and crystal facets, and reducing the particle dimensions [33-36]. Studies have found that nanostructured Cu materials possess large geometric surface areas, a high surface roughness factor, large electrochemically active surface areas, and have the capacity to form different crystal facets.

Several studies endeavored to understand the effects of these properties on the electrochemical reduction of CO<sub>2</sub>, and reports have shown that significant improvements in catalytic performance were achieved through the use of nanostructured Cu materials, over the typical Cu metal electrodes as electrocatalysts for the reduction of CO<sub>2</sub> [34-37]. Tang et al. studied the effects of surface morphology by synthesising three different types of polycrystalline Cu electrodes for the electrochemical reduction of CO<sub>2</sub> [38], with the corresponding SEM images of the electrodes displayed in Figure 2.3. The results revealed that the Cu nanoparticles (Ø50-100 nm) covered the electrodes, and had a 10 times higher current density than that of an electropolished Cu surface and an argon sputtered Cu electrode at -0.75 V (vs. RHE) measured through a CV technique in a CO<sub>2</sub>-saturated 0.1 M KClO<sub>4</sub> solution. Moreover, hydrocarbon fuels were the primary products of reduced CO<sub>2</sub> on the nanoparticle covered Cu surface compared with the other two electrodes, which indicated that surface morphology played a vital role in enhancing catalytic activity beyond solely increasing the surface area. Similar phenomena were observed when comparing



**Figure 2.3** Scanning electron microscopy of three surfaces: (a) Sample A (electropolished surface), (b) Sample B (copper nanoparticle covered surface) and (c) Sample C (sputtered surface). Reprinted with permission from ref. [38]. Copyright © 2012 The Royal Society of Chemistry.



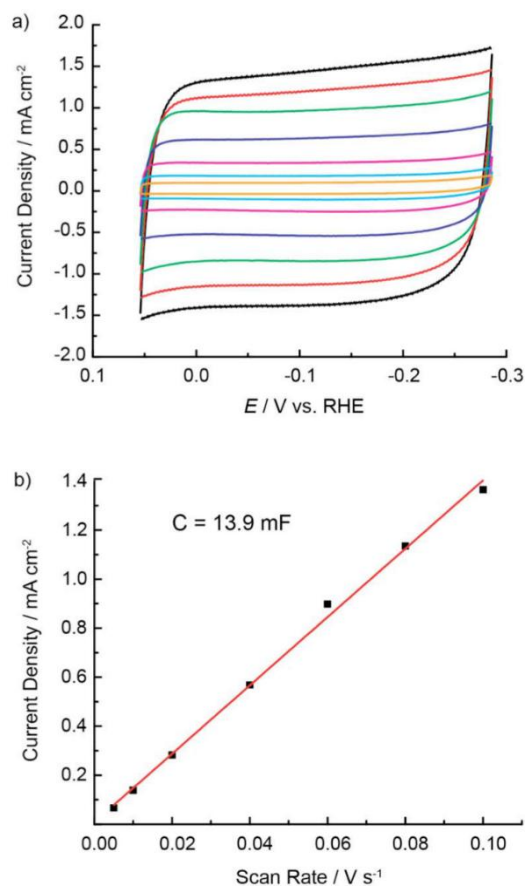


**Figure 2.4** (A) CO<sub>2</sub> reduction current as a function of time for catalysts A (Cu mesocrystals), B (Cu nanoparticles), and C (electropolished Cu). Potential applied:  $-0.99$  V. The inset is a zoomed-in picture of the reduction currents at the start of the CO<sub>2</sub> reduction process. (B) Faradaic efficiencies of the CO<sub>2</sub> electroreduction products of catalyst A as a function of potential. A comparison of the (C) Faradaic efficiencies and (D) production rates of CO<sub>2</sub> electroreduction products on catalysts A, B, and C at  $-0.99$  V. Reprinted with permission from ref. [39]. Copyright @ 2015 The Royal Society of Chemistry.

the catalytic performance of Cu mesocrystals with Cu nanoparticles and electropolished Cu electrodes for the electrochemical reduction of CO<sub>2</sub> in 0.1 M KHCO<sub>3</sub>, as shown in Figure 2.4 [39]. For instance, the current density obtained at  $-0.99$  V (vs. RHE) on the Cu mesocrystals was approximately twice and three times higher than those of the Cu nanoparticles and

electropolished Cu, respectively (Figure 2.4A). Selective C<sub>2</sub>H<sub>4</sub> formation was observed to have a significant preference for Cu mesocrystals catalysts, with a FA of 27.2% at -0.99 V, as shown in Figure 2.4B. The FA of C<sub>2</sub>H<sub>4</sub> was ~81% using Cu mesocrystals of the total carbonaceous product yields, which was much higher than the C<sub>2</sub>H<sub>4</sub> yields of 45% and 40% obtained on Cu nanoparticles and electropolished Cu catalysts (Figure 2.4C). Moreover, the Cu mesocrystals exhibited much higher hydrocarbon production rates than the other catalysts (Figure 2.4D). All of the results in Figure 2.3 also revealed that the surface structure of the Cu mesocrystals played a significant role in the selective electroreduction of CO<sub>2</sub> to C<sub>2</sub>H<sub>4</sub>.

Several studies have reported that oxide derived Cu nanomaterials (OD-Cu) have a much better catalytic performance for the electrochemical reduction of CO<sub>2</sub> [33,35,40]. The OD-Cu nanomaterials electrodes were prepared by the annealing of Cu<sub>2</sub>O, which was obtained by the ambient air oxidation of Cu foils, whereafter OD-Cu was formed followed by the reduction of Cu<sub>2</sub>O, either electrochemically, or through annealing in the presence of H<sub>2</sub>. The annealing process alters the surface structure of polycrystalline Cu, where the derived nanomaterials form interconnected nanocrystalline networks among nanocrystallites and exhibit small crystallite sizes, as well as a large electrochemical surface area and high roughness factor, which favors C-C coupling formation during electrochemical reduction of CO<sub>2</sub> [33,35,40,41]. Li et al. initially prepared OD-Cu electrodes by annealing Cu foils in the presence of air at different temperatures, followed by the electrochemical reduction of the formed Cu<sub>2</sub>O layers [35]. The resulting OD-Cu



**Figure 2.5** Determination of double-layer capacitance for an electrode annealed at 500 °C for 12 h and subsequently reduced in 0.5 M NaHCO<sub>3</sub> at -0.5 vs. RHE. a) CVs taken over a range of scan rates in a potential window where only double-layer charging and discharging is relevant. b) Current due to double-layer charge/discharge plotted against CV scan rate. Reprinted with permission from ref. [35]. Copyright © 2012 American Chemical Society.

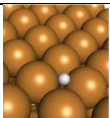
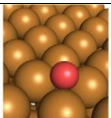
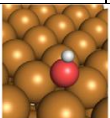
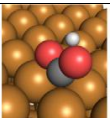
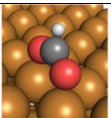
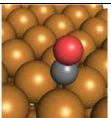
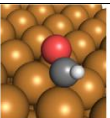
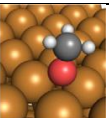
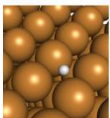
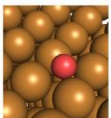
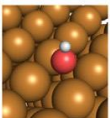
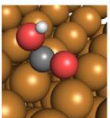
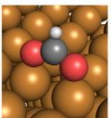
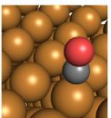
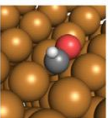
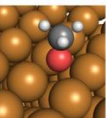

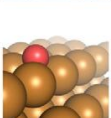
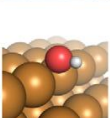
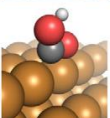
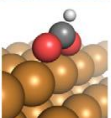
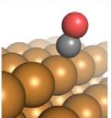
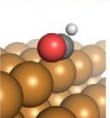
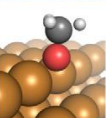
electrodes exhibited large roughness factors and their catalytic performance was indistinguishable from that of polycrystalline Cu for the electroreduction of CO<sub>2</sub> and the formation of hydrocarbons at very low overpotentials. The electrochemical surface area of the formed OD-Cu electrodes was determined by measuring double layer capacitances through the performance of CVs in a 0.1 M HClO<sub>4</sub> electrolyte (Figure 2.5). The OD-Cu obtained from Cu

foil annealed at 500 °C for 12h exhibited the highest double layer capacitance of 13.9 mF cm<sup>-2</sup> and had a considerably large roughness factor (RF ~475) among the synthesized electrodes. The FA of the CO<sub>2</sub> electroreduction of these OD-Cu electrodes were also consistent with RF values; the electrode had a higher RF value that exhibited a high catalytic performance and favored the formation of hydrocarbons. For instance, the main product on the polycrystalline Cu electrode was H<sub>2</sub> (>90% current density) with a very small FA of CO and HCO<sub>2</sub>H at -0.5 V (vs. RHE) in a CO<sub>2</sub>-saturated 0.5 M NaHCO<sub>3</sub> solution. The OD-Cu electrode obtained from the annealing of the Cu foil at 300 °C for 5 h improved a small RF of 69, and exhibited noticeable effect on the catalysis for the reduction of CO<sub>2</sub> under these conditions, which showed a FE of 35% and 24% for CO and HCOOH under the same applied electrode potential, respectively. Annealing at 500 °C for 15 min. resulted in a current density of ~2 mA cm<sup>-2</sup> with stable CO production over 7 h of electrolysis. Further increasing the annealing temperature to 500 °C for 5 h resulted in a thicker Cu<sub>2</sub>O layer. The formed OD-Cu was followed by the electrochemical reduction of Cu<sub>2</sub>O, which formed interconnected Cu nanoparticles that obtained the highest RF of 475, and demonstrated a superior catalytic performance for the reduction of CO<sub>2</sub>. A current density of 2.7 mA cm<sup>-2</sup> at -0.5 V with a CO production of ~40% FE throughout the electrolysis, 33% FE of HCOOH within a few percentage points of CH<sub>4</sub> and C<sub>2</sub>H<sub>4</sub> (at electrode potential < -0.5 V) were obtained over the 7 h analysis. These results revealed that the morphology and high degree of roughness of the Cu electrodes provided a path for CO<sub>2</sub> reduction over H<sub>2</sub>O in aqueous solutions.

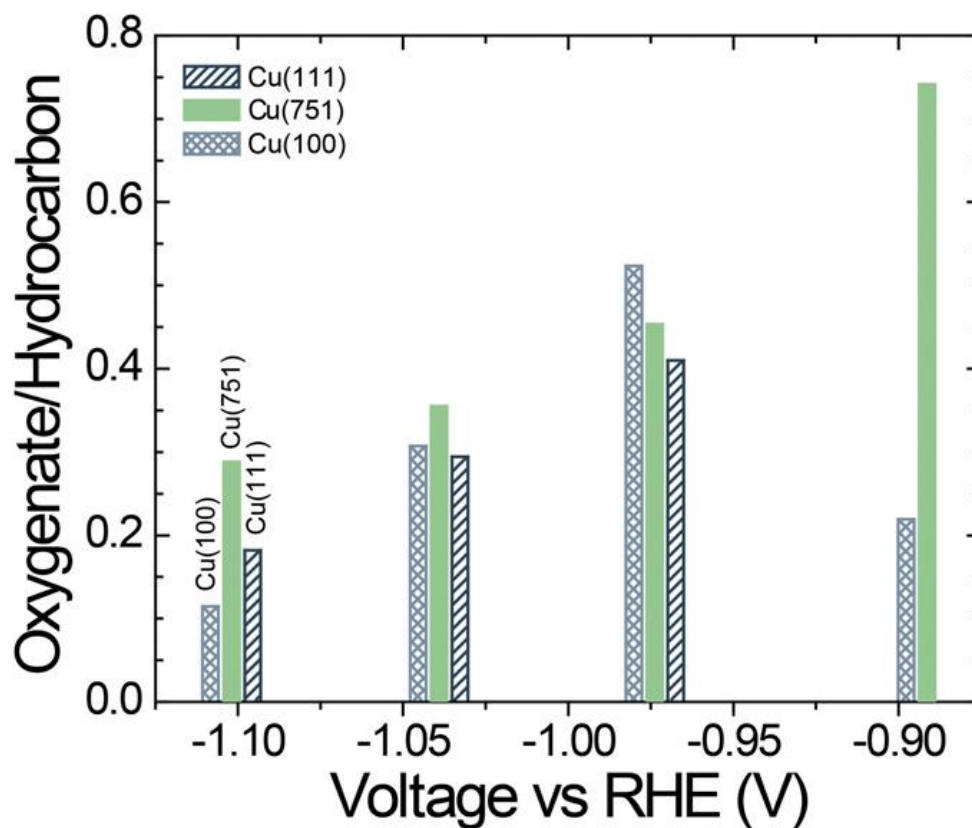
The atomic configurations of the Cu crystal orientations on the electrode surface had an extreme influence on activity and selectivity during the electroreduction of CO<sub>2</sub>. Various single-crystal studies have investigated the effects of the different types of Cu crystals and their orientations for the electrochemical reduction of CO<sub>2</sub> [7,31,36,42-45]. Frese found that the

**Table 2.1** Calculated free energies of adsorption, in eV, of key adsorbates on the (111), (100), and (211) crystal facets, shown with their optimized binding geometries, where a lower number indicates stronger binding. Reported energies are referenced to the electronic energy of a clean slab and reference atoms for H, C, and O of  $1/2$  H<sub>2</sub>, graphene, and (H<sub>2</sub>O–H<sub>2</sub>), respectively.

Reprinted with permission from ref. [36]. Copyright @ 2011 Elsevier

	H	O	OH	COOH	OCHO	CO	CHO	OCH <sub>3</sub>
(111)	0.20	1.16	0.66	2.21	1.34	1.42	2.22	1.40
(100)	0.19	0.83	0.46	1.92	1.03	1.31	2.09	1.23
(211)	0.06	1.01	0.25	1.75	0.76	1.19	1.86	1.06
(111)								
(100)								
(211)								

Formation of CH<sub>4</sub> was favored in the order of Cu(111), Cu(110), and Cu(100) [46], whereas C-C coupling was prompted on Cu(100) terrace surfaces [7]. Higher than C<sub>2</sub> products are abundantly yielded products on Cu(S)-[n(111) × ((111))], while oxygenated hydrocarbons such as CH<sub>3</sub>COOH, CH<sub>3</sub>CHO, and C<sub>2</sub>H<sub>5</sub>OH are formed in large volumes on the Cu(110) electrodes [47]. Hence, a number of theoretical studies were further undertaken to understand the fundamental facts involved in the electrochemical reduction of CO<sub>2</sub> on different Cu crystal facets [36,48]. Durand et al. calculated the adsorption free energies of different intermediate species on several



**Figure 2.6** Oxygenate/hydrocarbon ratios for  $>2e^-$  reduction products as a function of potential for Cu (111), (751), and (100). Reprinted with permission from ref. [42]. Copyright @ 2017 Proceedings of the National Academy of Sciences of the United States of America.

Cu crystal facets, listed in Table 2.1 [36]. As seen in the table, all of the intermediates, except for O, showed low optimized binding energies on the Cu(211) facet, which indicated strong binding by the Cu(211) facet, which was followed by Cu(100) and Cu(111). The O binds rather more strongly to the three-fold sites of the (211) terrace. This study indicated that the Cu(211) facet might be the most active crystal surface, which may produce low hydrocarbons with H<sub>2</sub> and CO as the byproducts of CO<sub>2</sub> electroreduction. Recently, Hahn et al. engineered Cu surfaces to selectively obtain hydrocarbons and oxygenates from the electrochemical reduction of CO<sub>2</sub> [42]. They found that both Cu(100) and Cu(751) films showed higher catalytic performance with an excellent selective C-C coupling formation than the Cu(111) surface. Moreover, oxygenate

formation was increased on the Cu(751) facet at low overpotentials. Figure 2.6 compares the ratio between oxygenate and hydrocarbon on different Cu crystal facets under variously applied electrode potentials. The oxygenate/hydrocarbon ratio was higher on both Cu(751) and Cu(100) than that of Cu(111), at a low cathodic potential of -0.89 V (vs. RHE), which revealed the formation of more oxygenates at the Cu surfaces at this potential. Further, there was a gradual increase of the cathodic potentials on all of the Cu facets, whereas oxygenate/hydrocarbon values decreased continuously, which indicated the formation of lower oxygenate populations under higher cathodic potentials. Therefore, these results suggested that the orientation of the Cu crystals played important roles for the enhancement of catalytic performance, and the selective formation of products during the electrocatalysis of CO<sub>2</sub>.

Moreover, efforts over the last few years have been focused on the formation of supernanostructures of Cu and the synthesis of different types of Cu nanostructures as advanced catalysts for the electrochemical reduction of CO<sub>2</sub> [21,25-27,33,40,49-52]. Highly dense Cu nanowires were synthesized through the oxidation of Cu mesh, which were then reduced by following either electrochemical treatment, or annealing in a hydrogen environment as electrocatalysts for the reduction of CO<sub>2</sub> [33]. The Cu nanowires obtained by electrochemical treatment exhibited the highly active and selective formation of CO, at overpotential of only 0.3 V with a FA of ~60% from CO<sub>2</sub> electrolysis in a 0.1 M KHCO<sub>3</sub> solution. A Cu nanoparticle ensemble on carbon paper exhibited the selective formation of C<sub>2</sub>H<sub>4</sub>, CH<sub>3</sub>CH<sub>2</sub>OH, and CH<sub>3</sub>CH<sub>2</sub>CH<sub>2</sub>OH at an onset potential of -0.53 V (vs. RHE). An overall FE of 50% was attained under an electrode potential of -0.75 V at as current density of 10 mA cm<sup>-2</sup> over 10 h of stable catalysis, which suggested that the proper decoration of Cu nanoparticles would be a promising electrocatalyst for the efficient reduction of CO<sub>2</sub> [49]. Xie et al. synthesized Cu nanoflowers as

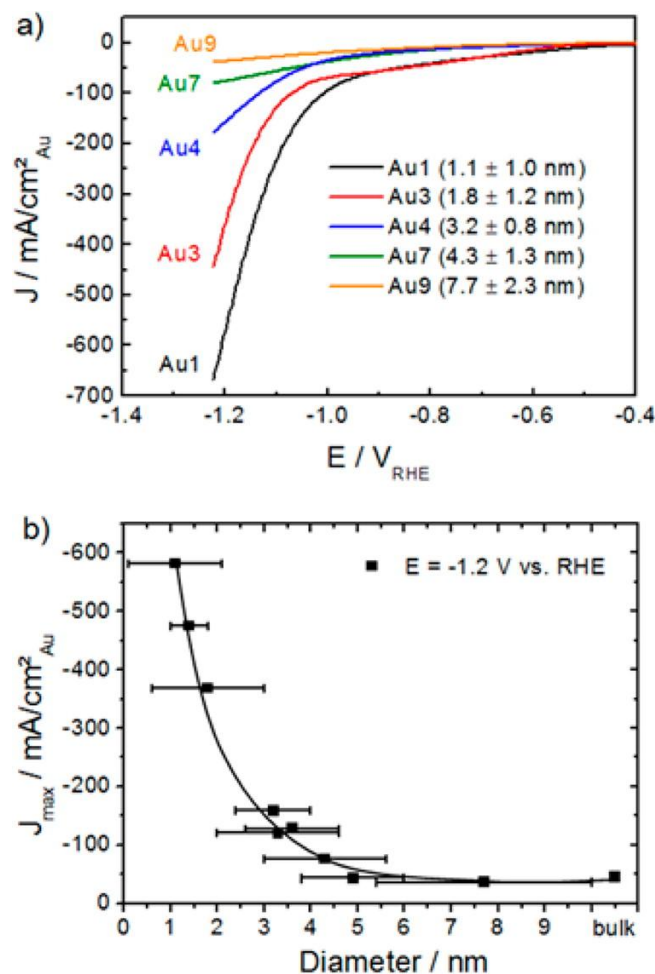
an efficient CO<sub>2</sub> electrocatalyst from CuO, where Cu foils were electropolished in a mixture of H<sub>3</sub>PO<sub>4</sub> and H<sub>2</sub>SO<sub>4</sub>, followed by electrochemical anodic oxidation in composite solutions of NaOH and NaCl to obtain CuO [26]. The formed Cu nanoflowers effectively reduced CO<sub>2</sub> to HCOOH, CH<sub>4</sub>, and C<sub>2</sub>H<sub>4</sub> at only 0.4 V of overpotential over 9 h in contrast to regular Cu foils. Cu nanofoams with pore diameters of 20-50 μm were synthesized as electrocatalysts for the reduction of CO<sub>2</sub> through the manipulation of Cu foils, where copper nanoparticles were electrodeposited on a polished Cu foil, which was used as a cathode, by applying a high current density (>500 mA cm<sup>-2</sup>) in a mixed 1.5 M H<sub>2</sub>SO<sub>4</sub> and 0.2 M CuSO<sub>4</sub> solution [27]. The Cu nanofoams demonstrated the efficient electrochemical reduction of CO<sub>2</sub> to HCOOH, and hydrocarbons at a low cathodic potential with a high FE. Dutta et al. synthesized oxide derived mesoporous Cu foams, which were identified as electrocatalysts for the reduction of CO<sub>2</sub>, which was highly selective toward C<sub>2</sub>H<sub>4</sub> and C<sub>2</sub>H<sub>6</sub>, attaining a FA of 55% at -0.9 V (vs. RHE) [40]. Their study found that the surface sites Cu(100), and pore diameters (50-100 μm) played important roles in the formation of C<sub>2</sub> during the CO<sub>2</sub> electrolysis. The thickness of the Cu nanoparticle (NP) film had a significant influence on the formation of CH<sub>4</sub>, as the thickness of the Cu NPs had an immense impact on the surface morphology [25]. The study reported that a thin film (3 nm) of Cu nanoparticles with average diameters of 52 ± 21, supported on glassy carbon exhibited excellent methanation with high FE of 80%. Robust CO<sub>2</sub> electrolysis at high rates was performed by developing a three-dimensional (3D) Cu porous hollow fiber, where the CO formation rate was 10 times higher than nanocrystalline Cu with a FE of 75% at -0.4 V (vs. RHE) [51]. It was observed that the hollow 3D structures provided a large surface area and a three-phase boundary assisted with gas-liquid reactions. A recent study was focused on the development of nanodendritic Cu via an in situ electrodeposition method under a high electrode



potential. This nanocatalyst exhibited excellent selectivity in the formation of  $C_2H_4$ , 57% FE, at a cathodic current density of  $170 \text{ mA cm}^{-2}$  during  $CO_2$  electrolysis, which proved that the Cu electrode surface structure had a significant impact on hydrocarbon selectivity [50]. Additionally, in order to enhance the electrocatalytic activity of the nanostructured Cu with rapid catalyst preparation, oxide derived Cu catalysts were synthesized using tunable  $O_2$  plasma treatments. The plasma-treated Cu achieved lower onset potentials for CO,  $HCOO^-$ , and  $C_2H_4$ , as well as 60% FE, for  $C_2H_4$  at a applied potential of -0.9 V (vs. RHE) [52].

### 2.2.2 Gold (Au) catalysts

Gold (Au) is one of the promising electrocatalysts for efficient  $CO_2$  reduction, when the appropriate experimental conditions are employed. Generally, Au electrodes are highly active and selectively form CO with high yields from  $CO_2$  electrolysis in aqueous solutions [7,47,53]. More interestingly, the formation of CO on the Au electrodes is independent of the electrolyte pH during the reduction of  $CO_2$  [54,55]. Various types of Au electrodes have been developed as catalysts for the electrochemical reduction of  $CO_2$  including polycrystalline Au, porous Au film [56], and nanostructured Au including nanoparticles [57], nanowires [53], nanoneedles [58], and other gold based nanomaterials [59-62]. Noda et al. reported that pure polycrystalline metal Au electrodes produced CO with a FE of 81.5% at -1.6 V (vs. Ag/AgCl) in a 0.1 M  $KHCO_3$  electrolyte [63]. In an attempt to synthesize Au nanoparticles, sputtering and vapor deposition techniques were employed to prepare Au electrodes as the  $CO_2$  electrocatalysts [56,64]. The results revealed that the surface morphology and surface area of the Au electrodes affected reduction potentials in aqueous solutions. Recent studies have focussed mainly on the preparation of nanostructured Au electrodes, which can impart much higher catalytic activity compared to typical Au electrodes toward the electrochemical reduction of  $CO_2$  [65,66]. This



**Figure 2.7** (a) Linear sweep voltammetry of CO<sub>2</sub> electroreduction over Au NP catalyst samples. Data were acquired at room temperature in 0.1 M KHCO<sub>3</sub> with a  $-5$  mV/s scan rate, and were normalized by the respective Au surface areas after the subtraction of a background signal measured on clean glassy carbon. (b) Faradaic current densities at  $E = -1.2$  V vs RHE as a function of Au NP size, with error bars indicating NP size distributions. Reprinted with permission from ref. [57]. Copyright © 2014 American Chemical Society.

may be attributed to large electrochemically active surface areas (EASAs) and different crystal facets [11,67,68]. Experimental results have also shown that the structures and morphologies of these nanocatalysts play a significant role in the enhancement of catalytic activity, for instance,

lowering the overpotential, improving the Faradaic efficiency, and accelerating the reaction rate for the electrochemical reduction of CO<sub>2</sub> [8,9,11,69-73].

With respect to increasing the surface area of polycrystalline Au foils, island-like nanostructured Au catalysts were prepared by treating Au foils with oxygen plasma, which demonstrated a higher current density and lowered the onset potential to 100 mV, compared to bare Au foils, for the selective electrochemical reduction of CO<sub>2</sub> to CO with a FE of 95% at -1.73 to -1.93 V (vs. NHE) [74]. The electrocatalytic activity of the Au nanoparticles was also observed by varying the nanoparticles on a layered film [75]. It was noticed that the catalytic activity and selectivity of the CO<sub>2</sub> electroreduction varied with the surface morphology of the Au electrodes. The thin Au layer with an average nanoparticle size of  $4.4 \pm 0.2$  nm exhibited a remarkable CO formation with a FE of  $\sim 78\%$  at -0.59 V (vs. RHE) in contrast to the tiny layered and thick layered Au. Mistry et al. synthesized different types of Au nanoparticles, varying their size from  $\sim 1-8$  nm in diameter toward the electroreduction CO<sub>2</sub> to understand the role of particle size during CO<sub>2</sub> catalysis [57]. As can be seen in Figure 2.7a, decreasing the particle sizes resulted in a drastic increase in the current density measured by linear sweep voltammetry, which indicated that the catalytic activity relied on the size of the Au nanoparticles. For instance, at -1.2 V (vs. RHE), Au nanoparticles of  $1.1 \pm 1.0$  nm displayed over 100 times the catalytic activity for the CO formation than did the largest nanoparticles (Figure 2.7b). Oxide derived Au nanoparticles, resulting of the reduction of thick Au oxide films, obtained a high electrochemical surface area with a large number of active sites that remarkably enhanced the electrocatalytic activity, while exhibiting high selectivity for CO formation from CO<sub>2</sub> reduction, with excellent stability at a very low overpotential of 140 mV [67].

Other than Au nanoparticles, attempts have also made to synthesize different types of nanostructured Au materials to increase electrocatalytic activity and selectivity for the robust reduction of CO<sub>2</sub>. For example, ultrathin Au nanowires (2 nm wide) were prepared from Au salts using a facile chemical reduction method, which electrocatalyzed CO<sub>2</sub> to CO at an onset potential of -0.2 V (vs. RHE), where the FE of CO achieved was 94% at -0.35 V [53]. Another effort showed that the deposition of Au nanoparticles on a mesostructured template may enhance the catalytic activity of Au for CO<sub>2</sub> electrolysis [76]. The results revealed that the formed mesostructured Au film electrode could catalyze the CO<sub>2</sub>, with CO<sub>2</sub> formation selectivity of almost 100% at an overpotential of 0.4 V. Furthermore, to compare the catalytic performance of the different nanostructured Au for the electrochemical reduction of CO<sub>2</sub>, Liu et al. synthesized Au nanoneedles, nanorods, and nanoparticles [58]. They discovered that the Au nanoneedles had superior catalytic activity among the studied catalysts, which achieved a current density of 22 mA cm<sup>-2</sup> for selective CO production at an overpotential of only 0.24 V in a CO<sub>2</sub>-saturated 0.5 M KHCO<sub>3</sub> solution. The extremely high catalytic activity of the formed Au nanoneedles was explained by the proper utilization of localized electric fields by the sharp tip of the nanoneedles. Therefore, these studies showed that formed nanostructures, surface morphologies, increasing the surface area, and the introduction additional active sites on the electrode surface play vital roles toward the enhancement of the electrocatalytic performance of the Au electrodes for CO<sub>2</sub> conversion and utilization.

### **2.2.3 Ag catalysts**

Similar to Cu and Au, Ag electrodes also show good catalytic activity for the electroreduction of CO<sub>2</sub>. When using Ag metal as an electrocatalyst in aqueous media, CO is the primary product of CO<sub>2</sub> reduction [63,77,78]. Some studies have reported that HCOO<sup>-</sup>

accompanied with CO were also obtained as CO<sub>2</sub> reduction products on a single crystal (fcc) of Ag [79,80]. Recent reports have mainly focused on the preparation of nanostructured Ag as efficient electrocatalysts for the reduction of CO<sub>2</sub> [81-85]. Salehi-Khojin et al. studied the effects of Ag nanoparticle size in the electroreduction of CO<sub>2</sub> and found that superior catalytic activity was obtained with nanoparticles having dimensions of 5 nm, which exhibited ~10 times higher catalytic activity than both a bulk Ag electrode and a single crystal Ag electrode [81]. This study also observed that nanoparticles smaller than 5 nm exhibited a strong binding affinity with reaction intermediates. Similar phenomena were also observed by Kim et al. who noticed that immobilized carbon supported Ag nanoparticles at Ø5 nm showed the highest current density of 1 mA cm<sup>-2</sup> at an overpotential of 0.3 V for CO production with a FE of 79.2% at -0.75 V (vs. RHE) [83]. With the hint of OD-Cu nanoparticles, synthesized nanostructured Ag following the reduction of Ag<sub>2</sub>O was also tested for the electroreduction of CO<sub>2</sub> [84]. This nanocatalyst exhibited a 0.4 V overpotential, which was lower than polycrystalline Ag electrodes in the formation of CO. Moreover, the OD-Ag achieved a 80% FE of CO at about 0.5 V of overpotential, and the study concluded that surface morphology played a critical role in the enhancement of the catalytic activity. With the preparation of mesostructured electrodes containing Ag nanoparticles (Ag-IO), Yoon et al. synthesized a mesostructured Ag inverse opal electrode for the electrochemical reduction of CO<sub>2</sub> [82]. The formed Ag-IO showed an excellent CO<sub>2</sub> reduction activity to CO and established that the formation of a mesostructure of nanostructured Ag is a good strategy for the abundant production of CO. Furthermore, in order to further increase the catalytic performance of Ag, Lu et al. synthesized nanoporous Ag, which obtained a 150 times larger electrochemical surface area and exhibited a 3000 times higher current density than a polycrystalline Ag electrode for CO production with a FE of 92% at an

overpotential of  $>0.5$  V [85]. All of these studies revealed that formation of supernanostructures by altering surface morphologies extended the catalytic performance of Ag with excellent selectivity for the electroreduction of  $\text{CO}_2$ .

#### **2.2.4 Other metal catalysts**

Several other metal based electrodes such as cobalt (Co), tin (Sn), palladium (Pd), zinc (Zn), indium (In), lead (Pb), gallium (Ga), cadmium (Cd), mercury (Hg), and more, have also been studied and tested as electrocatalysts for the reduction of  $\text{CO}_2$  [86]. Many of these metal electrodes have proved to be poor catalysts as they could produce either CO or HCOOH, and were not able to form new C-C bonds during the electroreduction of  $\text{CO}_2$ . The metallic Zn electrocatalysis of  $\text{CO}_2$  produced  $\text{HCOO}^-$  as the primary reduced product. A number of studies showed that CO was obtained as the main product on Zn metal [80,86,87]. However, nanoscale Zn prepared by electrochemical anodization, followed by reduction, exhibited very high selective CO formation with a FE of 93% at -1.6 V (vs. SCE) in a  $\text{CO}_2$ -saturated NaCl solution [88]. Electrodeposited Zn produced HCOOH as the primary product with a FE of 78.4% at -1.5 V during the  $\text{CO}_2$  electrolysis in a  $\text{KHCO}_3$  solution; however, the stability was very poor as it was not active for more than 10 min. [89]. Hence, the reported results still kept the discrepancy alive, that this might have been due to the application of different experimental conditions during electrolysis. Both Sn and Pb metal electrodes produced HCOOH as the predominant product of  $\text{CO}_2$  electrolysis in a  $\text{KHCO}_3$  electrolyte, but required very high overpotentials [90]. The nanostructured Pb synthesized from  $\text{PbO}_2$  obtained a high roughness factor, which was  $\sim 100\%$  for  $\text{HCOO}^-$  for the reduction of  $\text{CO}_2$  in the potential range of from between -1.0 to -0.75 V (vs. RHE) in a 0.5 M  $\text{NaHCO}_3$  solution [91]. CO and  $\text{HCOO}^-$  were the major products of  $\text{CO}_2$  electrolysis on a Pd metal electrode in an aqueous solution [87,92]. Carbon supported Pd

nanoparticles exhibited high activity in the electrochemical reduction of CO<sub>2</sub> for HCOO<sup>-</sup> production with a current density of 50-80 mA g<sup>-1</sup> at overpotential of 0.2 V in a bicarbonate solution, revealed that the formation of Pd nanostructures favored increasing catalytic performance [93]. Metallic Cd and Hg electrodes reduced CO<sub>2</sub> to HCOOH with a FE of 39% and 94%, respectively [63]. A Co metal electrode also produced HCOO<sup>-</sup> from CO<sub>2</sub> electrolysis. A recent study by Gao et al. reported that atomically thin layers of Co had higher catalytic activity in the formation of HCOO<sup>-</sup> at a lower overpotential than did bulk layers of Co. Moreover, partially oxidized atomically thin layers of Co exhibited significantly enhanced catalytic performance, with a current density of 10 mA cm<sup>-2</sup> at 0.24 V overpotential, with high stability over 40 h of electrolysis in the generation of HCOO<sup>-</sup> [71]. The researchers pointed out that the creation of atomic-scale catalyst structures might serve as a new pathway to elucidate the fundamental facts, reaction mechanisms, and scale up of electrolysis, as well as to give further insights into the electroreduction of CO<sub>2</sub>.

### **2.2.5 Alloy catalysts**

Toward the development of electrocatalysts for the reduction of CO<sub>2</sub>, different alloys have been synthesized and investigated. The alloying of different metals has shown to enhance catalytic performance by lowering overpotentials, and increasing production rates, increasing selectivity, stability, and FE as well, in contrast to pure metal electrodes. Different Cu, and Au alloys and their nanoalloys, such as Cu-Au, Cu-In, Cu-Pd, Cu-Pt, Au-Cd, Au-Pd, and others, have been synthesized as efficient electrocatalysts for the reduction of CO<sub>2</sub> [11,29,61,62,94-97]. For instance, Kim et al. synthesized different compositions of bimetallic Au-Cu nanoparticles via the co-reduction of metal precursors to understand their catalytic activity, and found that the electronic and geometric effects of the formed alloys were involved with the binding of reaction

intermediates, which influenced the overall catalytic performance in CO<sub>2</sub> electrolysis [11]. The size-dependence of Au-Cu nanoparticles alloys as catalysts for the electrochemical reduction of CO<sub>2</sub> revealed that the selectivity of the products was minimally dependent on the nanoparticle sizes; however, the activity significantly increased with at smaller sizes [94]. A Cu-In alloy, as a CO<sub>2</sub> electrocatalyst, was synthesized by the in situ electrochemical reduction of Cu<sub>2</sub>O and InSO<sub>4</sub>, where In was distributed on rough Cu surfaces, which selectively produced CO at a low overpotential with a high FE and stability [96]. A bimetallic nanocluster film of Cu and Pd was synthesized as a CO<sub>2</sub> electrocatalyst, revealing that a synergistic effect was present within the nanoalloy, which exhibited the enhanced formation of CH<sub>4</sub> from the CO<sub>2</sub> electrolysis, in contrast to that of pure Cu catalysts [97]. An Au-Pd alloy was also designed and synthesized to catalyze CO<sub>2</sub>, which had the capacity to produce up to C<sub>5</sub> hydrocarbons [62]. The formation of hydrocarbons began at -0.8 V (vs. RHE) on the formed Au-Pd alloys. Furthermore, the selectivity for hydrocarbon increased with the increase of Pd on Au electrode, which indicated that Pd-rich Au-Pd alloy favors the production of hydrocarbon fuels. Additionally, several theoretical studies indicated that nanoalloys of Au-Cd, Cu-Pt, Cu-Ni, Cu-Co, and Cu-Rh could be designed as electrocatalysts for the reduction of CO<sub>2</sub> with enhanced catalytic activity, high selectivity, low overpotentials, and excellent stability [29,61].

### **2.2.6 Carbon and carbon-based electrocatalysts**

Aside from metal-based catalysts, carbon-based materials have also garnered noticeable attention as electrocatalysts for the efficient electrochemical reduction of CO<sub>2</sub>. For example, carbon nanofibers [98], nitrogen-doped graphene quantum dots [99], nitrogen-doped carbon coated multi-walled carbon nanotubes [100], nitrogen-doped carbon nanotubes [101], nitrogen-doped nanodiamond [102], boron-doped diamond [103], nitrogen-doped graphene foam [104],



boron-doped graphene [105], nitrogen-doped carbon [106] copper nanoparticle/nitrogen-doped graphene [107], carbon nanotube/copper sheets [15], graphene-supported Cu nanoparticles [16], Pd-Cu/graphene [17], carbon-supported Cu nanoparticles [14] and more, have recently been identified as promising catalysts for the electrochemical reduction of CO<sub>2</sub>. These carbon-based materials have a high surface area, high electronic conductivity, high-temperature stability, resistance to acids and bases, extremely high mechanical strength, are environmentally compatible, and have high natural abundance as well, in comparison to metal-based electrocatalysts [108]. Hence, carbon materials are under serious consideration for the development CO<sub>2</sub> electrocatalysts.

Recently, Kumar et al. synthesised carbon nanofibers (CNFs) through the carbonization of poly-acrylonitrile (PAN) nanofibers, via the electrospinning of a PAN solution, which is metal free, which showed a very low overpotential of 0.17 V for the reduction of CO<sub>2</sub> and exhibited ~13 times higher current density than a bulk Ag electrode at -0.573 V (vs. RHE) for selective CO production from CO<sub>2</sub> electrolysis [98]. Systematic studies also revealed that the binding energies between CNF surfaces and reaction intermediates was high, which raised the possibility of replacing metal electrodes with carbon materials. The introduction of heteroatoms such as N, B, and S in carbon materials (e.g., black carbon, CNFs, carbon nanotube, graphene, etc.) through doping, which can alter the electronic nature of carbon platforms, might exhibit efficient CO<sub>2</sub> reduction catalytic activities [109]. For instance, (graphene-like) nitrogen doped carbon showed a six fold higher activity than did Cu electrodes with an extremely high FE (93.5%) for CH<sub>4</sub> in a [Bmim]BF<sub>4</sub> electrolyte at an applied potential of -1.4 V vs. Ag/Ag<sup>+</sup> (0.01 M AgNO<sub>3</sub> in 0.1 M TBAP-MeCN) [106]. Wu et al. synthesized N-doped carbon nanotubes (NCNTs) with a 5% N atom content via a liquid chemical vapor deposition method as electrocatalysts for the reduction

of CO<sub>2</sub> [101]. The formed NCNTs showed a higher catalytic activity over pristine CNTs by displaying some unique features, including a low free energy for CO<sub>2</sub> activation during the reduction process and a low affinity for hydrogen evolution by enhancing energy barriers. Further, it possessed preferable catalytic sites that facilitated reduction reaction rates, resulting in a 80% FE of CO at a very low overpotential of 0.26 V [101]. A N-doped nanodiamond on Si rod array substrate was found to be a catalyst for the selective formation of acetate from CO<sub>2</sub> electrolysis, with a FE of 91.2-91.8% at -0.8 to -1.0 V (vs. RHE) [102]. Formaldehyde was formed with high yields (FE 74%) as a CO<sub>2</sub> reduction product on a boron-doped diamond electrocatalyst using seawater as an electrolyte solution at -1.7 V (vs. Ag/Ag<sup>+</sup>) [103].

Graphene, by itself, does not have any intrinsic electrocatalytic activity for the reduction of CO<sub>2</sub>; however, heteroatom (N and B)-doped graphene exhibits good catalytic performance for the electroreduction of CO<sub>2</sub> [99,104,105,109,110]. Graphene with nitrogen defects exhibits enhanced activity for the catalytic reduction of CO<sub>2</sub> by lowering the free energy barrier to generate a high level of CO formation in contrast to pristine graphene [104]. Three-dimensional graphene with N defects has shown CO formation potential only at -0.19 V (vs. RHE), which further attained ~85% FE for CO generation at an overpotential of 0.47 V with 5 h of stability [104]. Multi-carbon products such as ethylene and ethanol were formed on a nitrogen-doped graphene quantum dot (NGQD) catalyst during CO<sub>2</sub> electrolysis [99]. The NGQD catalyst favors the formation of C-C bonds beyond the cathodic potential of -0.61 V (vs. RHE), and the overall FE attained was 90% at -0.75 V, with an ethylene and ethanol formation of 45%. Moreover, this metal-free NGQD catalyst had an affinity for the generation of C<sub>2</sub> and C<sub>3</sub> products at a higher cathodic potential [99]. Aside from N-doped graphene, boron-doped graphene also showed enhanced catalytic activity for the electrochemical reduction of CO<sub>2</sub>, where formate was

comparatively synthesized at a low overpotential, leading to a major reduced product, and it attained significant stability compared to pristine graphene [105].

The creation of a composite consisting of nanostructured metals (Cu, Sn, Pd) and carbon materials (carbon nanotubes, graphene oxide, graphene), or carbon material-supported metal nanostructures could combine the characteristics of both materials to enhance the catalytic activity of the formed catalysts for the electrochemical reduction of CO<sub>2</sub>. Baturina et al. studied the electrocatalytic nature of different types of carbon materials, such as carbon black-, single-wall carbon nanotubes- and Ketjen Black carbon-supported Cu nanoparticles toward the reduction of CO<sub>2</sub> [14]. Their study found that a homogeneous dispersion and smaller Cu nanoparticles were obtained on carbon materials than on electrodeposited Cu. The formed Cu nanoparticles supported on these carbon materials exhibited a large number of electrochemically active sites versus electrodeposited Cu, which attained a low onset potential and the highly selective formation of C<sub>2</sub>H<sub>4</sub> [14]. Catalysts comprised of CNT/Cu sheets also produced CO, CH<sub>4</sub>, and C<sub>2</sub>H<sub>4</sub> as CO<sub>2</sub> reduction products [15]. The catalytic activity of the CNT/Cu was further increased by an oxygen plasma treatment, which exhibited a higher production rate than did pristine CNT/Cu and CNT sheets. Defective graphene-supported Cu nanoparticles might also exhibit improved catalytic activity for the electrochemical reduction of CO<sub>2</sub> than pristine Cu nanoparticles, which has been studied by density function theory. It was demonstrated that the surface morphology and electronic properties of Cu might be modified by incorporating Cu nanoparticles into graphene. This would allow for the geometrical flexibility to have interactions with CHO\* intermediates, which might be a key step in the conversion of CO<sub>2</sub> into hydrocarbon fuels, such as CO, HCOOH, and CH<sub>4</sub> [16,111]. Composites comprised of Pd nanoparticles with graphene, Cu nanoparticles with graphene, and Pd and Cu nanoparticles with graphene have

been investigated for the electroreduction of CO<sub>2</sub>, and showed that bi-metal nanoparticle loading on graphene had a higher catalytic activity than mono-metal loading on graphene [17]. Different quantities (in wt%) of Cu, Pd, and both of them together were loaded onto graphene and their activity was compared by employing cyclic voltammograms in a CO<sub>2</sub>- and N<sub>2</sub>-saturated 0.5 M KHCO<sub>3</sub> solution. The current densities in the CO<sub>2</sub>-saturated solution were higher than the N<sub>2</sub>-saturated solution, indicating that all of the catalysts had CO<sub>2</sub> reduction activity. In contrast, 1% Pd nanoparticles attained a current density of -1.88 mA, which was superior compared to other loading contents of Pd on graphene. Similarly, the highest current density (-2.25 mA) was obtained with 1% Cu nanoparticles among the other loadings of Cu on graphene. Loading both 1% Pd and 1% Cu together on graphene showed a lower current density than the mono-metallic nanoparticle loading. Surprisingly, the activity suddenly increased to -2.80 mA while increasing the Cu loading by 1% on the bi-metallic nanoparticle catalyst sample; however, it decreased further with higher Cu loading. Hence, among the studied composites, the optimal catalytic performance was achieved at 1% Pd-2% Cu supported on graphene. Lei et al. synthesized Sn nanoparticles (15 nm) supported on graphene, and Sn quantum sheets, which were restricted in graphene via a spatially confined reduction process as electrocatalysts for the reduction of CO<sub>2</sub> [18]. The highest catalytic activity was obtained on Sn quantum sheets confined in graphene, compared to the 15 nm Sn nanoparticles supported on graphene, 15 nm Sn nanoparticles, and bulk Sn electrodes. For instance, graphene confined Sn quantum sheets achieved a current density of 21.1 mA cm<sup>-2</sup> with more than 85% FE of formate generation at -1.8 V (vs. SCE) over 50 h of electrolysis. The results indicated that other metal quantum dots confined in graphene might have a higher catalytic activity for the electroreduction of CO<sub>2</sub> than that of metal nanoparticles supported on graphene. Reduced graphene oxide (rGO) synthesized through a

chemical or electrochemical reduction process, possessed similar characteristics to graphene. Combining rGO and metal nanoparticles might obtain synergistic effects that may enhance the catalytic performance of metal nanoparticle catalysts. Recently, rGO supported Cu nanoparticles were used as electrocatalysts for the reduction of CO<sub>2</sub> [112]. A large cathodic current density and low onset potential were obtained on a Cu NP supported rGO nanosheets compared to a Cu film and Cu NPs. For instance, the Cu film attained a current density of -0.24 mA cm<sup>-2</sup> at -1.54 V (vs. NHE), which was four times smaller than that of the CuNPs/rGO electrode. Moreover, the formed CuNPs/rGO exhibited high stability and no Cu NP degradation from the electrode surface during the electrolysis of CO<sub>2</sub>.

### **2.3 Reaction pathways of CO<sub>2</sub> electroreduction**

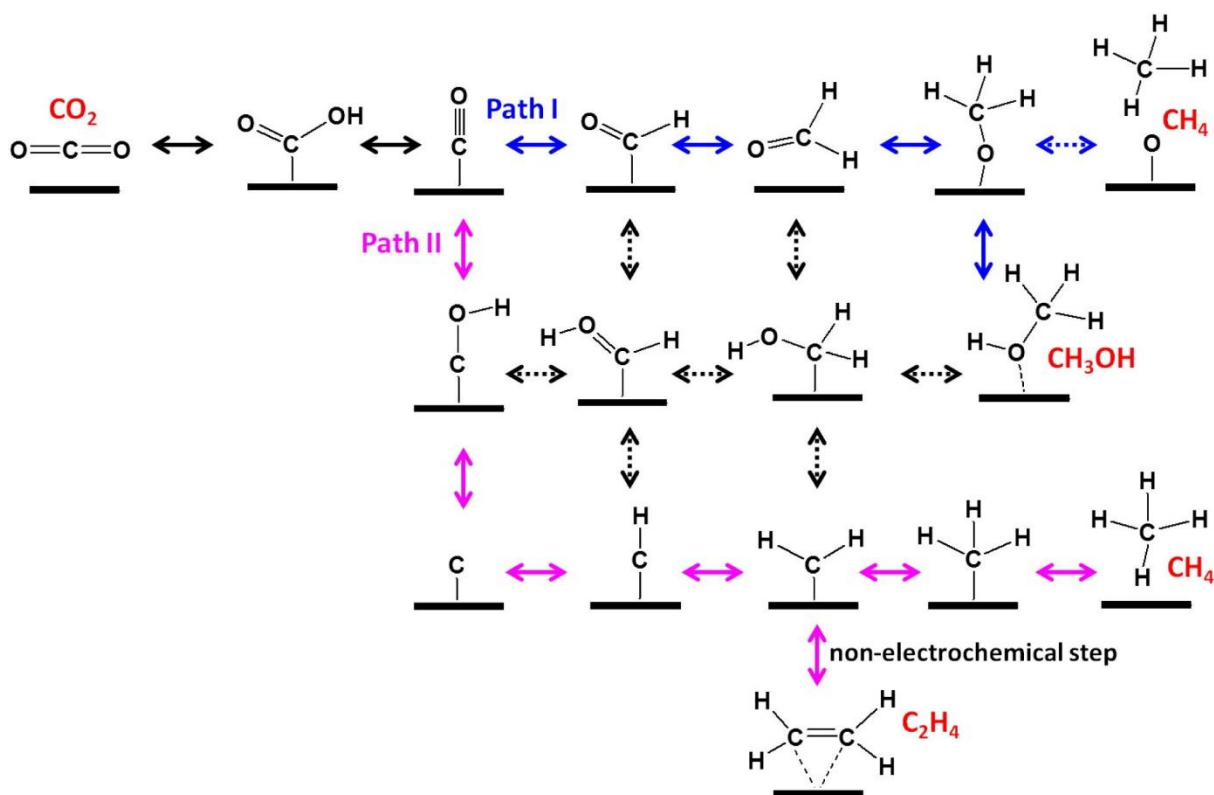
Over the last three decades, a large number of research articles have been published that focus on the electrochemical reduction of CO<sub>2</sub>. Different types of efficient electrocatalysts have been developed to synthesize usable chemicals as the reduction products of CO<sub>2</sub>. In addition, substantial efforts have been invested in the determination of reaction mechanisms to elucidate the fundamental kinetics of the electrochemical reduction of CO<sub>2</sub>, both experimentally and theoretically [9,29,69,113-117]. The reaction kinetics are contingent on the types of catalyst and product selectivity. Several researchers have proposed different reaction mechanisms for selective production formation, even using same the electrocatalyst following identical experimental conditions. For instance, the proposed mechanisms for the formation of CH<sub>4</sub> on Cu electrodes are still under debate. Hori et al. proposed that hydroxymethylidyne (CHO\*) is the reaction intermediate and the rate-determining step might be the further reduction of the formed intermediate of CHO\* [118], whereas the Gattrell group have suggested that CO is the intermediate of the CO<sub>2</sub> reduction reaction, and rate-determining step occurs during CO

formation, but the mechanism goes through CHO\* formation, followed by breaking the C-OH bond to form CH<sub>4</sub> on Cu electrodes [31]. However, it is highly challenging to determine the proper reaction mechanisms in aqueous media by obtaining the experimental products, which could lead to the proposal of various intermediates and pathways, even arriving at the identical reduced species. Theoretical studies might provide a proper pathway to identify the reaction intermediates and kinetics of the electroreduction of CO<sub>2</sub>. For example, density function theory (DFT) calculations might provide a better idea to study the reaction paths on specific catalyst surfaces. Several research groups have demonstrated CO<sub>2</sub> reduction reaction mechanisms by conducting DFT studies on Cu, defective graphene supported Cu, Cu-based alloys, and other catalyst surfaces [16,29,113,116,119]. In this section, we will discuss recent progress in the design of reaction mechanisms for CO<sub>2</sub> reduction to attain various products on different catalyst surfaces by both theoretical and proposed pathways that have been sketched on the basis of experimental results.

### **2.3.1 Theoretical insights**

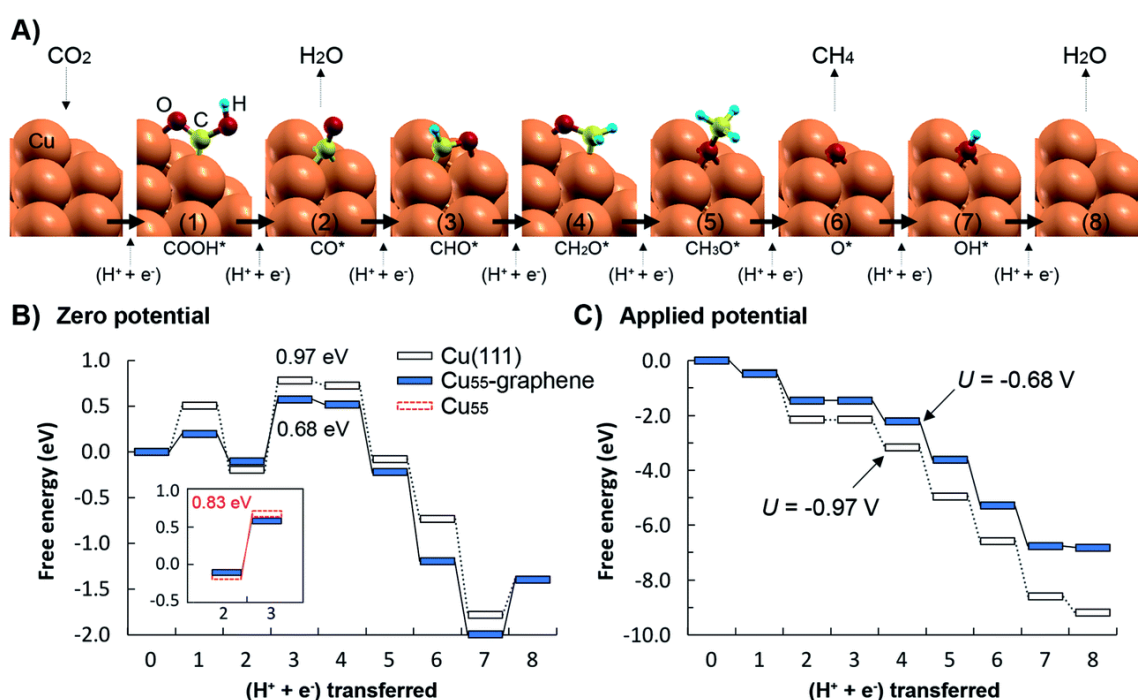
DFT is one of the primary platforms, and a first-principle theoretical study, that could provide a unique tool to model the possible reaction pathways on different catalyst surfaces for the electrochemical reduction of CO<sub>2</sub>. The reaction free energies and kinetic barriers involved with the formation of bonds to obtain new species depending on applied potentials are the main considerations of the DFT study. Among the studied CO<sub>2</sub> electrocatalysts, Cu has been the most investigated material, both experimentally and theoretically. A broad range of products (approximately 16 species) mostly hydrocarbon and oxygenate fuels can be formed on Cu electrodes with high efficiency during the electrolysis of CO<sub>2</sub> within the function of potentials [69]. Although some research groups have proposed several reaction mechanisms based on the

experimental results, the reaction intermediates and rate determining steps for products selectivity are still under debate. Peterson et al. have used DFT calculations coupled with a computational hydrogen electrode (CHE) model to elucidate different reaction pathways at different cathodic potentials on a Cu (211) surface [115]. They have examined this considering 41 different intermediate steps as pathways to the major products such as CO, HCOOH, CH<sub>4</sub>, and C<sub>2</sub>H<sub>4</sub>. Their results indicated that the formation of absorbed CHO via the protonation of absorbed CO is the initial key step to obtain hydrocarbons from the reduction of CO<sub>2</sub>. The activation barrier can be reduced if the absorbed CHO is stabilized on the electrode surface



**Figure 2.8** Proposed reaction paths for electrochemical CO<sub>2</sub> reduction on Cu(111), producing methane (CH<sub>4</sub>), methanol (CH<sub>3</sub>OH), and ethylene (C<sub>2</sub>H<sub>4</sub>). The (H<sup>+</sup> + e<sup>-</sup>) reactants and H<sub>2</sub>O product are left off the scheme. Reprinted with permission from ref. [116]. Copyright @ 2014 Elsevier.

compared to absorbed CO; hence, a more efficient process will take place at low overpotentials. Figure 2.8 displays the possible reaction paths to CH<sub>4</sub>, C<sub>2</sub>H<sub>4</sub>, and CH<sub>3</sub>OH from CO<sub>2</sub> on a Cu (111) surface, which was studied by Nie and co-workers [114,116]. They found that the adsorbed H\* with no H<sub>2</sub>O involvement formed C-H bonds on the Cu surface, whereas, CO<sub>2</sub>\* reduction to COOH\* occurred through the formation of O-H bonds due to the solvated H<sub>2</sub>O, which reduces the kinetic barrier. The formation of the products progresses through the two primary pathways, either forming the CHO\* intermediate (Path I) or a COH\* (Path II). As shown in Figure 2.8, both CH<sub>4</sub> and CH<sub>3</sub>OH are formed following Path I through the intermediate of CHO\*. The overall



**Figure 2.9** (A) The lowest energy pathways of CO<sub>2</sub> reduction on the Cu<sub>55</sub>-defective graphene. (B and C) Relative free energy diagrams without (B) and with (C) applied potential for CO<sub>2</sub> reduction on Cu(111) (empty rectangle with dashed lines), Cu<sub>55</sub>-defective graphene (filled rectangle with solid lines), and Cu<sub>55</sub> cluster (empty rectangle in the inset). Reprinted with permission from ref. [16]. Copyright @ 2014 Royal Society of Chemistry.



path for the formation of products according to  $\text{CO}_2^* \rightarrow \text{COOH}^* \rightarrow \text{CO}^* \rightarrow \text{CHO}^* \rightarrow \text{CH}_2\text{O}^* \rightarrow \text{CH}_3\text{O}^* \rightarrow \text{CH}_4 + \text{O}^*$  or  $\text{CH}_3\text{OH}^*$  where, the first formed  $\text{H}_2\text{O}$  and the reactants  $\text{H}^+$  and  $\text{e}^-$  are left off. Path II provides another path through the intermediate of  $\text{COH}^*$  to form  $\text{CH}_4$  by proceeding as  $\text{CO}_2^* \rightarrow \text{COOH}^* \rightarrow \text{CO}^* \rightarrow \text{COH}^* \rightarrow \text{C}^* \rightarrow \text{CH}^* \rightarrow \text{CH}_2^* \rightarrow \text{CH}_3^* \rightarrow \text{CH}_4^*$  (leaving off the formed  $\text{H}_2\text{O}$  and  $\text{H}^+ + \text{e}^-$ ). Moreover, the production of  $\text{C}_2\text{H}_4$  occurred in the presence of a  $\text{CH}_2^*$  intermediate in this path (Path II). Hasan and co-workers also suggested that the presence of  $\text{CH}_2^*$  intermediate favours the formation of  $\text{CH}_4$  and  $\text{C}_2\text{H}_4$  on a Cu (211) surface [120]. The hydrogenation of  $\text{CO}^*$  to  $\text{CHO}^*$  and  $\text{CO}^*$  to  $\text{COH}^*$  are the key selectivity steps to obtain the target products of Path I and Path II, respectively [114,116]. However, several studies have suggested that  $\text{HCO}^*$  is the key intermediate leading to  $\text{CH}_4$  formation by breaking the C-O bond, whereas, the formation of a CO dimer is the key first step to obtain  $\text{C}_2\text{H}_4$  and  $\text{CH}_3\text{CH}_2\text{OH}$  [4,121].

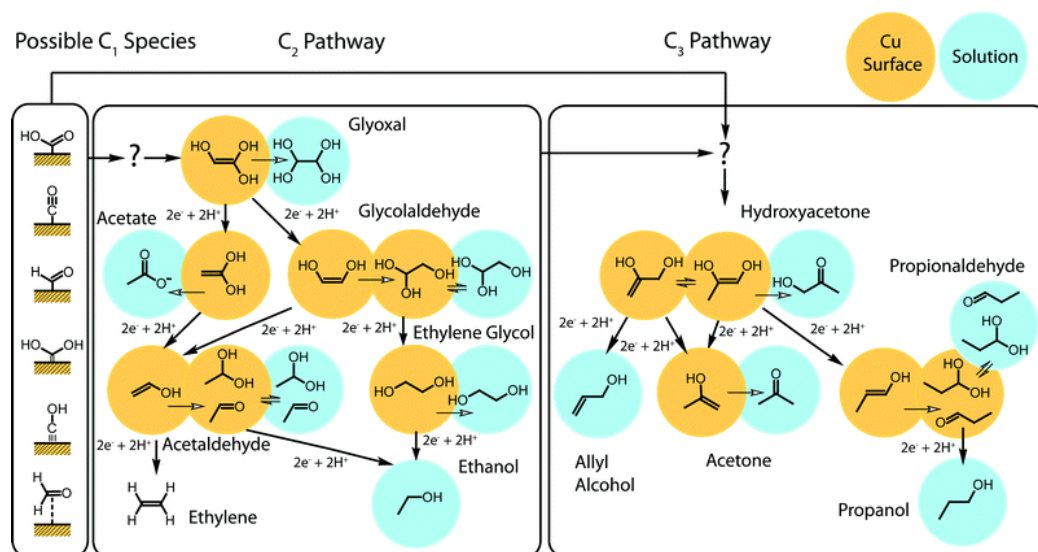
Metal alloys have also been developed and studied for the electrochemical reduction of  $\text{CO}_2$ . Alloying might alter the reaction pathways to obtain selective production, and could reduce the kinetic barrier; hence, theoretical study is required. Hirunshit and co-workers used DFT calculations to investigate the electrochemical reduction of  $\text{CO}_2$  to  $\text{CH}_4$  and  $\text{CH}_3\text{OH}$  on Cu-based alloys, such as  $\text{Cu}_3\text{Ag}$ ,  $\text{Cu}_3\text{Au}$ ,  $\text{Cu}_3\text{Co}$ ,  $\text{Cu}_3\text{Ni}$ ,  $\text{Cu}_3\text{Pd}$ ,  $\text{Cu}_3\text{Pt}$ ,  $\text{Cu}_3\text{Rh}$ , and  $\text{Cu}_3\text{Ir}$  [29,30]. These studies indicated that  $\text{CH}_4$  then  $\text{CH}_3\text{OH}$  are energetically formed on all of the Cu-based alloys except on the  $\text{Cu}_3\text{Pd}$  and  $\text{Cu}_3\text{Pt}$  catalysts, where they require an overpotential of  $\sim 0.7$  V for the production of  $\text{CH}_3\text{OH}$ . The formation of a  $\text{HOCO}^*$  intermediate on the  $\text{Cu}_3\text{Au}$  surface is the limiting potential step, whereas,  $\text{H}_2\text{O}$  formation and  $\text{COH}^*$  protonation are on the  $\text{Cu}_3\text{Co}$ . The  $\text{Cu}_3\text{Co}$ ,  $\text{Cu}_3\text{Ni}$ ,  $\text{Cu}_3\text{Pt}$ , and  $\text{Cu}_3\text{Rh}$  alloy surfaces thermodynamically favor  $\text{HCOOH}$  production at its equilibrium potential by the protonation of  $\text{CO}_2$  with electron transfer steps.

Carbon-based materials such as defective graphene-supported Cu NPs have been studied as an electrocatalyst for the reduction of CO<sub>2</sub> using DFT calculations associated with the CHE model [16]. The studied nanocomposite might have a higher electrocatalytic activity than pristine Cu NPs for the conversion of CO<sub>2</sub> to CO, HCOOH, and CH<sub>4</sub>, where the nanocomposite might obtain a favorable surface morphology and low energy barrier paths for the production of fuels. Figure 2.9 compares the lowest energy paths on Cu (111) and the formed Cu<sub>55</sub>-defective graphene surface from CO<sub>2</sub> electrolysis. The reaction path proceeded as COOH\* → CO\* → CHO\* → CH<sub>2</sub>O\* → CH<sub>3</sub>O\* → O\* → OH\* → H<sub>2</sub>O<sub>gas</sub> on graphene-Cu nanocomposite during gaseous CO<sub>2</sub> reduction (Figure 2.9A). The key potential-limiting step was the protonation of CO\* to CHO\* which required an energy barrier of 0.97 eV and 0.68 eV on Cu (111) and Cu<sub>55</sub>-defective graphene, respectively (Figure 2.9B). Moreover, the activation barrier for oxygen reduction reaction was higher on the Cu-graphene system (0.60 eV) than the Cu surface (0.39 eV), which indicated that nanocomposite might favors the formation of fuels in the reduction of CO<sub>2</sub>. Figure 2.9C shows that the CH<sub>4</sub> formation may occur at the applied potential of -0.97 V and -0.68 V on a Cu and Cu-graphene system, as the rate-limiting step in CO\* to CHO\* requires minimum energies of 0.97 eV and 0.68 eV, respectively. Therefore, graphene-supported metal nanoparticles could be the promising catalysts for the efficient electrochemical reduction of CO<sub>2</sub>; hence, both extensive theoretical and experimental studies are required.

### 2.3.2 Proposed pathways based on experimental results

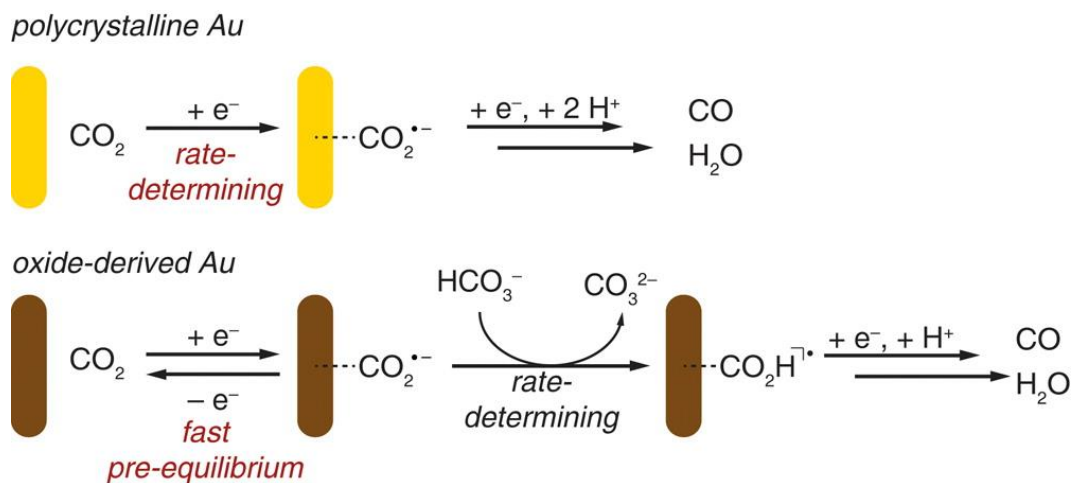
On the basis of experimental results, various reaction pathways have been proposed for different target products on several catalyst surfaces toward the electrochemical reduction of CO<sub>2</sub>. As Cu is the most studied catalyst for CO<sub>2</sub> reduction and potentially produces hydrocarbons and oxygenates, different reaction mechanism schemes were proposed by several research

groups [27,31,69,113]. For instance, Khul and co-workers identified a total of 16 products, including two hydrocarbons ( $\text{CH}_4$  and  $\text{C}_2\text{H}_4$ ) and 14 oxygenates, where 11 of them were  $\text{C}_2$  and  $\text{C}_3$  products obtained at different electrode potentials on a Cu electrode surface [69]. The formation of CO or HCOOH from  $\text{CO}_2$  requires a low overpotential due to having lower activation barriers, and they are involved with a two-electron reduction process. The more complex molecule is obtained at higher overpotentials because of the further reduction of the CO intermediate, which is kinetically more complicated. Figure 2.10 displays the possible reaction pathways for the  $\text{C}_2$  and  $\text{C}_3$  product formation. They have suggested that the key intermediates are enol-like species which are transformed into  $\text{C}_{2+}$  products with repeating dihydroxylations via the electrochemical steps of  $2\text{H}^+$  and  $2\text{e}^-$ . Though it



**Figure 2.10** Proposed reaction pathway for  $\text{C}_2$  and  $\text{C}_3$  products with enol-like surface intermediates. Arrows between overlapping circles indicate changes between the enol, keto, and diol forms of each product. Arrows between non-overlapping circles indicate electrochemical reduction steps involving the addition of  $2\text{H}^+$  and  $2\text{e}^-$ . For simplification, product names are intended to refer to all forms of the product. Reprinted with permission from ref. [69]. Copyright @ 2012 Royal Society of Chemistry.

is not yet clear what the involvement of  $C_1/C_2$  is for the formation of C-C coupling, the repeating replacements of  $OH^-$  group by forming  $H_2O$  molecule might explain the production of many more  $C_2$  and  $C_{2+}$  products. Thus, after forming a C-C bond,  $C_2H_4$  is formed by the quick loss of  $OH^-$  groups from the surface-adsorbed enol-like species, where the other products might be formed by the desorption of enol-like intermediates. Sen et al. synthesized HCOOH and hydrocarbons on their formed Cu nanofoams from the reduction of  $CO_2$  [27]. They predicted that the F-intermediate (OCHO) pathway leads to the formation of HCOOH whereas the C-intermediate (COOH) pathway provides for the higher production of hydrocarbons. Furthermore, the types of electrolyte and the pH of the solution might have an impact on the reaction mechanisms, where the adsorbed anions such as  $(CO_2)^-$  ionic dimer and  $CO_2^{\cdot-}$  intermediates may form under such conditions, and might also play an important role in the reaction pathways toward the formation of  $C_1$  and  $C_2$  products [113]. Chen et al. discovered an oxide-derived Au NPs (OD-Au) electrocatalyst that was highly active and selectively produced CO from  $CO_2$



**Figure 2.11** Proposed mechanisms for  $CO_2$  reduction to CO on polycrystalline Au and oxide-derived Au. Reprinted with permission from ref. [67]. Copyright @ 2012 American Chemical Society.

reduction in a CO<sub>2</sub>-saturated 0.5 M NaHCO<sub>3</sub> solution [67]. They proposed that the reaction mechanism of CO formation on polycrystalline Au involved the formation of a CO<sub>2</sub><sup>•-</sup> intermediate by a e<sup>-</sup> transfer to CO<sub>2</sub>, which was counted to be the rate determining step and followed by the protonating of H<sup>+</sup> ions and the transfer of another electron with the production of a H<sub>2</sub>O molecule (Figure 2.11). On the other hand, the developed OD-Au involved the formation of a CO<sub>2</sub><sup>•-</sup> ion with a reversible e<sup>-</sup> transfer to CO<sub>2</sub> (which was the initiation step) followed by H<sup>+</sup> consumption from HCO<sub>3</sub><sup>-</sup> (rate determining step) and subsequent transfers of another e<sup>-</sup> and H<sup>+</sup> to form CO. The mechanism of CO formation from the CO<sub>2</sub> reduction on a nanoscale Zn catalysts was also involved by forming an intermediate of CO<sub>2</sub><sup>•-</sup> ion, which had faster reaction rate in NaCl solution, but was slow in a NaHCO<sub>3</sub> electrolyte, due to competitive H<sub>2</sub>O reduction [88]. However, the formed CO<sub>2</sub><sup>•-</sup> ion was protonated and further reduced giving HCOOH as a reduction product associated with the bicarbonate ion on a polyethyleneimine functionalized N-doped carbon nanomaterials, which was proposed by Zhang and co-workers [122].

#### **2.4 Stability and activity degradation of catalysts**

Catalyst stability is generally evaluated by their electrolysis performance over longer periods [123]. A good electrocatalyst should acquire low overpotential and high FE with a long-term durability of reduction catalysis performance. For most catalysts, although some exhibit high catalytic activity, they suffer from poor stability and survive for less than 100 h, which is not sufficient for practical applications [47]. Studies have reported that a polycrystalline Cu electrode quickly lost its activity in the electroreduction of CO<sub>2</sub>, which might be due to the formation of graphitic carbon on its surface [26,35,124]. Stevens et al. observed that the catalytic activity of a porous Au film decreased by 40% following 100 min. of electrolysis at an applied potential of -2.1 V (Ag/AgCl), which might be due to the further reduction of the formed CO to

elemental carbon that blocked the active sites of the porous Au film [56]. Cu nanoflowers produced  $C_2H_4$  from the electroreduction of  $CO_2$ ; however, the production rate gradually decreased after 2 h of electrolysis [26]. Moreover, it was observed that corrosion of the particles from the electrode surface limited the stability of the electrocatalysts for the reduction of  $CO_2$  [125]. However, obtaining high stability for catalyst remains one of the most significant challenges in the development of  $CO_2$  electrocatalysts. Several studies have reported on the issue of catalyst deactivation, which indicated the formation of pollutant intermediates, the decaying of electrode materials, and the deposition of by-products on the electrode surface as being the primary causes [47,126]. With respect to catalyst durability, some of the possible factors have been summarized below [126-128]:

- (i) Using metal as electrodes, metal impurities interact with the electrolyte solution.
- (ii) A trace amount of organic substance might contaminate the water that is used to prepare the electrolyte solution.
- (iii) Contaminants from the ion-exchange membranes that are used as a separator between the cathode and anode chamber.
- (iv) Poisonous intermediate species produced during  $CO_2$  electrolysis may adsorb on the electrode surface.
- (v) Morphology changes of the electrode surface, aggregation of the catalyst particles, or corrosion of the particles from the catalyst surface.
- (vi) Adsorption of non-catalytic species on the electrode surface from the contaminants.

- (vii) Deposition of anode material particles on the cathode catalysts and formation of gas bubbles on the anode surface that prevents cathodic polarization during electrolysis because of large electrode potentials.
- (viii) Increasing the amount of liquid products, and in the meantime decreasing the concentration of CO<sub>2</sub> in the electrolyte solution due to long running electrolysis.

In addition to these factors, the electrolysis mode and experimental conditions could also affect the stability of the catalysts [35,129,130]. For example, a Cu cathode was deactivated after only 3 h of electrolysis at a constant potential mode; however, the activity was retained for 7 h once superimposed potential was applied [124].

## **2.5 Summary and perspectives**

The electrochemical conversion of CO<sub>2</sub> could be an inexpensive and green source of fuels and chemical synthesis. The catalytically mediated electroreduction of CO<sub>2</sub> may provide an elegant pathway to mitigate the global energy crisis and to balance the global carbon cycle. Various electrocatalysts that have been explored for the electrochemical reduction of CO<sub>2</sub> over the last few decades, as reported in the literature, have been summarized as Cu, Au, Ag, alloys, carbon and carbon-based materials in this chapter. The catalytic reaction mechanisms proposed by experimental results and theoretical insights into different catalysts were also discussed widely in the introduction section. Altogether, due to recent advancements in the field, the electrochemical CO<sub>2</sub> reduction method is an energy efficient technology, a potential path for the synthesis of fuels, and a promising candidate as sustainable energy source. However, the transformation of CO<sub>2</sub> into fuels on a large scale via electrochemical technology remains insufficient as the result of several severe limitations. These persistent constraints include low catalytic activity, low production rate, poor product selectivity, and inadequate catalyst stability.

Thus, further catalyst and technology development is required to overcome these challenges; therefore we propose several emerging research approaches to address these limitations:

**(i) Advancement of nanostructured catalysts.** In the development of CO<sub>2</sub> electrocatalysts, various pure metal electrodes, their nanostructured materials, alloys, and nanocomposites have been prepared and employed for the electrochemical reduction of CO<sub>2</sub>, and some of them have exhibited pronounced catalytic performance. However, the catalytic activity is not energy efficient and sufficient for industrial applications to commercialize the generated products. Therefore, intensified efforts are required to achieve excellent catalyst performance. To enhance catalytic activity, efforts should continue in the design and synthesis of various new nanostructured materials, such as nanoparticles, nanoneedles, nanorods, nanofoams, nanodendrites, nanoflowers, and nanoalloys comprised of heavy metals, rare-earth metals, and metalloids. Nanostructured materials have unique surface morphologies, large surface areas, more active sites, different crystal facets, whereas nanoalloys could have synergistic interactions. Hence, the integration of advanced nanostructured materials might provide an optimal condition to achieve high catalytic activity.

**(ii) Exploring of carbon-based materials at the nanoscale:** Different types of carbon materials such as glassy carbon, carbon nanotubes, graphene materials, nanodiamond, and others have been identified as promising electrocatalysts for the reduction of CO<sub>2</sub>. Moreover, heteroatom-doped carbon materials, namely N-doped graphene, B-doped diamond, N-doped carbon nanotubes, S,N-doped carbon, B-doped graphene, and carbon material supported metal nanoparticles have recently garnered significant attention as highly efficient catalysts for the electrochemical reduction of CO<sub>2</sub>. However, redoubled efforts should be invested to achieve the extraordinary catalytic performance of carbon based catalysts for CO<sub>2</sub> electrolysis. Carbon



materials have large surface areas, high electrical conductivity, and could have strong synergistic interactions with metal nanoparticles. The incorporation of heteroatoms in the carbon matrix, making nanocomposite carbon materials with various metal nanoparticles, and synthesizing metal quantum dots might introduce, or significantly increase, the electrocatalytic activity of pristine carbon materials. Moreover, carbon materials can stabilize and prevent the agglomeration of metal particles upon deposition. Additional carbon-based CO<sub>2</sub> electrocatalysts could be explored along with the consideration of their superior electrochemical properties. The development of single atom-doped or heteroatom-doped carbon materials, heteroatom-doped carbon material decorated metal particles, carbon material supported hetero metal particles as CO<sub>2</sub> electrocatalysts, might provide a novel strategy for improved efficiency for the reduction of CO<sub>2</sub>. Hence, controllable synthesis with desirable structures and the composition of carbon-based materials are essential requirements to achieve high catalytic performance for the electrochemical reduction of CO<sub>2</sub>.

**(iii) High selectivity:** Many CO<sub>2</sub> electrocatalysts exhibit low selectivity, though some show high catalytic activity. Product selectivity is highly variable among catalysts, where even the same catalyst can produce different products under identical experimental conditions. The surface morphology, electrochemical active sites, crystal facets, material compositions, experimental conditions, such as electrolytes, solution pH, and applied electrode potential play a crucial roles in product selectivity and yields. Therefore, the consideration of these properties when designing catalysts may overcome poor selectivity in the electroreduction of CO<sub>2</sub>. For example, Cu materials are known as hydrocarbon fuel producing catalysts, whereas some carbon materials have been observed to facilitate C-C bond formation; hence, the development of an

optimized composition of nanostructured Cu with graphene might obtain high selectivity in the production of hydrocarbons.

**(iv) Long-term stability:** Most developed catalysts suffer from poor stability in the electrochemical reduction of CO<sub>2</sub>, where can survive 100 h of electrolysis, which is insufficient for industrial applications. Hence, catalyst stability remains one of the severe challenges that constrain the development of efficient CO<sub>2</sub> catalysts. Therefore, several factors should be considered to overcome this limitation, such as a) ensuring the purity of precursor materials while synthesizing catalysts, b) ensuring that the electrolyte solution is free of contaminants, c) poisonous intermediates should be identified and completely removed, d) optimizing the operation conditions such as the electrode potential, pH, and electrolyte solution, e) gently circulate the electrolytes in the cathode chamber to prevent the gathering the generated products on the catalyst surfaces, f) find a way to prevent the corrosion of catalyst particles on the electrode surface, g) increase the concentration of CO<sub>2</sub> in the electrolyte solution and find a way to maintain the same concentration during the entire electrolysis process, and h) transfer the generated products from the reactor and introduce new electrolyte without disturbing the system.

**(v) Increasing the CO<sub>2</sub> concentration in the system:** Generally, electrochemical CO<sub>2</sub> reduction is performed in an aqueous solution, where the solubility of CO<sub>2</sub> in the aqueous solution is typically low. The aqueous solution contains H<sup>+</sup>, HCO<sub>3</sub><sup>-</sup> ions, and solvated CO<sub>2</sub>. The affinity of H<sup>+</sup> to reduce H<sub>2</sub> gas on the cathode surface is high and, therefore, there is a competition between protons and solvated CO<sub>2</sub> to participate in the reduction on the catalyst surfaces upon applying the cathodic potential. By increasing the quantity of solvated CO<sub>2</sub> in the system there is a high probability of having a sufficient population of CO<sub>2</sub> molecules on the electrode surface, which could suppress H<sub>2</sub> evolution. Hence, to enhance the CO<sub>2</sub> reduction rate

and stability of the electrode the concentration of solvated CO<sub>2</sub> in the electrolyte solution should be increased. The utilization of a high-pressure CO<sub>2</sub> aqueous/non-aqueous solution system, the continuous purging of CO<sub>2</sub> into the electrolyte solution, and the design of a system that has the capacity to use highly concentrated supercritical CO<sub>2</sub>-aqueous/non-aqueous system, might be potential strategies for supplying sufficient amounts of CO<sub>2</sub> to the surfaces of the catalysts.

**(vi) Understanding fundamental insights:** As CO<sub>2</sub> is a fully oxidized and thermodynamically stable molecule; it is energetically expensive to convert CO<sub>2</sub> to its derivatives. To synthesize complex molecules from CO<sub>2</sub>, it is critical to overcome activation barriers and to form new chemical bonds. However, the determination of the proper reaction mechanisms and understanding the roles of intermediates are quite challenging during the catalysis of CO<sub>2</sub>. To enhance catalytic activity, while improving product selectivity and catalyst stability; a better understanding of fundamental insights is necessary for both theoretical modeling and for obtaining experimental products. Hence, the design and optimization of catalyst structures, elucidating the relationships between intermediates and catalyst active sites, reaction mechanisms, and the role of operation conditions could be examined through the combination of DFT studies and experimental confirmations. More theoretical studies should be conducted with various nanostructured materials and different metal crystal facets for improved fundamental analysis. Moreover, the synthesis of new nanomaterials, nanocomposites, and changing experimental conditions during CO<sub>2</sub> electrolysis, will facilitate the acquisition of insights for a more complete fundamental understanding.

**(vii) System designs for scale up applications and economic benefits:** A vast amount of CO<sub>2</sub> is available for transformation to fuels and chemicals. Among various technologies, electrochemical technologies have strong potential to synthesize fuels and useful chemical

powered by renewable energy. However, the current state of CO<sub>2</sub> electrochemical reduction technologies is not practical for fuel production. Small reactor systems, tiny electrodes, insufficient quantities of catalysts, low concentrations of CO<sub>2</sub> in the electrolyte solution, low catalytic activity, and rapid deactivation of the catalyst performance, are considered to be the major limitations to scaled up production. The synthesis of highly active and cheap catalysts, increasing the geometric surface areas of the electrode, optimizing operation conditions, enlarging the reactor size by interconnecting several cathode chambers in parallel with the cathode immersion in each chamber, designing new techniques to properly introduce CO<sub>2</sub> gas into the system, such as continuous purging with the circulation of gas bubbles into the solution, and selecting appropriate ion-exchange membranes as separators might be viable strategies to scale up production using CO<sub>2</sub> electrochemical technologies.

In summary, electrochemical CO<sub>2</sub> reduction technologies can provide an elegant pathway to produce fuels and value-added chemicals; hence, they could serve as sustainable green sources for energy production, which could contribute to mitigating the global energy crisis, reducing the average global temperature, as well as to balance the global carbon cycle driven by renewable energy. Although electrochemical technologies still face a number of severe challenges, these are not insurmountable. Recent advances in this field, in particular, the development of various highly active nanostructured materials, have strong potential for the development of extraordinary catalysts for the electrochemical conversion of CO<sub>2</sub>, which will serve as an efficient strategy for the production of energetic hydrocarbon fuels and value added chemicals at industrial scales in the near future.

**Reference:**

- [1] A. Rosas-Hernández, H. Junge, M. Beller, M. Roemelt, R. Francke, *Catal. Sci. Technol.* **2017**, *7*, 459.

- [2] C. W. Machan, J. Yin, S. A. Chabolla, M. K. Gilson, C. P. Kubiak, *J. Am. Chem. Soc.* **2016**, 138, 8184.
- [3] S. Back, J. Lim, N.-Y. Kim, Y.-H. Kim, Y. Jung, *Chem. Sci.* **2017**, 8, 1090.
- [4] K. J. P. Schouten, Y. Kwon, C. J. M. van der Ham, Z. Qin, M. T. M. Koper, *Chem. Sci.* **2011**, 2, 1902.
- [5] K. J. P. Schouten, Z. Qin, E. P. Gallent, M. T. M Koper, *J. Am. Chem. Soc.* **2012**, 134, 9864.
- [6] C. W. Li, J. Ciston, M. W Kanan, *Nature* **2014**, 508, 504.
- [7] Y. Hori, In *Modern Aspects of Electrochemistry*, Vol. 42 (Eds: C. G. Vayenas, R. E. White, M. E. Gamboa-Aldeco), Springer, New York, **2008**, 89.
- [8] A. A. Peterson, J. K. Nørskov, *J. Phys. Chem. Lett.* **2012**, 3, 251.
- [9] H. A. Hansen, J. B. Varley, A. A. Peterson, J. K. Nørskov, *J. Phys. Chem. Lett.* **2013**, 4, 388.
- [10] I. Ganesh, *Renew. Sustain. Energy Rev.* **2014**, 31, 221.
- [11] D. Kim, J. Resasco, Y. Yu, A. M. Asiri, P. Yang, *Nature Commun.* **2014**, 5, 4948.
- [12] K. S. Udupa, G. S. Subramanian, H. V. K. Udupa, *Electrochim. Act.* **1971**, 16, 1593.
- [13] Y. Hori, A. Murata, *Chem. Lett.* **1991**, 181.
- [14] O. A. Baturina, Q. Lu, M. A. Padilla, L. Xin, W. Li, A. Serov, K. Artyushkova, P. Atanassov, F. Xu, A. Epshteyn, T. Brintlinger, M. Schuette, G. E. Collins, *ACS Catal.* **2014**, 4, 3682.
- [15] Y. Koo, R. Malik, N. Alvarez, L. White, V. N. Shanov, M. Schulz, B. Collins, J. Sankara, Y. Yun, *RSC Adv.* **2014**, 4, 16362.
- [16] D.-H. Lim, J. H. Jo, D. Y. Shin, J. Wilcox, H. C. Ham, S. W. Nam, *Nanoscale* **2014**, 6, 5087.
- [17] X. Liu, L. Zhu, H. Wang, G. He, Z. Bian, *RSC Adv.* **2016**, 6, 38380.
- [18] F. Lei, W. Liu, Y. Sun, J. Xu, K. Liu, L. Liang, T. Yao, B. Pan, S. Wei, Y. Xie, *Nature Commun.* **2016**, 7, 12697.
- [19] M. N. Hossain, J. Wen, S. K. Konda, M. Govindhan, A. Chen, *Electrochem. Commun.* **2017**, 82, 16.
- [20] M. N. Hossain, J. Wen, A. Chen, *Sci. Rep.* **2017**, 7, 3184.

- [21] G. Keerthiga, B. Viswanathan, R. Chetty, *Catal. Today* **2015**, 245, 68.
- [22] R. Reske, M. Duca, M. Oezaslan, K. J. P. Schouten, M. T. M. Koper, P. Strasser, *J. Phys. Chem. Lett.* **2013**, 4, 2410.
- [23] R. L. Cook, R. C. Macduff, A. F. Sammells, *J. Electrochem. Soc.* **1987**, 134, 2375.
- [24] R. L. Cook, R. C. Macduff, A. F. Sammells, *J. Electrochem. Soc.* **1990**, 137, 607.
- [25] K. Manthiram, B. J. Beberwyck, A. P. Alivisatos, *J. Am. Chem. Soc.* **2014**, 136, 13319.
- [26] J.-F. Xie, Y.-X. Huang, W.-W. Li, X.-N. Song, L. Xiong, H.-Q. Yu, *Electrochim. Acta* **2014**, 139, 137.
- [27] S. Sen, D. Liu, G. T. R. Palmore, *ACS Catal.* **2014**, 4, 3091.
- [28] Q. Feng, S. Liua, X. Wang, G. Jin, *Appl. Sur. Science* **2012**, 258, 5005.
- [29] P. Hirunsit, W. Soodsawang, J. Limtrakul, *J. Phys. Chem. C* **2015**, 119, 8238.
- [30] P. Hirunsit, *J. Phys. Chem. C* **2013**, 117, 8262.
- [31] M. Gattrell, N. Gupta, A. Co, *J. Electroanal. Chem.* **2006**, 594, 1.
- [32] Y. Hori, A. Murata, R. Takahashi, *J. Chem. Soc. Faraday Trans. 1* **1989**, 85, 2309.
- [33] D. Raciti, K. J. Livi, C. Wang, *Nano Lett.* **2015**, 15, 6829.
- [34] R. Reske, H. Mistry, F. Behafarid, B. R. Cuenya, P. Strasser, *J. Am. Chem. Soc.* **2014**, 136, 6978.
- [35] C. W. Li, M. W. Kanan, *J. Am. Chem. Soc.* **2012**, 134, 7231.
- [36] W. J. Durand, A. A. Peterson, F. Studt, F. Abild-Pedersen, J. K. Norskov, *Surf. Sci.* **2011**, 605, 1354.
- [37] Y. Hori, I. Takahashi, O. Koga, N. Hoshi, *J. Phys. Chem. B* **2002**, 106, 15.
- [38] W. Tang, A. A. Peterson, A. S. Varela, Z. P. Jovanov, L. Bech, W. J. Durand, S. Dahl, J. K. Nørskov, I. Chorkendorff, *Phys. Chem. Chem. Phys.* **2012**, 14, 76.
- [39] C. S. Chen, A. D. Handoko, J. H. Wan, L. Ma, D. Ren, B. Siang Yeo, *Catal. Sci. Technol.* **2015**, 5, 161.
- [40] A. Dutta, M. Rahaman, N. C. Luedi, M. Mohos, Peter Broekmann, *ACS Catal.* **2016**, 6, 3804.

- [41] W. K. Han, J. W. Choi, G. H. Hwang, S. J. Hong, J. S. Lee, S. G. Kang, *Appl. Surf. Sci.* **2006**, 252, 2832.
- [42] C. Hahn, T. Hatsukade, Y.-G. Kim, A. Vailionis, J. H. Baricuatro, D. C. Higgins, S. A. Nitopi, M. P. Soriaga, T. F. Jaramillo, *PNAS* **2017**, 114, 5918.
- [43] Y. Hori, H. Wakebe, T. Tsukamoto, O. Koga, *Surf. Sci.* **1995**, 335, 258.
- [44] I. Takahashi, O. Koga, N. Hoshi, Y. Hori, *J. Electroanal. Chem.* **2002**, 533, 135.
- [45] Y. Hori, I. Takahashi, O. Koga, N. Hoshi, *J. Mol. Catal. A: Chem.* **2003**, 199, 39.
- [46] K. W. Frese, Jr., in *Electrochemical and Electrocatalytic Reactions of Carbon Dioxide*, Ed. by B. P. Sullivan, K. Krist, H. E. Guard, Elsevier, New York, **1993**, 191.
- [47] J. Qiao, Y. Liu, F. Hong, J. Zhang, *Chem. Soc. Rev.* **2014**, 43, 631.
- [48] C. Liu, T. R. Cundari, A. K. Wilson, *J. Phys. Chem. C* **2012**, 116, 5681.
- [49] D. Kima, C. S. Kleyd, Y. Li, P. Yang, *PNAS* **2017**, 114, 10560.
- [50] C. Reller, R. Krause, E. Volkova, B. Schmid, S. Neubauer, A. Rucki, M. Schuster, G. Schmid, *Adv. Energy Mater.* **2017**, 7, 1602114.
- [51] R. Kas, K. K. Hummadi, R. Kortlever, P. de Wit, A. Milbrat, M. W. J. Luiten-Olieman, N. E. Benes, M. T. M. Koper, G. Mul, *Nat. Commun.* **2016**, 7, 10748.
- [52] H. Mistry, A. S. Varela, C. S. Bonifacio, I. Zegkinoglou, I. Sinev, Y.-W. Choi, K. Kisslinger, E. A. Stach, J. C. Yang, P. Strasser, B. R. Cuenya, *Nat. Commun.* **2016**, 7, 12123.
- [53] W. Zhu, Y.-J. Zhang, H. Zhang, H. Lv, Q. Li, R. Michalsky, A. A. Peterson, S. Sun, *J. Am. Chem. Soc.* **2014**, 136, 16132.
- [54] Y. Hori, A. Murata, R. Takahashi, S. Suzuki, *J. Chem. Soc. Chem. Commun.* **1987**, 728.
- [55] H. Noda, S. Ikeda, A. Yamamoto, H. Einaga, K. Ito, *Bull. Chem. Soc. Jpn.* **1995**, 68, 1889.
- [56] G. B. Stevens, T. Reda, B. Raguse, *J. Electroanal. Chemistry* **2002**, 526, 125.
- [57] Mistry, R. Reske, Z. Zeng, Z.-J. Zhao, J. Greeley, P. Strasser, B. R. Cuenya, *J. Am. Chem. Soc.* **2014**, 136, 16473.
- [58] M. Liu, Y. Pang, B. Zhang, P. D. Luna, O. Voznyy, J. Xu, X. Zheng, C. T. Dinh, F. Fan, C. Cao, F. P. G. de Arquer, T. S. Safaei, A. Mepham, A. Klinkova, E. Kumacheva, T. Filleter, D. Sinton, S. O. Kelley, E. H. Sargent, *Nature* **2016**, 537, 382.

- [59] H.-E. Lee, K. D. Yang, S. M. Yoon, H.-Y. Ahn, Y. Y. Lee, H. Chang, D. H. Jeong, Y.-S. Lee, M. Y. Kim, K. T. Nam, *ACS Nano* **2015**, 9, 8384.
- [60] F. Jia, X. Yu, L. Zhang, *J. Power Sources* **2014**, 252, 85.
- [61] Z. P. Jovanov, H. A. Hansen, A. S. Varela, P. Malacrida, A. A. Peterson, J. K. Nørskov, I. E. L. Stephens, I. Chorkendorff, *J. Catalysis* **2016**, 343, 215.
- [62] R. Kortlever, I. Peters, C. Balemans, R. Kas, Y. Kwon, G. Mul, M. T. M. Koper, *Chem. Commun.* **2016**, 52, 10229.
- [63] H. Noda, S. Ikeda, Y. Oda, K. Imai, M. Maeda, K. Ito, *Bull. Chem. Soc. Jpn.* **1990**, 63, 2459.
- [64] T. Ohmori, A. Nakayama, H. Mametsuka, E. Suzuki, *J. Electroanal. Chem.* **2001**, 514, 51.
- [65] D. R. Kauffman, D. Alfonso, C. Matranga, H. Qian, R. Jin, *J. Am. Chem. Soc.* **2012**, 134, 10237.
- [66] T. Cheng, Y. Huang, H. Xiao, W. A. Goddard III, *J. Phys. Chem. Lett.* **2017**, 8, 3317.
- [67] Y. H. Chen, C. W. Li, M. W. Kanan, *J. Am. Chem. Soc.* **2012**, 134, 19969.
- [68] S. Back, M. S. Yeom, Y. Jung, *ACS Catal.* **2015**, 5, 5089.
- [69] K. P. Kuhl, E. R. Cave, D. N. Abram, T. F. Jaramillo, *Energy Environ. Sci.* **2012**, 5, 7050.
- [70] B. A. Rosen, A. Salehi-Khojin, M. R. Thorson, W. Zhu, D. T. Whipple, P. J. A. Kenis, R. I. Masel, *Science* **2011**, 334, 643.
- [71] S. Gao, Y. Lin, X. Jiao, Y. Sun, Q. Luo, W. Zhang, D. Li, J. Yang, Y. Xie, *Nature* **2016**, 529, 68.
- [72] M. Aresta, A. Dibenedetto, A. Angelini, *Chem. Rev.* **2014**, 114, 1709.
- [73] A. M. Appel, J. E. Bercaw, A. B. Bocarsly, H. Dobbek, D. L. DuBois, M. Dupuis, J. G. Ferry, E. Fujita, R. Hille, P. J. A. Kenis, C. A. Kerfeld, R. H. Morris, C. H. F. Peden, A. R. Portis, S. W. Ragsdale, T. B. Rauchfuss, J. N. H. Reek, L. C. Seefeldt, R. K. Thauer, G. L. Waldrop, *Chem. Rev.* **2013**, 113, 6621.
- [74] J. H. Koh, H. S. Jeon, M. S. Jee, E. B. Nursanto, H. Lee, Y. J. Hwang, B. K. Min, *J. Phys. Chem. C* **2015**, 119, 883.
- [75] E. B. Nursanto, H. S. Jeon, C. Kim, M. S. Jee, J. H. Koh, Y. J. Hwang, B. K. Min, *Catal. Today* **2016**, 260, 107.
- [76] A. S. Hall, Y. Yoon, A. Wuttig, Y. Surendranath, *J. Am. Chem. Soc.* **2015**, 137, 14834.



- [77] Y. Hori, K. Kikuchi, S. Suzuki, *Chem. Lett.* **1985**, 1695.
- [78] T. Hatsukade, K. P. Kuhl, E. R. Cave, David N. Abram, T. F. Jaramillo, *Phys. Chem. Chem. Phys.* **2014**, 16, 13814.
- [79] N. Hoshi, M. Kato, Y. Hori, *J. Electroanal. Chem.* **1997**, 440, 283.
- [80] M. Azuma, K. Hashimoto, M. Hiramoto, M. Watanabe, T. Sakata, *J. Electrochem. Soc.* **1990**, 137, 1772.
- [81] A. Salehi-Khojin, H.-R. M. Jhong, B. A. Rosen, W. Zhu, S. Ma, P. J. A. Kenis, R. I. Masel, *J. Phys. Chem. C* **2013**, 117, 1627.
- [82] Y. Yoon, A. S. Hall, Y. Surendranath, *Angew. Chem. Int. Ed.* **2016**, 55, 15282.
- [83] C. Kim, H. S. Jeon, T. Eom, M. S. Jee, H. Kim, C. M. Friend, B. K. Min, Y. J. Hwang, *J. Am. Chem. Soc.* **2015**, 137, 1384.
- [84] M. Ma, B. J. Trzesniewski, J. Xie, W. A. Smith, *Angew. Chem. Int. Ed.* **2016**, 55, 9748.
- [85] Q. Lu<sup>1</sup>, J. Rosen<sup>1</sup>, Y. Zhou, G. S. Hutchings, Y. C. Kimmel, J. G. Chen, F. Jiao, *Nat. Commun.* **2014**, 5, 3242.
- [86] Y. Hori, H. Wakebe T. Tsukamoto, O. Koga, *Electrochim. Act.* **1994**, 39, 1833.
- [87] S. Ikeda, T. Takagi, K. Ito, *Bull. Chem. Soc. Jpn.* **1987**, 60, 2517.
- [88] F. Quan, D. Zhong, H. Song, F. Jia, L. Zhang, *J. Mater. Chem. A* **2015**, 3, 16409.
- [89] V. S. K. Yadav, M. K. Purkait, *New J. Chem.* **2015**, 39, 7348.
- [90] F. Koleli, T. Atilan, N. Palamut, A. M. Gizir, R. Aydin, C. H. Hamann, *J. Appl. Electrochem.* **2003**, 33, 447.
- [91] C. H. Lee, M. W. Kanan, *ACS Catal.* **2015**, 5, 465.
- [92] M. Azuma, K. Hashimoto, M. Watanabe, T. Sakata, *J. Electroanal. Chem.* **1990**, 294, 299.
- [93] X. Min, M. W. Kanan, *J. Am. Chem. Soc.* **2015**, 137, 4701.
- [94] H. Mistry, R. Reske, P. Strasser, B. R. Cuenya, *Catal. Today* **2017**, 288, 30.
- [95] G. G. Li, E. Villarreal, Q. Zhang, T. Zheng, J.-J. Zhu, H. Wang, *ACS Appl. Mater. Interfaces* **2016**, 8, 23920.
- [96] S. Rasul, D. H. Anjum, A. Jedidi, Y. Minenkov, L. Cavallo, K. Takanabe, *Angew. Chem. Int. Ed.* **2015**, 54, 2146.

- [97] S. Zhang, P. Kang, M. Bakir, A. M. Lapides, C. J. Dares, T. J. Meyer, *PNAS* **2015**, 112, 15809.
- [98] B. Kumar, M. Asadi, D. Pisasale, S. Sinha-Ray, B. A. Rosen, R. Haasch, J. Abiade, A. L. Yarin, A. Salehi-Khojin, *Nat. Commun.* **2013**, 4, 2819.
- [99] J. Wu, S. Ma, J. Sun, J. I. Gold, C. S. Tiwary, B. Kim, L. Zhu, N. Chopra, I. N. Odeh, R. Vajtai, A. Z. Yu, R. Luo, J. Lou, G. Ding, P. J.A. Kenis, P. M. Ajayan, *Nat. Commun.* **2016**, 7,13869.
- [100] H.-R. M. Jhong, C. E. Tornow, B. Smid, A. A. Gewirth, S. M. Lyth, P. J. A. Kenis, *ChemSusChem* **2017**, 10, 1094.
- [101] J. Wu, R. M. Yadav, M. Liu, P. P. Sharma, C. S. Tiwary, L. Ma, X. Zou, X.-D. Zhou, B. I. Yakobson, J. Lou, P. M. Ajayan, *Acs Nano* **2015**, 9, 5364.
- [102] Y. Liu, S. Chen, X. Quan, H. Yu, *J. Am. Chem. Soc.* **2015**, 137, 11631.
- [103] K. Nakata, T. Ozaki, C. Terashima, A. Fujishima, Y. Einaga, *Angew. Chem. Int. Ed.* **2014**, 53, 871.
- [104] J. Wu, M. Liu, P. P. Sharma, R. M. Yadav, L. Ma, Y. Yang, X. Zou, X.-D. Zhou, R. Vajtai, B. I. Yakobson, J. Lou, P. M. Ajayan, *Nano Lett.* **2016**, 16, 466.
- [105] N. Sreekanth, M. A. Nazrulla, T. V. Vineesh, K. Sailaja, K. L. Phani, *Chem. Commun.* **2015**, 51, 16061.
- [106] X. Sun, X. Kang, Q. Zhu, J. Ma, G. Yang, Z. Liu, B. Han, *Chem. Sci.* **2016**, 7, 2883.
- [107] Y. Song, R. Peng, D. K. Hensley, P. V. Bonnesen, L. Liang, Z. Wu, H. M. Meyer, III, M. Chi, C. Ma, B. G. Sumpter, A. J. Rondinone, *ChemistrySelect* **2016**, 1, 6055.
- [108] X. Duan, J. Xu, Z. Wei, J. Ma, S. Guo, S. Wang, H. Liu, S. Dou, *Adv. Mater.* **2017**, 1701784.
- [109] A. Vasileff, Y. Zheng, S. Z. Qiao, *Adv. Energy Mater.* **2017**, 1700759.
- [110] H. Wang, Y. Chen, X. Hou, C. Ma, T. Tan, *Green Chem.* **2016**, 18, 3250.
- [111] V. Tripkovic, M. Vanin, M. Karamad, M. E. Bjorketun, K. W. Jacobsen, K. S. Thygesen, J. Rossmeisl, *J. Phys. Chem. C* **2013**, 117, 9187.
- [112] D. C. B. Alves, R. Silva, D. Voiry, T. Asefa, M. Chhowalla, *Mater. Renew. Sustain. Energy* **2015**, 4, 2.

- [113] R. Kortlever, J. Shen, K. J. P. Schouten, F. Calle-Vallejo, M. T. M. Koper, *J. Phys. Chem. Lett.* **2015**, 6, 4073.
- [114] X. Nie, M. R. Esopi, M. J. Janik, A. Asthagiri, *Angew. Chem. Int. Ed.* **2013**, 52, 2459.
- [115] A. A. Peterson, F. Abild-Pedersen, F. Studt, J. Rossmeisl, J. K. Nørskov, *Energy Environ. Sci.* **2010**, 3, 1311.
- [116] X. Nie, W. Luo, M. J. Janik, A. Asthagiri, *J. Catal.* **2014**, 312, 108.
- [117] M. Dunwell, Q. Lu, J. M. Heyes, J. Rosen, J. G. Chen, Y. Yan, F. Jiao, B. Xu, *J. Am. Chem. Soc.* **2017**, 139, 3774.
- [118] Y. Hori, R. Takahashi, Y. Yoshinami, A. Murata, *J. Phys. Chem. B* **1997**, 101, 7075.
- [119] J. H. Montoya, A. A. Peterson, J. K. Nørskov, *ChemCatChem* **2013**, 5, 737.
- [120] H. A. Hansen, J. H. Montoya, Y.-J. Zhang, C. Shi, A. A. Peterson and J. K. Nørskov, *Catal. Lett.* **2013**, 143, 631.
- [121] F. Calle-Vallejo, M. T. M. Koper, *Angew. Chem. Int. Ed.* **2013**, 52, 7282.
- [122] S. Zhang, P. Kang, S. Ubnoske, M. K. Brennaman, N. Song, R. L. House, J. T. Glass, T. J. Meyer, *J. Am. Chem. Soc.* **2014**, 136, 7845.
- [123] A. Schizodimou, G. Kyriacou, *Electrochim. Acta* **2012**, 78, 171.
- [124] J. Lee, Y. Tak, *Electrochim. Acta* **2001**, 46, 3015.
- [125] H. A. Hansen, C. Shi, A. C. Lausche, A. A. Peterson, J. K. Nørskov, *Phys. Chem. Chem. Phys.* **2016**, 18, 9194.
- [126] Y. Hori, H. Konishi, T. Futamura, A. Murata, O. Koga, H. Sakurai and K. Oguma, *Electrochim. Acta* **2005**, 50, 5354.
- [127] L. M. Chiacchiarelli, Y. Zhai, G. S. Frankel, A. S. Agarwal, N. Sridhar, *J. Appl. Electrochem.* **2012**, 42, 21.
- [128] J. J. Wu, F. G. Risalvato, F. S. Ke, P. J. Pellechia, X. D. Zhou, *J. Electrochem. Soc.* **2012**, 159, F353.
- [129] M. Le, M. Ren, Z. Zhang, P. T. Sprunger, R. L. Kurtz, J. C. Flake, *J. Electrochem. Soc.* **2011**, 158, E45.
- [130] R. S. Kumar, S. S. Kumar, M. A. Kulandainathan, *Electrochem. Commun.* **2012**, 25, 70.

## **Chapter 3: Electrochemical and FTIR spectroscopic study of CO<sub>2</sub> reduction at a nanostructured Cu/reduced graphene oxide thin film**

### **3.1 Introduction**

The combustion of fossil fuels, changes in land-use, and the redundancy of industrial activities have been identified as the primary causes for the continuous rise of the CO<sub>2</sub> emission. CO<sub>2</sub> is known as one of the main greenhouse gases; and the utilization and the conversion of CO<sub>2</sub> to valuable chemicals/fuels have garnered significant interests worldwide [1,2]. Although the practical application of the current electrochemical technology for CO<sub>2</sub> reduction remains a big challenge [3], there are significant fundamental interests to understand the CO<sub>2</sub> reduction phenomenon at the electrode/electrolyte interface. Electrochemical reduction of CO<sub>2</sub> can be performed under ambient conditions; and it might provide an alternative approach to the utilization of CO<sub>2</sub> via the transformation of CO<sub>2</sub> to valuable chemicals and fuels in the future [4,5]. Various electrocatalysts have been explored for CO<sub>2</sub> reduction [6-9]; and Cu is considered as a prominent catalyst, which facilitates the formation of low carbon fuels such as CO, HCOOH, alcohols and CH<sub>4</sub> during the electrochemical reduction of CO<sub>2</sub> in an aqueous solution [8,10-13]. However, large overpotentials are needed to obtain the target products with the energy-efficient conversion because of the high rate hydrogen evolution in an aqueous environment [14,15].

Graphene and graphene oxide (GO) possess several remarkable electrical, thermal and mechanical properties; and they have been widely explored in the development of advanced clean technologies, in particular in the areas of sustainable energy storage and conversion [16-18]. GO contains various oxygen functional groups such as carbonyls and hydroxyls; and

graphene-like reduced graphene oxide (rGO) may be prepared by partial removal of these functional groups. Recently, rGO decorated with metal nanoparticles have been attracted in various sustainable green technologies such as energy storage, water splitting, hydrogen sorption and storage etc. due to the high surface area, good electrical conductivity and synergistic interaction with metal particles, resulting in a significant enhancement of the catalytic activity and stability [19-21]. In the present study, we have demonstrated a facile approach for the synthesis of a novel nanostructured Cu/rGO thin film, which exhibits excellent catalytic activity and high stability toward the electrochemical reduction of CO<sub>2</sub>. A significant synergistic effect was also observed when Cu nanoparticles were integrated with rGO sheets due to the physicochemical interaction between different functional groups of rGO and Cu nanoparticles. Further, we have shown that linear sweep voltammetric (LSV) and chronoamperometric (CA) techniques could be effectively employed to study the effect of the applied electrode potential and to determine the current efficiency of the electrochemical reduction of CO<sub>2</sub>.

### 3.2 Methods

CuSO<sub>4</sub>·5H<sub>2</sub>O (99.999%), graphene oxide (GO), NaHCO<sub>3</sub> (≥99.0%), Na<sub>2</sub>SO<sub>4</sub> (≥99.5%) and a 10.0 wt.% Nafion solution were purchased from Sigma-Aldrich. Ultra-pure CO<sub>2</sub> (99.999%) and Ar (99.998%) were obtained from Praxair. A mixture of GO (0.5 mg mL<sup>-1</sup>), Nafion (0.5%) and CuSO<sub>4</sub> (15.0 mM) was prepared as the precursor solution. Then a 10.0 μL of the precursor was cast on a glassy carbon electrode (GCE) (0.07 cm<sup>2</sup>) and allowed to air dry. The simultaneous formation of the nanostructured Cu/rGO thin film was enabled via cyclic voltammetry carried out in an Ar-saturated 0.1M Na<sub>2</sub>SO<sub>4</sub> solution in the potential range between 0.0 and -1.2 V (vs. Ag/AgCl) at the scan rate of 10 mV s<sup>-1</sup> for five cycles. For comparison, Cu and rGO thin films were also synthesized using the identical experimental procedure, where GO was absent while in

the preparation of Cu nanoparticles (NPs) thin film and vice versa. The surface morphology, composition and oxidation states of the formed thin films were characterized using field-emission scanning electron microscopy (FE-SEM) equipped with energy dispersive X-ray spectrometer (EDX) (Hitachi SU70) and X-ray photoelectron spectroscopy (XPS) (Thermo Fisher, 400  $\mu\text{m}$  X-ray spot size) with an Al K $\alpha$  monochromatic source, where XPSPEAK 4.1 software was used to analyze the XPS spectra.

Electrochemical studies were carried out with a CHI 660B workstation (CH Instrument Inc. USA) in a one-compartment three-electrode cell. A platinum coil (10  $\text{cm}^2$ ) was utilized as the counter electrode, whereas an Ag/AgCl (3.0 M KCl) was used as the reference electrode. The electrode potentials quoted in this study was converted to the reversible hydrogen electrode (RHE) reference scale using the following equation:

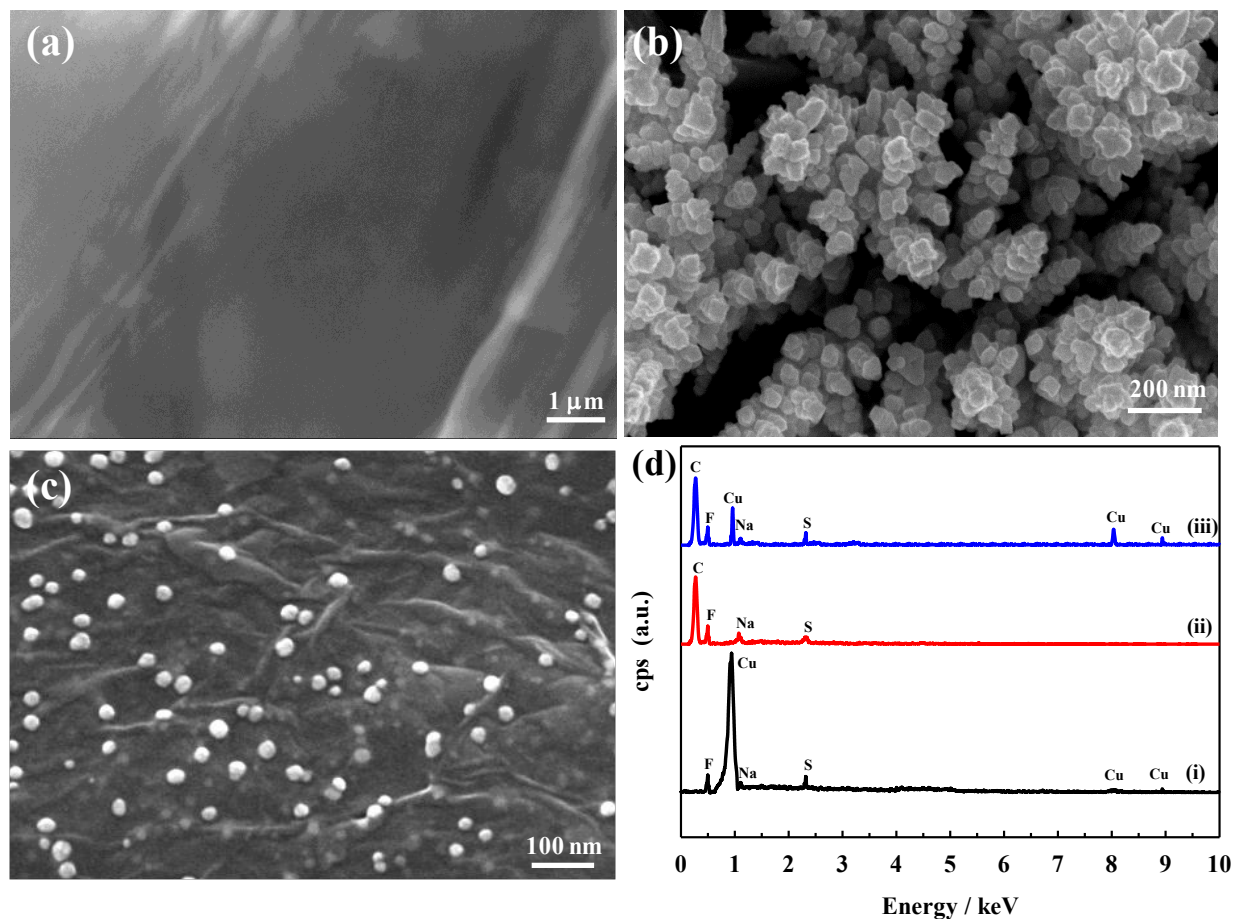
$$E \text{ (vs. RHE)} = E \text{ (vs. Ag/AgCl)} + 0.210 \text{ V} + 0.0591 \text{ V} \times \text{pH}$$

In situ electrochemical ATR-FTIR measurements were performed using an 8700 Nicolet Fourier transform infrared spectrometer equipped with a ZnSe window and a liquid N<sub>2</sub>-cooled MCT detector. All interferograms were acquired at a 4  $\text{cm}^{-1}$  resolution for 100 scans. The IR spectra were calculated using the following equation [22]:

$$\Delta R/R = [R(E_2) - R(E_1)] / R(E_1)$$

where  $R(E_1)$  and  $R(E_2)$  are the reflectivities from the electrode surface recorded at the applied electrode potential  $E_1$  (+0.1 V vs. RHE) and  $E_2$ , respectively.

For the analysis of the products, the electrochemical reduction of CO<sub>2</sub> was carried out in an air-tight two-compartment cell, where a cationic exchange membrane (CMI-7000S) was employed as a separator. Each compartment contained 35.0 ml of a CO<sub>2</sub>-saturated 0.1M

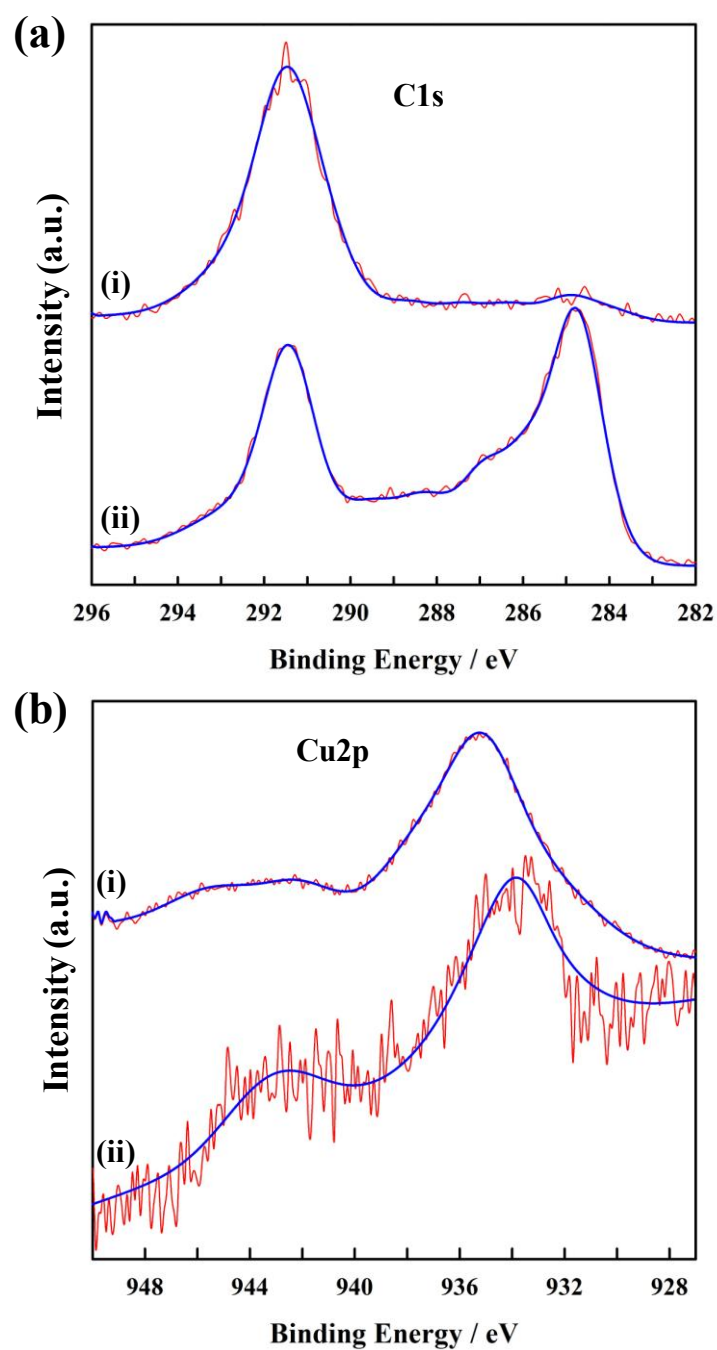


**Figure 3.1** SEM images of rGO (a), Cu NPs (b), and Cu/rGO thin film (c); (d) EDX spectra of Cu NPs (i), rGO (ii), and Cu-rGO thin film (iii).

NaHCO<sub>3</sub> solution and the pH of the solution was measured to be 6.65. Gas chromatography (GC, Shimadzu GC-2014) was employed to analyze the gas products, while the formed liquid Products were qualitatively analyzed using HPLC (Varian Prostar 230). All the experiments were carried out at room temperature ( $20 \pm 2$  °C).

### 3.3 Results and Discussion

As seen from the FE-SEM images, a graphene-like thin film was formed following the electrochemical reduction of graphene oxide (Figure 3.1a), while a crystal-like cluster structure of Cu NPs appeared subsequent to the electrochemical reduction of the CuSO<sub>4</sub> precursor (Figure

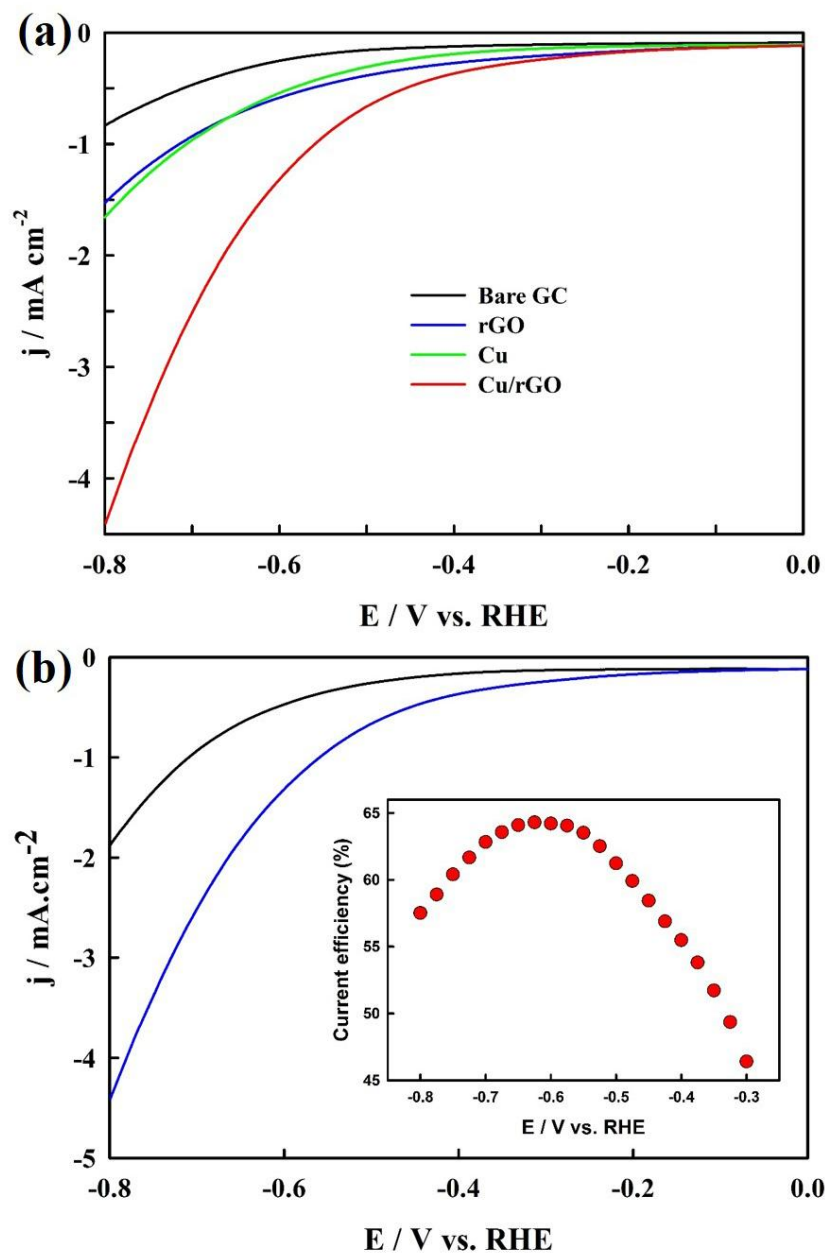


**Figure 3.2** XPS spectra of the C1s region (a) and the Cu2p region (b) of the precursor mixture film before (i) and after (ii) the cyclic voltammetric treatment, where red and blue lines represent the raw data and the total fitting curve, respectively.



3.1b). The simultaneous formation of the Cu/rGO thin film was achieved following the electrochemical reduction of the mixed GO and CuSO<sub>4</sub> precursor (Figure 3.1c), where Cu NPs with ~20 nm were uniformly distributed on the rGO sheets. Comparison of Figure 3.1b and 3.1c reveals that the Cu NPs were much larger in size and aggregated in the absence of the rGO. Figure 3.1d depicts the EDX spectra of the formed Cu, rGO, and Cu/rGO thin films, where the F peak and S peak were derived from Nafion. The appearance of the strong Cu peak in the Cu and Cu/rGO electrodes as well as the strong C peak in the rGO and Cu/rGO electrodes confirmed the composition of the prepared three different thin films. The C1s XPS spectra of the precursor mixture film before (i) and after (ii) the CV treatment are displayed in Figure 3.2a. The sp<sup>2</sup> C peak centered at 284.78 eV increased tremendously following the CV treatment, demonstrating that the electrochemical reduction had a significant effect on the diminution of oxygen-containing functional groups of GO to form rGO [23,24]. Figure 3.2b presents the Cu2p XPS spectra of the mixture film prior to (i) and following (ii) the electrochemical treatment. The strong peak centered at 935.28 eV, corresponding to Cu(II) (Spectrum i), was shifted to 933.88 eV (Spectrum ii), which may be attributed to Cu(0) [20,25]. All the aforementioned results confirm that the facile CV treatment can effectively grow the nanostructured Cu/rGO thin film.

In order to compare the electrochemical activity of the prepared electrodes, Figure 3.3a presents the LSVs of the bare GCE and the GCEs modified with rGO, Cu and Cu/rGO recorded in a CO<sub>2</sub>-saturated 0.1 M NaHCO<sub>3</sub> solution at the scan rate of 20 mV s<sup>-1</sup>. The highest electrocatalytic activity was demonstrated by the Cu/rGO thin film. For instance, at -0.8 V, the cathodic current of the Cu/rGO electrode reached 4.40 mA cm<sup>-2</sup>, which was much higher than that of the Cu NPs (1.66 mA cm<sup>-2</sup>) and the rGO (1.53 mA cm<sup>-2</sup>); and a strong synergetic effect was observed for the nanostructured Cu/rGO thin film. It is well known that both CO<sub>2</sub> reduction

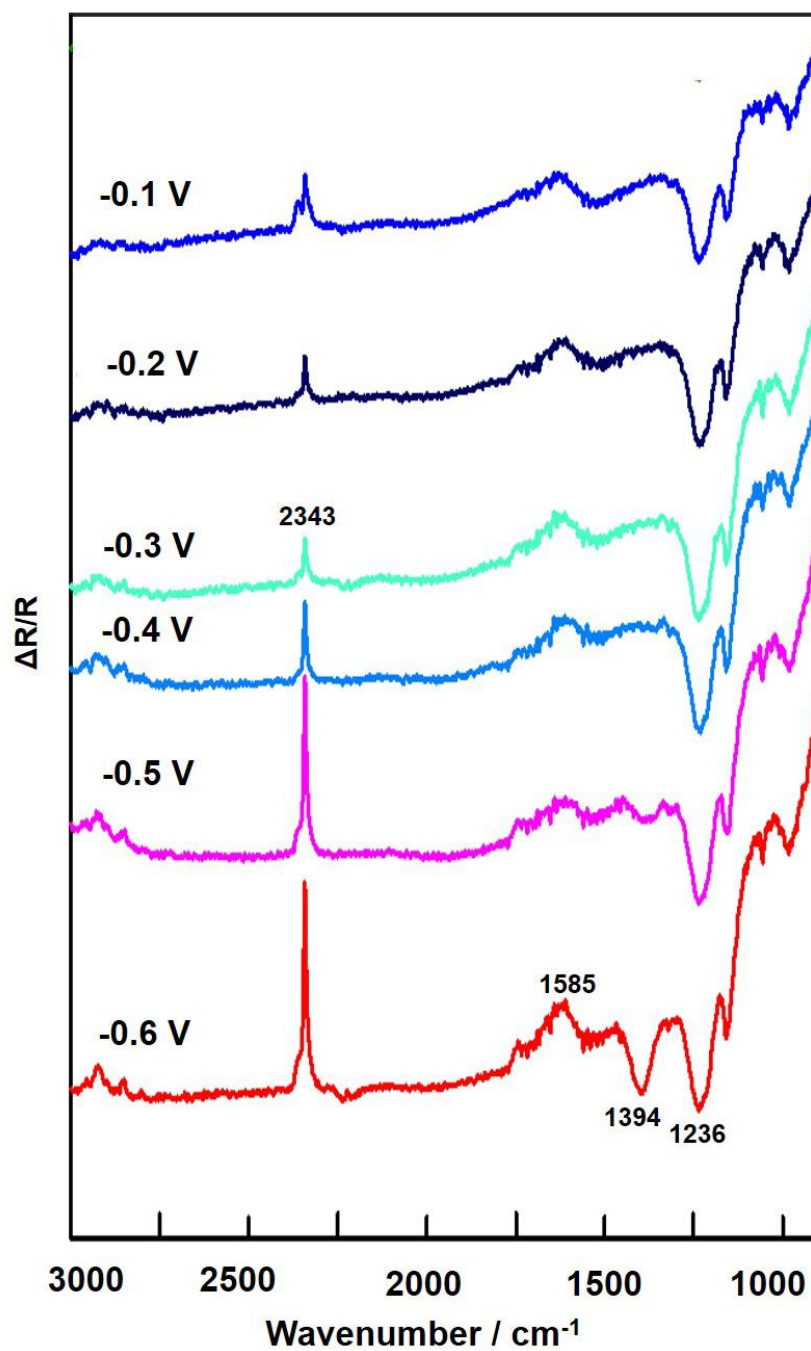


**Figure 3.3** (a) LSVs of the bare GCE and the GCEs modified with rGO, Cu NPs, and Cu/rGO thin films recorded in a  $\text{CO}_2$ -saturated  $0.1\text{M NaHCO}_3$  solution; (b) LSVs of the Cu/rGO thin film measured in the  $\text{CO}_2$ -saturated  $0.1\text{M NaHCO}_3$  solution (blue) and in the  $\text{Ar}$ -saturated  $0.05\text{M Na}_2\text{SO}_4$  solution whose pH was adjusted to 6.65 (black) at  $20 \text{ mV s}^{-1}$ ; the insert displays the calculated instant current efficiency.

and hydrogen evolution might occur under the experimental condition. In order to determine the catalytic activity of the Cu/rGO thin film toward CO<sub>2</sub> reduction, Figure 3.3b displays two LSVs: one was measured in a CO<sub>2</sub>-saturated 0.1 M NaHCO<sub>3</sub> solution (pH 6.65), where CO<sub>2</sub> was continuously purged into the solution during the measurements; and the other was recorded in an Ar-saturated 0.05 M Na<sub>2</sub>SO<sub>4</sub> solution whose pH was adjusted to 6.65 by adding a small volume of acid, where Ar was constantly purged into the solution during the experiment. The current density obtained in the CO<sub>2</sub>-saturated NaHCO<sub>3</sub> was higher than that in the Ar-saturated Na<sub>2</sub>SO<sub>4</sub>, confirming that the Cu/rGO thin film has the high catalytic activity for CO<sub>2</sub> reduction. It is worthy to note that the cathodic current density of the synthesized nanostructured Cu/rGO thin film for CO<sub>2</sub> reduction was higher than that of most electrocatalysts reported in the literature so far, for instance nanostructured Cu (~0.8 mA cm<sup>-2</sup> at -1.3 V vs. Ag/AgCl) [26], carbon supported Cu nanoparticles (~2.5 mA cm<sup>-2</sup> at -1.6 V vs. Ag/AgCl) [27], Cu NPs/rGO (0.97 mA cm<sup>-2</sup> at -1.54 V vs. NHE) [20], and copper nanoparticle/N-doped graphene (~1.5 mA cm<sup>-2</sup> at -1.2 V vs. RHE) [28]. The corresponding instant current efficiency (%) for CO<sub>2</sub> reduction at different potentials was calculated from the LSVs using the following equation:

$$\text{Current efficiency (\%)} = [(j_A - j_B) / j_A] \times 100 \quad (1)$$

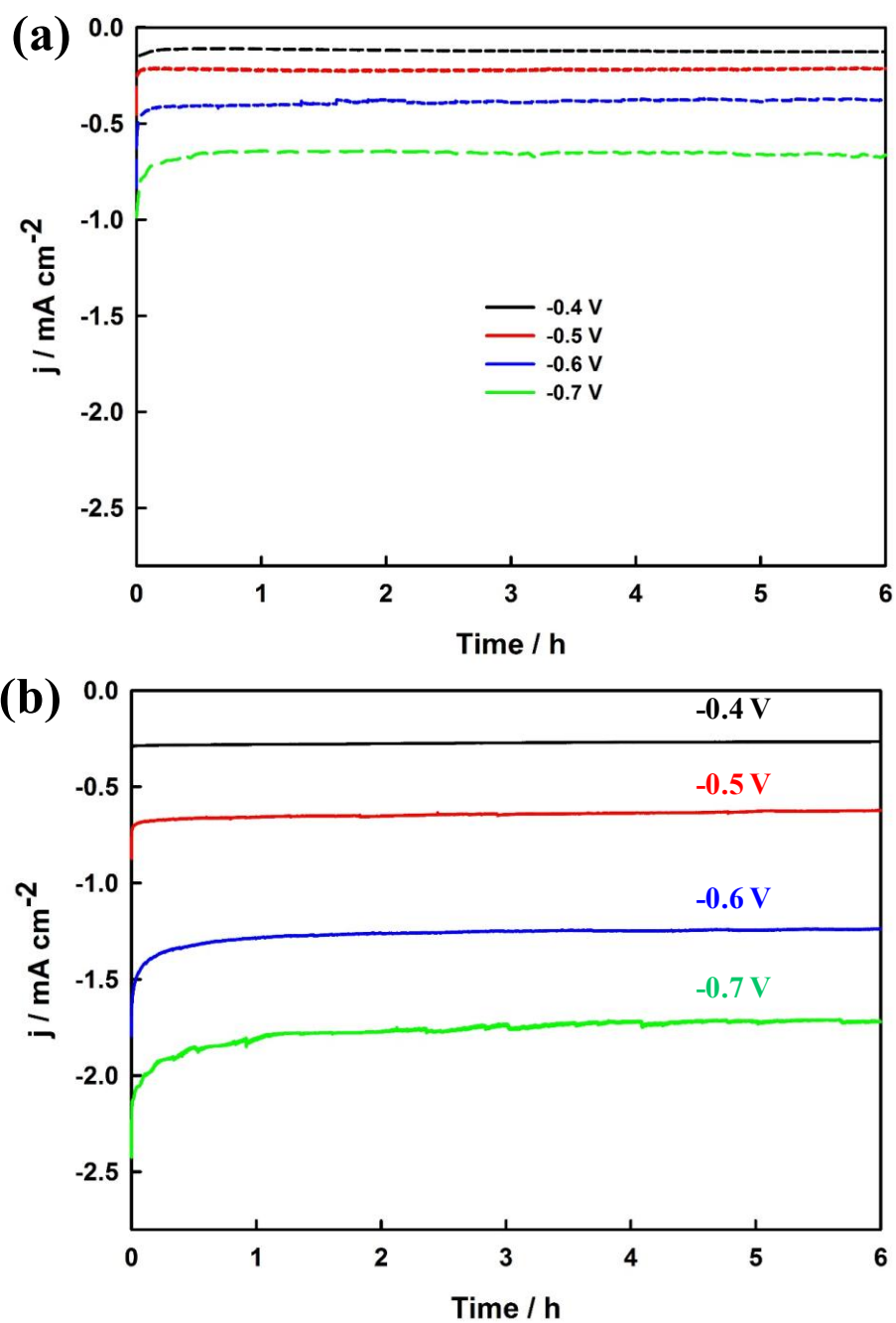
where  $j_A$  was the current density measured in the CO<sub>2</sub>-saturated 0.1M NaHCO<sub>3</sub> solution; and  $j_B$  was the current density obtained in the Ar-saturated 0.05 M Na<sub>2</sub>SO<sub>4</sub> solution. As seen in the insert of Figure 3.3b, the instant current efficiency was increased with the increase of the cathodic potential from -0.3 to -0.6 V; but it was gradually decreased with the further increase of the cathodic potential. The highest current efficiency (64.3%) was achieved at around -0.6 V, which could be the optimal potential for the bulk electrolysis of CO<sub>2</sub> reduction using the nanostructured Cu/rGO thin film.



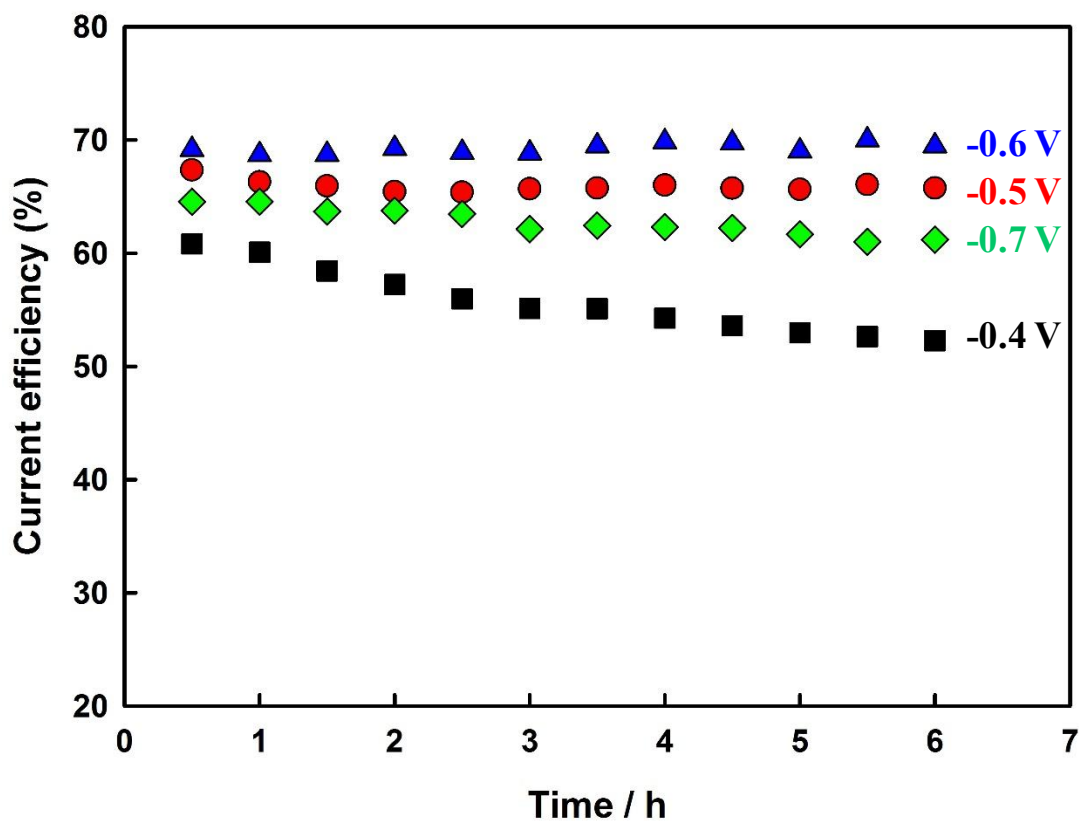
**Figure 3.4** In situ electrochemical ATR-FTIR spectra recorded during the electrochemical reduction of  $\text{CO}_2$  at the Cu/rGO thin film at the different applied potentials varied from -0.1 to -0.6 V vs. RHE in a  $\text{CO}_2$ -saturated 0.1M  $\text{NaHCO}_3$  solution.

In situ electrochemical ATR-FTIR spectroscopy was also employed to understand the CO<sub>2</sub> reduction at the Cu/rGO thin film in the CO<sub>2</sub>-saturated 0.1 M NaHCO<sub>3</sub>. A positive band in the spectrum may indicate the consumption of reactants; whereas a negative peak denotes the formation of intermediates/products [29,30]. As seen in Figure 3.4, the broad peak centred at ~1585 cm<sup>-1</sup> could be ascribed to the deformation of interfacial water molecules [31]. The negative band observed at ~1236 cm<sup>-1</sup> might be attributed to the formation of HCO<sub>3</sub><sup>-</sup>. The intensity of the CO<sub>2</sub> peak centred at 2343 cm<sup>-1</sup> was significantly increased when the applied cathodic potential was increased from -0.3 to -0.6 V, indicating the increase of the CO<sub>2</sub> reduction. The appearance of the new peak centred at 1394 cm<sup>-1</sup> confirmed the formation of formate during the electrochemical CO<sub>2</sub> reduction [32,33].

Chronoamperometry was further employed to determine the steady-state current efficiency and to investigate the stability of the formed Cu/rGO thin film. Figure 3.5a and 3.5b present four CA curves recorded in an Ar-saturated 0.05 M Na<sub>2</sub>SO<sub>4</sub> solution (pH was adjusted to 6.65) and in a CO<sub>2</sub>-saturated 0.1 M NaHCO<sub>3</sub> solution for six hours, where Ar and CO<sub>2</sub> were continuously purged into the solutions during the tests, respectively. Almost constant current density was obtained for each applied potential, indicating the high stability of the formed nanostructured Cu/rGO thin film. As expected, the cathodic current density measured in the Ar-saturated Na<sub>2</sub>SO<sub>4</sub> solution, due to the hydrogen evolution reaction, was increased with the increase of the cathodic potential from -0.4 to -0.7 V as seen in Figure 3.5a. In contrast, the steady-state current densities obtained in the CO<sub>2</sub>-saturated NaHCO<sub>3</sub> solution (Figure 3.5b) were much higher at all the applied potentials in comparison to the CA curves displayed in Figure 3.5a, further confirming that the CO<sub>2</sub> reduction occurred at those cathodic potentials. Our GC analysis revealed that both H<sub>2</sub> and CO were found at all of the applied potentials in the gas



**Figure 3.5** CA curves of the Cu/rGO thin film recorded in the Ar-saturated 0.05M  $\text{Na}_2\text{SO}_4$  solution (a) and the  $\text{CO}_2$ -saturated 0.1M  $\text{NaHCO}_3$  solution (b) at the different applied potentials of -0.4, -0.5, -0.6 and -0.7 V.



**Figure 3.6** Corresponding steady-state current efficiency (%) for CO<sub>2</sub> reduction calculated from the CA curves displayed in Figure 3.5a and 3.5b.

products; whereas formate was identified as the main liquid product at the applied cathodic potentials higher than -0.4 V through HPLC analysis, which is consistent with our in situ ATR-FTIR study. The steady-state current efficiency for CO<sub>2</sub> reduction was calculated from the CA curves using Equation (1); and the corresponding plots are presented in Figure 3.6. The overall steady-state current efficiency was increased when the cathodic potential was increased from -0.4 to -0.6 V; but it was decreased with the further increase of the cathodic potential -0.7 V, which is consistent with the instant current efficiency calculated from the LSVs (Insert of Figure 3.3b). The highest steady-state current efficiency of the Cu/rGO thin film for the CO<sub>2</sub> reduction

was calculated to be 69.4% at the applied potential of -0.6 V, which is slightly higher than the instant current efficiency determined from the LSVs. This is due to the fact that both Faradic and non-Faradic currents are involved in LSV; whereas only Faradic current was measured in CA.

### 3.4 Conclusions

A novel nanostructured Cu/rGO thin film was directly formed on the GCE surface via a facile one-step electrochemical reduction of their precursor mixture. The SEM images showed that Cu nanoparticles were uniformly distributed on the rGO nanosheets. LSV and CA were employed to study the effect of the applied potential on the electrochemical reduction of CO<sub>2</sub> and to determine the instant and the steady-state current efficiency of the Cu/rGO thin film, demonstrating that the Cu/rGO thin film was highly efficient for CO<sub>2</sub> reduction. The optimal potential was determined; and the highest instant and steady-state current efficiencies were attained at -0.6 V to be 64.3% and 69.4%, respectively. GC, HPLC and in situ electrochemical ATR-FTIR spectroscopy were used to analyze the products, where CO was identified as the gas product and formate was detected as the major liquid product. The facile fabrication, high catalytic activity and good stability make this novel nanostructured Cu/rGO thin film promising for electrochemical conversion of CO<sub>2</sub> to valuable chemicals and fuels. In addition, the approach described in the present study opens a door to develop myriad graphene supported metal nanoparticles for clean and green environmental and energy applications.

### References

- [1] M. Liu, Y. Pang, B. Zhang, P.D. Luna, O. Voznyy, J. Xu, X. Zheng, C.T. Dinh, F. Fan, C. Cao, F. P. G. de Arquer, T. S. Safaei, A. Mepham, A. Klinkova, E. Kumacheva, T. Filleter, D. Sinton, S. O. Kelley, E. H. Sargent, *Nature* **2016**, 537, 382.
- [2] N. V. Rees, R. G. Compton, *Energy Environ. Sci.* **2011**, 4, 403.



- [3] D. Pletcher, *Electrochem. Commun.* **2015**, 61, 97.
- [4] J. L. Qiao, Y. Y. Liu, F. Hong, J. J. Zhang, *Chem. Soc. Rev.* **2014**, 43, 631.
- [5] Y. Hori, In *Modern Aspects of Electrochemistry*; C. G., Vayenas, R. E., White, M. E., Gamboa-Aldeco, Eds.; Springer: **2008**, 42, 89.
- [6] S. Gao, Y. Lin, X. Jiao, Y. Sun, Q. Luo, W. Zhang, D. Li, J. Yang, Y. Xie, *Nature* **2016**, 529, 68.
- [7] T. Sekimoto, M. Deguchi, S. Yotsuhashi, Y. Yamada, T. Masui, A. Kuramata, S. Yamakoshi, *Electrochem. Commun.* **2014**, 43, 95.
- [8] K.P. Kuhl, E.R. Cave, D.N. Abram, T.F. Jaramillo, *Energy Environ. Sci.* **2012**, 5, 7050.
- [9] K. Sakai, Y. Kitazumi, O. Shirai, K. Takagi, K. Kano, *Electrochem. Commun.* **2016**, 73, 85.
- [10] C. W. Li, M. W. Kanan, *J. Am. Chem. Soc.* **2012**, 134, 7231.
- [11] S. Sen, D. Liu, G. T. R. Palmore, *ACS Catal.* **2014**, 4, 3091.
- [12] K. Manthiram, B. J. Beberwyck, A. P. Alivisatos, *J. Am. Chem. Soc.* **2014**, 136, 13319.
- [13] D. Raciti, K. J. Livi, C. Wang, *Nano Lett.* **2015**, 15, 6829.
- [14] C. Zhao, J. Wang, J. B. Goodenough, *Electrochem. Commun.* **2016**, 65, 9.
- [15] A. A. Peterson, F. Abild-Pedersen, F. Studt, J. Rossmeisl, J. K. Nørskov, *Energy Environ. Sci.* **2010**, 3, 1311.
- [16] A. A. Balandin, *Nat. Mater.* **2011**, 10, 569.
- [17] E. P. Randviir, D. A. C. Brownson, C. E. Banks, *Mater. Today* **2014**, 17, 426.
- [18] D. R. Dreyer, S. Park, C. W. Bielawski, R. S. Ruoff, *Chem. Soc. Rev.* **2010**, 39, 228.
- [19] S. K. Konda, A. Chen, *Electrochem. Commun.* **2015**, 60, 148.
- [20] D. C. B. Alves, R. Silva, D. Voiry, T. Asefa, M. Chhowalla, *Mater. Ren. Sus. Energy* **2015**, 4, 2.
- [21] D.-H. Lim, J. H. Jo, D. Y. Shin, J. Wilcox, H. C. Ham, S. W. Nam, *Nanoscale* **2014**, 6, 5087.
- [22] B. D. Adams, R. M. Asmussen, C. K. Ostrom, A. Chen, *J. Phys. Chem. C* **2014**, 118, 29903.

- [23] M. Govindhan, A. Chen, *J. Power Sources* **2015**, 274, 928.
- [24] M. Govindhan, B. Mao, A. Chen, *Nanoscale* **2016**, 8, 1485.
- [25] X. Liu, L. Zhu, H. Wang, G. He, Z. Bian, *RSC Adv.* **2016**, 6, 38380.
- [26] Á. Díaz-Duque, A. P. Sandoval-Rojas, A. F. Molina-Osorio, J. M. Feliu, M. F. Suárez-Herrera, *Electrochem. Commun.* **2015**, 61, 74.
- [27] O. A. Baturina, Q. Lu, M. A. Padilla, L. Xin, W. Li, A. Serov, K. Artyushkova, P. Atanassov, F. Xu, A. Epshteyn, T. Brintlinger, M. Schuette, G. E. Collins, *ACS Catal.* **2014**, 4, 3682.
- [28] Y. Song, R. Peng, D. K. Hensley, P. V. Bonnesen, L. Liang, Z. Wu, H. M. Meyer, III, M. Chi, C. Ma, B. G. Sumpter, A. J. Rondinone, *ChemistrySelect* **2016**, 1, 6055.
- [29] B. Innocent, D. Pasquier, F. Ropital, F. Hahn, J.-M. Leger, K. B. Kokoh, *Appl. Catal. B: Environ.* **2010**, 94, 219.
- [30] H. Wang, B. Jiang, T.-T. Zhao, K. Jiang, Y.-Y. Yang, J. Zhang, Z. Xie, W.-B. Cai, *ACS Catal.* **2017**, 7, 2033.
- [31] M. H. Shao, R. R. Adzic, *Electrochim. Acta* **2005**, 50, 2415.
- [32] D. B. Clarke, D. K. Lee, M. J. Sandoval, A. T. Bell, *J. Catal.* **1994**, 150, 81.
- [33] B. D. Mistry, *A Handbook of Spectroscopic Data Chemistry (UV, IR, PMR, <sup>13</sup>CNMR and Mass Spectroscopy)*, Edition **2009**, Oxford Book Company, 43.

## **Chapter 4: Unique copper and reduced graphene oxide nanocomposite toward the efficient electrochemical reduction of carbon dioxide**

### **4.1 Introduction**

Increasing levels of CO<sub>2</sub> in the atmosphere have created a highly concerning situation that continues to elevate global average temperatures. There is a growing frequency of reports related to the impacts of global climate change due to increasing greenhouse gas emissions via the continuous combustion of fossil fuels. One of the most notorious of the greenhouse gases is CO<sub>2</sub>, which is released by both natural and anthropogenic processes. There is a great interest in capture and sequestration of CO<sub>2</sub> emissions prior to their release into the ambient atmosphere, or the conversion of this gas to useful products such as fuels [1-5]. Over the last few decades, various electrocatalysts have been explored for the electrochemical reduction of CO<sub>2</sub> to valuable fuels [6-10], and a wide range of gas and liquid products may be formed. Therefore, it is essential to accurately determine both the produced gases and the liquid fuels in order to precisely assess the FE. On one hand, the primary gas products include CO, methane (CH<sub>4</sub>), and ethane, which may be determined using GC and gas chromatography mass spectrometry (GC-MS) [11,12]. On the other hand, potential liquid products include formate, acetate, aldehyde, alcohols, and so on, which strongly depend on the electrocatalysts employed and the applied electrode potentials. Although high performance liquid chromatography (HPLC), ion chromatography (IC) and nuclear magnetic resonance (NMR) have been employed to analyze the liquid products [11,13-15], it remains quite challenging and time-consuming to quantify the various liquid products in order to determine the overall Faradaic efficiency (FE) and assess the activity of the catalysts. A chemical oxygen demand (COD) method is commonly used in environmental analysis, and is based upon the complete oxidation of all organic species to CO<sub>2</sub>,

which is exactly the reverse of the CO<sub>2</sub> reduction process[16,17]. In this study, for the first time we propose and employ the COD analysis to determine the overall FE associated with the conversion of CO<sub>2</sub> to liquid chemicals and fuels.

Graphene nanosheets have been widely doped and/or modified for catalytic and energy conversion applications [18-22]. The unique electronic and physical properties of graphene may augment the reduction kinetics of CO<sub>2</sub>, and enhance the reaction kinetics of noble metal nanoparticles [23,24]. Copper is considered to be one of the eminent catalysts for the electrochemical reduction of CO<sub>2</sub> to low-carbon fuels for high-density renewable energy storage [7,8,11,25]. It has been reported that CO, CH<sub>4</sub>, C<sub>2</sub> hydrocarbon, alcohols, formate, and acetate could be formed when Cu was used as an electrode in an aqueous solution [11,12,25-27]. Several studies have been reported wherein the selectivity of Cu catalysts for the reduction of CO<sub>2</sub> was specifically dependent on its crystal facets [7,28,29]. The surface structures of Cu electrodes, in conjunction with the applied electrode potential, are of intense interest for product selectivity [30-33]. Density Function Theory studies have indicated that defective graphene-supported Cu nanoparticles may modify the structural and electronic properties of copper, toward enhancing the electrochemical reduction of CO<sub>2</sub> to fuels (e.g., CH<sub>4</sub>, CO, and HCOOH) [23,24,34-38]. However, despite the high catalytic activity of such Cu catalysts, they still suffer from low stability and large reaction overpotentials. Herein we report on the high-performance CO<sub>2</sub> reduction that is enabled by a unique nanocomposite of Cu nanoparticles (NPs) and reduced graphene oxide (rGO) supported on a Cu substrate with high FE and stability for the efficient conversion of CO<sub>2</sub> to valuable fuels, including CO, CH<sub>4</sub>, and formate.

## **4.2 Methods**

### **4.2.1 Materials**

Graphene oxide,  $\text{CuSO}_4 \cdot 5\text{H}_2\text{O}$  (99.999%),  $\text{NaHCO}_3$  ( $\geq 99.0\%$ ),  $\text{Na}_2\text{SO}_4$  ( $\geq 99.5\%$ ) and a 10 wt.% Nafion solution were obtained from Sigma Aldrich. Copper foil (99.9985%, 0.5 mm thick) was purchased from Alfa Aesar; copper wire (99.9%, 1.0 mm diameter) was purchased from Sigma Aldrich; and carbon dioxide (99.9%) was purchased from Praxair. All electrochemical experiments were conducted in a 0.1 M  $\text{NaHCO}_3$  electrolyte solution under  $\text{CO}_2$  saturation. Double distilled water treated by a Nanopure Diamond water purification system (18 M $\Omega$  cm) was used in the preparation of all the solutions. All chemicals were used directly without further treatment.

#### **4.2.2 Synthesis of Cu-rGO nanocomposites**

To optimize the concentration of Cu precursor, a 50  $\mu\text{L}$  mixed solution of Nafion (0.5%), GO ( $0.5 \text{ mg mL}^{-1}$ ) and  $\text{CuSO}_4 \cdot 5\text{H}_2\text{O}$  (5.0, 10.0, 15.0, 20.0, and 25.0 mM) was cast on a  $1.0 \text{ cm}^2$  Cu foil, which was etched for 30 s in 35%  $\text{HNO}_3$ , washed with deionized water, and dried. To optimize the concentration of GO, a 50  $\mu\text{L}$  suspension of Nafion (0.5%),  $\text{CuSO}_4 \cdot 5\text{H}_2\text{O}$  (10 mM), and GO ( $0.25, 0.5, 0.75, 1.0$  and  $1.50 \text{ mg mL}^{-1}$ ) was cast onto the etched  $1.0 \text{ cm}^2$  Cu foil. Similarly, to optimize the Cu-rGO thickness, altered volumes of the suspension solution (25, 50, 75, 100 and 150  $\mu\text{L}$ ) containing 10.0 mM  $\text{CuSO}_4 \cdot 5\text{H}_2\text{O}$ , 0.5% Nafion, and a  $0.5 \text{ mg mL}^{-1}$  GO were cast on the etched  $1.0 \text{ cm}^2$  Cu substrate.

The simultaneous formation of the Cu-rGO nanocomposite was carried out in 0.1 M  $\text{Na}_2\text{SO}_4$  via cyclic voltammetry in the potential range between 0.0 to -1.2 V (vs. Ag/AgCl) for five cycles. The prepared Cu-rGO nanocomposites were subsequently rinsed with a copious volume of water and employed for further surface characterization and electrochemical measurements.

For comparison, Cu nanoparticles (NPs) were prepared using the same electrochemical reduction approach in the absence of GO. Briefly, a mixture of  $\text{CuSO}_4 \cdot 5\text{H}_2\text{O}$  (10.0 mM) and Nafion (0.5%) in water was prepared and sonicated for 20 minutes. Subsequently, 75  $\mu\text{L}$  of the mixture was cast on the etched Cu foil surface and dried in ambient air at room temperature. The rGO sheet electrode was then prepared by applying the identical conditions mentioned above for the Cu NPs; however, only GO (0.5  $\text{mg mL}^{-1}$ ) with Nafion was used.

#### **4.2.3 Structural characterization**

Morphological surface studies and EDX analysis were carried out using a FE-SEM (Hitachi SU-70). XPS spectra were recorded via a Thermo Fisher XPS system, where the size of the X-ray spot was 400  $\mu\text{m}$ , with an Al K $\alpha$  monochromatic source. XPSPEAK 4.1 software was used for all of the data processing.

#### **4.2.4 Electrochemical characterization**

Linear Sweep Voltammetry and chronoamperometry were carried out with a CHI660E electrochemical workstation (CH Instrument Inc. USA) utilizing a conventional one-compartment three-electrode cell, whereas a platinum coil (10  $\text{cm}^2$ ) was used as the counter electrode. A silver/silver chloride electrode (Ag/AgCl, 3.0 M) was utilized as the reference electrode and all the aforementioned electrode potentials were converted to the reversible hydrogen electrode (RHE) scale using the following equation:

$$E (\text{vs. RHE}) = E (\text{vs Ag/AgCl}) + 0.210 \text{ V} + 0.0591 \text{ V} \times \text{pH}$$

A VoltaLab potentiostat (PGZ-301) was employed for the Electrochemical Impedance Spectroscopic (EIS) measurements, and the frequency was varied from 100 kHz to 10 mHz with an a.c. voltage amplitude of 10 mV. Data acquisition and analyses were performed using Z-view software, which was employed to fit and obtain an equivalent circuit for EIS data. The solution

was purged with CO<sub>2</sub> in order to achieve a CO<sub>2</sub>-saturated condition. All electrochemical experiments were conducted at ambient room temperature (20 ± 2 °C).

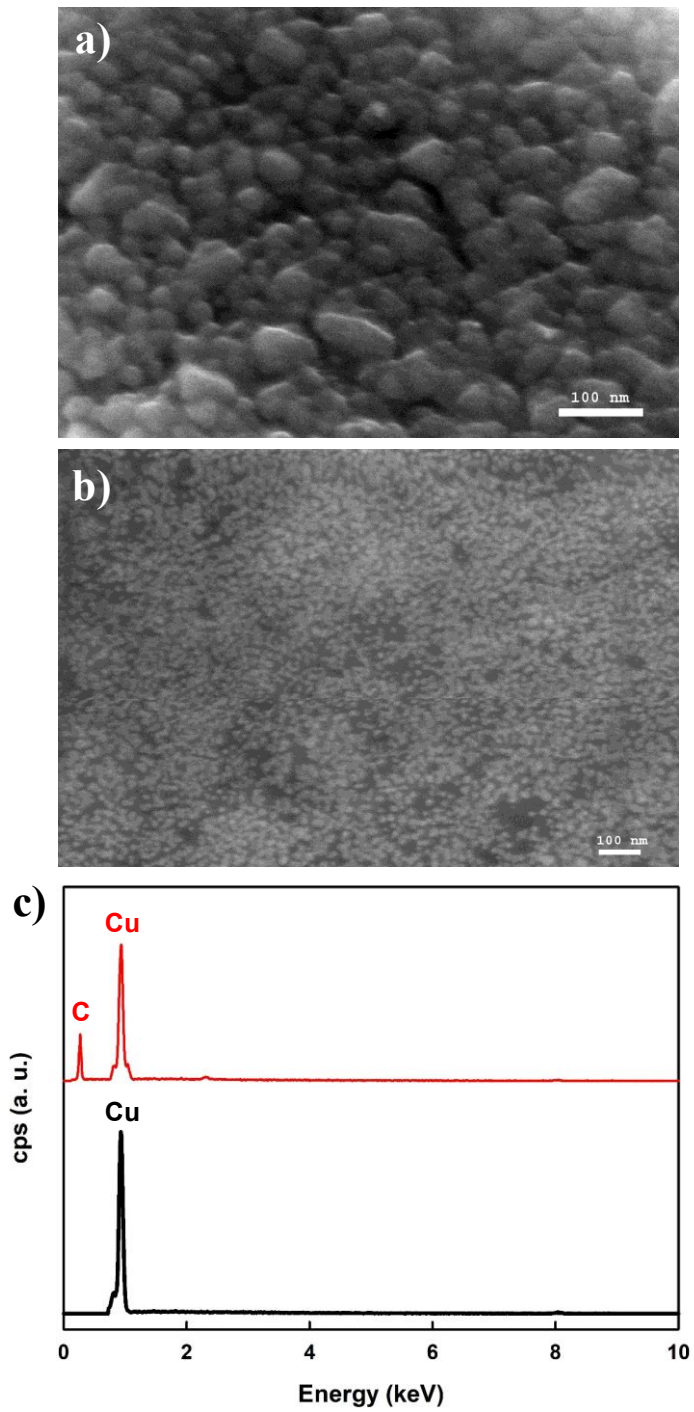
#### **4.2.5 Product analysis**

A gas-tight two-compartment electrochemical cell was used for the product formation and analysis. A cationic exchange membrane (CMI-7000S) was utilized as a separator in the cell. Each compartment contained 35.0 ml of the electrolyte; the working electrode and reference electrode (Ag/AgCl) were in the same compartment, whereas the counter electrode was in a separate compartment. Prior to testing, the electrolyte was purged once again with CO<sub>2</sub> gas for at least 30 minutes. A gas-tight syringe (Hamilton<sup>TM</sup>, 50 µL) was used to transfer the evolved gases into the gas chromatography (Varian 450-GC) to analyze the gas products. The resulting liquid products were qualitatively analyzed using HPLC (Varian Prostar 230 with a Symmetry®C8 column containing dimethyloctylsilyl bonded amorphous silica-acetonitrile). The COD analysis was conducted using 174-334 accu-TEST standard range (5-150 mg/l) twist cap vials for quantitative determination. The solution (2.0 mL) was then transferred to a vial that contained a chromic acid solution, heated to 150 °C for two hours and then allowed to cool. To establish the actual COD values, the results were subtracted from the values of a blank solution (CO<sub>2</sub> saturated 0.1 M NaHCO<sub>3</sub> solution). The UV absorbance was recorded at 420 nm using an HACH-DR 2800 portable spectrophotometer.

### **4.3 Results**

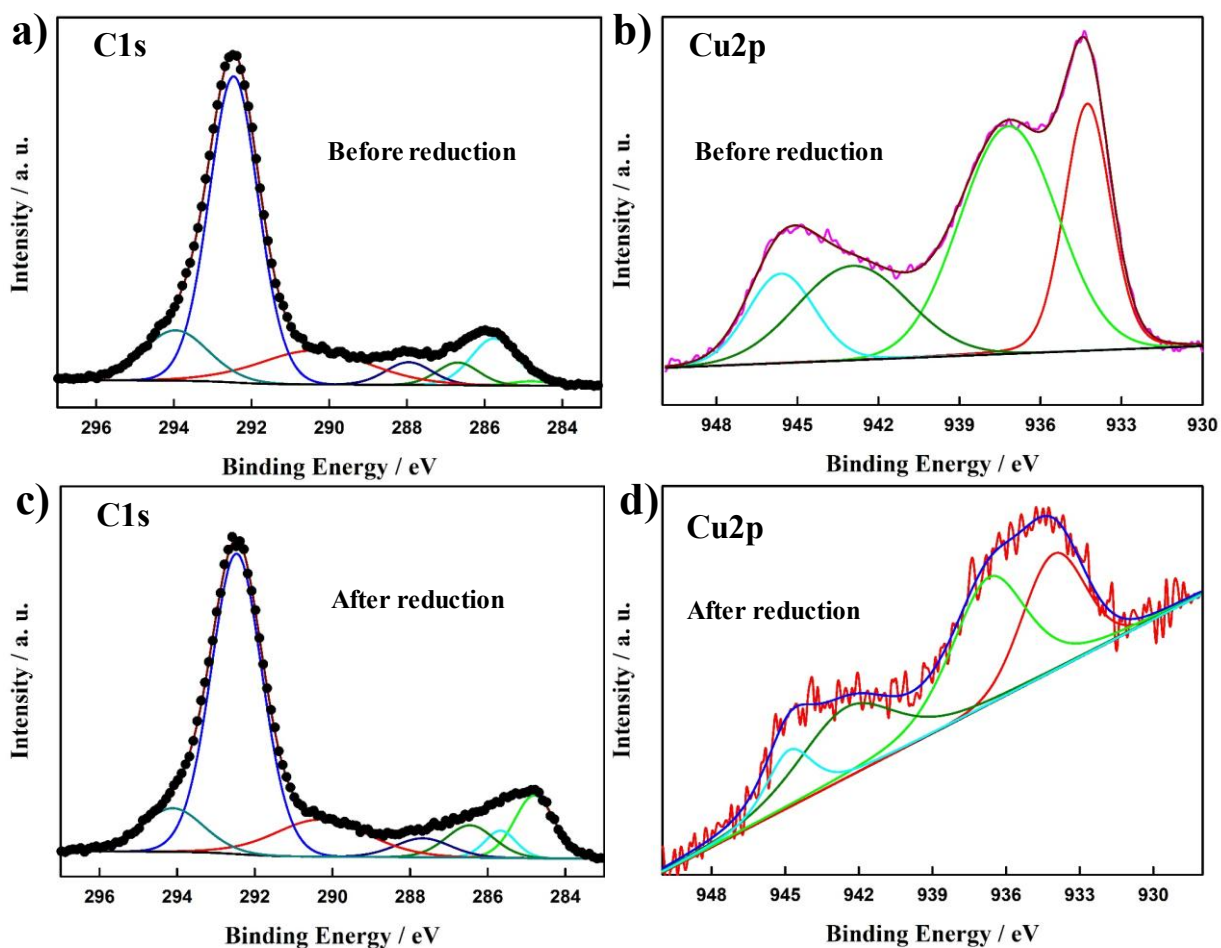
#### **4.3.1 Syntheses and characterization of Cu-rGO nanocomposites**

The Cu-rGO nanocomposite was formed directly on a Cu substrate using a facile electrochemical reduction method. A mixture of GO and Cu<sup>2+</sup> precursors was cast on an etched Cu substrate; and the simultaneous formation of Cu-rGO nanocomposite was achieved via cyclic



**Figure 4.1** SEM images of the formed Cu NPs (a) and the Cu-rGO nanocomposite (b) on a Cu substrate. (c) EDX spectra of the Cu NPs (i) and the Cu-rGO nanocomposite electrode (ii).





**Figure 4.2** High-resolution XPS spectra of the C1s region (a and c) and the Cu2p region (b and d) of the CuSO<sub>4</sub>-GO thin film before the electrochemical treatment and the formed Cu-rGO nanocomposite.

voltammetry (CV), which was carried out in 0.1 M Na<sub>2</sub>SO<sub>4</sub> in the potential range from 0.62 to -0.58 V vs. RHE for five cycles. The composition and thickness of the formed Cu-rGO nanocomposite were also optimized, with the experimental details described in the Methods. Figure 4.1a and 4.1b display the scanning electron microscope (SEM) images of the formed Cu NPs in the absence of GO, and the Cu-rGO nanocomposite, respectively. It is evident that large grain-sized Cu particles were formed in the absence of GO. In contrast, Cu NPs with an average

**Table 4.1** XPS analysis of C1s peak of the CuSO<sub>4</sub>-GO thin film before the electrochemical treatment and the formed Cu-rGO nanocomposite.

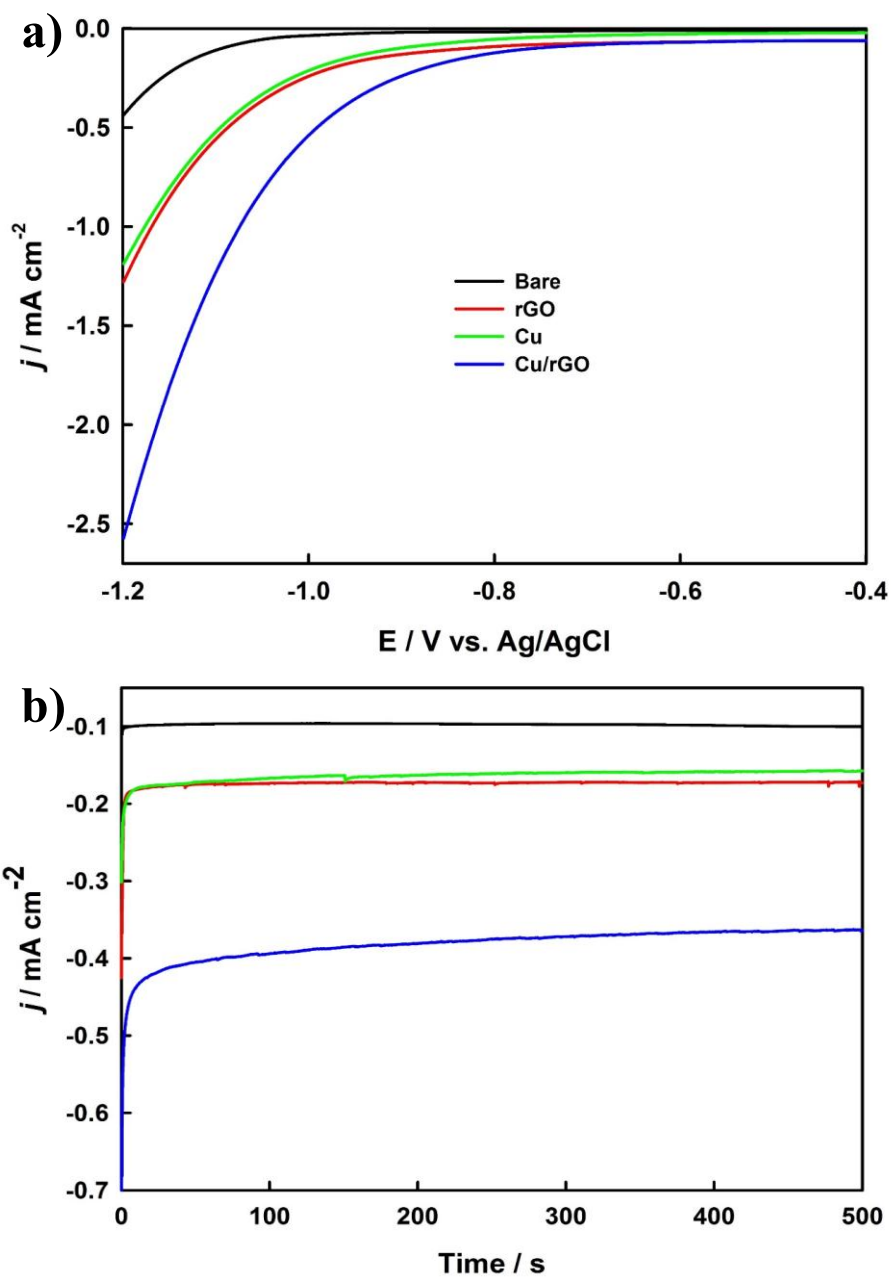
XPS	Peak position / eV	Peak assignments	At (%)
Before the electrochemical treatment	284.80	sp <sup>2</sup> C	2.17
	285.76	C-OH	26.56
	286.69	C-O	11.70
	287.95	C=O	13.06
	290.39	HO-C=O	46.50
Following the electrochemical treatment	284.80	sp <sup>2</sup> C	29.49
	285.67	C-OH	9.02
	286.46	C-O	10.41
	287.67	C=O	11.08
	290.29	HO-C=O	36.99

**Table 4.2** XPS analysis of the Cu2p<sup>3/2</sup> peak of the CuSO<sub>4</sub>-GO thin film before the electrochemical treatment and the formed Cu-rGO nanocomposite.

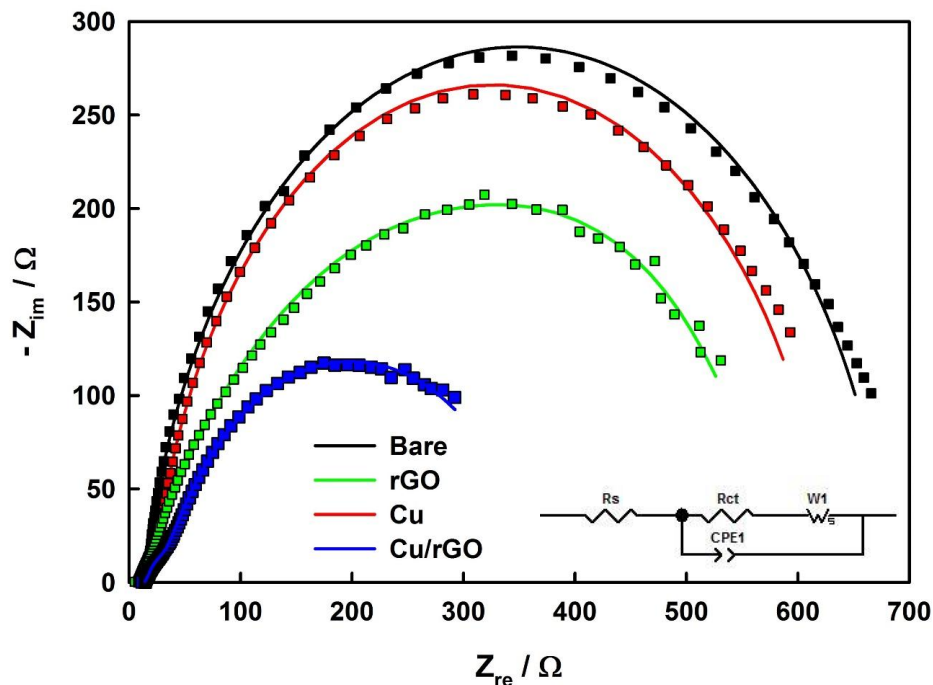
XPS	Peak position / eV	Peak assignments
Before the electrochemical treatment	934.23	Cu (II)
	937.17	Cu (II)
	942.17	Cu <sup>2+</sup> satellites
	945.60	
Following the electrochemical treatment	934.06	Cu (0)
	936.69	Cu (II)
	942.49	Satellites
	944.83	

diameter of ~10 nm were distributed homogeneously on the rGO. Energy dispersive X-ray spectra (Figure 4.1c) exhibited a strong Cu peak for the Cu NPs (Curve i) and an additional strong C peak for the Cu-rGO nanocomposite electrode (Curve ii). X-ray photoelectron spectroscopic (XPS) measurements were further carried out for mixture of the GO and Cu precursor mixture as well as for the formed Cu-rGO nanocomposite electrode. Figure 4.2a and 4.2c display the high-resolution C1s XPS spectra prior to and following the electrochemical reduction, respectively. A series of fitting peaks were observed at 284.80, 285.76, 286.69, 287.95, and 290.39 eV, corresponding to  $sp^2$  C, C-OH, C-O, C=O, and HO-C=O bonds, respectively, as observed in GO [21,22]. The peaks centred at 292.46 and 293.96 eV are due to the C-F<sub>3</sub> and C-F<sub>2</sub> groups of Nafion, which was used as the binding material of the nanocomposite to the substrate. As seen in Table 4.1, following the electrochemical reduction, the peaks of oxygen-containing groups decreased; and the proportion of C=C group increased enormously, revealing that the electrochemical treatment had a significant effect on the diminution of oxygen-containing functional groups. In the case of Cu, prior to the electrochemical treatment, three Cu2p peaks were observed in Figure 4.2b, which might be attributed to the physicochemical interactions of Cu(II) species with the different functional groups of GO [15,39-41]. Subsequent to the electrochemical treatment (Figure 4.2d), a strong Cu(0) peak appeared at 934.12 eV and a small Cu(I) peak was observed at 931.78 eV. The associated Cu2p peak position, and assignment before and after the electrochemical treatment are listed in Table 4.2. All the aforementioned results show that the GO and Cu<sup>2+</sup> precursor can be effectively reduced to form the Cu-rGO nanocomposite.

The electrocatalytic activity of the formed Cu-rGO nanocomposite was initially studied using linear sweep voltammetry (LSV) and chronoamperometry (CA) in the presence of CO<sub>2</sub> in



**Figure 4.3** (a) LSV curves of the bare Cu substrate, rGO, Cu NPs and Cu-rGO nanocomposite electrodes; and (b) corresponding CA curves of the bare Cu substrate (black), Cu NPs (red), rGO (green), Cu-rGO nanocomposite (blue) electrodes recorded at -0.4 V in a CO<sub>2</sub>-saturated 0.1 M NaHCO<sub>3</sub> solution.



**Figure 4.4** Nyquist plots measured at the potential of  $-0.4$  V in a  $\text{CO}_2$ -saturated  $0.1$  M  $\text{NaHCO}_3$  solution on different electrodes. Inset: the equivalent electric circuit used for fitting the EIS data, where  $R_s$  = solution resistance; CPE = constant phase element;  $R_{ct}$  = charge-transfer resistance;  $W_s$  = Warburg impedance (short).

$0.1$  M  $\text{NaHCO}_3$  (pH 6.65). Figure 4.3a compares the LSV curves of the bare Cu substrate, Cu NPs, rGO, and the Cu-rGO nanocomposite recorded at  $20$   $\text{mV s}^{-1}$ . The Cu-rGO nanocomposite exhibited a much higher current density and earlier onset potential in contrast to the bare Cu substrate, Cu NPs, and rGO. The CA curves of these electrodes were measured at  $-0.4$  V and compared in Figure 4.3b, showing that the steady-state current was increased in the following order: bare Cu < rGO  $\approx$  Cu NPs < Cu-rGO. It is noteworthy that the current density of the Cu-rGO nanocomposite was much higher, and the onset potential was much lower in comparison

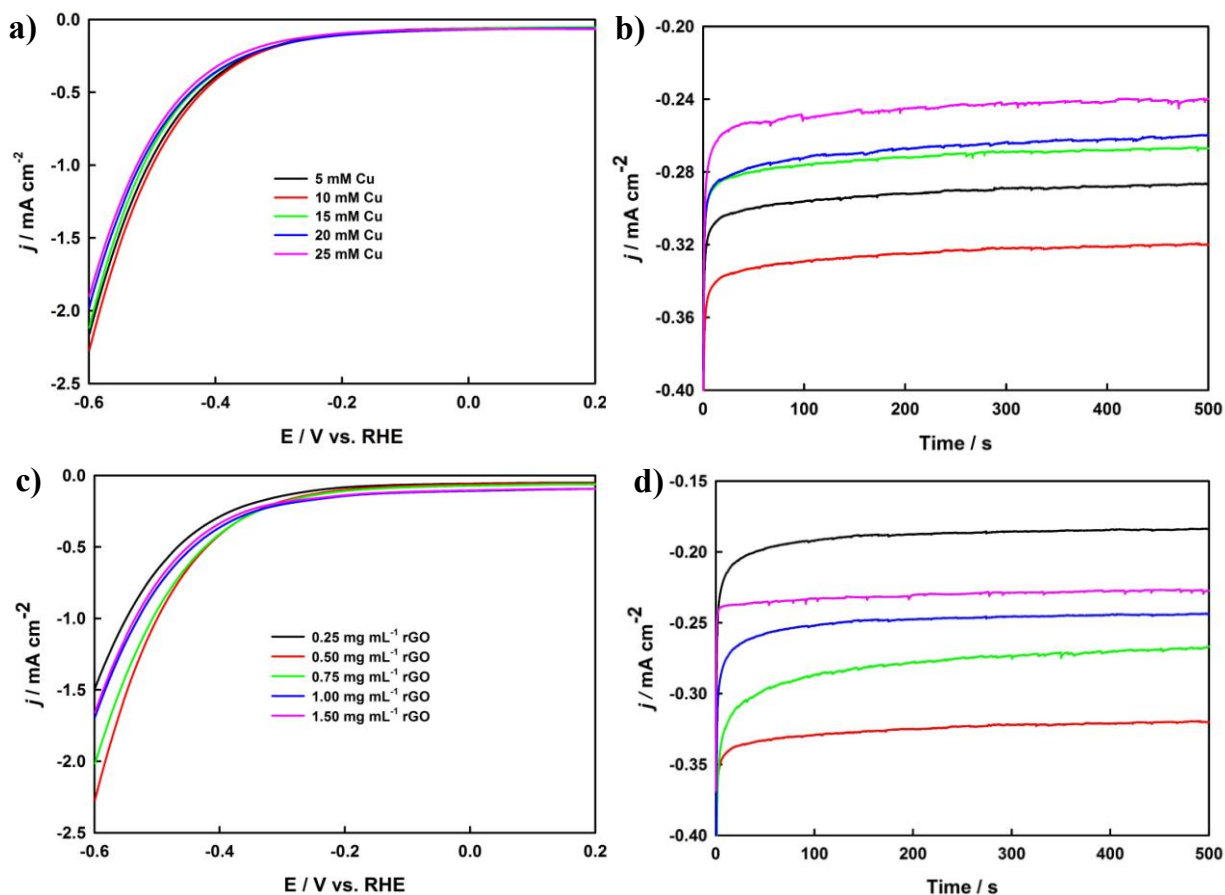
**Table 4.3** Values of the elements in equivalent electric circuit fitted in the Nyquist plots of Figure 4.4 (error percentage for each element is given in parentheses).

Elements	Bare	rGO	Cu NPs	Cu-rGO
$R_s$ ( $\Omega \text{ cm}^{-2}$ )	20.58 (0.46)	7.82 (0.94)	15.58 (0.78)	13.77 (0.67)
CPE-T ( $\mu\text{F cm}^{-2}$ )	191.06 (1.60)	781.40 (3.84)	427.38 (1.95)	1817.60 (4.07)
CPE-P	0.90 (0.75)	0.83 (2.60)	0.89 (2.93)	0.80 (3.61)
$R_{ct}$ ( $\Omega \text{ cm}^{-2}$ )	668.80 (2.67)	624.60 (3.27)	612.90 (2.27)	355.40 (3.12)
W-R ( $\Omega \text{ cm}^{-2}$ )	20.75 (3.89)	14.75 (2.90)	18.29 (9.78)	6.48 (3.02)
W-T (s)	0.007 (4.44)	0.008 (3.87)	0.007 (6.90)	0.013 (3.54)
W-P	0.47 (7.08)	0.42 (3.33)	0.42 (1.89)	0.45 (3.67)

$R_s$ : solution resistance; CPE-T/CPE-P: elements of constant phase element;  $R_{ct}$ : charge transfer resistance; W-R/W-T/W-P: elements of Warburg impedance associated to diffusion resistance.

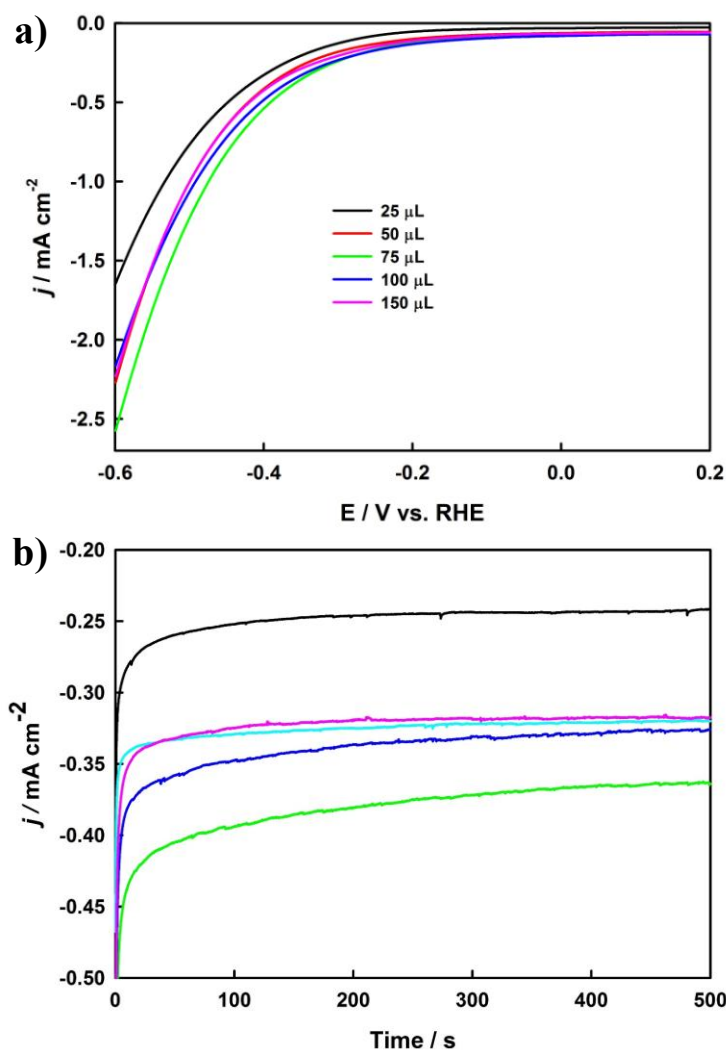
with other copper-based catalysts for the electroreduction of  $\text{CO}_2$  that have been recently reported in the literature [36-38,42-44].

Electrochemical impedance spectroscopy (EIS) was employed to determine the charge-transfer resistance. Nyquist plots (Figure 4.4) of the bare Cu, Cu NPs, rGO, and Cu-rGO nanocomposite electrodes were recorded in  $\text{CO}_2$ -saturated 0.1 M  $\text{NaHCO}_3$  aqueous solutions at -0.4 V. All of the impedance curves exhibited a semi-circle in the low-frequency region, which may correspond to the charge transfer resistance of the  $\text{CO}_2$  reduction [45]. The equivalent electrical circuit displayed in the inset was employed to fit the experimental data using the Z-view software, and the corresponding fitted results were summarized along with the percentage of errors in Table 4.3. All of the solution resistances ( $R_s$ ) were small, and the low error percentages indicated that the employed equivalent circuit fitted the impedance data well. All of the CPE-P values were  $>0.8$ , which signified that the constant phase element (CPE) behaviours were capacitor-like. The Cu-rGO nanocomposite exhibited the highest CPE-T value (1817.60  $\mu\text{F}$



**Figure 4.5** LSV curves (a) and CA plots (b) of the Cu-rGO nanocomposite electrodes prepared with a constant GO concentration ( $0.5 \text{ mg mL}^{-1}$ ) while the concentration of the Cu precursor was changed from 5 to 25 mM as listed in Figure 4.5a. LSV curves (c) and CA plots (d) for the optimization of the GO mg concentration while the concentration of the Cu precursor was maintained at 10 mM.

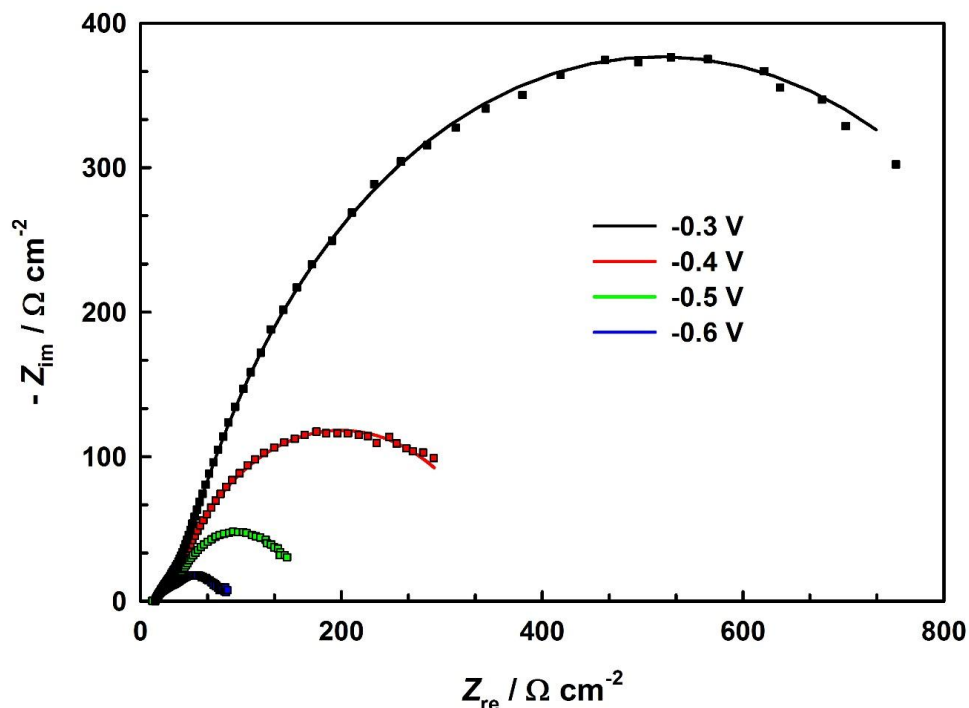
$\text{cm}^{-2}$ ), which was over four-fold larger than that of the Cu NPs ( $427.38 \mu\text{F cm}^{-2}$ ) and over two-fold greater than that of the rGO ( $781.40 \mu\text{F cm}^{-2}$ ). Moreover, the Cu-rGO nanocomposite exhibited much lower charge-transfer resistance  $R_{ct}$  ( $355.40 \Omega \text{ cm}^{-2}$ ), which was almost half of the Cu NPs ( $612.90 \Omega \text{ cm}^{-2}$ ). A short Warburg impedance ( $W_s$ ) associated with  $R_{ct}$  was included



**Figure 4.6** LSV curves (a) and CA plots (b) of the Cu-rGO nanocomposite electrodes prepared with the optimized GO ( $0.5 \text{ mg mL}^{-1}$ ) and Cu ( $10 \text{ mM}$ ) concentration while the volume of the mixed solution was altered from 25 to 150  $\mu\text{L}$  as listed in Figure 4.6a.

in the equivalent circuit in order to effectively fit the impedance spectra, indicating that the diffusion resistance also played an important role during the electrochemical reduction of  $\text{CO}_2$ . All of the EIS results further demonstrated that the Cu-rGO nanocomposite exhibited much





**Figure 4.7** Nyquist plots of the optimized Cu-rGO nanocomposite electrode recorded at -0.3, -0.4, -0.5, and -0.6 V in a CO<sub>2</sub> saturated 0.1 M NaHCO<sub>3</sub> solution. The symbols denote the experimental data and the solid lines correspond to the fitted results using the equivalent electrical circuit (inset). The amplitude of the modulation potential was 10 mV and the frequency was altered from 100 kHz to 10 mHz.

higher catalytic activity toward the electrochemical reduction of CO<sub>2</sub> in comparison to the Cu NPs and rGO.

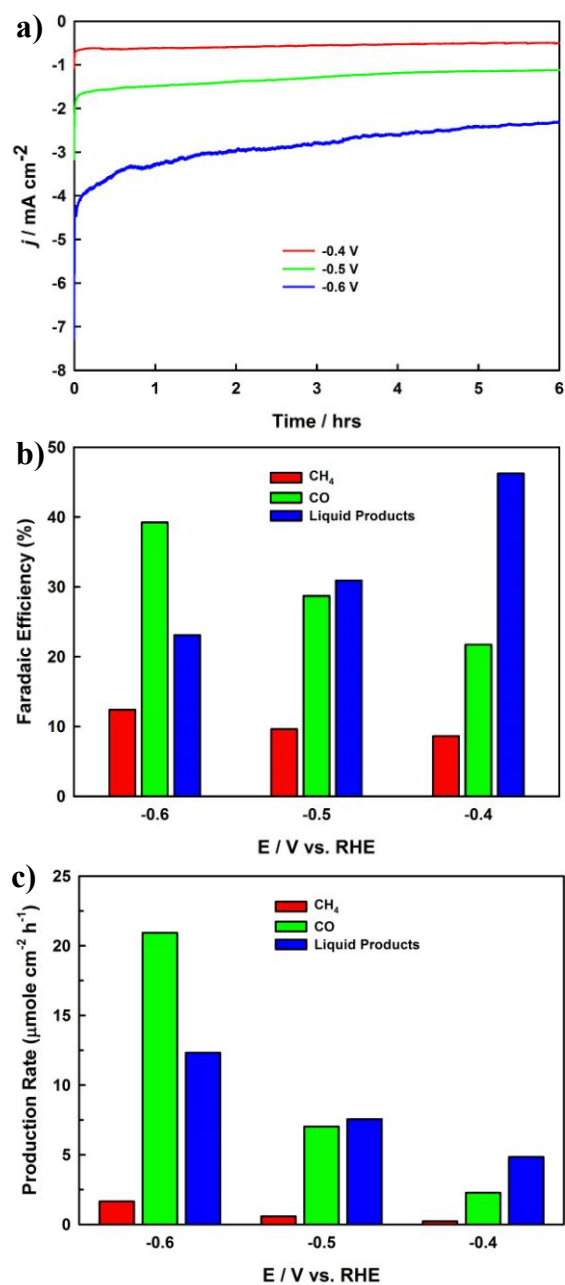
In order to optimize the composition and quantity of the nanocomposite, different Cu-rGO nanocomposites were prepared and studied. Figure 4.5 presents the LSV and CA curves of the prepared Cu-rGO nanocomposites, where the concentration of the Cu precursor was altered from 5 to 25 mM, and the GO concentration was varied from 0.25 to 1.5 mg mL<sup>-1</sup>. As shown in both LSV (Figure 4.5a) and CA (Figure 4.5b) plots, the highest current density was achieved

**Table 4.4** Values of the elements in equivalent electric circuit fitted in the Nyquist plots of Figure 4.7. (Error percentage of each element is given in the parentheses).

Elements	-0.30 V	-0.4 V	-0.5 V	-0.6 V
$R_s$ ( $\Omega \text{ cm}^{-2}$ )	12.88 (0.36)	13.77 (0.67)	13.87 (0.45)	14.03 (0.45)
CPE-T ( $\mu\text{F cm}^{-2}$ )	1907 (4.67)	1817.60 (4.07)	1785.80 (3.24)	1700.34 (4.57)
CPE-P	0.86 (2.73)	0.80 (3.61)	0.78 (2.61)	0.76 (2.87)
$R_{ct}$ ( $\Omega \text{ cm}^{-2}$ )	976.00 (1.05)	355.40 (3.12)	151.00 (3.78)	70.26 (3.31)
W-R ( $\Omega \text{ cm}^{-2}$ )	20.67 (4.56)	16.48 (3.02)	14.34 (1.90)	10.12 (7.44)
W-T (s)	0.008 (2.22)	0.013 (3.54)	0.026 (3.42)	0.043 (2.29)
W-P	0.36 (4.58)	0.45 (3.67)	0.45 (4.07)	0.48 (1.67)

Rs: solution resistance; CPE-T/CPE-P: elements of constant phase element;  $R_{ct}$ : charge transfer resistance; W-R/W-T/W-P: elements of Warburg impedance associated to diffusion resistance.

with the 10.0 mM Cu precursor. In the case of GO, the highest activity was observed when 0.5 mg mL<sup>-1</sup> GO was used, as seen in Figure 4.5c and Figure 4.5d. To study the effects of the thickness of the nanocomposite, similar experiments were conducted with the optimized composite mixture of the 10 mM Cu precursor and 0.5 mg mL<sup>-1</sup> GO, where the volume was changed from 25 to 150  $\mu\text{L}$ . The highest current density was attained with 75  $\mu\text{L}$  of the composite mixture, as shown in both the LSV and CA curves (Figure 4.6a and 4.6b). EIS was further carried out to investigate the charge-transfer resistance of the optimized Cu-rGO nanocomposite (75  $\mu\text{L}$  of 10 mM Cu and 0.5 mg mL<sup>-1</sup> GO mixture) at four different applied electrode potentials (Figure 4.7). The EIS curves were effectively fitted with the electrical circuit (inset of Figure 4.7) with the results listed in Table 4.4, revealing that the charge-transfer



**Figure 4.8** (a) CA curves of the optimized Cu-rGO nanocomposite recorded at the selected potentials of -0.4, -0.5, and -0.6 V for product analysis. (b) The corresponding Faradaic efficiency of the formed products at the different applied potentials over the six hours. (c) The rates of product formation during the electrochemical reduction of CO<sub>2</sub> at the applied potentials on the Cu-rGO nanocomposite electrode.

resistance was significantly decreased from 976.0 to 70.26  $\Omega \text{ cm}^{-2}$ , with the increase of the cathodic potential from -0.3 to -0.6 V.

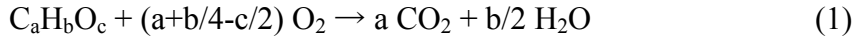
### 4.3.2 Bulk electrolysis of $\text{CO}_2$

In an attempt to achieve the bulk electrolysis of  $\text{CO}_2$ , we selected three potentials (-0.4, -0.5, and -0.6 V) for six hours of electrolysis using the optimized Cu-rGO nanocomposite in a  $\text{CO}_2$ -saturated 0.1 M  $\text{NaHCO}_3$  electrolyte (pH 6.65). Figure 4.8a shows that the current density increased with the elevation of the cathode potentials during the bulk electrolysis of  $\text{CO}_2$ , which was indicative of accelerated  $\text{CO}_2$  reduction reaction rates at more negative potentials. The formation of a large quantity of product was also observed at more negative potentials, revealing that the Cu-rGO nanocomposite facilitated the charge-transfer for the  $\text{CO}_2$  reduction, while increasing the cathodic potential. Our GC analysis showed that CO and  $\text{CH}_4$  were the primary gas products generated from the electrochemical reduction of  $\text{CO}_2$ . To confirm that whether rGO served as the potential carbon source, we have conducted two control experiments: (i) running the CA experiment at -0.5 V vs RHE for six hours in an Ar-saturated 0.1 M  $\text{NaHCO}_3$  solution using the rGO electrode; and (ii) performing the same CA test in an Ar-saturated 0.1 M  $\text{Na}_2\text{SO}_4$  solution using the Cu-rGO nanocomposite. Only hydrogen was detected in the GC analysis for both cases, confirming that the CO and  $\text{CH}_4$  products were formed from the electrochemical reduction of  $\text{CO}_2$  using the Cu-rGO nanocomposite as the electrocatalyst. The FE for the formation of CO and  $\text{CH}_4$  at the different applied electrode potentials were calculated and plotted in Figure 4.8b, showing that more CO was generated than  $\text{CH}_4$  and that the FE for the formation of the gas products was increased with the raising of the cathodic potential from -0.4 to -0.6 V.

**Table 4.5** Comparison of some promising Cu-based catalysts for the electrochemical reduction of CO<sub>2</sub> recently reported in the literature.

Electrocatalyst	Applied potential	Products (FE%)	Total FE%	Ref.
Oxide derived Cu	-0.40 V vs. RHE	CO (38.5); HCOO <sup>-</sup> (10.8)	49.3	39
Cu nanowire	-0.795 V vs. RHE	CO (2.4); C <sub>2</sub> H <sub>4</sub> (7.2); C <sub>2</sub> H <sub>6</sub> (8.3); HCOO <sup>-</sup> (9.6); CH <sub>3</sub> CH <sub>2</sub> OH (10.8)	38.64	46
Carbon nanotube/copper sheets (CNT/Cu)	-2.8 V vs. Ag/AgCl	CO (1.6); CH <sub>4</sub> (6.8)	7.6	43
	-5.0 V vs. Ag/AgCl	CO (5.1); CH <sub>4</sub> (15.5); C <sub>2</sub> H <sub>4</sub> (1.1)	21.7	
Copper nanoparticles supported on carbon black (40 wt% Cu/VC)	-1.2 V vs. Ag/AgCl	CO (~15.0)	15.0	44
20% Cu/CNT	-1.7 V vs. SCE	CH <sub>3</sub> OH (38.4)	38.4	47
Carbon nanospire electrode with electronucleated Cu nanoparticles (Cu/CNS)	-0.7 V vs. RHE	CO (23.0); CH <sub>4</sub> (12.0)	25.0	36
Graphene confined Sn quantum sheets	-1.2 V vs. SCE	HCOO <sup>-</sup> (30.0)	30.0	48
Cu NPs loaded on glassy carbon (Cu NP/GC)	-1.3 V vs. RHE	CO (5.5); CH <sub>4</sub> (40.1); C <sub>2</sub> H <sub>4</sub> (2.3); HCOOH (1.9); CH <sub>3</sub> COOH (0.7)	50.5	35
Oxide derived Cu foam	-1.0 V vs. RHE	CO (~5.0); HCOO <sup>-</sup> (~5.0); C <sub>2</sub> H <sub>4</sub> (~20.0); C <sub>2</sub> H <sub>6</sub> (~25.0)	55.0	49
Copper nanoparticles supported on glassy carbon (n-Cu/C)	-0.95 vs. RHE	CH <sub>4</sub> (~15.0)	15.0	25
Cu mesocrystals	-0.99 V vs. RHE	CO (~2.0); CH <sub>4</sub> (~3.0); C <sub>2</sub> H <sub>4</sub> (~27.0)	32.0	50
Cu nanoflower	-1.6 V vs. RHE	HCOOH (~50.0); CH <sub>4</sub> (~5.0); C <sub>2</sub> H <sub>4</sub> (~10.0)	65.0	28
<b>Cu-rGO</b>	<b>-0.4 V vs. RHE (-1.0 V vs. Ag/AgCl)</b>	<b>CO (21.7); CH<sub>4</sub> (8.6); Liquid products ( 46.2)</b>	<b>76.6</b>	<b>Present work</b>

As mentioned in the introduction, the COD analysis is just the opposite of the CO<sub>2</sub> reduction; and this reverse conversion allows us to rapidly determine the total amount of electrons that are used in the electrochemical reduction of CO<sub>2</sub> to produce the various organic liquid fuels as they will be completely oxidized via the following general equation during the COD analysis [16,17]:



Where a, b, and c represent the stoichiometric ratio of carbon, hydrogen, and oxygen in the formed organic compounds, respectively. Since each O<sub>2</sub> molecule corresponds to a four-electron transfer:



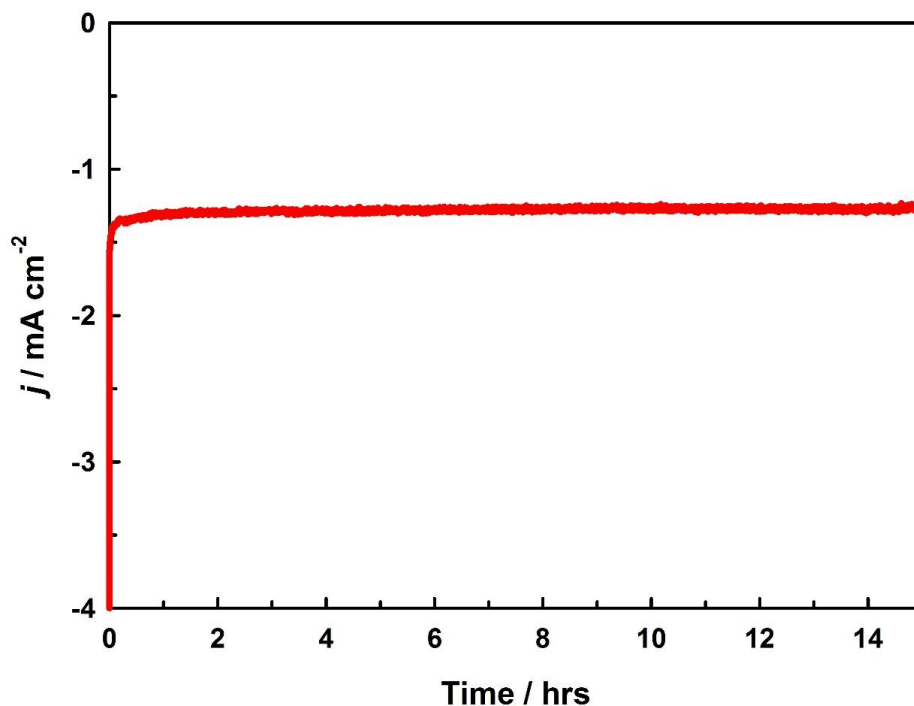
We may use the following equation to calculate the total charge (Q<sub>COD</sub>), which was consumed for the formation of the liquid fuels during the electrochemical reduction of CO<sub>2</sub>:

$$Q_{COD} = COD [mg L^{-1} O_2] \times (4 F V / 32000) \quad (3)$$

Where *F* is the Faraday constant and *V* is the volume of the solution. Thus, the Faradaic efficiency for the formation of the liquid products may be calculated as follows:

$$FE_{COD}\% = Q_{COD} / Q \times 100 \quad (4)$$

Where *Q* is the overall charge passed during the electrochemical reduction of CO<sub>2</sub>. The FE<sub>COD</sub> at the different potentials was calculated and plotted in Figure 4.8b, showing that the FE in the formation of liquid chemicals/fuels was decreased when the cathodic potential was raised from -0.4 to -0.6 V. Our further HPLC analysis confirmed that the primary liquid product was formate with a trace amount of acetate. For comparison, the CA experiment was also performed at -0.5 V in an Ar-saturated 0.1 M Na<sub>2</sub>SO<sub>4</sub> solution for six hours using the Cu-rGO nanocomposite. The subsequent COD analysis was carried out and no COD change of the solution was observed prior



**Figure 4.9** The stability test of the optimized nanocomposite electrode carried at -0.5 V in a  $\text{CO}_2$ -saturated 0.1 M  $\text{NaHCO}_3$  solution under continuous  $\text{CO}_2$  purging.

to and after the CA test, further confirming that the increase of the COD value in the electrolysis experiment performed in the  $\text{CO}_2$ -saturated 0.1 M  $\text{NaHCO}_3$  solution was resulted from the electrochemical reduction of  $\text{CO}_2$ . The total FE of the optimized Cu-rGO nanocomposite for the reduction of  $\text{CO}_2$  included two parts (the formation of the gas and liquid products); and it was calculated to be 76.6%, 69.2%, and 74.7% at the applied electrode potentials of -0.4, -0.5, and -0.6 V vs RHE, respectively, and the rest ~25% might be attributed to the hydrogen evolution. The rates of the formation of the products at the different applied electrode potentials are presented in Figure 4.8c, revealing that all the production rates were increased with the increase of the cathodic potential from -0.4 to -0.6 V and that a significant increase of the CO formation was observed in comparison of the formation of the other gas and liquid products. Various Cu-

based materials have been explored for the electrochemical reduction of CO<sub>2</sub>, and some of the promising results recently reported in the literature are compared in Table 4.5, showing that the unique Cu-rGO nanocomposite developed in the present study exhibited excellent FE for the efficient electrocatalytic reduction of CO<sub>2</sub> at a relative low overpotential.

Finally, the stability of the optimized Cu-rGO nanocomposite was tested at -0.5 V in one liter of CO<sub>2</sub>-saturated 0.1 M NaHCO<sub>3</sub> over 15 hours, via the chronoamperometric method (Figure 4.9), where CO<sub>2</sub> was continuously purged into the solution during the course of the test. Impressively, the current density was almost identical during the entire CO<sub>2</sub> reduction electrolyses, which demonstrated the high stability of the Cu-rGO nanocomposite electrode. The superior stability was further confirmed by inductively coupled plasma atomic emission spectroscopic (ICP-AES) analysis, where no Cu was detected in the electrolyte following the electrolysis.

#### **4.4 Discussion**

A unique Cu-rGO nanocomposite has been developed in the present study as a high-performance electrocatalyst for the efficacious reduction of CO<sub>2</sub> in an aqueous solution, with a high current density and a low cathodic potential. The superior electrocatalytic activity and stability of the Cu-rGO nanocomposite achieved in our study can be attributed to the uniformly distributed small Cu nanoparticles on the rGO and the synergistic coupling effect of the formed nanocomposite. The electron transfer between the rGO and Cu nanoparticles may increase localized electron concentrations, resulting in significant enhancement of the catalytic activities of the nanocomposite for the electrochemical reduction of CO<sub>2</sub>. The GC measurements indicated that CO and CH<sub>4</sub> were the primary gas products, while our HPLC analysis revealed that HCOO<sup>-</sup> was the dominant liquid product. In addition, we have employed COD analysis to quantify the



overall liquid products, which provides a facile, rapid, and accurate method for the determination of the total FE for the conversion of CO<sub>2</sub> to liquid products. The COD analysis may become a universal approach for quantification of the overall liquid products generated in other CO<sub>2</sub> conversion processes, for instance, photochemical and photoelectrochemical reduction of CO<sub>2</sub>. The easy fabrication, cost-effectiveness, high intrinsic activity, superior stability, and excellent FE make the Cu-rGO nanocomposite developed in this study a very promising catalyst for the efficient electrochemical conversion of CO<sub>2</sub> to valuable fuels. This might enable a new strategy for the restoration of the carbon balance, while contributing to the resolution of the climate change.

#### Reference:

- [1] S. Gao, Y. Lin, X. Jiao, Y. Sun, Q. Luo, W. Li D. Zhang, J. Yang, Y. Xie, *Nature* **2016**, 529, 68.
- [2] J. Wu, S. Ma, J. Sun, J. I. Gold, C. Tiwary, B. Kim, L. Zhu, N. Chopra, I. N. Odeh, R. Vajtai, A. Z. Yu, R. Luo, J. Lou, G. Ding, P. J. A. Kenis, P. M. Ajayan, *Nature Commun.* **2016**, 7, 13869.
- [3] M. Liu, Y. Pang, B. Zhang, P. D. Luna, O. Voznyy, J. Xu, X. Zheng, C. T. Dinh, F. Fan, C. Cao, F. P. G. de Arquer, T. S. Safaei, A. Mepham, A. Klinkova, E. Kumacheva, T. Filleter, D. Sinton, S. O. Kelley, E. H. Sargent, *Nature* **2016**, 537, 382.
- [4] M. Asadi, K. Kim, C. Liu, A. V. Addepalli, P. Abbasi, P. Yasaei, P. Phillips, A. Behranginia, J. M. Cerrato, R. Haasch, P. Zapol, B. Kumar, R. F. Klie, J. Abiade, L. A. Curtiss, A. Salehi-Khojin, *Science* **2016**, 353, 467.
- [5] Z. N. Zahran, E. A. Mohamed, Y. Naruta, *Sci. Rep.* **2016**, 6, 24533.
- [6] Y. Hori, in *Modern Aspects of Electrochemistry*, Vol. 42 (Eds.: C. G. Vayenas, R. E. White, M. E. Gamboa-Aldeco), Springer, New York, **2008**, 89.
- [7] A. A. Peterson, F. A. Pedersen, F. Studt, J. Rossmeisl, J. K. Nørskov, *Energ. Environ. Sci.* **2010**, 3, 1311.

- [8] A. A. Peterson, J. K. Nørskov, *J. Phys. Chem. Lett.* **2012**, 3, 251.
- [9] J. Zhang, K. Xie, H. Wei, Q. Qin, W. Qi, L. Yang, C. Ruan, Y. Wu, *Sci. Rep.* **2014**, 4, 7082.
- [10] F. Jin, X. Zeng, J. Liu, Y. Jin, L. Wang, H. Zhong, G. Yao, Z. Huo, *Sci. Rep.* **2014**, 4, 4503.
- [11] C. W. Li, J. Ciston, M. W. Kanan, *Nature* **2014**, 508, 504.
- [12] X. Y. Wang, S. Q. Liu, K. L. Huang, Q. J. Feng, D. L. Ye, B. Liu, J. L. Liu, G. H. Jin, *Chin. Chem. Lett.* **2010**, 21, 987–990.
- [13] L. Sun, G. K. Ramesha, P. V. Kamat, J. F. Brennecke, *Langmuir* **2014**, 30, 6302.
- [14] S. Lee, H. Ju, R. Machunda, S. Uhm, J. K. Lee, H. J. Leed, J. Lee, *J. Mater. Chem. A* **2015**, 3, 3029.
- [15] A. N. Grace, S. Y. Choi, M. Vinoba, M. Bhagiyalakshmi, D. H. Chu, Y. Yoon, S. C. Nam, S. K. Jeong, *Appl. Energ.* **2014**, 120, 85.
- [16] Z. Zhang, X. Chang, A. Chen, *Sens. Actuators B* **2016**, 223, 664.
- [17] X. Qu, M. Tian, S. Chen, B. Liao, A. Chen, *Electroanalysis* **2011**, 23, 1267.
- [18] P. V. Kamat, *J. Phys. Chem. Lett.* **2011**, 2, 242.
- [19] L. Qu, Y. Liu, J.-B. Baek, L. Dai, *ACS Nano* **2010**, 4, 1321.
- [20] P. V. Kamat, *J. Phys. Chem. Lett.* **2010**, 1, 520.
- [21] M. Govindhan, A. Chen, *J. Power Sources* **2015**, 274, 928.
- [22] M. Govindhan, B. Mao, A. Chen, *Nanoscale* **2016**, 8, 1485.
- [23] D.-H. Lim, J. H. Jo, D. Y. Shin, J. Wilcox, H. C. Hama, S. W. Nama, *Nanoscale* **2014**, 6, 5087.
- [24] V. Tripovic, M. Vanin, M. Alramad, M. E. Barketun, K. W. Jacobsen, K. S. Thygesen, J. Rossmeisl, *J. Phys. Chem. C* **2013**, 117, 9187.
- [25] K. Manthiram, B. J. Beberwyck, A. P. Alivisatos, *J. Am. Chem. Soc.* **2014**, 136, 13319.
- [26] H. Noda, S. Ikeda, Y. Oda, K. Imai, M. Maeda, K. Ito, *Bull. Chem. Soc. Jpn.* **1990**, 63, 2459.
- [27] H. Shibata, J. A. Moulijn, G. Mul, *Catal. Lett.* **2008**, 123, 186.

- [28] J.-F. Xie, Y.-X. Huang, W.-W. Li, X.-N. Song, L. Xiong, H.-Q. Yu, *Electrochim. Acta* **2014**, 139, 137.
- [29] K. J. P. Schouten, Z. Qin, E. P. Gallent, M. T. M. Koper, *J. Am. Chem. Soc.* **2012**, 134, 9864.
- [30] R. Reske, M. Duca, M. Oezaslan, K. J. Schouten, M. T. Koper, P. Strasser, *J. Phys. Chem. Lett.* **2013**, 4, 2410.
- [31] M. R. Goncalves, A. Gomes, J. Condeco, T. R. C. Fernandes, T. Pardal, C. A. C. Sequeira, J. B. Brancoc, *Electrochim. Acta* **2013**, 102, 388.
- [32] D. R. Kauffman, P. R. Ohodnicki, B. W. Kail, C. Matranga, *J. Phys. Chem. Lett.* **2011**, 2, 2038.
- [33] W. Tang, A. A. Peterson, A. S. Varela, Z. P. Jovanov, L. Bech, W. J. Durand, S. Dahl, J. K. Norskov, I. Chorkendorff, *Phys. Chem. Chem. Phys.* **2012**, 14, 76.
- [34] Y. Li, H. Su, S. H. Chan, Q. Sun, *ACS Catal.* **2015**, 5, 6658.
- [35] Y. Lum, Y. Kwon, P. Lobaccaro, L. Chen, E. L. Clark, A. T. Bell, J. W. Ager, *ACS Catal.* **2016**, 6, 202.
- [36] Y. Song, R. Peng, D. K. Hensley, P. V. Bonnesen, L. Liang, Z. Wu, H. M. Meyer, III, M. Chi, C. Ma, B. G. Sumpter, A. J. Rondinone, *ChemistrySelect* **2016**, 1, 1.
- [37] D. C. B. Alves, R. Silva, D. Voiry, T. Asefa, M. Chhowalla, *Mat. Ren. Sust. Energ.* **2015**, 4, 2.
- [38] X. Liu, L. Zhu, H. Wang, G. He, Z. Bian, *RSC Adv.* **2016**, 6, 38380.
- [39] F. Jia, X. Yu, L. Zhang, *J. Power Sources* **2014**, 252, 85.
- [40] Y. Koo, R. Malik, N. Alvarez, L. White, V. N. Shanov, M. Schulz, B. Collins, J. Sankara, Y. Yun, *RSC Adv.* **2014**, 4, 16362.
- [41] O. A. Baturina, Q. Lu, M. A. Padilla, L. Xin, W. Li, A. Serov, K. Artyushkova, P. Atanassov, F. Xu, A. Epshteyn, T. Brintlinger, M. Schuette, G. E. Collins, *ACS Catal.* **2014**, 4, 3682.
- [42] F. Koleli, T. Ropke, C. H. Hamann, *Electrochim. Acta* **2003**, 48, 1595.
- [43] C. W. Li, M. W. Kanan, *J. Am. Chem. Soc.* **2012**, 134, 7231.

- [44] D. Raciti, K. J. Livi, C. Wang, *Nano Lett.* **2015**, 15, 6829.
- [45] S. S. Hossain, S. Rahman, S. Ahmed, *J. Nanomater.* **2014**, 2014, 374318.
- [46] F. Lei, W. Liu, Y. Sun, J. Xu, K. Liu, L. Liang, T. Yao, B. Pan, S. Wei, Y. Xie, *Nat. Commun.* **2016**, 7, 12697.
- [47] A. Dutta, M. Rahaman, N. C. Luedi, M. Mohos, P. Broekmann, *ACS Catal.* **2016**, 6, 3804.
- [48] C. S. Chen, A. D. Handoko, J. H. Wan, L. Ma, D. Ren, B. S. Yeo, *Catal. Sci. Technol.* **2015**, 5, 161.
- [49] D. Kim, J. Resasco, Y. Yu, A. M. Asiri, P. Yang, *Nat. Commun.* **2014**, 5, 4948.
- [50] K. Yan, A. Chen, *Fuel* **2014**, 115, 101–108.

# **Chapter 5: Synthesis, electrochemical and in situ FTIR study of Cu nanodendrites toward efficient CO<sub>2</sub> reduction**

## **5.1 Introduction**

CO<sub>2</sub> is considered a primary greenhouse gas that plays a central role in raising average global temperatures. The emission of CO<sub>2</sub> results mainly from the combustion of fossil fuels in industry, automobiles, domestic use, and naturally via volcanic eruptions. However, the global reserves of fossil fuels will soon be depleted by continuous anthropogenic use, and humanity will face intense challenges toward the implementation of viable replacements, along with their associated infrastructures. Hence, is an urgent need to discover a new and sustainable energy source, and/or to devise strategies for the use of renewable energies. The conversion of CO<sub>2</sub> to fuel using an electrochemical reduction technology might serve as a feasible approach for the generation of renewable energy [1,2]. Over the last few decades, scientists have developed various electrocatalytic materials for the reduction of CO<sub>2</sub> that are active in aqueous solutions; however, their performance has not been sufficient enough for practical use, in terms of energy efficiency and stability [3-12]. Metal-based electrodes have been employed extensively for electrochemical the reduction of CO<sub>2</sub> [6-9]. Among them, copper-based materials have garnered particular attention, as these catalysts have the capacity to produce hydrocarbon fuel products, such as formic acid (HCOOH), acetic acid (CH<sub>3</sub>COOH), methanol (CH<sub>3</sub>OH), methane (CH<sub>4</sub>), and ethane (C<sub>2</sub>H<sub>4</sub>), and more. However, they still require a high overpotential, which generates significant hydrogen evolution in conjunction with CO<sub>2</sub> reduction in aqueous solutions, and have a low Faradaic efficiency of CO<sub>2</sub>-reduced products [10-14]. Moreover, the selectivity and stability of CO<sub>2</sub> reduction products on these materials is poor [10-12]. For example,

polycrystalline Cu requires more than 0.5 V of overpotential to attain a current density of 1 mA cm<sup>-2</sup> for the conversion of CO<sub>2</sub> to CO and HCOOH, and >0.8 V for further reduction to obtain CH<sub>4</sub> and C<sub>2</sub>H<sub>4</sub> [13,14].

Different classes of Cu electrodes have been explored toward the electrochemical reduction of CO<sub>2</sub>, such as bulk Cu, thin Cu metal, Cu coated gas diffusion, electrodeposited Cu on glassy carbon, nanostructured Cu such as nanowires, nanoflowers, nanofoams, nanoporous, and copper-based alloys, to overcome these boundaries [13,15-22]. Nanostructured Cu materials have a high surface roughness factor, large electrochemical surface area, and different crystal facets. Several studies have been conducted to understand the effects of these properties on the electrochemical reduction of CO<sub>2</sub>, and reports indicate that significant improvements in catalytic performance have been achieved through the use of nanostructured Cu materials over typical metal electrodes, as electrocatalyst for the reduction of CO<sub>2</sub> [10,23,24]. Recently, oxide-derived Cu nanomaterials (OD-Cu) have garnered wide attention and been studied as electrocatalysts for the reduction of CO<sub>2</sub> and CO [10,13,25-27]. Nanomaterials comprised of OD-Cu are formed through the electrochemical reduction of copper oxides, which are synthesised via the thermal treatment of typical Cu NPs. The thermal process alters the surface structures of polycrystalline nanoparticles that might exhibit enhanced catalytic activity in the reduction of CO<sub>2</sub> and CO. The derived nanomaterials form interconnected nanocrystalline networks among nanocrystallites, and exhibit small crystallite sizes, as well as a large electrochemical surface area and high roughness factor that favors the formation of C-C couples during electrochemical reduction of CO<sub>2</sub> and CO [10,13,25-29]. The formation of CO and HCOOH on these OD-Cu nanomaterials occurs at low overpotentials, whereas CH<sub>4</sub> and C<sub>2</sub> hydrocarbons are comparatively generated at a high overpotential for the electrochemical reduction of CO<sub>2</sub> [10,26,30].

Moreover, significant efforts have been invested in understanding the mechanisms and formation of the electroreducible products of CO<sub>2</sub> on Cu electrodes [31,32-36]. In situ electrochemical attenuated total reflection Fourier-transform infrared (ATR-FTIR) spectroscopy is a powerful technique for observing the species that are adsorbed on catalyst surfaces, and carrying out electrokinetic studies to determine the kinetics of the formation of reduced products. Studies have revealed that CO is the primary species that is adsorbed onto Cu electrode surfaces during CO<sub>2</sub> electrolysis, which serves as an intermediate for the formation of other reduced products [32,33,37-39]. However, there remains a gap in understanding of the mechanisms for the formation of products and the kinetics of CO<sub>2</sub> reduction, between the intimate and bulk electrolysis of CO<sub>2</sub> on the Cu NP surface.

Herein, we attempted to develop Cu nanoparticles with a high electrochemically active surface area (EASA), as a robust electrocatalyst for the reduction of CO<sub>2</sub>. The Cu nanocatalyst was derived from CuO, where for our approach; Cu nanoparticles were initially deposited on a Ti substrate through an electrodeposition method. Subsequently, calcination was performed in the presence of different modifying agents to convert the Cu to CuO. To synthesize the most highly active catalyst, the quantities of modifying agents, as well as the calcination temperature and calcination time were optimized. Finally, the calcinated electrode was electrochemically reduced to obtain cedar leaf-like Cu nanodendrites as an electrocatalyst for the reduction of CO<sub>2</sub>. The developed electrocatalyst facilitated the reduction of CO<sub>2</sub> at a low overpotential to generate different hydrocarbons and oxygenates at cathodic potentials of higher than -0.2 V vs. RHE. The oxide-derived nanocrystalline Cu was more favorable for the reduction of CO to produce multi-carbon oxygenates in the potential range of from between -0.3 V and -0.7 V (vs. RHE) [25,27,40], whereas our synthesized tree-like Cu nanodendrites might overcome this barrier (CO

reduction), which could catalyze CO<sub>2</sub> at those applied potentials, with a remarkable current efficiency of up to 82% at -0.4 V. Furthermore, we employed in situ electrochemical ATR-FTIR spectroscopy to investigate the consumption of CO<sub>2</sub>, and the formation of intermediates and products, at different applied electrode potentials on the synthesized cedar leaf-like Cu nanodendrites during the electrochemical reduction of CO<sub>2</sub>.

## **5.2 Experimental section**

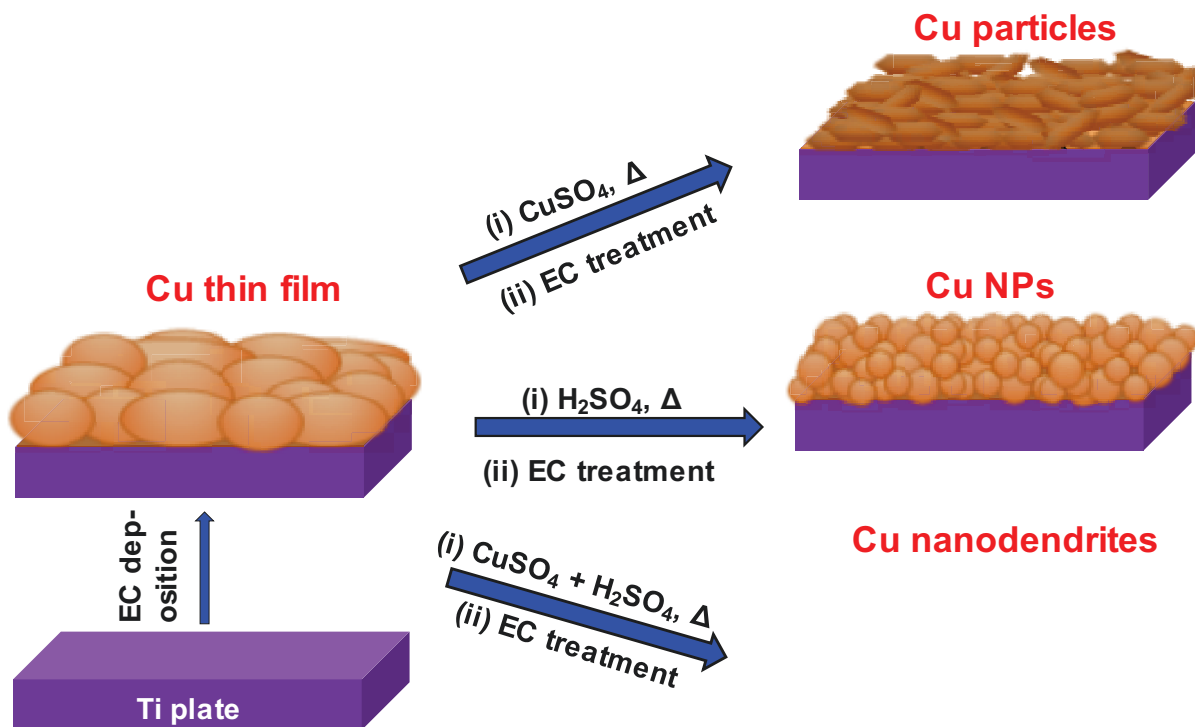
### **5.2.1 Chemicals and materials**

CuSO<sub>4</sub>·5H<sub>2</sub>O (99.999%), Na<sub>2</sub>SO<sub>4</sub> (≥99.5%), H<sub>2</sub>SO<sub>4</sub> (≥99.99%), D<sub>2</sub>O (99.9 at.%), TMS (99.5%) and NaHCO<sub>3</sub> (≥99.0%) solutions were obtained from Sigma Aldrich; copper foil (99.9985%, 0.5 mm thick) was purchased from Alfa Aesar; the Ti substrates (99.2%, 1.25 cm × 0.80 cm × 0.5 mm) were purchased from Sigma Aldrich; carbon di\*oxide (99.999%) and Ar (99.995%) gases were purchased from Praxair. All CO<sub>2</sub> reduction analyses were conducted in a CO<sub>2</sub>-saturated 0.1 M NaHCO<sub>3</sub> electrolyte solution. Deionized H<sub>2</sub>O was produced by a Nanopure Diamond TM UV ultrapure water purification system (18.2 MΩ cm), and used in the preparation of all electrolyte solutions.

### **5.2.2 Fabrication of electrodes**

A Ti plate (1.0 cm<sup>2</sup>), serving as a substrate, was cleaned with acetone using an ultrasonic cleaner for 10 min., followed by 10 min. of immersion in deionized H<sub>2</sub>O, and then etching in 5.0 M HCl at approximately 85 °C for 20 min.. Meanwhile, copper foils were etched for 1 min. in 35% HNO<sub>3</sub>, rinsed with a copious amount of deionized water, and then dried using a flow of N<sub>2</sub> gas. Scheme 5.1 illustrates the formation of the Cu thin film and different oxide-derived nanostructured Cu. In an attempt to synthesize different Cu nanostructures, the Ti plate was used as a cathode, and copper foil was taken as an anode in a mixture of 0.1 M CuSO<sub>4</sub> and 0.5 M





**Scheme 5.1** Schematics of the preparation of the Cu thin film and different oxide-derived nanostructured Cu.

$\text{H}_2\text{SO}_4$  in a three electrode cell system, with Ag/AgCl as the reference electrode. Cyclic Voltammetry (CV) was employed in the potential window of from 0.0 to -0.5 V (vs. Ag/AgCl) at a scan rate of  $50 \text{ mV s}^{-1}$  for 50 cycles to facilitate the deposition of copper onto the Ti substrate, which was referred to as a Cu thin film (Scheme 5.1). The formed Cu thin film was annealed at  $500^\circ\text{C}$  for 1 h, followed by applying a cathodic current density of  $10 \text{ mA cm}^{-2}$  for 30 min. with the continuous purging of  $\text{CO}_2$  in a  $\text{CO}_2$ -saturated 0.1 M  $\text{NaHCO}_3$  solution (which was referred to as the EC treatment) to form an oxide-derived (OD) Cu thin film. In order to form Cu particles and Cu nanoparticles, 50  $\mu\text{L}$  of 0.1 M  $\text{CuSO}_4$  and 50  $\mu\text{L}$  0.5 M  $\text{H}_2\text{SO}_4$  were deposited on a Cu thin film during calcination, respectively, whereas a 50  $\mu\text{L}$  mixture of a treating agent (0.1 M  $\text{CuSO}_4$  and 0.5 M  $\text{H}_2\text{SO}_4$ ) was cast on the Cu thin film during calcination to obtain Cu

nanodendrites (Scheme 5.1). The thickness of the Cu nanodendrites was optimized by changing the volume of the treating agent, from 30 to 70  $\mu\text{L}$  at 500  $^{\circ}\text{C}$  for 1 h. To study the effects of the calcination temperature, it was changed from 400 to 600  $^{\circ}\text{C}$  with 50  $\mu\text{L}$  of the treating agent, and the effects of the calcination time were studied from 30 to 90 min. at 500  $^{\circ}\text{C}$  using the same volume of the treating agent.

### 5.2.3 Characterization of electrodes

Scanning electron microscope (SEM) images were obtained and energy dispersive X-ray (EDX) analysis was performed using a FE-SEM (Hitachi SU-70) at 10.0 kV to study the morphologies, structures, and surface composition of the prepared electrodes. X-ray photoelectron spectroscopic (XPS) characterization was carried out using a Thermo Scientific XPS system, where the samples were adjusted to a take-off angle of  $90^{\circ}$  (relative to the surface). The size of the X-ray spot was 400  $\mu\text{m}$  using an Al  $\text{K}\alpha$  monochromatic source and XPSPEAK 4.1 software was employed for all data processing. Crystalline phase analysis was performed via a Phillips PW 1050-3710 with a Cu  $\alpha_1$  of 1.54060  $\text{\AA}$  as the radiation source, to record X-ray diffraction (XRD) patterns. The full range of  $2\theta$  data was obtained with a step of  $0.01^{\circ}/2\theta$  width. The Scherrer Equation  $L = 0.94\lambda/\beta \cos\theta$  (where,  $\lambda$  stands to the Cu  $\text{K}\alpha$  radiation, and  $\beta$  corresponds to the full width at half-maximum for a reflection maximum) was used to calculate the crystallite size (L) of each sample. PANalytical X'Pert HighScore Plus software was utilized to process the raw data and to fit the XRD spectra.

### 5.2.4 Electrochemical characterization

A CHI 660E workstation (CH Instrument Inc. USA) was used for electrochemical analysis via cyclic voltammetry (CV), Linear Sweep Voltammetry (LSV), and chronoamperometry (CA) in a conventional one compartment three electrode cell system. A

platinum coil (10.0 cm<sup>2</sup>) was used as the counter electrode, which was cleaned via flame annealing and quenching with deionized H<sub>2</sub>O prior to each experiment. The reference electrode employed was an Ag/AgCl (3.0 M KCl) electrode, which was converted to a reversible hydrogen electrode (RHE) scale (E versus RHE) using the Nernst equation:

$$E \text{ (vs. RHE)} = E \text{ (vs. Ag/AgCl)} + 0.0591 \text{ V} \times \text{pH} + 0.210 \text{ V}$$

A CO<sub>2</sub> saturated 0.1 M NaHCO<sub>3</sub> solution at pH 6.65 was used as the electrolyte for all electrochemical CO<sub>2</sub> reduction experiments.

### **5.2.5 Electrochemically active surface area (EASA) determination**

Surface roughness factors for the electrodeposited Cu thin film, OD-Cu thin film, and Cu nanodendrites were estimated, relative to the polycrystalline Cu electrode, by determining their double layer capacitances [27]. The CVs were obtained in the same electrochemical cell as for the electrochemical characterization with a 0.1 M HClO<sub>4</sub> electrolyte. No faradaic reactions were observed from the selected potential windows of the CVs for each electrode. The geometrical current densities versus the scan rates of the CV were plotted for each electrode, where the capacitance was estimated from the slope of the linear regression.

### **5.2.6 In situ electrochemical ATR-FTIR study**

All in situ attenuated total reflection-Fourier transform infrared spectroscopy (ATR-FTIR) investigations were carried out using an 8700 Nicolet Fourier transform 8700 infrared spectrometer with a ZnSe window and liquid N<sub>2</sub>-cooled MCT detector. A spectroelectrochemical cell, consisting of a Teflon chamber where the synthesized Cu nanodendrites were on the Ti substrate, served as the working electrode and was in contact with ZnSe hemispheres associated with the spectrometers. The incidence angle of the infrared beam was set to 60° with a customized in-house produced variable angle accessory for all experiments. The spectra were

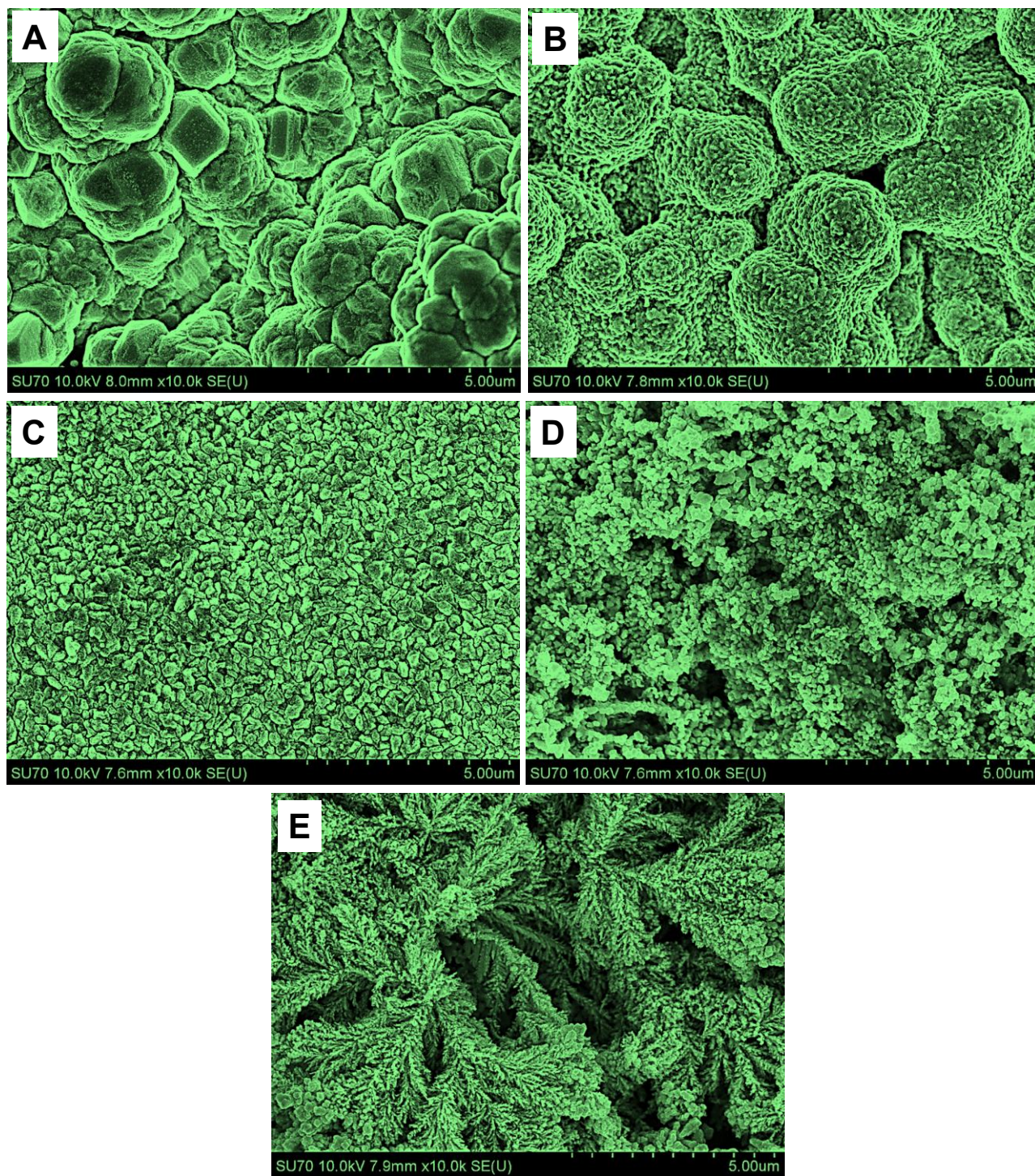
recorded using a single potential step procedure in which the electrode potential was controlled by a potentiostat and decreased by increments of -0.1 V beginning at +0.2 V. All interferograms were acquired at 4 cm<sup>-1</sup> resolution for 32 and 8 scans at different applied electrode potentials, and at -0.4 V, respectively, which were added and averaged. The interferograms were shown in terms of the relative change of the electrode reflectivity, which was calculated using following equation [41]:

$$\Delta R/R = [R(E_2) - R(E_1)] / R(E_1)$$

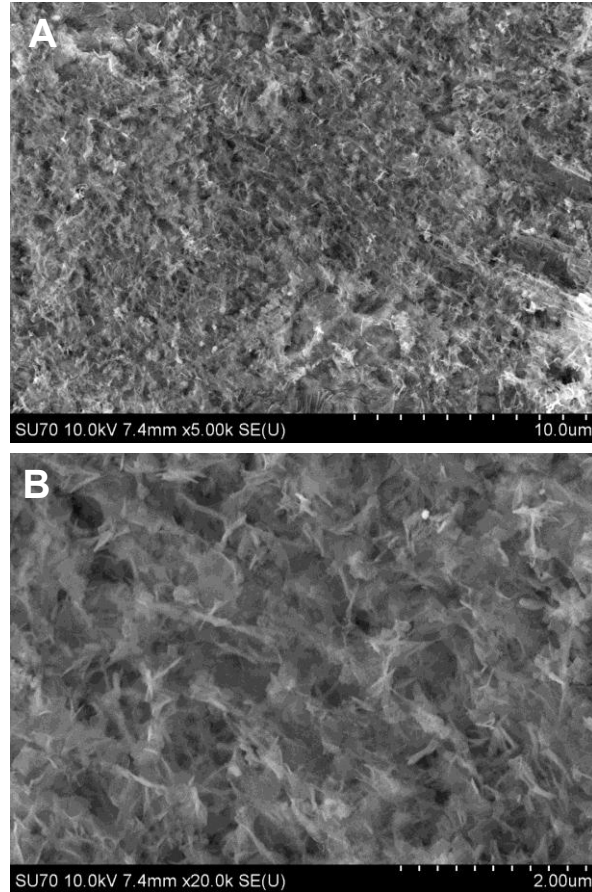
Where  $R(E_1)$  and  $R(E_2)$  are the reflectivities from the electrode surface at  $E_1$  and  $E_2$  potentials, respectively. The spectra recorded at  $E_1 = +0.2$  V was employed as background.

### **5.2.7 Bulk electrolysis of CO<sub>2</sub>**

The electrochemical reduction of CO<sub>2</sub> was performed in a liquid-tight two compartment cell with an installed cationic exchange membrane (CMI-7000S) as a separator at room temperature. The working and reference electrodes (Ag/AgCl) were placed together in one compartment, and CO<sub>2</sub> was continuously purged during electrolysis (to maintain CO<sub>2</sub> saturation in the 0.1 M NaHCO<sub>3</sub> solution), whereas the other compartment contained the counter electrode (Pt coil) in the CO<sub>2</sub> saturated 0.1 M NaHCO<sub>3</sub> solution. The working electrode and counter electrode chambers were filled with 160 mL and 40 mL of electrolyte, respectively. To identify the formed liquid CO<sub>2</sub> reduction products, a Varian Unity Inova 500 was employed to record the one-dimensional <sup>1</sup>H NMR spectra. A mixture of a 0.07 M sample of the electrolyte solution and 20% D<sub>2</sub>O was used to measure the spectrum, where 0.05 μL TMS (tetramethylsilane) was added to the sample as an internal reference.



**Figure 5.1** SEM images depict the uncalcined Cu thin film (A); OD-Cu thin film (B); Cu particles (C); Cu NPs (D); Cu nanodendrites (E).



**Figure 5.2** Surface morphology of the formed copper oxides; (A) Low magnification SEM image, (B) High magnification SEM images.

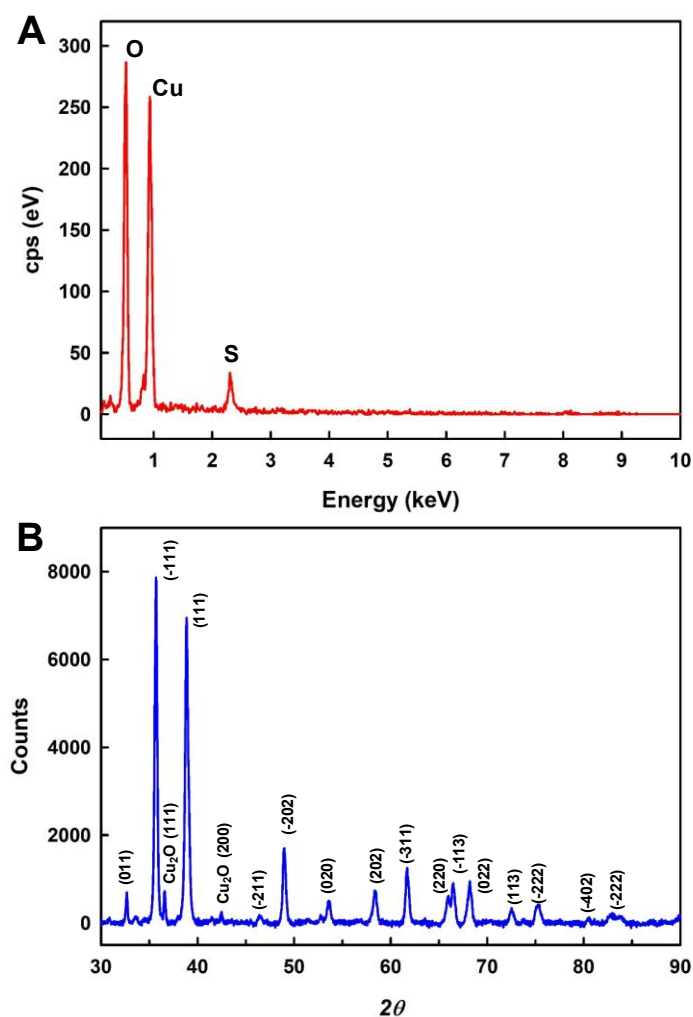
## **5.3 Results and discussion**

### **5.3.1 Characterization of electrodes**

Figure 5.1 displays the SEM images of the different Cu nanostructures. In our attempt, the Cu thin film was initially electrodeposited on the Ti substrate via an electrodeposition method (details can be found in the experimental sections), showing that large particulates were formed (Figure 5.1A). The formed Cu thin film was further calcinated at 500 °C for 1 h to form copper oxides. A rough surface was obtained for the Cu thin film following the EC treatment of the formed oxides (Figure 5.1B). Figure 5.1C depicts the grain sized Cu particles when the Cu

thin film was calcinated with  $\text{CuSO}_4$ , indicating the deposition of Cu particles on the Cu thin film, as the result of  $\text{CuSO}_4$  deposition during calcination. A significant change through the formation of Cu NPs (~100 to 200 nm) on the surface of the Cu thin film was observed under the treatment with  $\text{H}_2\text{SO}_4$  during calcination (Figure 5.1D), where  $\text{H}_2\text{SO}_4$  served as an etching agent to form the NPs. A thin layer of copper oxides was obtained following the calcination of the Cu thin film with 50  $\mu\text{L}$  of the treating agent mixture as shown in Figure 5.2, prior to the EC treatment. Surprisingly, dendritic segments with tertiary branches were formed following the EC treatment of the formed oxides to Cu (0), as shown in Figure 5.1E, which indicated the simultaneous formation and etching of Cu nanoparticles, while the  $\text{CuSO}_4$  and  $\text{H}_2\text{SO}_4$  mixture was employed during calcination. Moreover, a synergistic interaction between  $\text{CuSO}_4$  and  $\text{H}_2\text{SO}_4$  might have played a vital role in the formation of the nanodendritic structures.

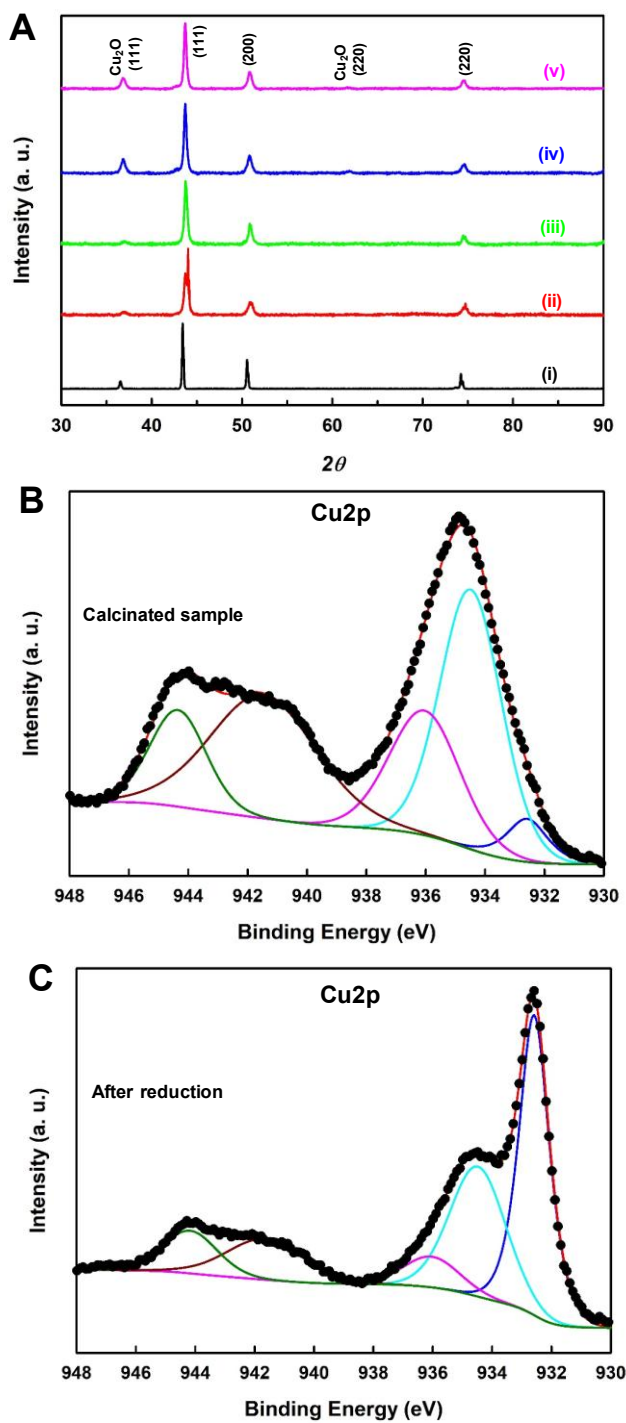
Figure 5.3 depicts the EDX spectra of the copper oxides film, which confirmed that the O and Cu peaks were associated with a small S peak; the latter resulting due to undissociated  $\text{CuSO}_4$  which remained on the oxide surfaces even after rinsing with water. The crystalline phase of the formed Cu electrodes and the copper oxides was determined via XRD analysis, as shown in Figures 5.4A and 5.3B, respectively, where  $\text{Cu}_2\text{O}$  was specially leveled (Figure 5.3B). Various crystallite planes of CuO and  $\text{Cu}_2\text{O}$  appeared in the XRD patterns of the formed oxide samples prior to their reduction to Cu, as shown in Figure 5.3B, which indicated that the calcination temperature of 500 °C for 1 h was sufficient under experimental conditions to form copper oxides. The XRD patterns of the variously formed nanostructured Cu indicated that all the electrodes were comprised of different Cu crystallites with a small quantity of  $\text{Cu}_2\text{O}$  crystallites, the latter might have been formed due to the exposure of the samples to ambient air. The peaks for Cu in the XRD patterns were observed at the expected position for all of the synthesized



**Figure 5.3** EDX spectra (A) and XRD pattern of the formed CuO.

electrodes. All Cu crystallite sizes were calculated using the Scherrer Equation and are listed in Table 5.1, revealing that Cu nanodendrites exhibited the smallest crystallite sizes at 27.51, 27.27, and 15.23 nm for Cu (111), Cu (200), and Cu (220) planes, respectively. Figure 5.4B depicts the high-resolution Cu2p XPS spectra of the copper oxides which were synthesized with the treating agent mixture at 500 °C for 1 h. A current density of  $-10 \text{ mA cm}^{-2}$  was applied for 1000 s in a



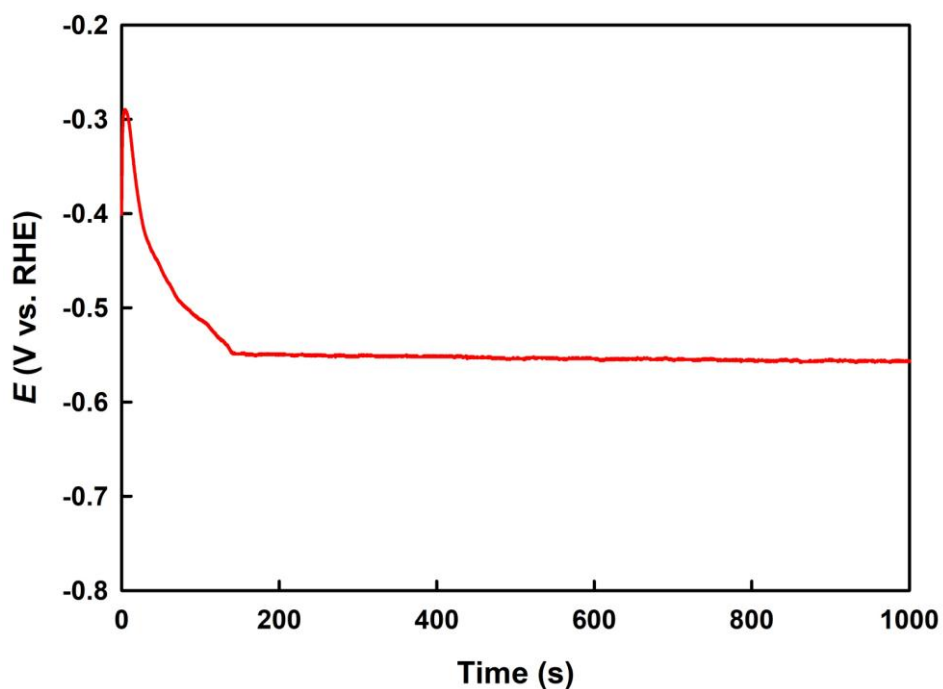


**Figure 5.4** (A) XRD spectrum of the differently formed Cu electrodes, (i) Cu thin film, (ii), OD-Cu thin film, (iii) Cu particles, (iv) Cu NPs, (v) Cu nanodendrites; XPS spectrum at  $\text{Cu}2p$  region of copper oxides, prior to electrochemical reduction, (B); and Cu nanodendrites, following electrochemical reduction (C).

**Table 5.1** Different crystallite size of Cu and Cu<sub>2</sub>O of the formed Cu samples.

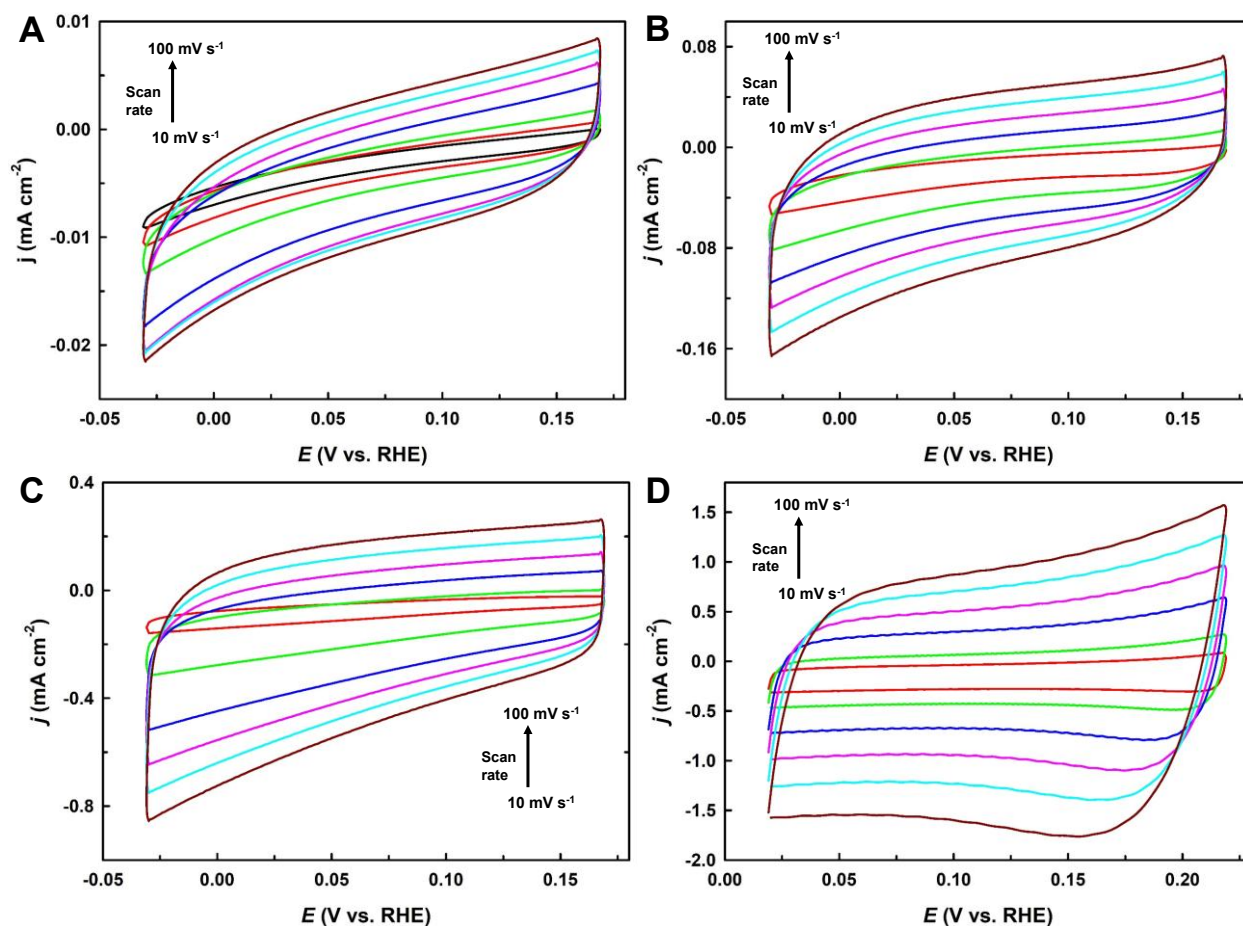
Electrode	Cu (111) nm	Cu (200) nm	Cu (220) nm
Cu thin film	54.18	68.17	56.13
OD-Cu thin film	47.18	45.46	93.62
Cu particles	54.20	45.46	46.81
Cu NPs	33.05	45.42	46.18
Cu nanodendrites	27.51	27.27	15.60

CO<sub>2</sub>-saturated 0.1 M NaHCO<sub>3</sub> on the formed copper oxide film. Following an initial time period stabilization occurred at a certain potential, as shown in Figure 5.5, which verified that the formed oxides were reduced to Cu to form the Cu nanodendrites. Figure 5.4C presents the corresponding high-resolution Cu<sub>2</sub>p XPS spectra. Prior to the EC treatment, three Cu<sub>2</sub>p peaks

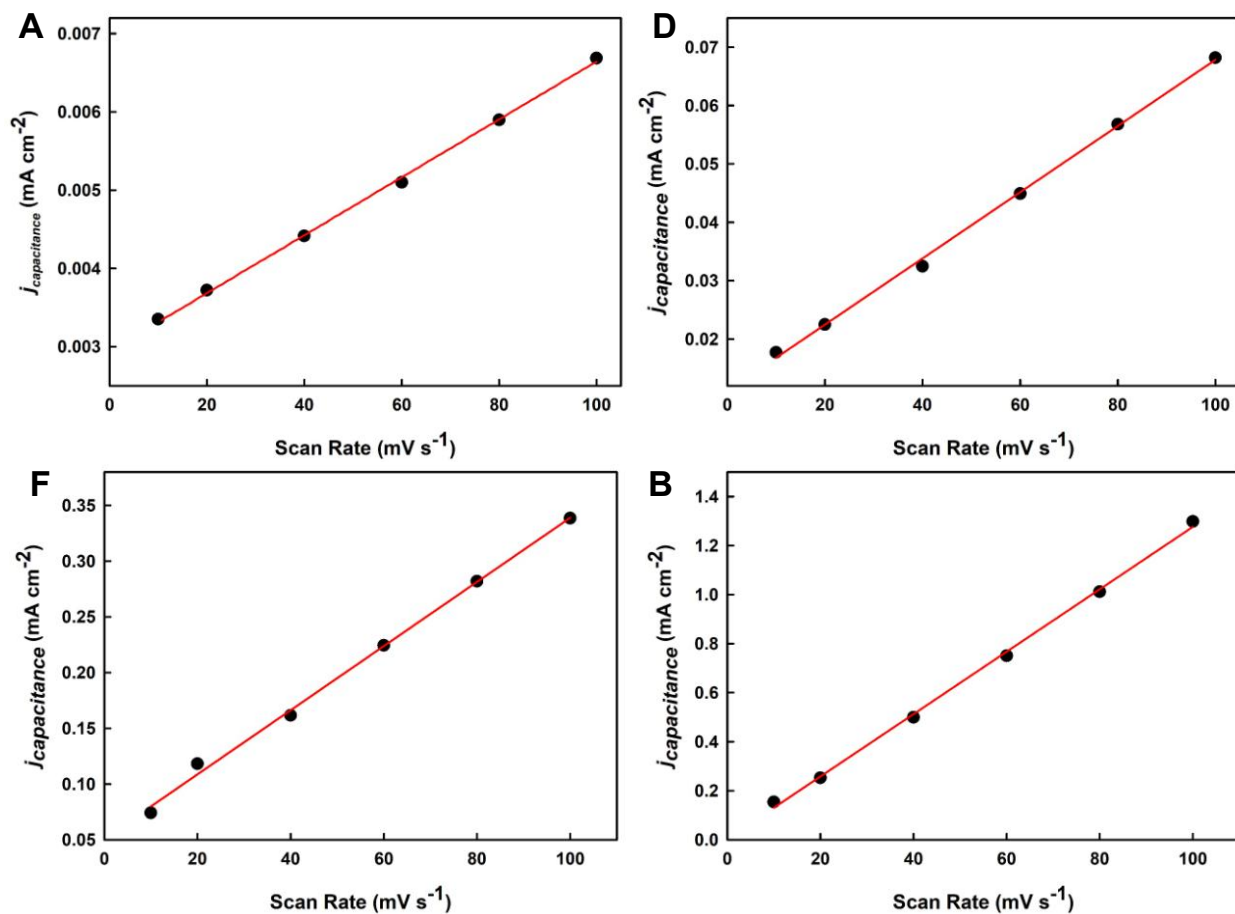


**Figure 5.5** Reduction of copper oxides to form the Cu nanodendrites applying  $-10 \text{ mA cm}^{-2}$  current density for 1800 s in a CO<sub>2</sub>-saturated 0.1 M NaHCO<sub>3</sub> solution.

centered at 934.48, 936.04, and two Cu<sup>2+</sup> satellites peaks at 941.48, 944.35 eV were obtained, as shown in Figure 5.4B, which might be attributed to the formation of the different types of copper oxides, while annealing the Cu thin film with the treating agent. A strong Cu(0) or Cu(I) peak centered at 932.58 eV was observed to be associated with two Cu(II) oxide peaks, subsequent to electrochemical reduction (Figure 5.4C), with the resulting oxides likely being formed via



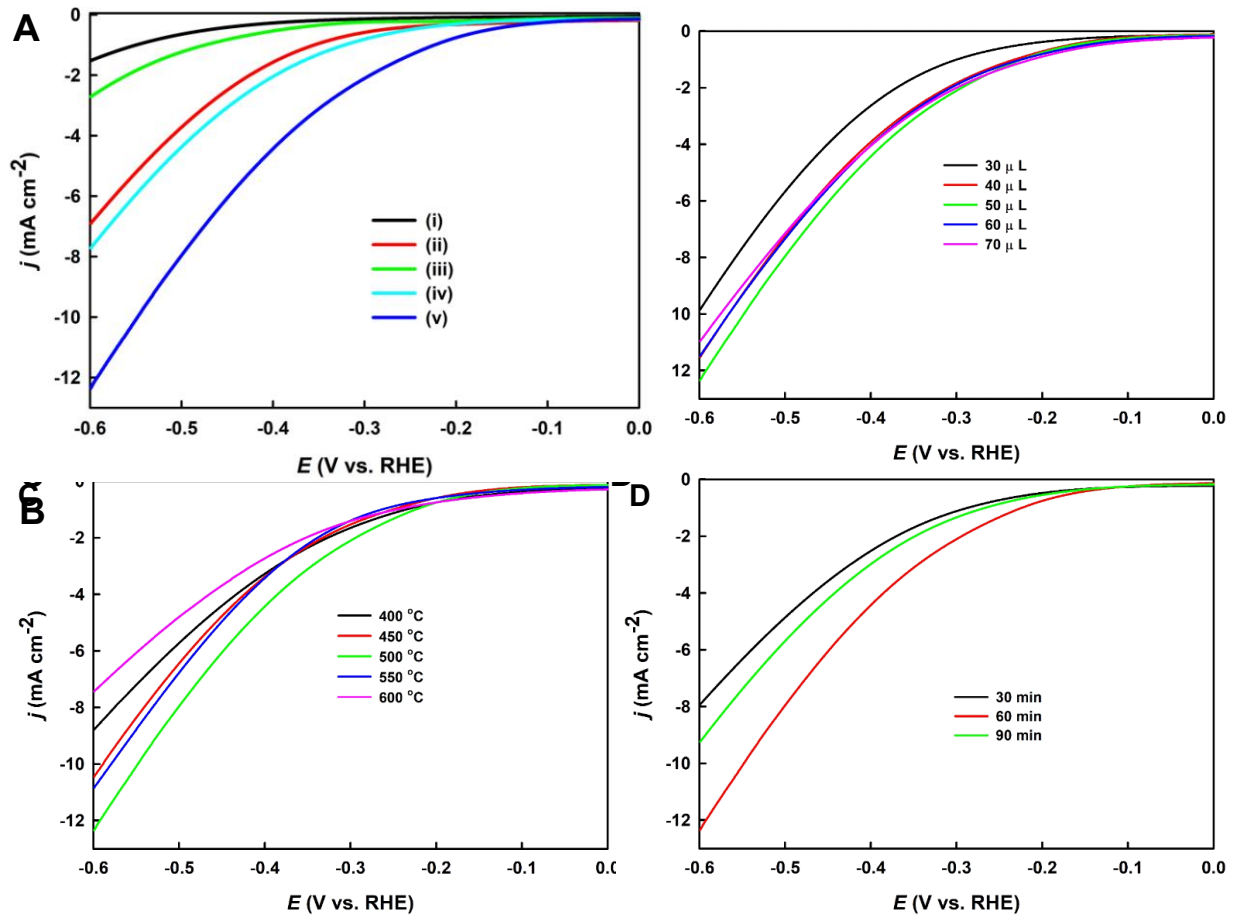
**Figure 5.6** Electrochemical surface area measurement; determination of double-layer capacitance by cyclic voltammograms over a range of scan rates for (A) Cu plate, (B) Cu thin film, (C) OD-Cu thin film, and (D) Cu nanodendrites in 0.1 M HClO<sub>4</sub> solution.



**Figure 5.7** Corresponding current due to double-layer charging/discharging plotted against cyclic voltammetry's scan rate of Figure 5.6; (A) Cu plate, (B) Cu thin film, (C) OD-Cu thin film, and (D) Cu nanodendrites.

**Table 5.2** Determination of capacitance values and surface roughness factors of the different nanostructured Cu electrodes using CV. The surface roughness factor for Cu plate is defined to be 1.

Electrode	Capacitance (cm <sup>-2</sup> )	Surface roughness factor
Cu plate	0.037 $\mu$ F	1
Cu thin film	0.56 mF	15
OD-Cu thin film	2.88 mF	78
Cu nanodendrites	12.34 mF	355



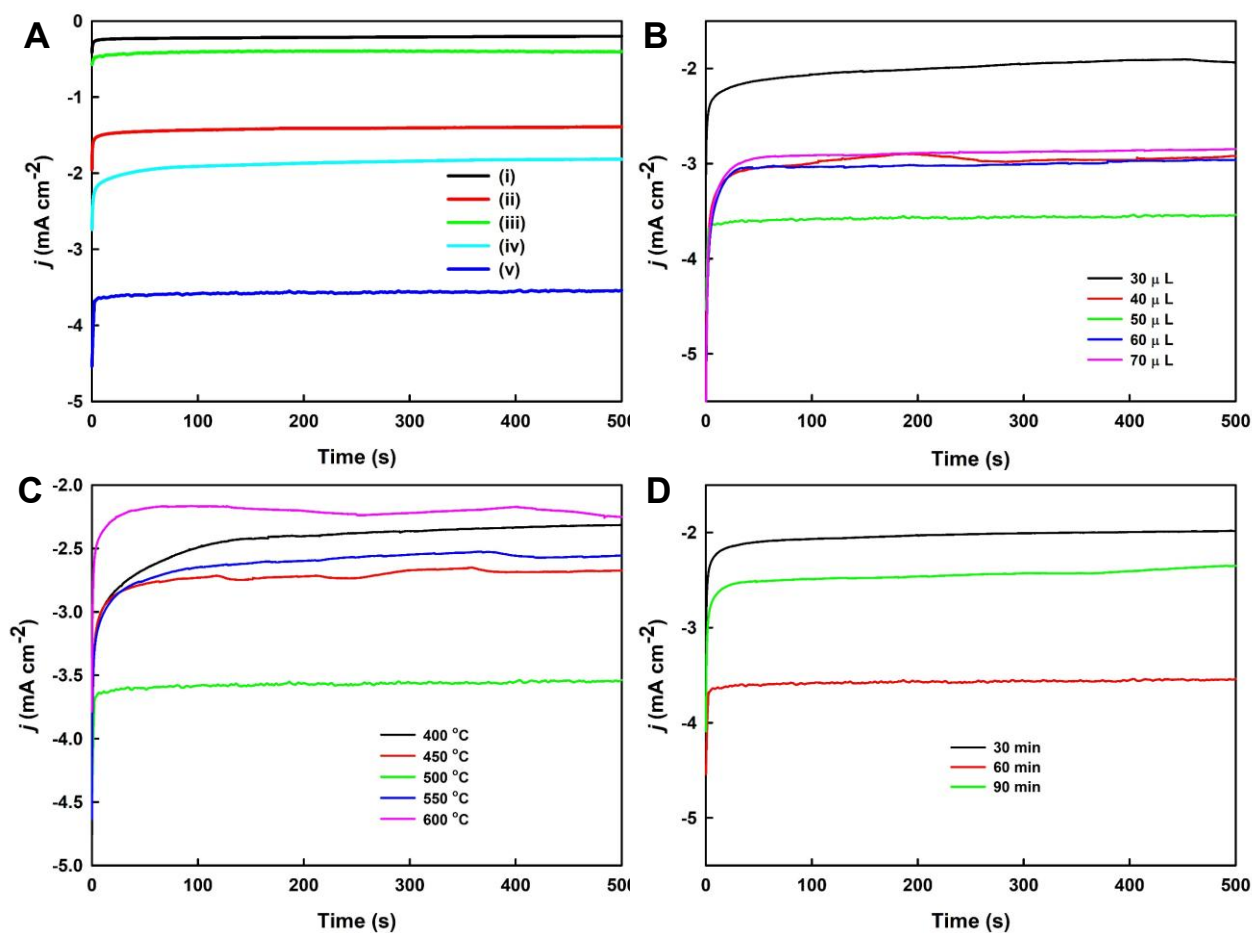
**Figure 5.8** LSV recorded on different nanostructured Cu, (A) Cu thin film (i), OD-Cu thin film (ii), Cu particles (iii), Cu NPs (iv), Cu nanodendrites (v); (B) Different Cu nanodendrites electrodes changing the volume of the mixture of the treating agent during calcination at 500 °C for 1 h; (C) Changing the calcination temperature where the volume of the treating agents was 50  $\mu\text{L}$  on etch electrode during 1 hour calcination; (D) Changing the calcination time where the volume of the mixture of the treating agents was 50  $\mu\text{L}$  on etch electrode during calcination at 500 °C; in a  $\text{CO}_2$ -saturated 0.1 M  $\text{NaHCO}_3$  solution.

exposure to ambient air during the preparation of the XPS sample. The EASA of the formed Cu thin film, OD-Cu thin film, and Cu nanodendrite electrodes was determined relative to the

polycrystalline Cu foil, by estimating their double layer capacitance in the 0.1 M HClO<sub>4</sub> solution [27]. The corresponding CV plots and the geometrical current densities against the scan rate are shown in Figures 5.6 and 5.7. It was observed that the current densities of all the CVs for the Cu nanodendrites at different scan rates achieved the highest values among the studied electrodes. A straight double layer capacitance line was obtained by the same electrode as seen in Figure 5.7D. The double layer capacitance and electrochemical roughness factors of the different electrodes are listed in Table 5.2, which revealed that the Cu nanodendrite electrode achieved the highest capacitance value over all of the other electrodes. It exhibited a roughness factor of 355 relative to the polycrystalline Cu foil as 1, whereas the Cu thin film and OD-Cu thin film electrodes had roughness factors of 15 and 78, respectively, which revealed that the formed Cu nanodendrites possessed an extensive surface area.

### 5.3.2 Electrochemical characterization

The electrocatalytic activity of the different synthesized Cu electrodes was initially investigated by employing LSV and CA techniques in a CO<sub>2</sub>-saturated 0.1 M NaHCO<sub>3</sub> (pH 6.65) solution. Figure 5.8A presents the LSV curves of the Cu-thin film, OD-Cu thin film, and other oxide-derived nanostructured Cu at a scan rate of 20 mV s<sup>-1</sup>. The Cu nanodendrites demonstrated the highest current densities and an earlier onset potential, in contrast to the other electrodes. For instance, the cathodic current of the Cu nanodendrites was measured to be 12.35 mA cm<sup>-2</sup>, which was much higher than that of the uncalcined Cu thin film (~8 times), Cu particles (~4.5 times), OD-Cu thin film (almost double), and Cu NPs (~1.6 times). The steady-state current density of these electrodes was measured at -0.4 V and the CA curves were compared (Figure 5.9A), which showed that the Cu nanodendrites attained the highest current densities. Both LSV and CA studies revealed the superior electrocatalytic activity of the Cu nanodendrites in comparison to



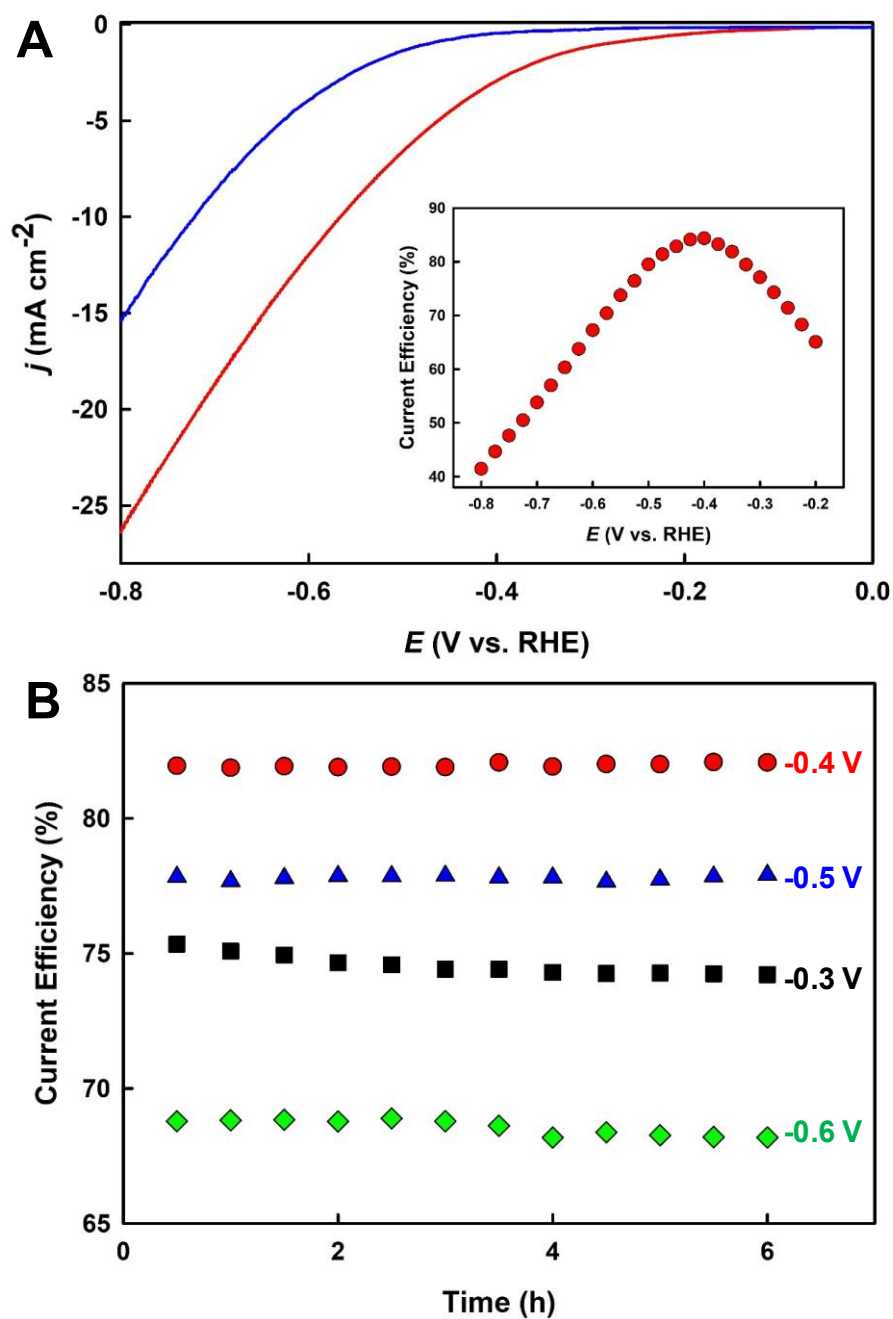
**Figure 5.9** CA recorded at  $-0.4$  V on different nanostructured Cu, (A) Cu thin film (i), OD-Cu thin film (ii), Cu particles (iii), Cu NPs (iv), Cu nanodendrites (v); (B) Different Cu nanodendrites electrodes changing the volume of the mixture of the treating agent during calcination at  $500$  °C for 1 h; (C) Changing the calcination temperature where the volume of the treating agents was  $50$   $\mu$ L on etch electrode during 1 hour calcination; (D) Changing the calcination time where the volume of the mixture of the treating agents was  $50$   $\mu$ L on etch electrode during calcination at  $500$  °C; in a  $\text{CO}_2$ -saturated  $0.1$  M  $\text{NaHCO}_3$  solution.

the other formed Cu electrodes, which indicated that the formed Cu nanodendrites might serve as efficient electrocatalysts for the reduction of  $\text{CO}_2$ . In order to obtain the best electrocatalytically

active electrode using the treating agent mixture, various electrodes were synthesized and studied by optimizing the conditions in terms of the volume of the mixture of the treating agents, calcination temperature, and annealing duration. Initially, the different volumes of the treating agent mixtures deposited on the Cu thin film during calcination at 500 °C for 1 h, was altered from 30 to 70  $\mu\text{L}$ , which revealed that when 50  $\mu\text{L}$  was deposited, comparatively higher current densities could be obtained in both the LSV and CA plots (Figures 5.8B and 5.9B, respectively). The calcination temperature was further varied from 400 to 600 °C for 1 h following the deposition of 50  $\mu\text{L}$  of the treating agents. It was observed that 500 °C was the optimal calcination temperature toward forming a highly active electrode that achieved the highest current densities in the LSV and CA plots, as shown in Figures 5.8C and 5.9C, respectively. Moreover, the calcination duration was also modified from 30 to 90 min., using 50  $\mu\text{L}$  of the treating agents at 500 °C. As can be seen in both the LSV and CA plots of Figures 5.8D and 5.9C, respectively, the highest activity was observed after 60 min.. All of the above studies confirmed that the optimal electrocatalytically active electrode was formed with the deposition of 50  $\mu\text{L}$  of the treating agents on the Cu thin film, which underwent calcination at 500 °C for 1h.

To observe the electrocatalytic performance of the optimized electrode toward the reduction of  $\text{CO}_2$ , a LSV was recorded in a  $\text{CO}_2$ -saturated 0.1 M  $\text{NaHCO}_3$  (pH 6.65) solution, where  $\text{CO}_2$  was continuously purged into the electrolyte during the experiment. A further LSV was measured in an Ar-saturated 0.05 M  $\text{Na}_2\text{SO}_4$  solution (a small volume of 0.01 M  $\text{H}_2\text{SO}_4$  was added to adjust the pH (6.65)), where Ar was continuously purged into the electrolyte throughout the measurement. Figure 5.10A compares these LSVs, revealing that the current density achieved in the  $\text{CO}_2$ -saturated 0.1 M  $\text{NaHCO}_3$  solution (red curve) was much higher than the Ar-saturated 0.1 M  $\text{Na}_2\text{SO}_4$  solution (blue curve), which indicated that the Cu nanodendrites





**Figure 5.10** (A) LSV recorded on Cu nanodendrites in an Ar-saturated 0.05 M Na<sub>2</sub>SO<sub>4</sub> solution (blue curve), and in a CO<sub>2</sub>-saturated 0.1 M NaHCO<sub>3</sub> solution (red curve); the inset presents the corresponding instant current efficiency; and (B) Steady-state current efficiency (%) for CO<sub>2</sub> reduction at different applied potentials.

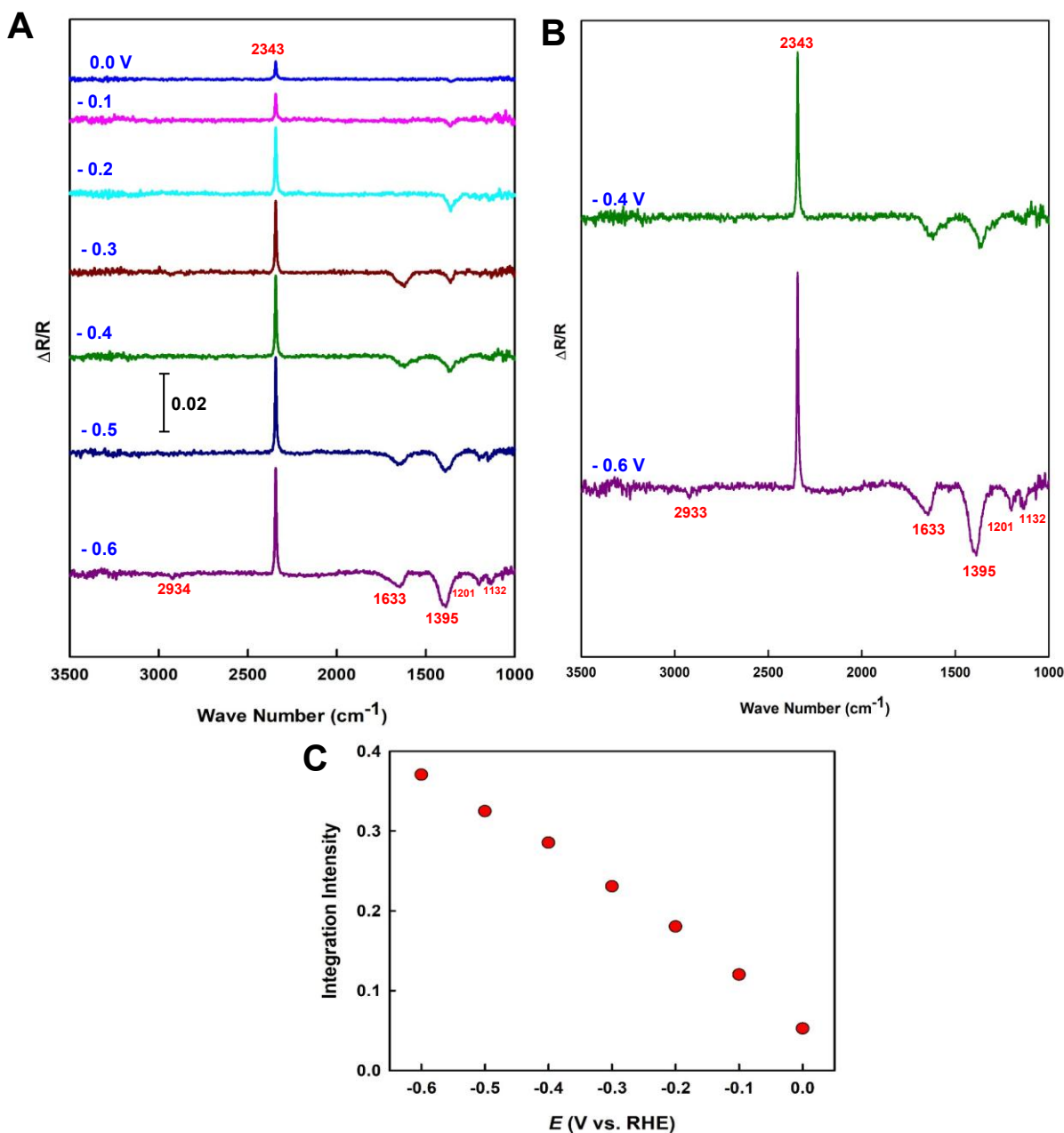
possessed high catalytic performance toward the reduction  $\text{CO}_2$ . The inset of Figure 5.10A shows the corresponding instant current efficiency (ICE) (%) for  $\text{CO}_2$  reduction at different potentials, which was calculated from the LSVs using the following equation [42]:

$$\text{ICE (\%)} = (j_C - j_A) \times 100 / j_C \quad (1)$$

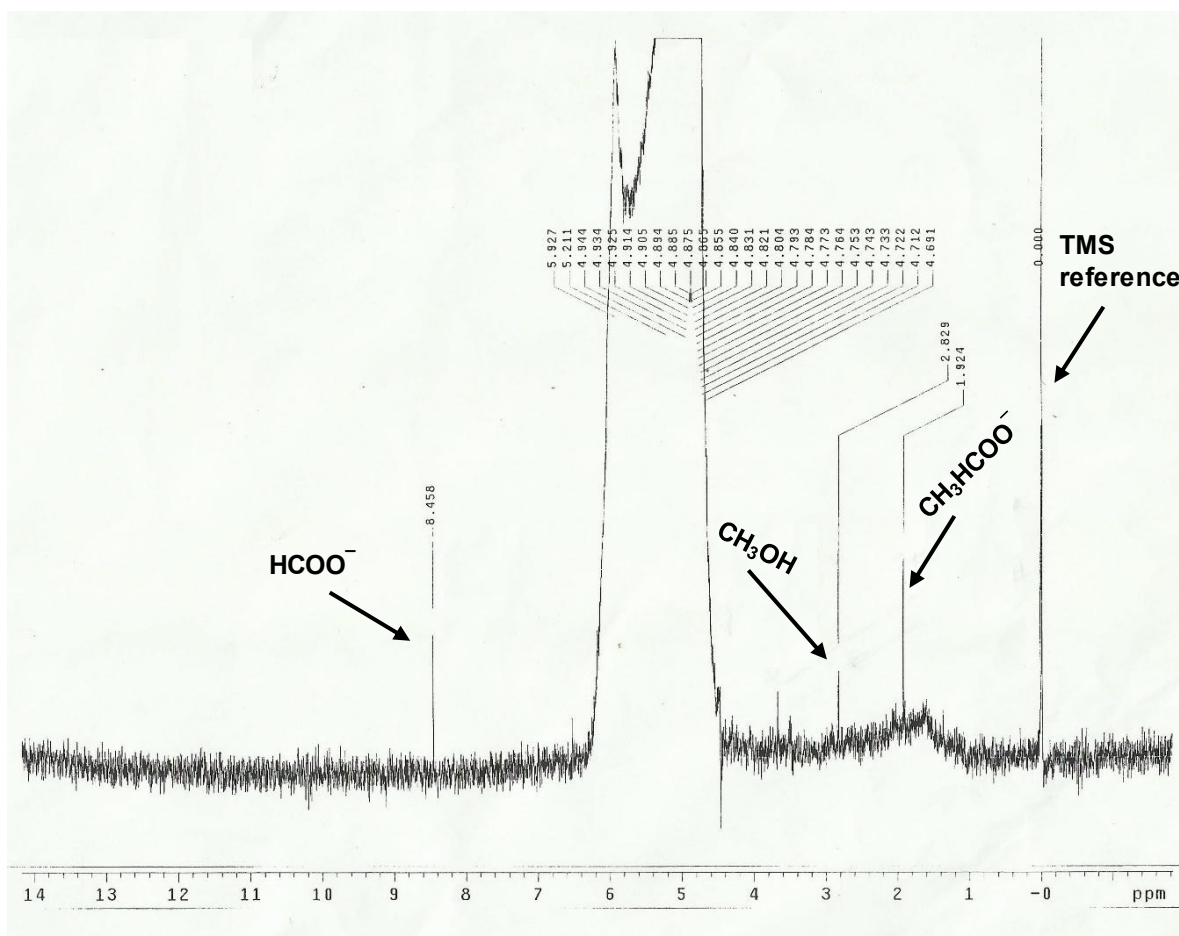
where  $j_C$  is the current density obtained in the  $\text{CO}_2$ -saturated 0.1 M  $\text{NaHCO}_3$  solution; and  $j_A$  is the current density measured in the Ar-saturated 0.05 M  $\text{Na}_2\text{SO}_4$  solution. The ICE was gradually increased with a higher cathodic potential, from -0.25 to -0.4 V; however, it was continuously decreased with further increases in the cathodic potential. The highest ICE obtained was 84.3% at -0.4 V, which might be the optimal cathodic potential for the bulk analysis of  $\text{CO}_2$  reduction using the Cu nanodendrites. The steady-state current efficiency (SSCE) for the reduction of  $\text{CO}_2$  was further determined by employing CAs at an applied potential of from between -0.3 and -0.6 V over 6 h of electrolysis. The CAs were recorded in both the  $\text{CO}_2$ -saturated 0.1 M  $\text{NaHCO}_3$  and the Ar-saturated 0.05 M  $\text{Na}_2\text{SO}_4$  (the pH of this electrolyte was adjusted to 6.65) solutions, where  $\text{CO}_2$  and Ar were continuously purged throughout the analysis, respectively. Figure 5.10B presents the steady state current efficiency (SSCE) (%), which was calculated using Eq. (1). The overall SSCE was stable at all applied potentials, which was increased from 75.2% to 82% when increasing the cathodic potential from -0.3 to -0.4 V; however, it was decreased to 77.8% and 68.5% with a further increase of the cathodic potential to -0.5 V and -0.6 V, respectively, which was similar to the ICE results (inset, Figure 5.10A). All of the above studies characterized the formed Cu nanodendrites as a promising catalyst for the electrochemical reduction of  $\text{CO}_2$ , which might overcome the boundaries that currently constrain the large scale reduction of  $\text{CO}_2$ , while increasing overall Faradaic efficiencies.

### 5.3.3 In situ electrochemical ATR-FTIR study

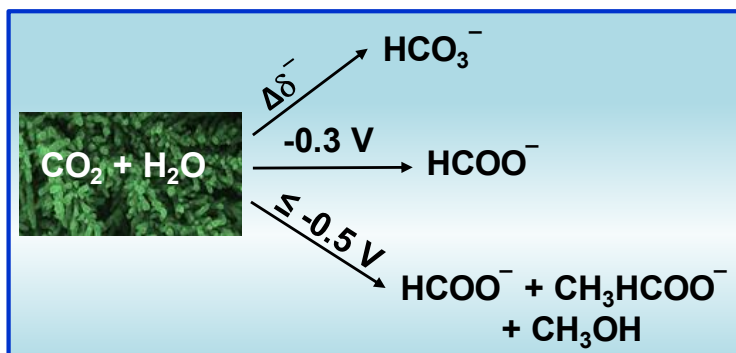
In situ ATR-FTIR spectroscopy was employed to detect surface-adsorbed intermediates and determine the level of CO<sub>2</sub> consumption on the electrode surface during the electrochemical reduction of CO<sub>2</sub> on the formed Cu nanodendrite surface in CO<sub>2</sub>-saturated 0.1 M NaHCO<sub>3</sub> solutions [31,43]. Figure 5.11A displays a series of spectra as a function of potential at 0.1 V intervals each, where CO<sub>2</sub> was continuously purged into the solution, and fresh CO<sub>2</sub>-saturated solution was supplied to the electrode surface in a Teflon chamber prior to performing analyses at each applied potential. To obtain each interferogram, 32 scans were added and averaged, and the reference spectra were recorded at +0.2 V (vs. RHE). As seen in Figure 5.11A, a positive band appeared, centered at 2343 cm<sup>-1</sup>, at all of the applied potentials due to the solvated CO<sub>2</sub> in the NaHCO<sub>3</sub> solution, and the intensity of the peaks increased with higher cathodic potentials [42]. As the centers of the peaks did not shift with the increase of cathodic potential, this indicated that the behavior of the solvated CO<sub>2</sub> in the bicarbonate solution was identical across different electrode potentials on the formed Cu nanodendrite surface. The consumption of CO<sub>2</sub> was determined during electrolysis at different potentials on the Cu nanodendrite electrode surface (Figure 5.11C). The CO<sub>2</sub> consumption rate increased with higher cathodic potentials, indicating that larger quantities of solvated CO<sub>2</sub> were involved in the reaction during the reduction at higher potentials, as an increased rate of reactions occurred at higher cathodic potentials. A small negative peak appeared, centered at 1395 cm<sup>-1</sup> at 0.0 V, could be ascribed to the formation of HCO<sub>3</sub><sup>-</sup> ions (Figure 5.11A), which resulted from the interaction between solvated CO<sub>2</sub> and H<sub>2</sub>O [42,44,45]. The intensity of HCO<sub>3</sub><sup>-</sup> ions was increased with higher cathodic potential, indicating that additional HCO<sub>3</sub><sup>-</sup> was formed at higher cathodic potentials. A new downward peak centered at ~1633 cm<sup>-1</sup> was formed at -0.3 V, which was also observed at more negative potentials and could thus be assigned to the asymmetric O-C=O stretching mode



**Figure 5.11** (A) In situ ATR-FTIR for the electrochemical reduction of CO<sub>2</sub> on Cu nanodendrites in a CO<sub>2</sub>-saturated 0.1 NaHCO<sub>3</sub> solution under different applied potentials (vs. RHE), (B) At -0.4 and -0.6 V (vs. RHE); (C) Integration area of CO<sub>2</sub> absorption at these potentials. The reference spectra were obtained at +0.2 V (vs. RHE) where all of the spectra were collected with 32 co-added scans.



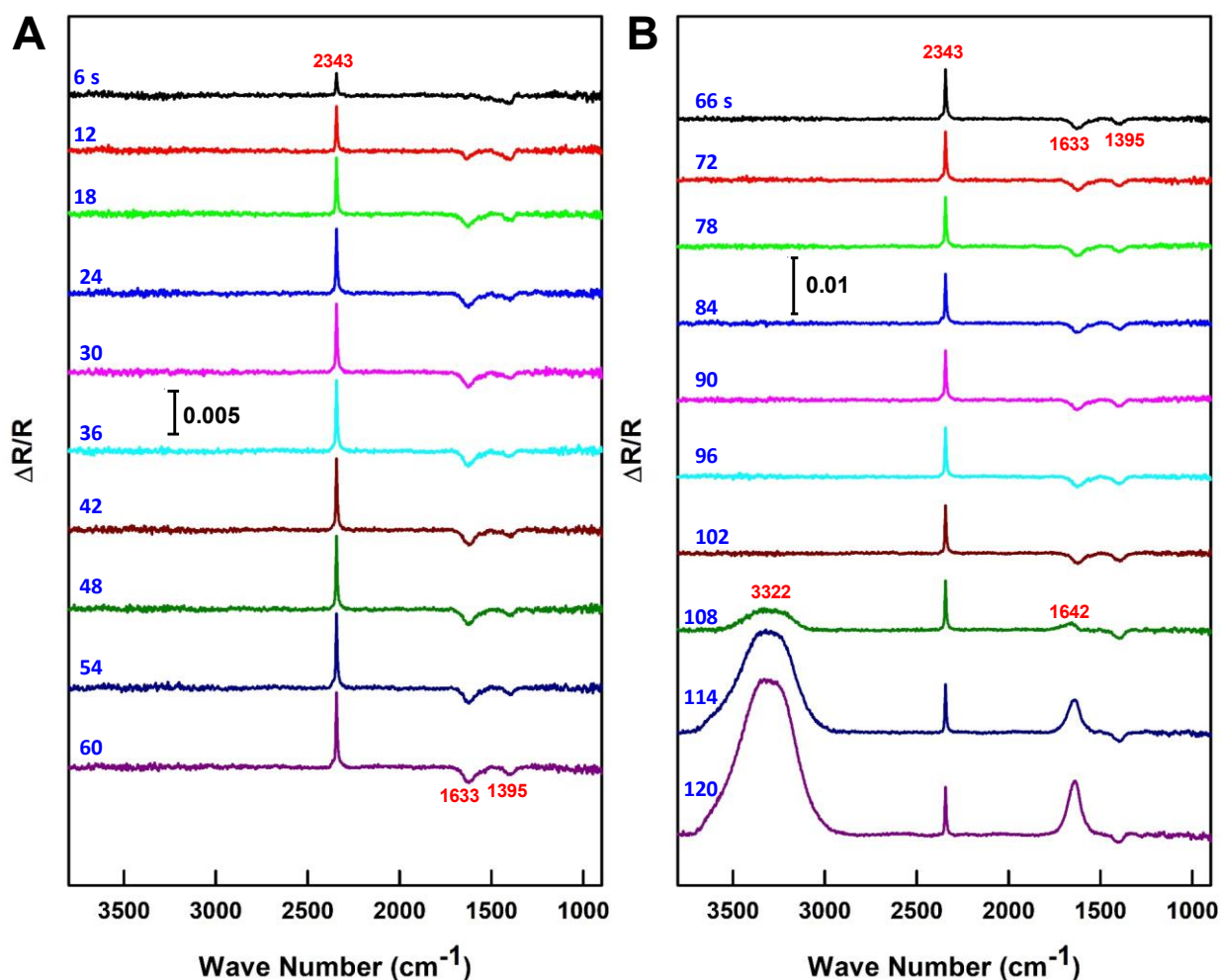
**Figure 5.12**  $^1\text{H}$  NMR spectra of the formed products from the electrochemical reduction of  $\text{CO}_2$  at  $-0.6$  V (vs. RHE) for 2 h on Cu nanodendrites catalysts. TMS is used as the reference.



**Scheme 5.2** Schematic representation of  $\text{CO}_2$  reduction product formation under different applied potentials on the formed Cu nanodendrites.

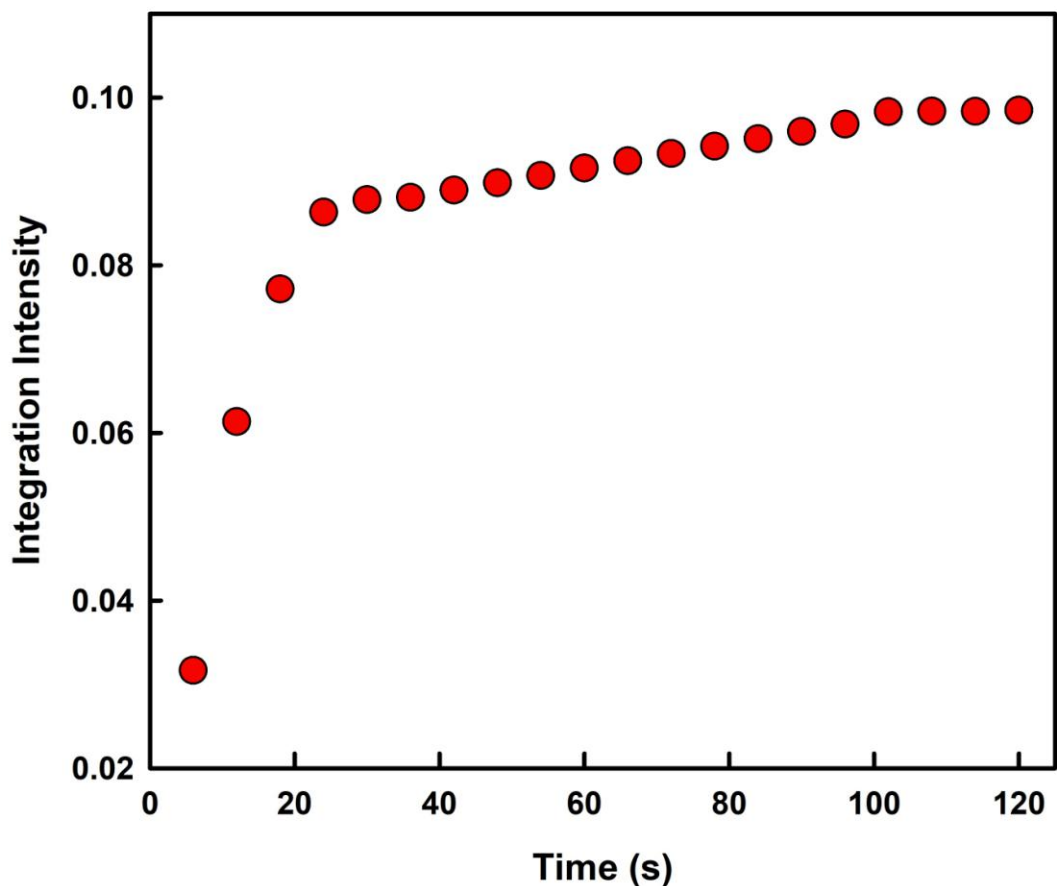
from  $\text{HCOO}^-$  ions, as shown in Figure 5.11A [44]. Two further small negative peaks at  $\sim 1201$  and  $\sim 1132 \text{ cm}^{-1}$  appeared at  $-0.5 \text{ V}$ , which might be attributed to the bending of  $\text{C}=\text{O}$  and  $\text{C}=\text{C}$  bonds, which were obtained during the electrochemical reduction of  $\text{CO}_2$  on Cu nanodendrites (Figure 5.11A) [46]. Moreover, a tiny peak down at  $2933 \text{ cm}^{-1}$  was observed at  $-0.6 \text{ V}$ , which might be the asymmetric stretching of the bonds between C and H of the formed hydrocarbons (Figure 5.11B) [46,47]. To identify the formed liquid products,  $^1\text{H}$  NMR was further recorded using  $\text{CO}_2$  electrolysis at  $-0.6 \text{ V}$  for 2 h. Figure 5.12 displays the one-dimensional  $^1\text{H}$  NMR spectrum, which showed the peaks of  $\text{HCOO}^-$ ,  $\text{CH}_3\text{COO}^-$ , and  $\text{CH}_3\text{OH}$ , which confirmed the formation of oxygenates on Cu nanodendrites at an applied potential of  $-0.6 \text{ V}$ . A corresponding reaction scheme was developed on the basis of both in situ FTIR and NMR results, which illustrated that the formation of products at different potentials such as formate, were generated at  $-0.3 \text{ V}$ , whereas other oxygenates began to form at  $-0.5 \text{ V}$  with formate (Scheme 5.2). The formation of  $\text{HCO}_3^-$  ions was observed at  $0.0 \text{ V}$  under higher cathodic potentials, which might have been due to interactions between solvated  $\text{CO}_2$  and  $\text{H}_2\text{O}$  molecules, where applied cathodic potentials could enhance the formation of  $\text{HCO}_3^-$  ions due to the affinity of  $\text{CO}_2$  molecules for the negative cathode. Hence, the results discussed above indicated that hydrocarbons and oxygenates might be formed at higher cathodic potentials, resulting in the reduction of  $\text{CO}_2$ .

Furthermore, the effects of time were investigated to observe the adsorption of  $\text{CO}_2$  and to change of the electroreducible species on the electrode surface during electrocatalysis at  $-0.4 \text{ V}$ , where 8 scans were added and averaged to obtain the interferograms (Figure 5.13). As the Cu nanodendrites had a high FE of  $\text{CO}_2$  electroreduction at  $-0.4 \text{ V}$ , with both ICE and SSEC,  $-0.4 \text{ V}$  was selected to further study the effects of time in a  $\text{CO}_2$  saturated  $0.1 \text{ M NaHCO}_3$  solution. A



**Figure 5.13** Time-resolved ATR-FTIR spectra of CO<sub>2</sub> electroreduction on Cu nanodendrites at -0.4 V (vs. RHE). (A) 6 to 60 s; (B) 66 to 120 s. The reference spectra were obtained at +0.2 V (vs. RHE), and all of the spectra were collected with 8 co-added scans.

sharp upward peak centered at  $\sim 2343\text{ cm}^{-1}$  appeared, and was assigned to CO<sub>2</sub>, and a HCO<sub>3</sub><sup>-</sup> peak at  $1395\text{ cm}^{-1}$  appeared on each spectrum. Following 6 s of reduction, a negative peak was observed and centered at  $1633\text{ cm}^{-1}$ , which was ascribed as being an asymmetric O-C=O stretching mode of HCOO<sup>-</sup> ions and observed to an electrolysis time of 102 s [44]. A small broad negative peak centered at  $\sim 1642\text{ cm}^{-1}$ , and a broad peak at  $\sim 3322\text{ cm}^{-1}$  were observed at



**Figure 5.14** Integration area of CO<sub>2</sub> adsorption from the figure (5.13A and 5.13B) during the electrolysis CO<sub>2</sub> on the formed Cu nanodendrites electrode surface at -0.4 V (vs. RHE).

108 s. This was assigned as being a H<sub>2</sub>O molecule associated with the formed HCOO<sup>-</sup> and the HO<sup>-</sup> bond stretching of H<sub>2</sub>O, which indicated that the Cu nanodendrite thin film consumed all of the solvated CO<sub>2</sub> that was resident on its surface. Subsequently, it began to reduce H<sub>2</sub>O due to the lack of CO<sub>2</sub> on the electrode surface, as the working electrode was in contact with ZnSe hemisphere [44,46]. Figure 5.14 shows the corresponding integration area of the CO<sub>2</sub> consumption rate, which sharply increased to 24 s, slowly rose to 102 s, and was finally stabilized thereafter. The consumption rate indicated that the Cu nanodendrite thin film quickly



absorbed CO<sub>2</sub> at the onset of electrolysis, whereas over time the CO<sub>2</sub> electrolysis continued to 102 s, with the formation of products extracting solvated CO<sub>2</sub> slowly from the electrode surface. Upon further continuing the analysis after 102 s, the consumption rate became constant, which indicated that all of the solvated CO<sub>2</sub> was converted to products, where the CO<sub>2</sub> was practically depleted on the electrode surface; hence, it began to reduce H<sub>2</sub>O molecules.

## 5.4 Conclusions

We demonstrated a facile and novel approach for the synthesis of nanodendrite structured oxide-derived Cu that exhibited enhanced catalytic activity for the electrochemical reduction of CO<sub>2</sub>. In our attempt, Cu NPs were thermally treated with the different modifying agents. Unique Cu nanodendritic structures were obtained when a mixture of a CuSO<sub>4</sub> and H<sub>2</sub>SO<sub>4</sub> solution was used during thermal treatment. The formed Cu nanodendrites exhibited the superior electrocatalytic activity for the reduction of CO<sub>2</sub> in a CO<sub>2</sub>-saturated 0.1 M NaHCO<sub>3</sub> solution. The effects of potential were studied for the electrochemical reduction of CO<sub>2</sub> on Cu nanodendrites, by employing LSV and CA techniques, which revealed that -0.4 V was the optimal electrode potential that achieved 84.3% ICE and 82% SSCE. In situ ATR-FTIR was then employed to further study the consumption of CO<sub>2</sub> and the formation of different electroreducible species during the electrocatalysis of CO<sub>2</sub> on the formed Cu nanodendrite surface, which indicated that hydrocarbons and oxygenates were formed under higher cathodic potentials. The novel approach of synthesising uniquely structured Cu nanodendrites, as well as their enhanced catalytic performance and high FE make these Cu nanodendrites promising electrocatalysts for the efficient conversion of CO<sub>2</sub> to usable chemicals. Moreover, it is hoped that this study might inspire researchers to study the role of different acids to synthesize various nanostructured electrocatalysts for the robust reduction of CO<sub>2</sub>.

## References

- [1] M. Liu, Y. Pang, B. Zhang, P. D. Luna, O. Voznyy, J. Xu, X. Zheng, C. T. Dinh, F. Fan, C. Cao, F. P. G. de Arquer, T. S. Safaei, A. Mephram, A. Klinkova, E. Kumacheva, T. Filleter, D. Sinton, S. O. Kelley, E. H. Sargent, *Nature* **2016**, 537, 382.
- [2] J. S. Gao, X. Jiao, Z. Sun, W. Zhang, Y. Sun, C. Wang, Q. Hu, X. Zu, F. Yang, S. Yang, L. Liang, J. Wu, Y. Xie, *Angew. Chem. Int. Ed.* **2016**, 55, 698.
- [3] Y. Hori, K. Kikuchi, S. Suzuki, *Chem. Lett.* **1985**, 14, 1695.
- [4] Y. Hori, In *Modern Aspects of Electrochemistry*, C. G. Vayenas, R. E. White, M. E. Gamboa-Aldeco, Eds., Springer: New York, **2008**, 42, 89.
- [5] Y. Chen, M. W. Kanan, *J. Am. Chem. Soc.* **2012**, 134, 1986.
- [6] T. Zhang, H. Zhong, Y. Qiu, X. Li, H. Zhang, *J. Mater. Chem. A* **2016**, 4, 16670.
- [7] M. N. Hossain, J. Wen, A. Chen, *Sci. Rep.* **2017**, 7, 3184.
- [8] H. Mistry, A. S. Varela, C. S. Bonifacio, I. Zegkinoglou, I. Sinev, Y.-W. Choi, K. Kisslinger, E. A. Stach, J. C. Yang, P. Strasser, B. R. Cuenya, *Nat. Commun.* **2016**, 7, 12123.
- [9] Y. Liu, S. Chen, X. Quan, H. Yu, *J. Am. Chem. Soc.* **2015**, 137, 11631.
- [10] C. W. Li, M. W. Kanan, *J. Am. Chem. Soc.* **2012**, 134, 7231.
- [11] G. A. Olah, G. K. S. Prakash, A. Goepfert, *J. Am. Chem. Soc.* **2011**, 133, 12881.
- [12] T. R. Cook, D. K. Dogutan, S. Y. Reece, Y. Surendranath, T. S. Teets, D. G. Nocera, *Chem. Rev.* **2010**, 110, 6474.
- [13] D. Raciti, K. J. Livi, C. Wang, *Nano Lett.* **2015**, 15, 6829.
- [14] T. T. H. Hoang, S. Ma, J. I. Gold, P. J. A. Kenis, A. A. Gewirth, *ACS Catal.* **2017**, 7, 3313.
- [15] G. Keerthiga, B. Viswanathan, R. Chetty, *Catal. Today* **2015**, 245, 68.
- [16] R. Reske, M. Duca, M. Oezaslan, K. J. P. Schouten, M. T. M. Koper, P. Strasser, *J. Phys. Chem. Lett.* **2013**, 4, 2410.
- [17] K. Manthiram, B. J. Beberwyck, A. P. Alivisatos, *J. Am. Chem. Soc.* **2014**, 136, 13319.

- [18] J.-F. Xie, Y.-X. Huang, W.-W. Li, X.-N. Song, L. Xiong, H.-Q. Yu, *Electrochim. Acta* **2014**, 139, 137.
- [19] S. Sen, D. Liu, G. T. R. Palmore, *ACS Catal.* **2014**, 4, 3091.
- [20] W. Luo, X. Nie, M. J. Janik, A. Asthagiri, *ACS Catal.* **2016**, 6, 219.
- [21] D. Kim, J. Resasco, Y. Yu, A. M. Asiri, P. Yang, *Nat. Commun.* **2014**, 5, 4948.
- [22] P. Hirunsit, *J. Phys. Chem. C*, 2013, 117, 8262.
- [23] R. Reske, H. Mistry, F. Behafarid, B. R. Cuenya, P. Strasser, *J. Am. Chem. Soc.* **2014**, 136, 6978.
- [24] W. J. Durand, A. A. Peterson, F. Studt, F. Abild-Pedersen, J. K. Nørskov, *Surf. Sci.* **2011**, 605, 1354.
- [25] E. Bertheussen, A. Verdaguer-Casadevall, D. Ravasio, J. H. Montoya, D. B. Trimarco, C. Roy, S. Meier, J. Wendland, J. K. Nørskov, I. E. L. Stephens, I. Chorkendorff, *Angew. Chem. Int. Ed.* **2016**, 55, 1450.
- [26] A. Dutta, M. Rahaman, N. C. Luedi, M. Mohos, P. Broekmann, *ACS Catal.* **2016**, 6, 3804.
- [27] C. W. Li, J. Ciston, M. W. Kanan, *Nature* **2014**, 508, 504.
- [28] D. W. Zhang, C. H. Chen, J. Zhang, F. J. Ren, *Mater. Sci.* **2008**, 43, 1492.
- [29] W. K. Han, J. W. Choi, G. H. Hwang, S. J. Hong, J. S. Lee, S. G. Kang, *Appl. Surf. Sci.* **2006**, 252, 2832.
- [30] A. Wuttig, Y. Surendranath, *ACS Catal.* **2015**, 5, 4479.
- [31] J. Heyes, M. Dunwell, B. Xu, *J. Phys. Chem. C* **2016**, 120, 17334.
- [32] A. Wuttig, C. Liu, Q. Peng, M. Yaguchi, C. H. Hendon, K. Motobayashi, S. Ye, M. Osawa, Y. Surendranath, *ACS Cent. Sci.* **2016**, 2, 522.
- [33] K. P. Kuhl, E. R. Cave, D. N. Abram, T. F. Jaramillo, *Energy Environ. Sci.* **2012**, 5, 7050.
- [34] K. J. P. Schouten, Y. Kwon, C. J. M. van der Ham, Z. Qin, M. T. M. Koper, *Chem. Sci.* **2011**, 2, 1902.
- [35] X. Nie, M. R. Esopi, M. J. Janik, A. Asthagiri, *Angew. Chem. Int. Ed.* **2013**, 52, 2459.

- [36] A. A. Peterson, F. Abild-Pedersen, F. Studt, J. Rossmeisl, J. K. Norskov, *Energy Environ. Sci.* **2010**, 3, 1311.
- [37] W. Tang, A. A. Peterson, A. S. Varela, Z. P. Jovanov, L. Bech, W. J. Durand, S. Dahl, J. K. Norskov, I. Chorkendorff, *Phys. Chem. Chem. Phys.* **2012**, 14, 76.
- [38] Y. Hori, O. Koga, H. Yamazaki, T. Matsuo, *Electrochim. Acta* **1995**, 40, 2617.
- [39] M. C. Figueiredo, I. Ledezma-Yanez, M. T. M. Koper, *ACS Catal.* **2016**, 6, 2382.
- [40] A. Verdager-Casadevall, C. W. Li, T. P. Johansson, S. B. Scott, J. T. McKeown, M. Kumar, I. E. L. Stephens, M. W. Kanan, I. Chorkendorf, *J. Am. Chem. Soc.* **2015**, 137, 9808.
- [41] B. D. Adams, R. M. Asmussen, C. K. Ostrom, A. Chen, *J. Phys. Chem. C* **2014**, 118, 29903.
- [42] M. N. Hossain, J. Wen, S. K. Konda, M. Govindhan, A. Chen, *Electrochem. Commun.* **2017**, 82, 16.
- [43] J. Wang, R. M. Asmussen, B. Adams, D. F. Thomas, A. Chen, *Chem. Mater.* **2009**, 21, 1716.
- [44] B. Innocent, D. Pasquier, F. Ropital, F. Hahn, J.-M. Le'ger, K. B. Kokoh, *Applied Catal. B: Environ.* **2010**, 94, 219.
- [45] K. Arihara, F. Kitamura, T. Ohsaka, K. Tokuda, *J. Electroana. Chem.* **2001**, 510, 128.
- [46] B. D. Mistry, *A Handbook of Spectroscopic Data Chemistry (UV, IR, PMR, <sup>13</sup>CNMR and Mass Spectroscopy)*, Edition Oxford Book Company, Jaipur, India, **2009**, 36-44.
- [47] R. Ortiz, O. P. Mfirquez, J. Mfirquez, C. Gutierrez, *J. Electroanal. Chem.* **1995**, 390, 99.

## **Chapter 6: Enhanced catalytic activity of nanoporous Au for the efficient electrochemical reduction of carbon dioxide**

### **6.1 Introduction**

Carbon dioxide (CO<sub>2</sub>) plays a primary role in climate change, where the concentration of CO<sub>2</sub> in the atmosphere has been increasing rapidly since the Industrial Revolution, and has recently reached its highest level (~405 ppm). Since the average global temperature is rising, and the Earth's climate system is being altered as well, scientists are investing great efforts in the identification of strategies to minimize CO<sub>2</sub> emissions [1,2]. However, it would be very helpful, beyond thinking only of ways to reduce or stop CO<sub>2</sub> emissions into the environment, if CO<sub>2</sub> might be transformed into renewable fuels. Among various technologies to convert CO<sub>2</sub>, the electrochemical method is considered a promising pathway to transform CO<sub>2</sub> into valuable chemicals and fuels. The primary target for the electrochemical technology is to develop an efficient electrocatalyst for robust reduction of CO<sub>2</sub> with high selectivity, low overpotential, fast kinetics, high stability and high energy efficiency.

CO<sub>2</sub> is recognized as an inert molecule, fully oxidized and thermodynamically stable, which represents significant challenges toward its chemical transformation to useful carbon based products [3-5]. It is therefore essential to develop an efficient technology that may convert CO<sub>2</sub> into valuable chemicals via a cost-effective process, while achieving high efficiency. It has been reported that the electrochemical reduction of CO<sub>2</sub> can produce hydrocarbons, aldehyde and alcohols [6-14]. Considerable efforts have been invested in deciphering the fundamental kinetics of the electrochemical reduction of CO<sub>2</sub>, both experimentally and theoretically [8-12]. Researchers have identified a wide variety of catalysts that have the ability to reduce CO<sub>2</sub> in

aqueous electrolytes [9,13,14]. In particular, Au is known as a promising catalyst that exhibits high activity and selectivity to form CO from the electrochemical reduction of CO<sub>2</sub> [15]. CO constitutes an important industrial chemical that may be converted to various synfuels and valuable chemicals using the Fischer–Tropsch process [16,17]. Different classes of Au electrodes have been reported for the electrochemical reduction of CO<sub>2</sub>, including nanoparticles [15], nanowires [18], nanoneedles [1], porous film [19], and other gold based nanomaterials [20,21], revealing that nanostructured Au electrodes can impart much higher catalytic activity compared to polycrystalline Au electrodes [22,23]. This may be attributed to large electrochemically active surface areas (EASAs) and different crystal facets [12,14,24]. Experimental results have also shown that the structures and morphologies of these nanocatalysts play a significant role in the enhancement of catalytic activity, for instance, lowering the overpotential, improving the Faradaic efficiency (FE), and accelerating the reaction rate for the electrochemical reduction of CO<sub>2</sub> [8-12,25]. However, current CO<sub>2</sub> electroreduction technologies are still quite distant from industrial applicability, due to high overpotential, low selectivity, and slow reduction rates. Therefore, further efforts are required to elucidate fundamental kinetics, and to tailor high-performance electrocatalysts for CO<sub>2</sub> conversion. In the present study, we demonstrated that acid-treated nanoporous Au possessed an extensive EASA, excellent electrocatalytic activity, high selectivity, low overpotential, and fast kinetics for the efficient conversion of CO<sub>2</sub> to CO.

## **6.2 Experimental section**

### **6.2.1 Chemicals and materials**

Gold microwire (127 μm in diameter, 99.99%), ZnCl<sub>2</sub> (≥98.0%), H<sub>2</sub>SO<sub>4</sub> (99.99%), and NaHCO<sub>3</sub> (≥99.0%) were obtained from Sigma Aldrich; Zn foil (99.98%, 0.25 mm thick) was purchased from Alfa Aesar; Ethylene glycol (Analytic grade) and ultrapure carbon dioxide

(99.999%) were purchased from ACP Chemical Inc. and Praxair, respectively. All chemicals were used directly as received. All of the solutions were prepared using double-distilled water (purified by a Nanopure Diamond water purification system, 18.2 M $\Omega$  cm).

### **6.2.2 Fabrication of nanoporous Au electrodes**

To prepare an Au microelectrode, a 10 cm long copper wire was passed into an 8.0 cm glass tube that had its end dipped into a conductive gold paste (Heraeus Inc., USA), which acted as conductive adhesive. Subsequently, a 5.0 or 8.0 mm long gold microwire was carefully passed through the glass tube until the microwire was gently attached to the copper wire. An epoxy resin was employed to wrap the top and end of the glass tube. The prepared electrode was subsequently introduced into an oven at 60 °C for 90 min., followed by being held vertically in ambient air to cool.

The NP Au was fabricated via an electrochemical alloying/dealloying method, which was based on a three-electrode system, where the Au microelectrode, Zn foil, and Zn wire served as the working electrode, counter electrode, and reference electrode, respectively. The alloying/dealloying of the Au microelectrode was carried out in a mixture of ethylene glycol and 1.5 M ZnCl<sub>2</sub> via cyclic voltammetry in the potential range between -0.80 and +1.80 V (vs. Zn) at a scan rate of 10 mV s<sup>-1</sup> for 20 cycles at 110 °C. To form the Au/Zn alloy, the last CV cycle was scanned from -0.8 and stopped at 0.0 V; whereas the last cycle was stopped at +1.8 V (vs. Zn) to obtain the NP Au electrode. The fabricated NP Au was further treated using the procedure as follows: the NP Au was soaked in concentrated H<sub>2</sub>SO<sub>4</sub> for 30 min, dried in an oven at 60 °C for 2 h, and calcinated at 150 °C in a furnace for 1 h. After cooling down, the electrode was thoroughly washed using pure water; and the obtained electrode was denoted as the acid treated NP Au.

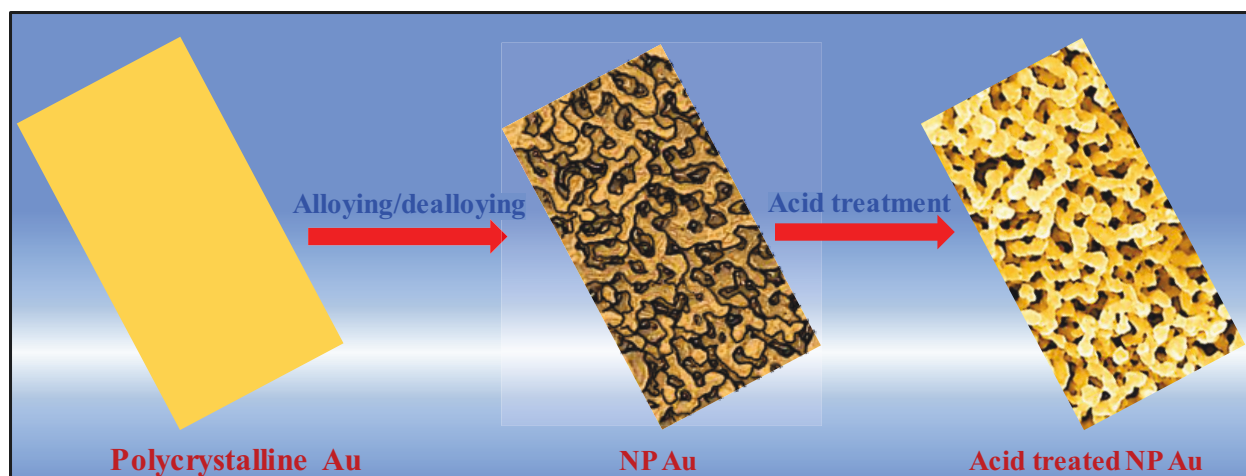
### 6.2.3 Structural characterization

The surface morphology and EDX analysis of the prepared samples were investigated by a field emission scanning electron microscope (FE-SEM, Hitachi SU-70) at 20 kV. X-ray diffraction (XRD) patterns were collected using a Phillips PW 1050-3710 with Cu  $\alpha$  1 of 1.5406 Å (radiation source) to determine the structural characteristic of the prepared Au electrodes. Data was obtained in the range from 10° to 90° of 2 $\theta$  with a step width of 0.01° /2 $\theta$ . XRD data analysis was performed using X'Pert High Score Plus software. X-ray photoelectron spectroscopy (XPS) spectra were recorded via a Thermo Fisher XPS system, where the size of the X-ray spot was 400 mm, with an Al K $\alpha$  monochromatic source. All of the XPS data was processed using XPSPEAK 4.1 software.

### 6.2.4 Electrochemical characterization

A CHI660E electrochemical workstation (CH Instrument Inc. USA) was employed to carry out Linear Sweep Voltammetry (LSV) and chronoamperometry (CA) utilizing a three-electrode cell system. Electrochemical Impedance Spectroscopic (EIS) measurements were performed using a VoltaLab potentiostat (PGZ-301), where the frequency was varied from 100 kHz to 40 mHz with an A.C. voltage amplitude of 10 mV. Z-view software was used to fit the data and to obtain an equivalent circuit for the EIS experimental data. A silver/silver chloride electrode (Ag/AgCl, 3.0 M) and a platinum coil (10 cm<sup>2</sup>) were used as the reference electrode and the counter electrode, respectively. The solution was initially purged with CO<sub>2</sub> for 20 min. in order to achieve a CO<sub>2</sub>-saturated condition, after which it was continuously purged into the solution while performing the analysis. All electrochemical experiments were conducted at ambient room temperature (20 ± 2 °C). All of the electrode potentials cited in the present work





**Figure 6.1** Schematics of the preparation of the NP Au and the acid treated NP Au.

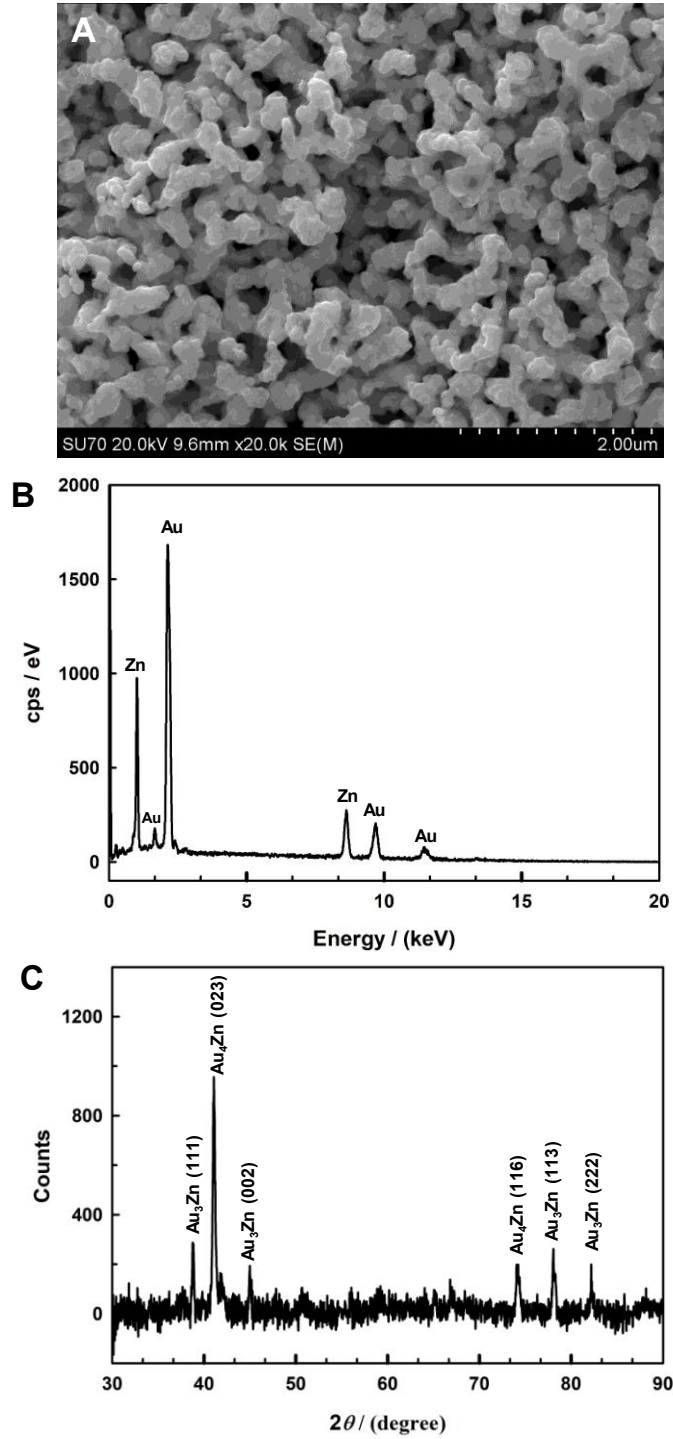
were converted to the reversible hydrogen electrode (RHE) reference scale using the following equation:

$$E(\text{vs. RHE}) = E(\text{vs. Ag/AgCl}) + 0.210 \text{ V} + 0.0591 \text{ V} \times \text{pH}$$

### **6.2.5 Electrochemically active surface area (EASA) measurement and roughness factor (RF) calculation**

To clean the Au, NP Au and acid treated NP Au electrodes and to determine their EASAs, cyclic voltammetry (CV) between 0.0 and +1.5 V (vs. Ag/AgCl) was continuously run in a 0.1 M H<sub>2</sub>SO<sub>4</sub> solution at a scan rate of 20 mV s<sup>-1</sup> until a stable CV curve was obtained. The formation of gold oxide in the forward scan, and subsequently, the reduction of the formed gold oxide in the reverse scan occurred, respectively. The EASA was determined by integrating the reduction peak (centered at ~0.9 V vs. Ag/AgCl) to calculate the charge that was associated with the reduction peak. The ratio between the calculated EASA and the geometrical area of the electrode is known as the roughness factor, and may be calculated using the following formula:

$$\text{RF} = \text{Electrochemical surface area/Geometrical area}$$



**Figure 6.2** (A) SEM image, (B) EDX spectra and (C) XRD patterns of the formed Au/Zn alloy.

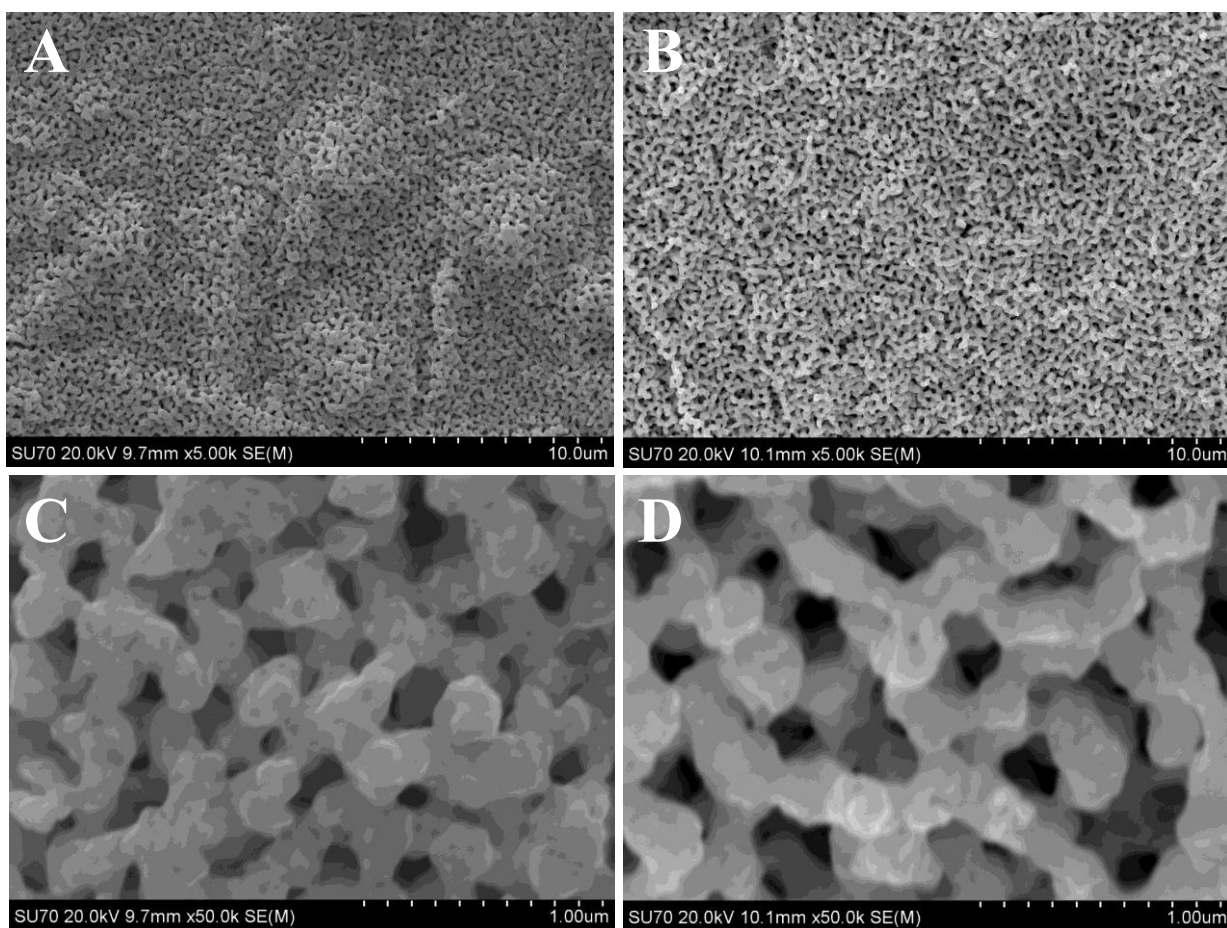
### 6.2.6 Product analysis

A three-compartment electrochemical cell, where the working electrode compartment was gas-tight, and CO<sub>2</sub> was initially purged for 60 min. to obtain the CO<sub>2</sub> saturated solution prior to electrolysis. The CO<sub>2</sub> was continuously purged within a linked working electrode chamber that was employed for the product analysis and stability tests. A cationic exchange membrane (CMI-7000S) was employed as a separator between the working electrode and counter electrode chamber in the cell. The working electrode and reference electrode (Ag/AgCl) were in the same compartment, whereas the counter electrode was in a separate compartment. The generated gas was transferred into the gas chromatography (GC, Shimadzu GC-2014, Column: Silica gel, thermal conductive detector (TCD), the column temperature was raised from 40 to 250 °C at a heating rate of 3 °C min<sup>-1</sup>; the injector temperature was set at 70 °C, with a heating velocity of 25 °C min<sup>-1</sup>; the sampling volume of 50 μL was taken by a gas-tight syringe (Hamilton<sup>TM</sup>, 50 μL) in order to analyze the gas products.

### 6.3 Results and discussion

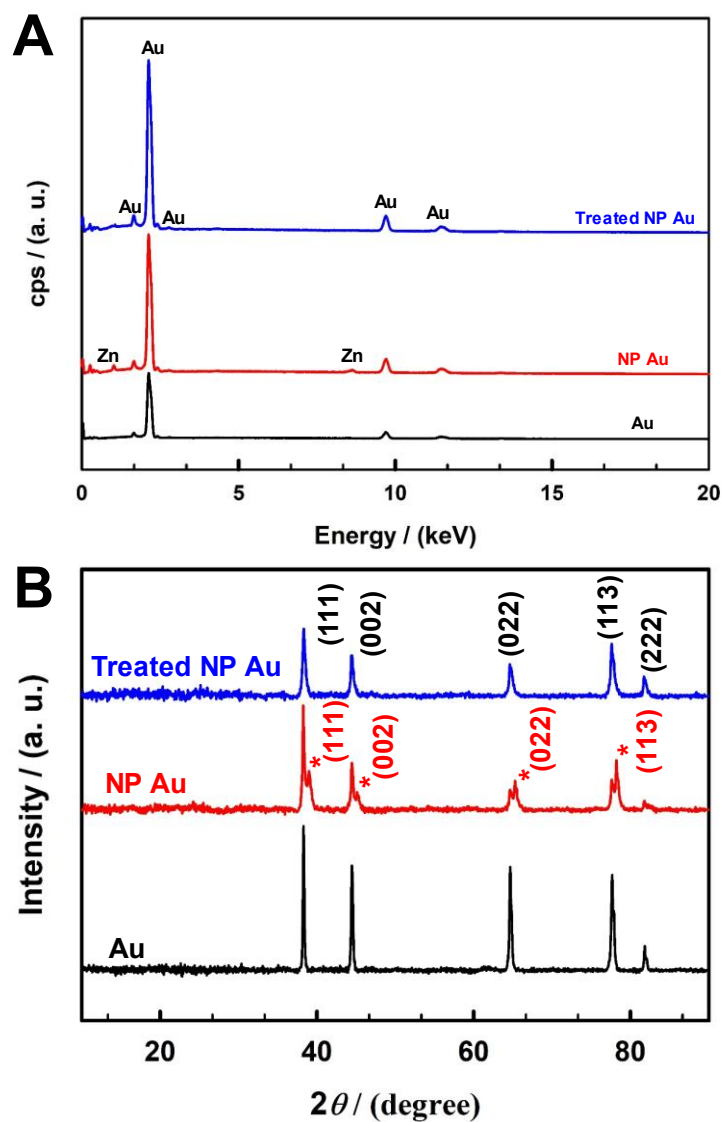
In order to form the nanoporous structure, a polycrystalline Au electrode was electrochemically alloyed and dealloyed in a mixture of ethylene glycol and 1.5 M ZnCl<sub>2</sub> using cyclic voltammetry. The experimental details are described in the experimental section of 6.2.2. Figure 6.1 presents a schematic diagram, illustrating the formation of the NP Au and the further acid treatment of the NP Au electrode. In electrochemical alloying/dealloying process, Zn was first electrodeposited on the gold electrode surface in the cathodic potential scan. In the subsequent anodic potential scan, dealloying of Zn took place, resulting in the formation of a nanostructured gold film. Performing cyclic voltammetry (CV) for 20 cycles, a 3D nanoporous Au was finally produced. Even though controlling the parameters of CV and cycles time, a small

amount residual Zn is present on the NP Au. A 3D nanoporous structure was formed as seen in the scanning electron microscopic (SEM) image (Figure 6.2A). Strong Zn and Au peaks appeared in the energy dispersive X-ray (EDX) spectrum (Figure 6.2B), showing the co-existence of both Au and Zn. Further X-ray diffraction (XRD) characterization (Figure 6.2B) confirmed the formation of  $\text{Au}_3\text{Zn}$  and  $\text{Au}_4\text{Zn}$  alloys [26,27].



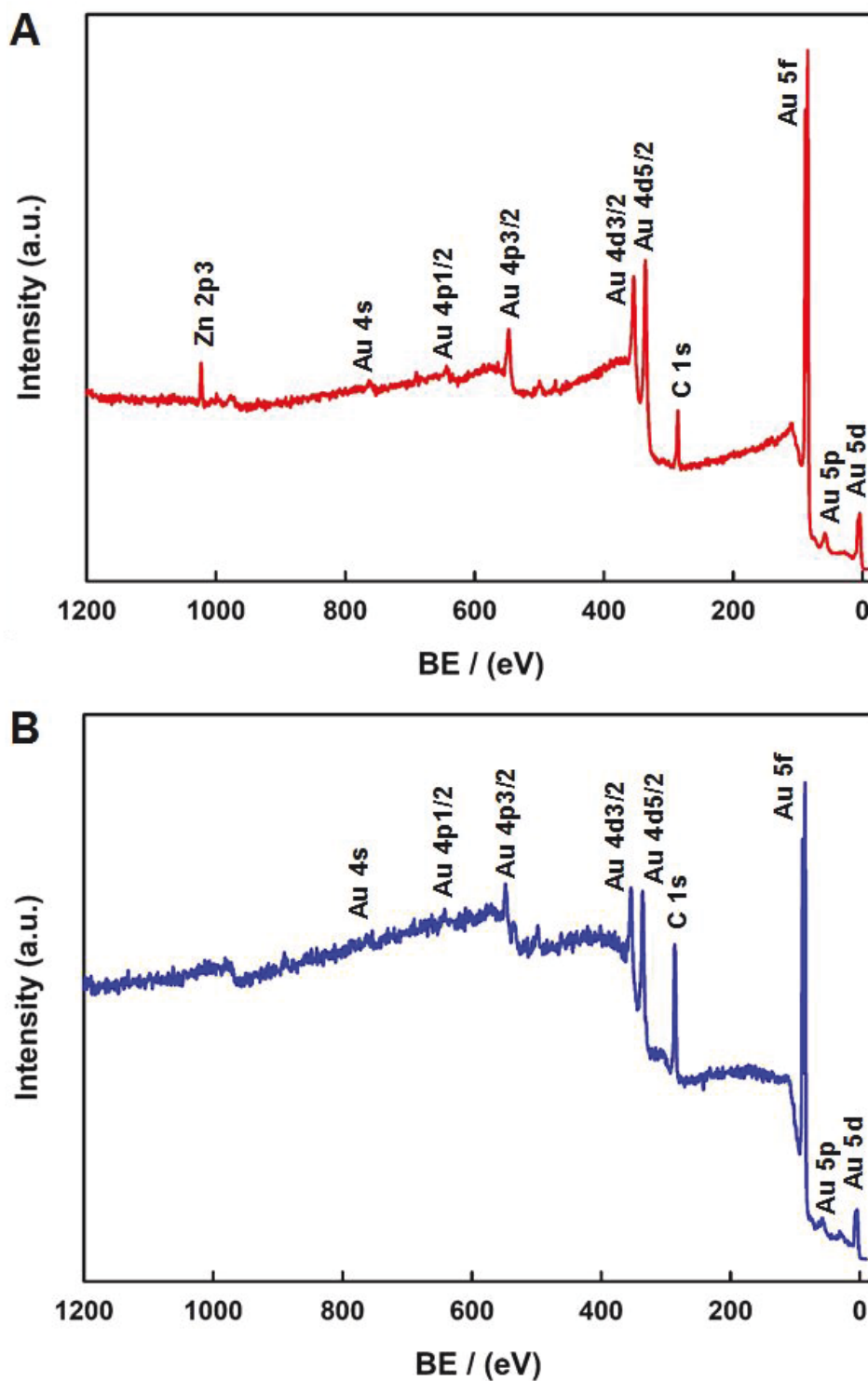
**Figure 6.3** Low-magnification SEM images of (A) the NP Au electrode, and (B) the acid-treated NP Au electrode; High-magnification SEM images of (C) the NP Au electrode and (D) the acid-treated NP Au electrode.

Figure 6.3A depicts a lower magnification SEM image of the formed NP Au, showing that interconnected networks were homogeneously formed on the Au surface. The pore sizes of the formed NP Au were from ~250 - 500 nm in diameter as seen in the higher magnification SEM image (Figure 6.3C). The formed NP Au was further treated with H<sub>2</sub>SO<sub>4</sub> followed by a

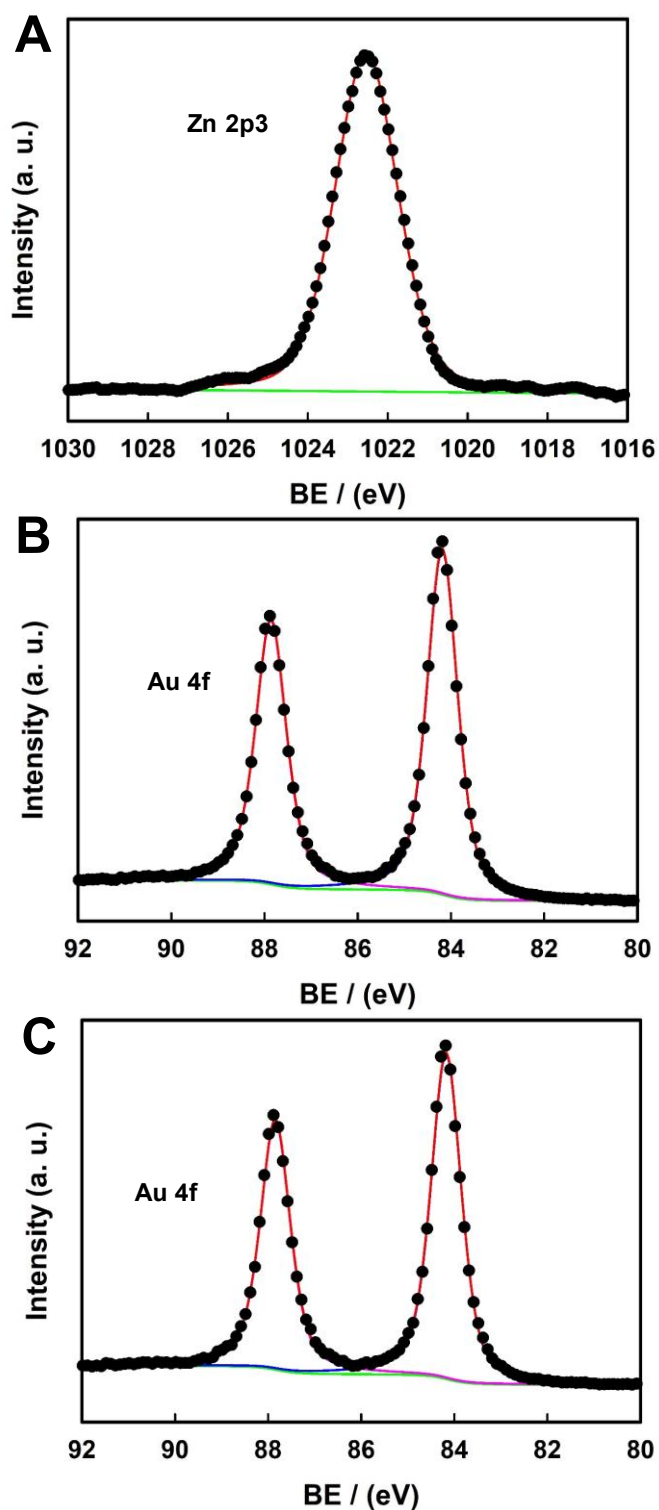


**Figure 6.4** (A) EDX spectra and (B) XRD patterns of the three different Au electrodes.

mild calcination at 150 °C for 1 h, resulting in the formation of larger sized nanopores with diameters ranging from ~750 to 1000 nm, as shown in the SEM images (Figure 6.3B and Figure 6.3D). Figure 6.4A presents the EDX spectra of the Au, NP Au, and treated NP Au electrodes. Two weak Zn peaks were observed in the NP Au, which confirmed that a small amount of Zn still remained during the electrochemical alloying/dealloying fabrication process. However, the incorporated Zn was removed by the acid treatment. The typical face-centered-cubic (fcc) Au diffraction peaks, including (111), (200), (220), (311), and (222) planes (JCPDS no. 01-1172) [26] were observed for all of the Au electrodes. The additional peaks labelled by asterisks were derived from the formed Au/Zn alloy (Figure 6.4B) [27]. It is worth noting that all the Au/Zn alloy diffraction peaks disappeared following the acid treatment, indicating that the incorporated Zn was removed from the NP Au. This was further confirmed via the X-ray photoelectron spectroscopic (XPS) survey scans. A noticeable Zn 2p<sub>3/2</sub> peak appeared at 1022.58 eV in the NP Au (Figure 6.5A), but disappeared after the acid treatment (Figure 6.5B). Further quantitative analysis revealed that the amount of Zn in the NP Au was ~7.0%. The high-resolution Zn 2p<sub>3/2</sub> XPS spectrum is displayed in Figure 6.6A, revealing that its binding energy was slightly higher (1022.58 eV) than that of pure Zn (1022.00 eV) [28]. Figures 6.6B and 6.6C present the high-resolution Au 4f XPS spectra of the NP Au, prior to and following the acid treatment, respectively. The Au 4f<sub>7/2</sub> and 4f<sub>5/2</sub> peaks for the untreated NP Au were observed at 84.19 and 87.86 eV, which shifted toward a lower binding energy of 0.01 and 0.02 eV of the treated NP Au (4f<sub>7/2</sub>, 84.18 eV, and 4f<sub>5/2</sub>, 87.84 eV), respectively. This further confirmed the formation of the Au/Zn alloy in the NP Au and the removal of Zn, subsequent to the acid treatment of the NP Au, which was consistent with the EDX and XRD results.

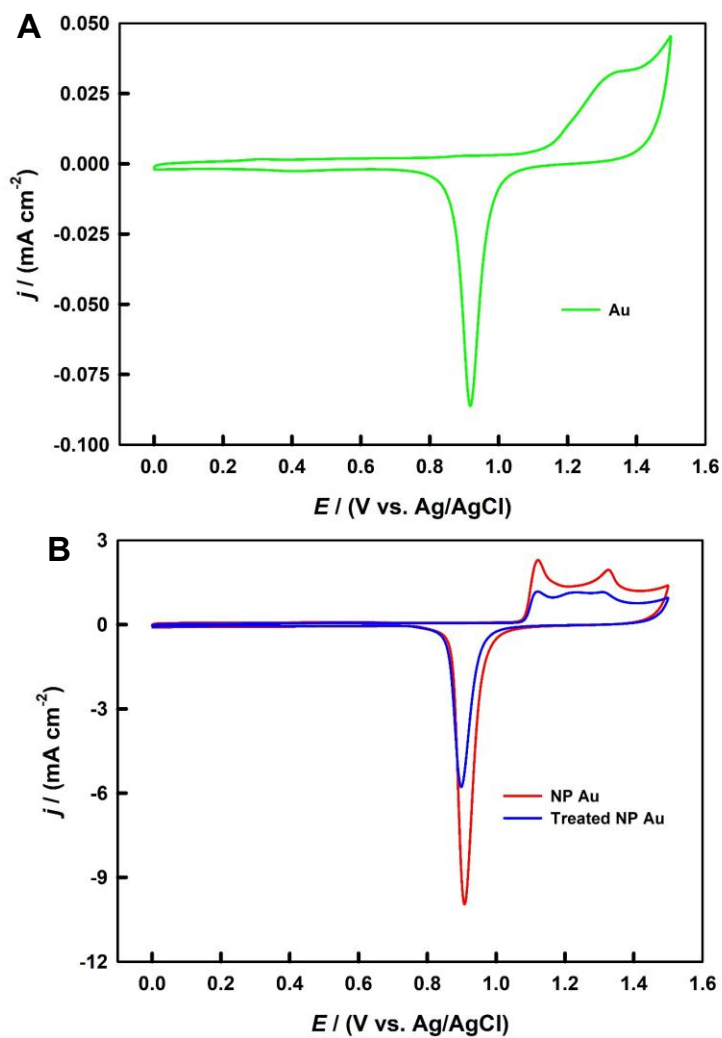


**Figure 6.5** The XPS survey spectra of the NP Au (A) and the acid treated NP Au (B) electrodes.



**Figure 6.6** High-resolution XPS spectra of the Zn 2p<sub>3/2</sub> region of the formed NP Au (A), the Au 4f region of the NP Au, (B) the treated NP Au (C) electrodes.





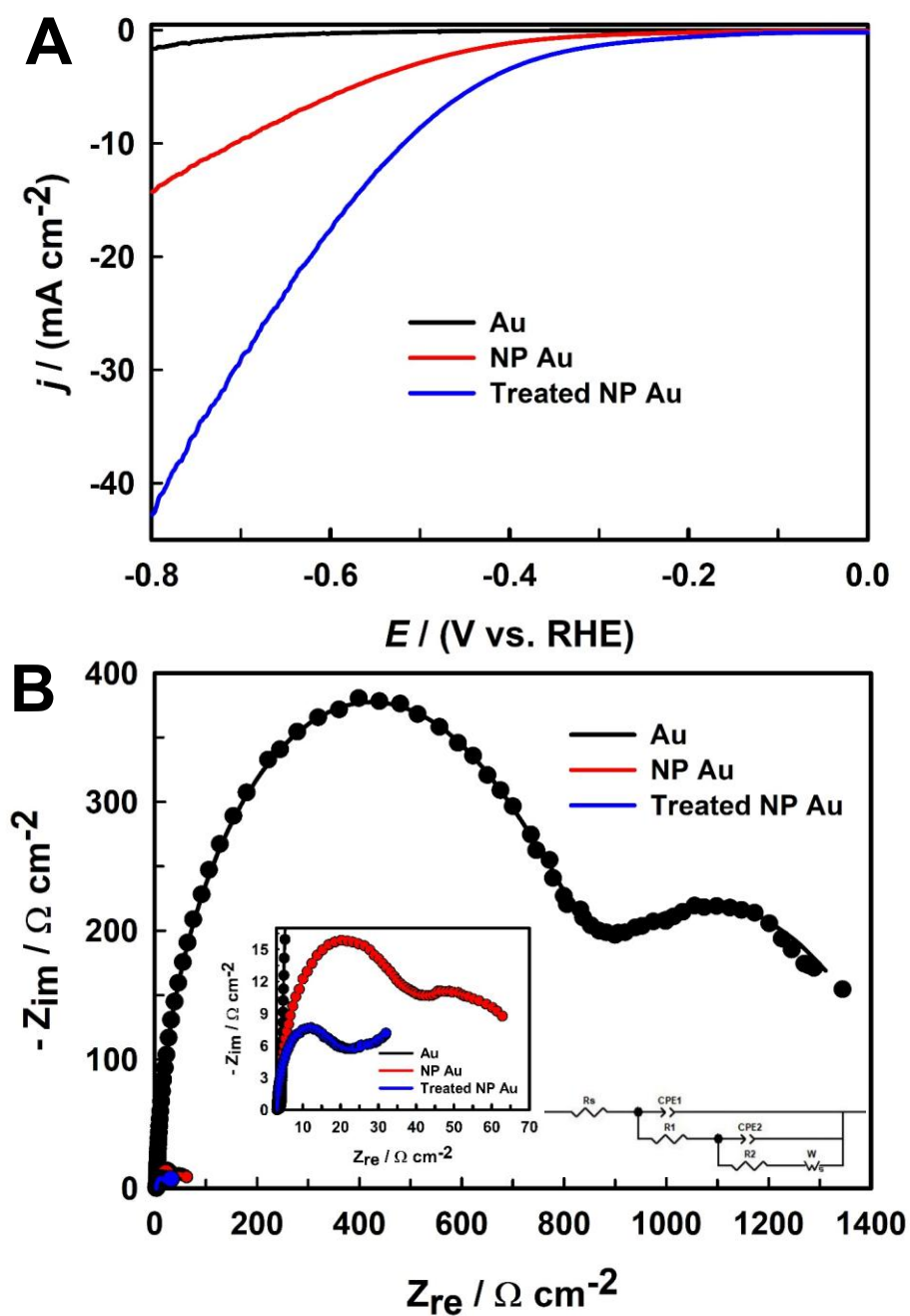
**Figure 6.7** Cyclic voltammograms of: (A) the smooth polycrystalline Au electrode; and (B) the NP Au electrode (red) and the acid treated NP Au electrode (blue). Scan rate:  $20 \text{ mV s}^{-1}$ ; Electrolyte:  $0.1 \text{ M H}_2\text{SO}_4$ .

**Table 6.1** Determination of the EASA of the three different Au electrodes.

Electrode	Geometric area ( $\text{cm}^2$ )	Charge ( $\mu\text{C}$ )	EASA ( $\text{cm}^2$ )	Roughness factor
Au	0.020	7.72	0.021	1.05
NP Au	0.032	990.95	2.54	79.37
Acid treated NP Au	0.032	619.50	1.59	49.68

The EASA of the Au, NP Au, and treated NP Au was estimated by the simultaneous formation and reduction of gold oxide. Figure 6.7 depicts the corresponding CVs of the three Au electrodes, showing that the untreated NP Au possessed the highest current density. The formation of gold oxide started at  $\sim 1.10$  V; one notable anodic peak was observed for the polycrystalline Au electrode; whereas two anodic peaks appeared for the nanoporous Au electrodes, indicating that the surface structure was changed during the alloying/dealloying process [29]. The reduction charge was calculated by integrating the area of the reduction peak centered at  $\sim 0.9$  V vs. Ag/AgCl [30]. As listed in Table 6.1, the smooth Au electrode had a roughness factor (RF) of 1.05; and the formed NP Au possessed the highest EASA ( $2.54 \text{ cm}^2$ ), which was over 79 times higher than its geometric surface area. However, following the acid treatment, the EASA was decreased to  $1.59 \text{ cm}^2$ ; thus the RF was decreased from 79.37 to 49.68, which was consistent with the SEM images displayed in Figure 6.3. After the acid treatment, the pore size was significantly increased due to the dissolution of the Zn species incorporated during the electrochemical alloying/dealloying process.

To study the electrocatalytic activity of the synthesized Au electrodes, linear sweep voltammograms (LSV) were recorded from 0.0 to -0.8 V (vs. RHE) in a  $\text{CO}_2$ -saturated 0.1 M  $\text{NaHCO}_3$  (pH 6.65) solution. Figure 6.8A compares the LSV curves of the Au, NP Au, and the acid treated NP Au electrodes recorded at  $20 \text{ mV s}^{-1}$ . The current density was dramatically increased from the Au to the treated NP Au electrode. For instance, at -0.8 V, the cathodic current of the treated NP Au was  $42.79 \text{ mA cm}^{-2}$ , which was 26 times higher than that of the Au ( $1.62 \text{ mA cm}^{-2}$ ), and three times higher than that of the NP Au ( $14.26 \text{ mA cm}^{-2}$ ), showing that the treated NP Au had superior catalytic activity toward the  $\text{CO}_2$  reduction.



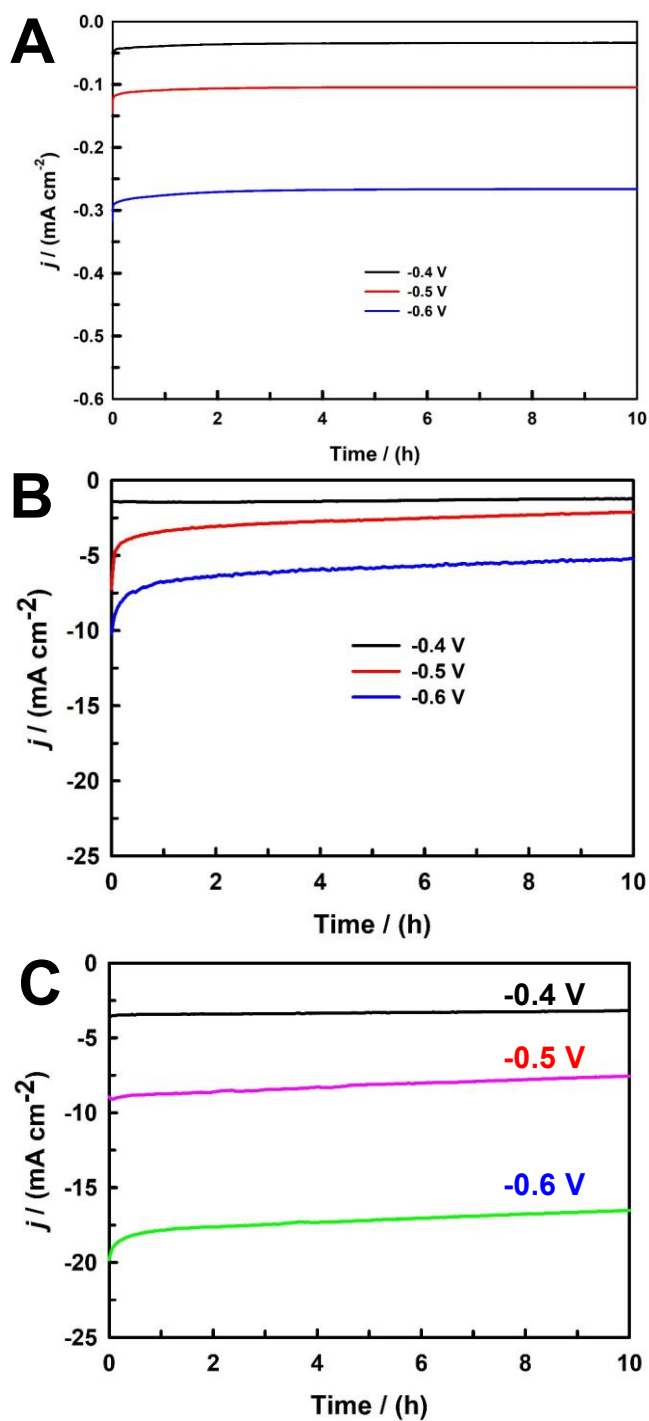
**Figure 6.8** (A) LSVs of the three different Au electrodes recorded in a CO<sub>2</sub>-saturated 0.1 M solution. (B) The corresponding Nyquist plots measured at -0.4 V. Inset: the equivalent electric circuit used for fitting the EIS data, where  $R_s$  = solution resistance;  $R1$  and  $R2$  = charge-transfer resistances;  $CPE1$  and  $CPE2$  = constant phase elements;  $W_s$  = Warburg impedance (short)

**Table 6.2** Values of the elements in an equivalent electric circuit fitted in the Nyquist plots shown in Figure 6.8B (error percentage for each element is given in parentheses)

Elements	Au (%)	NP Au (%)	Treated NP Au (%)
$R_s$ ( $\Omega \text{ cm}^{-2}$ )	11.49 (0.28)	2.77 (0.19)	2.56 (0.12)
CPE1-T ( $\mu\text{F cm}^{-2}$ )	0.45 (1.25)	23.03 (1.56)	50.99 (1.51)
CPE1-P	0.82 (0.17)	0.84 (0.47)	0.86 (0.41)
$R_1$ ( $\Omega \text{ cm}^{-2}$ )	781.40 (1.19)	32 (1.17)	13.65 (1.24)
CPE2-T ( $\mu\text{F cm}^{-2}$ )	2.19 (4.88)	789.97 (3.78)	1279.40 (3.43)
CPE2-P	0.80 (4.92)	0.83 (4.51)	0.85 (3.23)
$R_2$ ( $\Omega \text{ cm}^{-2}$ )	399.55 (3.80)	21.56 (4.08)	9.20 (4.23)
W-R ( $\Omega \text{ cm}^{-2}$ )	160.60 (3.95)	11.52 (4.78)	8.13 (4.47)
W-T (s)	6.16 (4.87)	3.51 (3.90)	1.74 (4.54)
W-P	0.50 (3.77)	0.50 (4.89)	0.50 (4.05)

$R_s$ : solution resistance; CPE-T/CPE-P: elements of constant phase element;  $R_1$  and  $R_2$ : charge transfer resistance; W-R/W-T/W-P elements of Warburg impedance associated to diffusion resistance

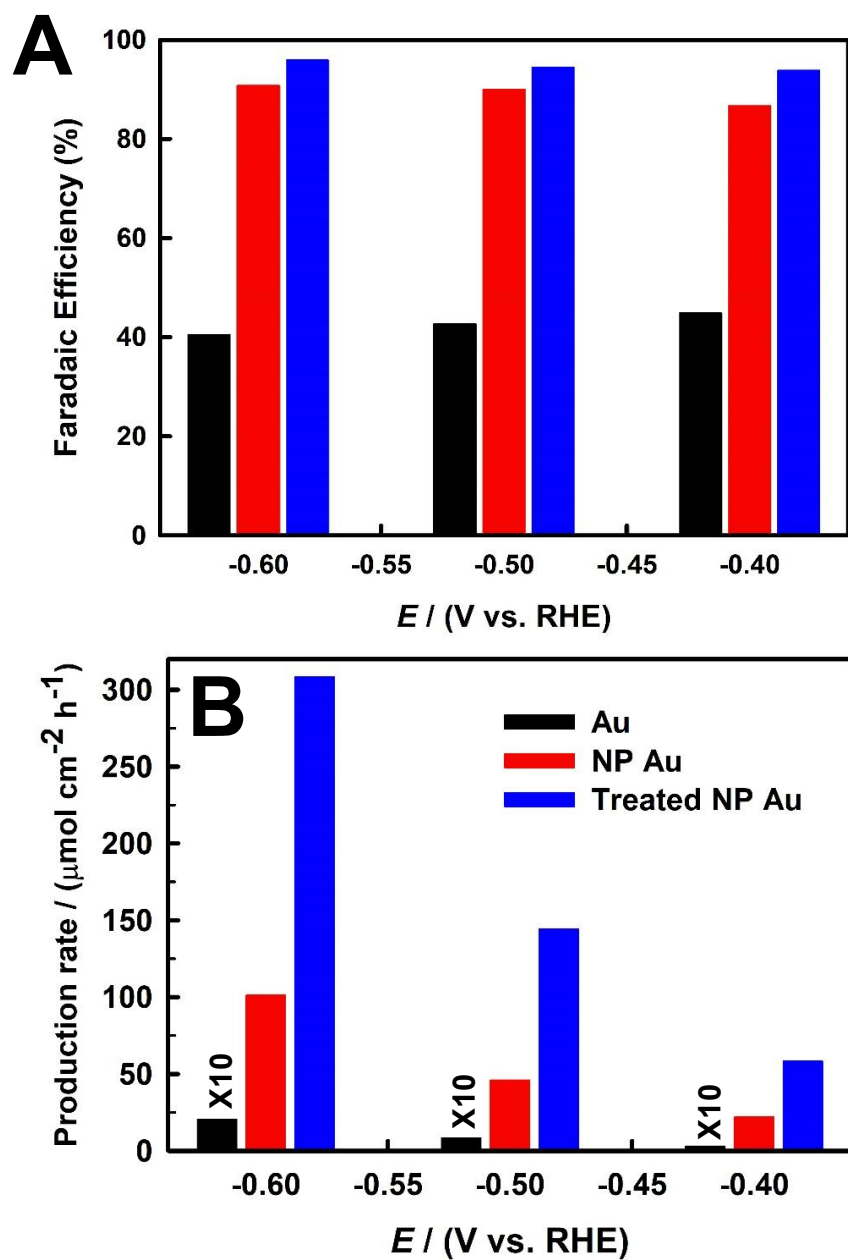
Electrochemical impedance spectroscopy (EIS) was employed to measure the charge-transfer resistance for the electrochemical reduction of  $\text{CO}_2$  on the prepared Au electrodes. Figure 6.8B displays the Nyquist plots of the Au, NP Au, and acid-treated NP Au electrodes recorded in a  $\text{CO}_2$ -saturated 0.1 M  $\text{NaHCO}_3$  solution at -0.4 V (vs. RHE), where  $Z_{re}$  and  $Z_{im}$  expressed the real and imaginary components, respectively. The impedance curves of the Au and NP Au electrodes revealed two semicircles in the full range of frequency, whereas the treated NP Au exhibited a semi-circle and a half semi-circle. The two semi-circles corresponded to the two charge transfer resistances ( $R_1$  and  $R_2$ ) [31,32] that appeared in the equivalent electrical circuit (insert, Figure 6.8B), which was employed to fit the EIS spectra. The corresponding fitted results for each element, along with the percentage of errors, are listed in Table 6.2. All of the fitting



**Figure 6.9** The CA curves of the polycrystalline Au electrode (A), the NP Au electrode (B) and the acid treated NP Au electrode (C), recorded under different applied electrode potentials in CO<sub>2</sub> saturated 0.1 M NaHCO<sub>3</sub> over the 10 h electrolysis.

element errors were less than 5%, indicating that the proposed equivalent electrical circuit effectively fitted the impedance data. It was noted that the treated NP Au electrode possessed a much lower charge-transfer resistance for both R1 and R2 than did the other Au electrodes. Moreover, a short Warburg impedance ( $W_s$ ) associated with R2, and two constant phase elements (CPE1 and CPE2) were included in the equivalent circuit to fit the impedance spectra effectively. This indicated that all of the Au electrodes exhibited some capacitor-like behavior, and that a diffusion resistance was also involved during the electrochemical reduction of  $\text{CO}_2$ .

To determine the Faradic efficiency (FE) and to assess the stability of the NP Au and the acid-treated NP Au electrodes, chronoamperometry (CA) was performed in a  $\text{CO}_2$ -saturated 0.1 M  $\text{NaHCO}_3$  solution for 10 h, where  $\text{CO}_2$  was continuously purged into the solution during the entire procedure. Figure 6.9B and Figure 6.9C present the CA curves of the NP Au and treated NP Au electrodes under applied potentials of -0.4, -0.5, and -0.6 V, respectively. For comparison, the CA curves of the smooth Au electrode are presented in Figure 6.9A. The current density was increased with the increase of the applied cathodic potential for all the electrodes, where the steady-state curves were obtained during the entire electrolysis, indicating the high stability of the electrodes. The current densities of the treated NP Au (Figure 6.9C) were much higher than that of the polycrystalline Au (Figure 6.9A) and the untreated NP Au (Figure 6.9B), further confirming that the acid treatment significantly enhanced the electrocatalytic activity of the NP Au for  $\text{CO}_2$  reduction. Our GC analysis revealed that CO was produced as the primary gas product under all applied potentials during the electrochemical reduction of  $\text{CO}_2$  on both the NP Au and treated NP Au, whereas  $\text{H}_2$  was the dominant product on the polycrystalline Au.



**Figure 6.10** (A) FE of the CO formation on the polycrystalline Au (black bar), the NP Au (red bar) and the acid-treated NP Au electrodes (blue bar); (B) the CO production rates during the electrolysis of CO<sub>2</sub> under different applied potentials on the Au, the NP Au and the acid-treated NP Au electrodes.

Figure 6.10A and 6.10B compare the FE and CO production rate of the polycrystalline Au, the NP Au and the acid-treated NP Au electrodes, respectively; and their corresponding values are summarized in Table 6.3, showing that the polycrystalline Au favoured the hydrogen evolution reaction with less than 45% FE for CO formation. In contrast, a superb affinity for the selective CO generation from the CO<sub>2</sub> reduction was attained with ~90% FE at the NP Au and ~95% FE at the treated NP Au electrodes. As the CO formation rate at the smooth Au electrode was so low, it was enlarged by 10 times in Figure 6.10B for comparison. The rate of the CO generation was increased with the increase of the cathodic potential from -0.4 to -0.6 V for all the Au electrodes. The rate of the CO formation on the NP Au and the acid treated NP Au electrodes was substantial higher than that at the smooth Au electrode, for instance, 49.8 times greater at the NP Au electrode and 151.8 times higher at the treated NP Au electrode at the applied potential of -0.6 V (Table 6.3).

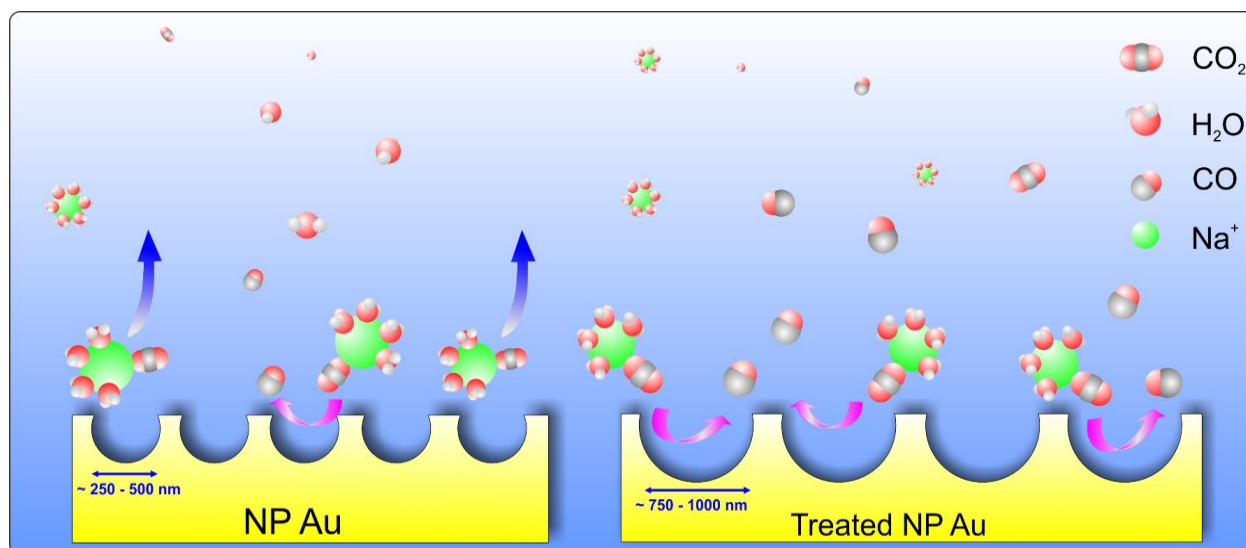
As shown in Figure 6.10A and 6.10B, the acid treated NP Au electrode exhibited greater FE and approximately three times higher CO generation rate than the NP Au electrode at all the applied cathodic potentials although it had a smaller EASA compared with the NP Au electrode

**Table 6.3** The FE and production rate of the CO at different Au electrodes at different applied electrode potentials.

Electrode	-0.4 V		-0.5 V		-0.6 V	
	FE (%)	PR ( $\mu\text{mol cm}^{-2} \text{h}^{-1}$ )	FE (%)	PR ( $\mu\text{mol cm}^{-2} \text{h}^{-1}$ )	FE (%)	PR ( $\mu\text{mol cm}^{-2} \text{h}^{-1}$ )
Au	44.89	0.30	42.68	0.84	40.47	2.03
NP Au	86.67	21.91	89.98	45.98	90.48	101.19
Acid treated NP Au	93.79	85.24	94.44	144.33	95.86	308.19

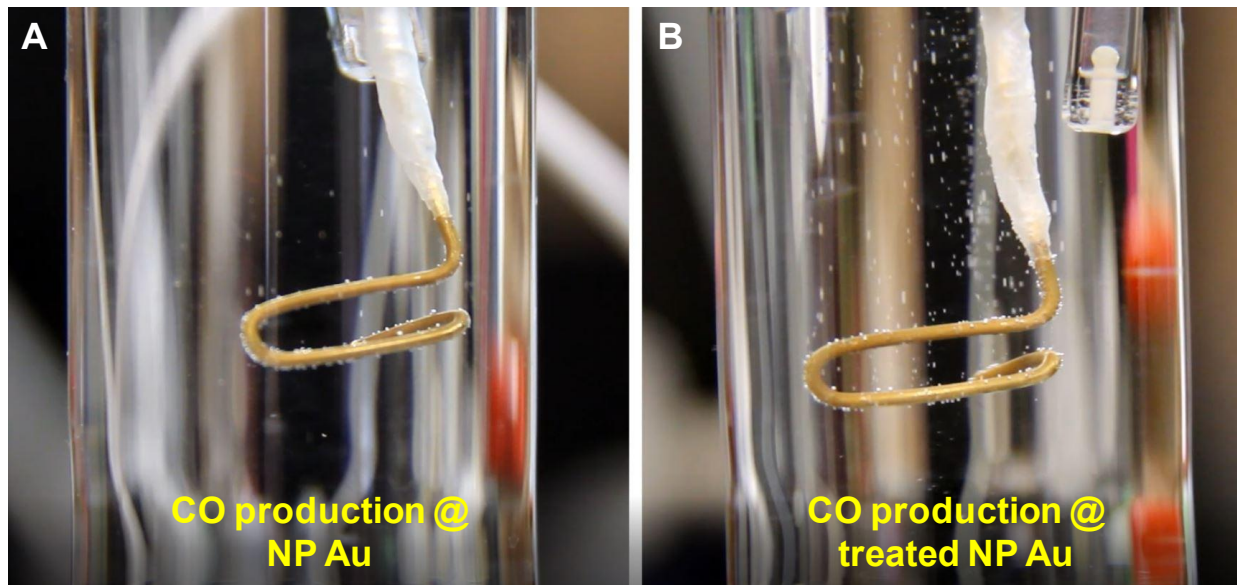
FE: Faradaic efficiency; PR: production rate





**Figure 6.11** Schematic diagram of the proposed mechanism for the accessibility of the solvated CO<sub>2</sub> into the pores of NP Au (left) and treated NP Au (right) during the electrochemical reduction of CO<sub>2</sub> to CO.

(Table 6.1). Such a significant increase in the catalytic activity after the acid treatment could be attributed to two major factors: the active sites effect and the pore size effect. As shown from the EDX, XRD and XPS analysis, the remaining Zn (~7%) in the NP Au was effectively removed by the acid treatment, which would create more active sites. This was supported by the EIS study (Figure 6.8B), where lower charge-transfer resistances R1 and R2 for the CO<sub>2</sub> reduction were observed at the acid treated NP Au electrode. In addition, as seen from the SEM images (Figure 6.1), the pore size was almost doubled after the acid treatment, which facilitated the transfer of the solvated CO<sub>2</sub> to the double-layer region and the departure of the generated CO gas from the pore cavity, as illustrated in Figure 6.11. In a CO<sub>2</sub>-saturated 0.1 M NaHCO<sub>3</sub> solution, the dissolved CO<sub>2</sub> molecules and the HCO<sub>3</sub><sup>-</sup> and CO<sub>3</sub><sup>2-</sup> ions are the possible electroactive species; and they reach equilibrium in the bulk electrolyte. It has been reported that the hydration number of CO<sub>2</sub>, HCO<sub>3</sub><sup>-</sup> and CO<sub>3</sub><sup>2-</sup> in a dilute solution is approximately 3.0, 5.5 and 10.2, respectively



**Figure 6.12** A video clip of CO evolution resulting from CO<sub>2</sub> electrolysis at -0.6 V in CO<sub>2</sub>-saturated 0.1 M NaHCO<sub>3</sub> on the NP Au electrode (A) and the acid treated NP Au electrode (B).

[33,34]. In addition, Na<sup>+</sup> ions could be solvated by CO<sub>2</sub> molecules, resulting in a large structured electroactive CO<sub>2</sub> species [35]. Moreover, the generated CO bubbles could be trapped in the pore cavity if the pore size of the NP Au was small, thus reducing the accessibility of the solvated CO<sub>2</sub> molecule to the active sites. This is consistent with the recent observation of the C<sub>2</sub>H<sub>4</sub> formation at porous Cu catalysts, where the pore diameter played an important role in the CO<sub>2</sub> reduction [36,37]. As illustrated in Figure 6.11, the accessibility for the solvated CO<sub>2</sub> into the pores of the NP Au and the treated NP Au played an important role in the electrochemical reduction of CO<sub>2</sub>. This was further supported by a photograph (Figure 6.12) that was captured during the electrochemical reduction of CO<sub>2</sub> in a CO<sub>2</sub>-saturated 0.1 M NaHCO<sub>3</sub> solution at -0.6 V, where a much larger CO evolution occurred on the treated NP Au in contrast to the untreated NP Au electrode.

## 6.4 Conclusions

In summary, we demonstrated a facile electrochemical alloying/dealloying approach in conjunction with an acid treatment to fabricate a unique 3D nanoporous Au network structure, which served as a high-performance electrocatalyst for the efficient and selective conversion of CO<sub>2</sub> to CO. The acid-treated NP Au showed a superb FE of 95.86% with an extremely high CO production rate at the applied potential of -0.6 V vs. RHE in a CO<sub>2</sub>-saturated 0.1 M NaHCO<sub>3</sub> solution. Aside from its high EASA, the pore dimensions of the formed 3D network structures and the additional active sites played a vital role toward increasing the catalytic activity of the Au, due to the high accessibility of the solvated CO<sub>2</sub> into the pore cavity, which enabled an effective utilization of the localized electric field. The high current density, low charge-transfer resistance, large production rate, and high stability make the acid-treated NP Au electrode promising for the efficient electrochemical reduction of CO<sub>2</sub>. Moreover, this study might inspire researchers to ponder the significant effects of the pore dimensions of nanoporous structures in order to design desirable electrocatalysts for robust CO<sub>2</sub> reduction.

#### Reference:

- [1] M. Liu, Y. Pang, B. Zhang, P. D. Luna, O. Voznyy, J. Xu, X. Zheng, C. T. Dinh, F. Fan, C. Cao, F. P. G. de Arquer, T. S. Safaei, A. Mepham, A. Klinkova, E. Kumacheva, T. Filleter, D. Sinton, S. O. Kelley, E. H. Sargent, *Nature* **2016**, 537, 382.
- [2] N. V. Rees, R. G. Compton, *Energy Environ. Sci.* **2011**, 4, 403.
- [3] T. Sheng, S.-G. Sun, *Chem. Commun.* **2017**, 53, 2594.
- [4] A. B. Soliman, R. R. Haikal, Y. S. Hassan, M. H. Alkordi, *Chem. Commun.* **2016**, 52, 12032.
- [5] M. N. Hossain, J. Wen, A. Chen, *Sci. Rep.* **2017**, 7, 3184.
- [6] X. Guo, Y. Zhang, C. Deng, X. Li, Y. Xue, Y.-M. Yan, K. Sun, *Chem. Commun.* **2015**, 51, 1345.

- [7] M. N. Hossain, J. Wen, S. K. Konda, M. Govindhan, A. Chen, *Electrochem. Commun.* **2017**, 82, 16.
- [8] B. A. Rosen, A. Salehi-Khojin, M. R. Thorson, W. Zhu, D. T. Whipple, P. J. A. Kenis, R. I. Masel, *Science* **2011**, 334, 643.
- [9] S. Gao, Y. Lin, X. Jiao, Y. Sun, Q. Luo, W. Zhang, D. Li, J. Yang, Y. Xie, *Nature* **2016**, 529, 68.
- [10] M. Aresta, A. Dibenedetto, A. Angelini, *Chem. Rev.* **2014**, 114, 1709.
- [11] H. A. Hansen, J. B. Varley, A. A. Peterson, J. K. Nørskov, *J. Phys. Chem. Lett.* **2013**, 4, 388.
- [12] D. Kim, J. Resasco, Y. Yu, A. M. Asiri, P. Yang, *Nat. Commun.* **2014**, 5, 4948.
- [13] J. S. Gao, X. Jiao, Z. Sun, W. Zhang, Y. Sun, C. Wang, Q. Hu, X. Zu, F. Yang, S. Yang, L. Liang, J. Wu, Y. Xie, *Angew. Chem. Int. Ed.* **2016**, 55, 698.
- [14] Y. H. Chen, C. W. Li, M. W. Kanan, *J. Am. Chem. Soc.* **2012**, 134, 19969.
- [15] H. Mistry, R. Reske, Z. Zeng, Z.-J. Zhao, J. Greeley, P. Strasser, B. R. Cuenya, *J. Am. Chem. Soc.* **2014**, 136, 16473.
- [16] E. B. Nursanto, H. S. Jeon, C. Kim, M. S. Jee, J. H. Koh, Y. J. Hwang, B. K. Min, *Catal. Today* **2016**, 260, 107.
- [17] G. A. Olah, G. K. S. Prakash, A. Goeppert, *J. Am. Chem. Soc.* **2011**, 133, 12881.
- [18] W. Zhu, Y.-J. Zhang, H. Zhang, H. Lv, Q. Li, R. Michalsky, A. A. Peterson, S. Sun, *J. Am. Chem. Soc.* **2014**, 136, 16132.
- [19] G. B. Stevens, T. Reda, B. Raguse, *J. Electroanal. Chemistry* **2002**, 526, 125.
- [20] Z. P. Jovanov, H. A. Hansen, A. S. Varela, P. Malacrida, A. A. Peterson, J. K. Nørskov, I. E. L. Stephens, I. Chorkendorff, *J. Catalysis* **2016**, 343, 215.
- [21] R. Kortlever, I. Peters, C. Balemans, R. Kas, Y. Kwon, G. Mul, M. T. M. Koper, *Chem. Commun.* **2016**, 52, 10229.
- [22] D. R. Kauffman, D. Alfonso, C. Matranga, H. Qian, R. Jin, *J. Am. Chem. Soc.* **2012**, 134, 10237.
- [23] T. Cheng, Y. Huang, H. Xiao, W. A. Goddard III, *J. Phys. Chem. Lett.* **2017**, 8, 3317.

- [24] S. Back, M. S. Yeom, Y. Jung, *ACS Catal.* **2015**, 5, 5089-5096.
- [25] A. A. Peterson, J. K. Nørskov, *J. Phys. Chem. Lett.* **2012**, 3, 251.
- [26] H. J. Wang, C. W. Zou, B. Yang, H. B. Lu, C. X. Tian, H. J. Yang, M. Li, C. S. Liu, D. J. Fu, J. R. Liu, *Electrochem. Commun.* **2009**, 11, 2019.
- [27] R. E. Cable, R. E. Schaak, *Chem. Mater.* **2007**, 19, 4098.
- [28] J. H. Lin, Y. J. Huang, Y. P. Su, C. A. Liu, R. S. Devan, C. H. Ho, Y. P. Wang, H. W. Lee, C. M. Chang, Y. Liou, Y. R. Ma, *RSC Adv.* **2012**, 2, 2123.
- [29] X. J. Chen, Y. Y. Wang, J. J. Zhou, W. Yan, Li, H. X. J. J. Zhu, *Anal. Chem.* **2008**, 80, 2133
- [30] Z. Liu, A. Nemeč-Bakk, N. Khaper, A. Chen, *Anal. Chem.* **2017**, 89, 8036.
- [31] D.-W. Yang, Q.-Y. Li, F.-X. Shen, Q. Wang, L. Li, N. Song, Y.-N. Dai, J. Shi, *Electrochim. Acta* **2016**, 189, 32.
- [32] V. Lates, A. Falch, A. Jordaan, R. Peach, R. J. Kriek, *Electrochim. Acta* **2014**, 128, 75.
- [33] T. Sadhukhan, I. A. Latif, Sambhu N. Datta, *J. Phys. Chem. B* **2014**, 118, 8782.
- [34] P. D. Dopieralski, A. Burakowski, Z. Latajka, I. Olovsson, *Chem. Phys. Lett.* **2011**, 507, 89.
- [35] L. J. Criscenti and R. T. Cygan, *Environ. Sci. Technol.* **2013**, 47, 87.
- [36] Y. Pang, T. Burdyny, C.-T. Dinh, M. G. Kibria, J. Z. Fan, M. Liu, E. H. Sargent, D. Sinton, *Green Chem.* **2017**, 19, 4023.
- [37] A. Dutta, M. Rahaman, N. C. Luedi, M. Mohos, P. Broekmann, *ACS Catal.* **2016**, 6, 3804.

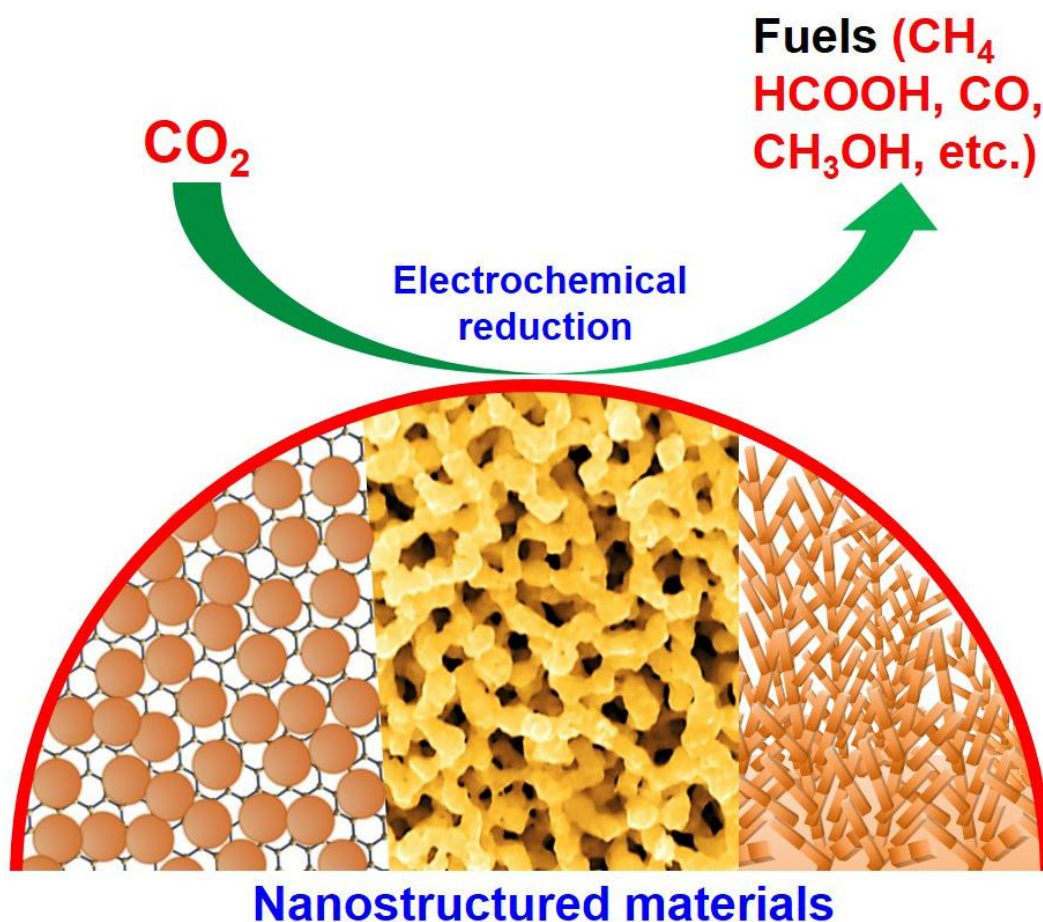
## Chapter 7: Summary and future directions

### 7.1 Summary

There is a great interest in the conversion of CO<sub>2</sub> to useful chemicals and fuels toward addressing the increasingly serious impacts of global climate change. The electrocatalytic reduction method is one of the potential technologies that could be employed to reduce CO<sub>2</sub> to value-added products under mild conditions. Over the last few decades, researchers have developed various electrocatalysts for the electrochemical reduction of CO<sub>2</sub> such as Cu, Au, Ag, metal alloys, and carbon-based materials. To enhance the catalytic performance of typical electrodes for the electroreduction of CO<sub>2</sub>, efforts have been invested in tailoring the formation of supernanostructures, modifying surface morphologies, increasing electrochemical surface areas and roughness factors, reducing particle dimensions, and introducing new crystal facets on electrode surfaces. Therefore, the possibility of developing highly active nanostructured catalysts for the efficient reduction of CO<sub>2</sub> is high. However, the synthesis of nanostructured materials using the conventional methods requires tedious multiple steps, including dispersion in a solvent, reaction, calcination, and drying, which is an intensive and time consuming experimental procedure. Hence, the design of facile methods for synthesizing novel nanostructured materials and new nanomaterials, while optimizing their surface structures might enhance catalytic activity and provide an efficient CO<sub>2</sub> electroreduction pathway. Therefore, this thesis project was dedicated to the development of new and novel nanostructured materials as CO<sub>2</sub> electrocatalysts through the application of novel and facile approaches. Herein, we demonstrated facile approaches for the synthesis of novel nanocomposites comprised of rGO and Cu nanoparticles, their composite thin film, Cu nanodendrites, and three-dimensional nanoporous Au toward the

efficient electrochemical reduction of CO<sub>2</sub>. The significant findings obtained in this Ph. D. project are briefly summarized below.

We successfully synthesized a novel nanostructured thin film consisting of rGO and Cu nanoparticles on a GEC surface via the facile one-pot electrochemical treatment of a precursor mixture. We also synthesized a unique nanocomposite consisting of Cu NPs and rGO, which was supported on a Cu substrate, following the same electrochemical treatment approach. To optimize the Cu-rGO catalyst surface structures, the composition and quantity of the nanocomposite were prepared and studied. Further, we developed a novel approach to synthesize uniquely structured Cu nanodendrites, which were synthesized by the electrodepositing of Cu NPs on a Ti substrate, followed by a thermal treatment with a mixed CuSO<sub>4</sub> and H<sub>2</sub>SO<sub>4</sub> solution and subsequent electrochemical treatment. Moreover, we successfully demonstrated a facile electrochemical alloying/dealloying approach, in conjunction with a H<sub>2</sub>SO<sub>4</sub> treatment, to fabricate a unique 3D nanoporous Au network structure. The morphology, surface composition, crystalline structure, and electronic state of the developed materials were examined by SEM, EDX, XRD, and XPS analysis. The SEM analysis revealed that for the optimized Cu-rGO nanocomposites, the Cu NPs with an average diameter of ~10 nm were homogeneously distributed on the rGO nanosheets. Dendritic segments with tertiary branches were formed during the synthesis of the Cu nanodendrites, whereas pore diameters ranging from ~750 to 1000 nm were obtained in the developed 3D nanoporous Au, which were revealed by SEM analysis. The co-existence of both Cu and C on the formed Cu/rGO film and Cu-rGO nanocomposites, Zn-free NP Au in the acid treated NP Au, and trace amounts of Cu(II) in the Cu nanodendrites, were confirmed by EDX and XPS analysis [1,2].



**Figure 7.1** Schematic representation of the electrocatalytic conversion of CO<sub>2</sub> into fuels on different nanostructured materials.

The electrocatalytic activity of the developed catalysts was initially investigated using LSV, CA, and EIS in the presence of CO<sub>2</sub> in 0.1 M NaHCO<sub>3</sub> (pH 6.65) with the continuous purging of CO<sub>2</sub> into the solution during the measurements. Figure 7.1 illustrates the electrochemical reduction of CO<sub>2</sub> on the developed nanostructured catalysts used in this PhD study. Very low onset potentials and high current densities on the formed catalysts were achieved by LSV and CA, respectively, indicating a high catalytic activity for the electroreduction of CO<sub>2</sub>. A much lower charge-transfer resistance for CO<sub>2</sub> reduction was observed by an EIS study of the synthesized Cu-rGO nanocomposites, whereas acid treated NP



Au revealed much higher catalytic activity toward the electrochemical reduction of CO<sub>2</sub> in an aqueous solution. Further, the effects of the applied potential on the electrochemical reduction of CO<sub>2</sub> was studied by both LSV and CA, which identified -0.6 V and -0.4 V (vs. RHE) as being the optimal applied electrode potentials for the Cu/rGO and Cu nanodendrites, respectively [1,2].

The bulk electrolysis of CO<sub>2</sub> was achieved on the developed catalysts at potentials of -0.4, -0.5, and -0.6 V (vs. RHE) in a CO<sub>2</sub>-saturated 0.1 M NaHCO<sub>3</sub> electrolyte (pH 6.65), showing that the highest SSCE of the Cu/rGO thin film for the reduction of CO<sub>2</sub> was calculated to be 69.4% at an applied potential of -0.6 V, whereas 82% SSCE was obtained on the Cu nanodendrites at -0.4 V. The GC, HPLC, and in situ electrochemical ATR-FTIR spectroscopy analyses revealed that CO, CH<sub>4</sub>, HCOOH, and oxygenates were the reduction products of CO<sub>2</sub> under the applied electrode potentials on the developed nanostructured catalysts. In addition, to the best of our knowledge, for the first time, we developed a COD analysis to quantify the overall liquid products, which provided a facile, rapid, and accurate method for the determination of the total FE for the conversion of CO<sub>2</sub> to liquid products. This COD analysis may emerge as a universal approach for quantification of the overall liquid products generated in other CO<sub>2</sub> conversion processes; for instance, the photochemical and photoelectrochemical reduction of CO<sub>2</sub>. The total FE of the Cu-rGO nanocomposite for the reduction of CO<sub>2</sub> included two parts (the formation of the gas and liquid products), which was calculated to be ~73.5% at applied electrode potentials of from between -0.4 and -0.6 V vs. RHE, whereas the FE for CO was calculated to be ~95% at the same applied electrode potentials on the acid-treated NP Au. Various metal and C-based materials have been explored for the electrochemical reduction of CO<sub>2</sub>; hence, some of the promising results that have been recently reported in the literature are compared in Table 7.1, showing that the Cu-rGO nanocomposite, Cu nanodendrites, and 3D NP

**Table 7.1** Products obtained on different catalysts from the electrochemical reduction of CO<sub>2</sub>.

Electrocatalyst	Electrode potential	Electrolyte (CO <sub>2</sub> -saturated)	Major product	Total FE (%)	Ref.
Cu NPs/GC	-1.25 V vs. RHE	0.1 M NaHCO <sub>3</sub>	CH <sub>4</sub>	76	3
AuCu <sub>3</sub>	-1.0 V vs. RHE	0.1 M KHCO <sub>3</sub>	CO	40	4
Dendritic Cu	-2.0 V vs. Ag/AgCl	0.1 M KHCO <sub>3</sub>	C <sub>2</sub> H <sub>4</sub>	80	5
Cu nanoflower	-1.6 V vs. RHE	0.1 M KHCO <sub>3</sub>	HCOOH	65	6
N-graphene	-0.84 V vs. RHE	0.5 M NaHCO <sub>3</sub>	HCOOH	73	7
Cu/CNT	-1.7 V vs. SCE	0.5 M NaHCO <sub>3</sub>	CH <sub>3</sub> OH	38.4	8
Ag/C	-0.75 V vs. RHE	0.5 M KHCO <sub>3</sub>	CO	79.2	9
OD-Cu foam	-0.8 V vs. RHE	0.5 M NaHCO <sub>3</sub>	C <sub>2</sub> H <sub>4</sub> , C <sub>2</sub> H <sub>6</sub>	55	10
Au NPs	-0.59 V vs. RHE	0.1 M NaHCO <sub>3</sub>	CO	78	11
Graphene-Sn quantum sheets	-1.8 V vs. SCE	0.1 M NaHCO <sub>3</sub>	HCOOH	89	12
OD-Cu	-0.6 V vs. RHE	0.1 M NaHCO <sub>3</sub>	HCOOH	60	13
Cu-porphyrin	-0.976 V vs. RHE	0.5 M KHCO <sub>3</sub>	CH <sub>4</sub>	37	14
B-diamond	-1.7 V vs. Ag/AgCl	CH <sub>3</sub> OH	HCHO	89	15
OD-Ag	-0.6 V vs. RHE	0.1 M KHCO <sub>3</sub>	CO	80	16
Cu <sub>2</sub> Pd	-1.8 V vs. Ag/AgNO <sub>3</sub>	0.1 M TBAPF <sub>6</sub> / CH <sub>3</sub> CN	CH <sub>4</sub>	51	17
Pd-Au	-0.6 V vs. RHE	0.1 M KH <sub>2</sub> PO <sub>4</sub> / 0.1 M K <sub>2</sub> HPO <sub>4</sub>	CO	30	18
Cu/rGO	-0.4, -0.5, -0.6 V vs. RHE	0.1 M NaHCO <sub>3</sub>	CO, HCOOH	76.6, 69.2, 74.7	Present work
Cu nanodendrites	-0.3, -0.4, -0.5, -0.6 V vs. RHE	0.1 M NaHCO <sub>3</sub>	HCOOH, Oxygenates	75.2 <sup>a</sup> , 82 <sup>a</sup> , 77.8 <sup>a</sup> , 68.5 <sup>a</sup>	Present work
Acid treated NP Au	-0.4, -0.5 and -0.6 V vs. RHE	0.1 M NaHCO <sub>3</sub>	CO	~95	Present work

a: current efficiency

Au developed in the present study exhibited excellent FE for the efficient electrocatalytic reduction of CO<sub>2</sub> at a relatively low overpotential. The rates of the formation of the products under the different applied electrode potentials were increased under higher cathodic potentials, from -0.4 to -0.6 V, and a significant increase in CO formation was observed in comparison to the formation of the other gas and liquid products on the Cu-rGO nanocomposites. The rate of the CO formation on the acid treated NP Au electrodes was substantially higher than that at the smooth Au electrode. For instance, it was 151.8 times higher at the treated NP Au electrode at an applied potential of -0.6 V, which might have been due to the high accessibility of the solvated CO<sub>2</sub> into the pore cavities that might enable the efficient utilization of the localized electric field. Moreover, the developed catalysts also demonstrated the high stability under different applied electrode potentials.

In situ electrochemical ATR-FTIR spectroscopy was further employed to investigate the consumption of CO<sub>2</sub> and the formation of intermediates and products under different applied electrode potentials, which showed that formation of formate was achieved at -0.6 V on the Cu/rGO thin film, whereas the formed Cu nanodendrites facilitate the generation of different hydrocarbons and oxygenates at an electrode potential of lower than -0.2 V vs. RHE during the electrochemical reduction of CO<sub>2</sub>. Therefore, the facile fabrication, cost-effectiveness, low charge-transfer resistance, high catalytic activity, large production rate, excellent FE, and superior stability make these materials promising for electrochemical conversion of CO<sub>2</sub> to valuable chemicals and fuels. The approach described in these studies offers a general technique to develop myriad graphene supported metal nanoparticles, to synthesize various nanostructured electrocatalysts, and to study the effects of the pore dimensions of nanoporous structures for the robust reduction of CO<sub>2</sub> [1,2].

## 7.2 Future work

Several significant achievements were made in this thesis project, including (i) the fabrication of new nanostructured catalysts for the efficient electrochemical reduction of CO<sub>2</sub>, (ii) employing a facile, rapid, and accurate COD analysis method to quantify the overall liquid products with the determination of the total FE, and (iii) a novel and facile acid treatment approach to modify the surface morphology of the metal electrodes that exhibit enhanced catalytic activity for the electroreduction of CO<sub>2</sub>. Therefore, I strongly believe that the developed nanostructured materials will be used as promising catalysts for the electrochemical reduction of CO<sub>2</sub> to value-added products toward addressing humanity's pressing environmental and energy challenges. Moreover, the novel facile synthesis approaches and COD analysis described herein may contribute to the development of new nanostructured materials, and facilitate the rapid quantitative liquid products analysis of CO<sub>2</sub> electrochemical conversions in the field, respectively. Since anthropogenic energy consumption is continuously increasing, which results in the gradual elevation of atmospheric CO<sub>2</sub> concentrations as a consequence; there is an urgent need to develop more efficient electrocatalysts and other competent technologies than those that currently exist, to balance the global carbon cycle.

The developed Cu/rGO thin film and its nanocomposites exhibited remarkable catalytic activity, high FE, and excellent stability for the electrochemical reduction of CO<sub>2</sub>. These developed nanomaterials may also be employed in various other applications, such as photochemical reduction, organic oxidation, organic synthesis, oxygen reduction, water splitting, and energy storage. Recently, rGO decorated metal nanoparticles have shown strong potential for enabling various sustainable green technologies due to their high surface area, excellent electrical conductivity, and synergistic interactions with metal particles, resulting in a significant

enhancement of catalytic activity and stability. Moreover, the facile one-step synthesis of Cu and rGO nanocomposites as CO<sub>2</sub> electrocatalysts opens the door for the development of carbon material supported transition metal nanoparticles for the efficient electrochemical reduction of CO<sub>2</sub>, as well as various other catalysis and energy applications. For example, CNT, heteroatom-doped graphene, or rGO decorated Au, Ag, Cd, Pd, or Fe nanoparticles and their nanocomposites may be synthesized following similar synthesis approaches used in this thesis project, toward efficient CO<sub>2</sub> electrolysis, water splitting, supercapacitors, and other environmental and energy applications. Furthermore, the developed COD method, which was employed to quantify the overall liquid products in this thesis project, could replace existing techniques such as HPLC, ion chromatography (IC) and NMR, for the analysis of the liquid products that are obtained from CO<sub>2</sub> electrolysis and to determine the FE.

We employed a novel and facile acid treatment approach to modify the surface morphologies of the Cu NPs and NP Au. The Cu NPs were transformed to Cu nanodendrites, and the NP Au acquired larger pores via an acid treatment. The developed Cu nanodendrites and treated NP Au, which exhibited enhanced catalytic activity for the electrochemical reduction of CO<sub>2</sub>, may, due to their versatility, also be utilized for applications spanning the areas of biochemical sensing, catalysis, optics, electronics, and spectroscopy. The formed Cu dendrites can be combined with Pt, Ag, Au, and Pd to be used as electrocatalysts in fuel cells and in water splitting for sustainable energy production. Bimetallic alloyed Cu-Au and Cu-Ag nanodendrites can be synthesized, which might be used as the efficient electrocatalysts for the reduction of CO<sub>2</sub> and increase product selectivity. On the other hand, the developed NP Au in this study could be used in sensing and actuator applications, such as the monitoring of NO in biological processes. Moreover, the facile acid treatment approach may be employed for other heavy metal electrodes

to modify their surfaces, form new nanostructures, increase the surface area, and to introduce additional electrochemically active sites. Therefore, the synthesis of different nanostructured materials using the acid treatment method could be employed to develop efficient electrocatalysts for the reduction of CO<sub>2</sub>, as well as in sensors and other environmental applications.

### Reference:

- [1] M. N. Hossain, J. Wen, S. K. Konda, M. Govindhan, A. Chen, *Electrochem. Commun.* **2017**, 82, 16.
- [2] M. N. Hossain, J. Wen, A. Chen, *Sci. Rep.* **2017**, 7, 3184.
- [3] K. Manthiram, B. J. Beberwyck, A. P. Alivisatos, *J. Am. Chem. Soc.* **2014**, 136, 13319.
- [4] D. Kim, J. Resasco, Y. Yu, A. M. Asiri, P. Yang, *Nat. Commun.* **2014**, 5, 4948.
- [5] C. Reller, R. Krause, E. Volkova, B. Schmid, S. Neubauer, A. Rucki, M. Schuster, G. Schmid, *Adv. Energy Mater.* **2017**, 7, 1602114
- [6] J.-F. Xie, Y.-X. Huang, W.-W. Li, X.-N. Song, L. Xiong, H.-Q. Yu, *Electrochim. Acta* **2014**, 139, 137.
- [7] H. Wang, Y. Chen, X. Hou, C. Ma, T. Tan, *Green Chem.* **2016**, 18, 3250.
- [8] S. S. Hossain, S. Rahman, S. Ahmed, *J. Nanomater.* **2014**, 374318.
- [9] C. Kim, H. S. Jeon, T. Eom, M. S. Jee, H. Kim, C. M. Friend, B. K. Min, Y. J. Hwang, *J. Am. Chem. Soc.* **2015**, 137, 13844.
- [10] A. Dutta, M. Rahaman, N. C. Luedi, M. Mohos, P. Broekmann, *ACS Catal.* **2016**, 6, 3804.
- [11] E. B. Nursanto, H. S. Jeon, C. Kima, M. S. Jee, J. H. Koh, Y. J. Hwang, B. K. Min, *Catal. Today* **2016**, 260 107.

- [12] F. Lei, W. Liu, Y. Sun, J. Xu, K. Liu, L. Liang, T. Yao, B. Pan, S. Wei, Y. Xie, *Nat. Commun.* **2016**, 7, 12697.
- [13] C. W. Li, M. W. Kanan, *J. Am. Chem. Soc.* **2012**, 134, 7231.
- [14] Z. Weng, J. Jiang, Y. Wu, Z. Wu, X. Guo, K. L. Materna, W. Liu, V. S. Batista, G. W. Brudvig, H. Wang, *J. Am. Chem. Soc.* **2016**, 138, 8076.
- [15] K. Nakata, T. Ozaki, C. Terashima, A. Fujishima, Y. Einaga, *Angew. Chem. Int. Ed.* **2014**, 53, 871.
- [16] M. Ma, B. J. Trzesniewski, J. Xie, W. A. Smith, *Angew. Chem. Int. Ed.* **2016**, 55, 9748.
- [17] S. Zhanga, P. Kanga, M. Bakirb, A. M. Lapidesa, C. J. Daresa, T. J. Meyer, *PNAS* **2015**, 112, 15809.
- [18] R. Kortlever, I. Peters, C. Balemans, R. Kas, Y. Kwon, G. Mulb, M. T. M. Koper, *Chem. Commun.* **2016**, 52, 10229.